Corso di dottorato di ricerca in

Informatica e Scienze Matematiche e Fisiche

Ciclo 32°

New versatile monolithic multipixel detector systems based on Silicon Drift Detectors

Dottorando

Dott. Daniela Cirrincione

Supervisore

Prof. Andrea Vacchi

Anno 2020

Se avete intenzione di insegnare alle persone a fare osservazioni, dovreste mostrare loro che ne possono tirar fuori qualcosa di meraviglioso.

Richard Feynman

Contents

List of Abbreviations and Acronyms

ASIC	Application Specific Integrated Circuit
BE	Back End
CMOS	Complementary Metal-Oxide Semiconductor
CSA	Charge Sensitive Amplifier
ENC	Equivalent Noise Charge
FBK	Fondazione Bruno Kessler
FE	Font End
FWHM	Full Width at Half Maximum
ICR	Input Count Rates
INAF	Instituto Nazionale di AstroFisica
INFN	Instituto Nazionale di Fisica Nucleare
KIT	Karlsruhe Institute of Technology
MIUR	Ministry of Education, University and Research
OCR	Output Count Rates
PCB	Printed Circuit Board
PixDD	Pixel Drift Detector
PMT	Photo-Multiplier Tube
ReDSoX	REsearch Drift for SOft X-rays
RMS	Root Mean Square
ROI	Region Of Interest
SiPM	Silicon Photo-Multiplier
SDD	Silicon Drift Detector
SESAME	Synchrotron-light for Experimental Science and Applications in the Middle East
SNR	Signal-to-Noise Ratio
XAFS	X-ray Absorption Fine Structure spectroscopy
XANES	X-ray Absorption Near Edge Structure spectroscopy
XRF	X-Ray Fluorescence

Abstract

The aim of this thesis is to present new versatile devices based on Silicon Drift Detectors (SDDs). They have excellent spatial and energy resolutions and can be used for high precision X spectroscopy for synchrotron light applications. A large number of projects was developed within the INFN ReDSoX Collaboration.

The research activity carried out, and presented in this thesis, has as its main objective the study of SDDs monolithic arrays and in particular, the development, tests, the quality and reliability evaluation of the monolithic multipixel SDD designs dedicated to the numerous specific applications in synchrotron radiation and astrophysics.

In detail for synchrotron radiation applications, the various phases of the developments are described:

- Customized sensor design based on the destination use of the detector
- Various progressive phases of testing and optimization of the SDD element
- Progression to improve the reliability and stability of the integrated system performance
- Optimisation and final characterization on the beamline of the complete system

In particular, monolithic arrays of SDDs in dedicated designs will be used for the XAFS beamline of the SESAME synchrotron in Jordan for EXAFS spectroscopy, and for the TwinMic beamline of the Elettra Trieste synchrotron, for spectromicroscopy.

This thesis work has led to the development and the substantial improvement of performances of detection systems for both XAFS-SESAME and TwinMic beamlines.

Introduction

Experimental physics faces new and unique challenges. In this context it is essential to have advanced tools that can face up to these challenges in the context of international competition where it is important to achieve high quality and performance. The advanced tools that are the subject of my doctoral study and of this thesis are the Silicon Drift Detectors (SDDs) and new versatile monolithic multipixel detector systems based on them, dedicated to the applications in astrophysics and to synchrotron radiation.

SDDs have good energy resolution due to the small size and capacity of the readout anode. Coupled to a dedicated low noise FrontEnd Electronics can be used for fast high precision X spectroscopy.

This sensor has a remarkable versatility, specifically the design is customizable for each project, the geometry can be adapted to the needs of measurement allowing assessable improvement in efficiency and solid angle coverage.

A complete production chain staring from a customized project has been setup according to the needs of the specific beamlines. My job has been to follow and coordinate this progression from the first test of the prototypes to the final characterization of the full detection system.

The most relevant output of this effort is the XAFS-SESAME detection system whose SDD sensors matrix is new and unique showing unmatched characteristics. It has to be noted that it is not a laboratory development but a completely engineered and integrated system that has been delivered to the SESAME laboratory in Amman. All characteristics have been previously of the delivery verified at the analogous XAFS beamline of Elettra Sincrotrone Trieste.

My personal contribution was to grant this work progression taking care of every step from testing and integration of the detection system to the edition of the user manual which is annex in this document.

Many of the intermediate results have already been published. In some cases in-depth analyses of the data are still in progress and the first qualitative results will be presented here.

This thesis is organized as follows:
the first chapter gives a brief overview about the Silicon Drift Detectors, from

the PN junction to the basic detector principles.

The second chapter describes one aspect of the sensor optimization which I personally followed namely the mapping of the single SDD cell collection area.

The third chapter introduces the customization aspect for synchrotron radiation detector system. The importance of dedicated design according to the specifications of the beamline scientist is underlined. In fact each beamline has different needs in order to achieve and optimize its scientific objectives.

In the fourth chapter the XAFS-SESAME Detector System is describes in detail together with a sample of the most significant tests and the results of the final characterization.

The fifth chapter is about the detector system dedicated to the TwinMic beamline at Elettra Sincrotrone Trieste. This is a different challenging dedicated development to which I have had the chance to give a significant contribution. This study was initiated in collaboration with beamline scientists and regarded also the possibility to exploit the detector geometry for topographic studies of samples.

In the sixth chapter a parallel effort, to which I contributed, for the use of similar detector in astrophysics is reported. It is an interesting application which extend the range of sensitivity of the detector system to higher energy.

The seventh chapter concerns the natural development of this state-of-the-art technology. A new multipixel detector is described.

Appendix A presents the ReDSoX Collaboration.

Appendix B gives the timeline of my work.

Appendix C contains the XAFS-SESAME Detector System datasheet and FICUS software manual which I personally wrote.

Below is a graphic representation of the thesis structure [Fig. 1].

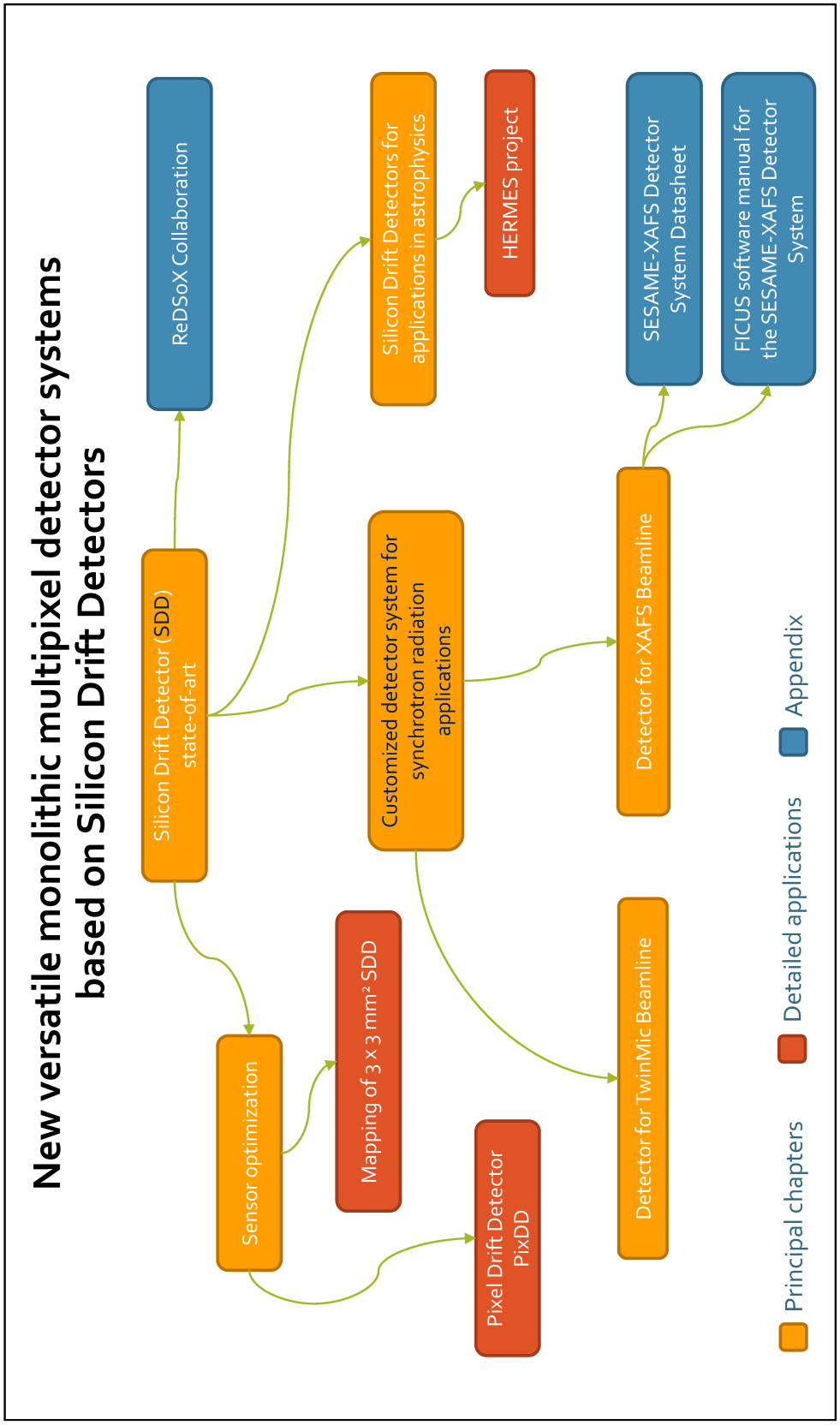

FIGURE 1: Infographic representing the structure of the thesis

Chapter 1

Brief introduction to Silicon Drift Detectors (SDDs)

The Silicon Drift Detectors (SDD) are radiation detectors and are part of the solid-state detector family. In the 1983 SDDs were proposed by Emilio Gatti and Pavel Rehak as a new type of solid-state drift chamber. The main feature of these devices is the possibility of having a small electrode collection, in this way you can have a very small capacity, with the effect of having a low noise electronic [46, 45, 47]. For this, and other features described below, suitable to be the ideal detector for high-resolution X-ray spectroscopy.

1.1 From silicon to SDD

The objective of any detection system is to measure a signal as accurately as possible. The challenge is to find the right way to do this, i.e. to find for each signal to be measured the best way to do it.

Especially with regard to the observation of high-energy emission phenomena, it has been necessary to develop, through new theories and technologies, more efficient sensors adapted to the needs of measurements in the X-band of the electromagnetic spectrum. Among the main X-ray detectors developed in recent decades are proportional counters, microcalorimeters, scintillators, and solid state detectors. In particular, the latter have had a great development linked to research carried out on semiconductors (silicon and germanium). In solid state detectors, the interaction of X-ray photons with the sensor electrons is therefore exploited. In fact, this type of detector base their operation on the generation of an electron - hole pair, implemented by the passage of an ionizing particle, within a sensitive area.

Semiconductors are elements belonging to group IV of the periodic table. They have a Face Centered Cubic (FCC) structure in which each atom is surrounded by 4 equidistant atoms. The 4 electrons of the outer orbital of each

atom are shared and form covalent bonds. At low temperature all the electrons are bound to the atoms, at higher temperature thermal vibrations can break these bonds and some electrons can pass from the valence band to the conduction band. This is possible because in semiconductors the band gap between the conduction and valence band is different from that of insulators and conductors: insulators in fact have a very large band gap (which makes it impossible for electrons to jump from the valence band to the conduction band), metals instead do not have the band gap because there is an overlap of the bands of valence and conduction [Fig. 1.1]. Typical value of the band gap at room temperature are 1.12 eV for silicon and 0.67 eV for Germanium, so compared this with the thermal voltage at room temperature, it occur that in semiconductors the electrons occupy the conduction band. In this process it must be underlined that the bonds left free by these electrons are called holes. the nearby valence electrons can fill the hole and leave another one in its previous place. The process can be iterated and thus give a general effect of a positive charge mode, holes in the valence band, as well as that of the electrons in the conduction band. In an intrinsic semiconductor there are the same number of electrons and holes [80, 53, 52].

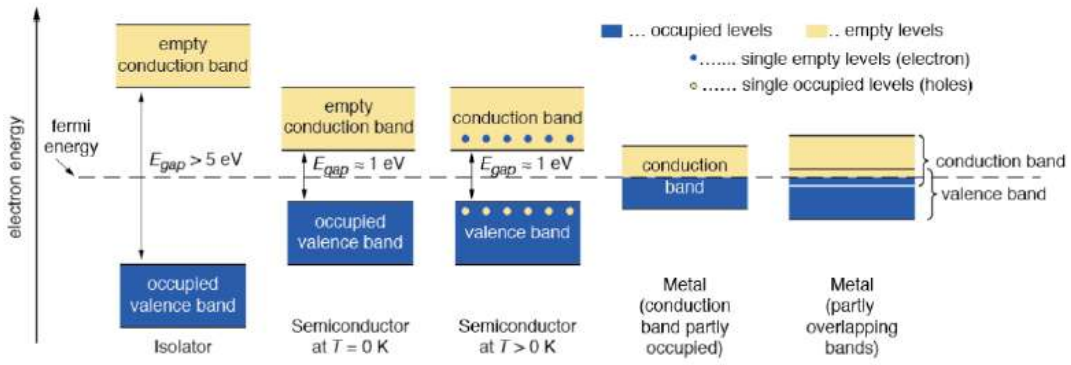

FIGURE 1.1: Scheme of energy band structure of materials.

It is possible to modify the characteristics of a semiconductor by doping, i.e. by replacing a small number of lattice atoms with atoms of elements of neighbouring groups in the periodic table:

- n-doping with an element of group V (donors), to have an additional valence electron
- p-doping with an element of group III (acceptors), to have one less electron of valence

In this case the doped semiconductor is called extrinsic. The addition of donor atoms introduces permitted energy levels for electrons just below the

conduction band. The addition of acceptor atoms introduces permitted energy levels for gaps just above the valence band [80, 53, 52].

1.1.1 PN junction

When two different semiconductors (one of p-type, one of n-type) are brought into contact with each other, a PN junction (or diode) is made [Fig. 1.2]. The electrons tend to move by diffusion from zone N to zone P, where they are in considerably smaller number, instead the holes will be diffused from zone P to zone N. The process of diffusion stops quickly once equilibrium is achieved. The electrons and holes leave the positive ions of the donor atoms and the negative ions of the acceptor atoms. The electrostatic field due to these charges, fixed in their reticular positions, opposes the diffusion motion by deforming the valence and conduction bands. A depletion zone is created in the junction area without free charge-carriers (depletion zone). If the dimensions of the two doped p and n conductors are different, the depletion region will be asymmetrical [80, 53, 57].

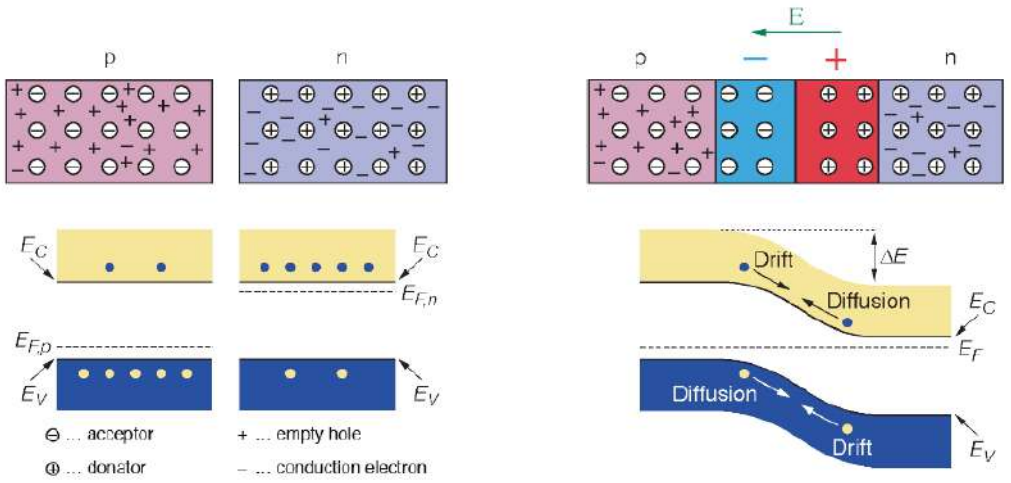

FIGURE 1.2: Pictures of two different semiconductors (one of p-type, one of n-type) on the left and of a PN junction on the right, and the respective schemes of the conduction and valence zones.

In Figure 1.3 the current-voltage characteristic of a PN junction. If an external potential Vp > Vn (direct polarization) is applied, electrons and holes move towards the emptied area. If the voltage is sufficient to overcome the existing potential barrier, the holes and electrons combine with each other, giving rise to a current, called diffusion current [Fig. 1.4 (**a**)]. Instead, by the application of an external potential Vn > Vp (reverse polarization), electrons and holes move away from the emptied zone and and increases the size of the latter. A potential barrier is generated that prevents the passage of the current,

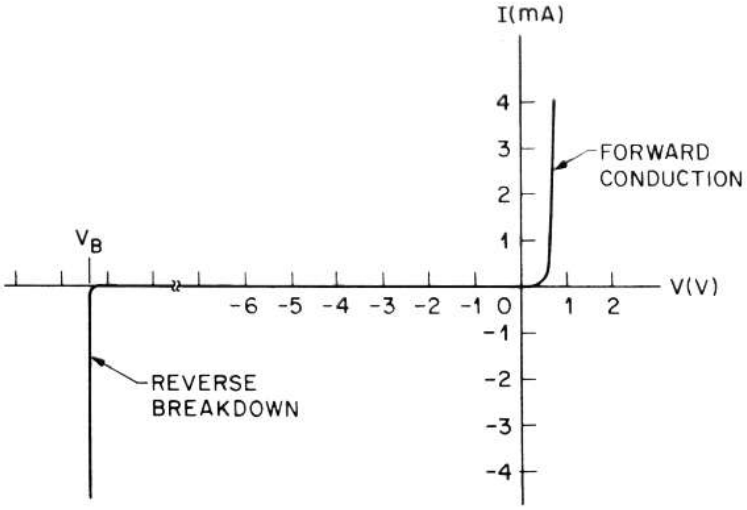

FIGURE 1.3: Current-voltage characteristic of a PN junction [80].

and only a very weak current is circulated due to minority charges called drift current [Fig. 1.4 (**b**)]. In a reverse polarization diode, however, flows a weak current called leakage current (depends on the quality of the silicon, the design and manufacturing method of the junction). This is caused by the thermally produced electron-hole pairs which, due to the applied electric field, do not recombine but are separated and their motion originates this current. In this case the depletion zone can be used as a detector [80, 53, 57].

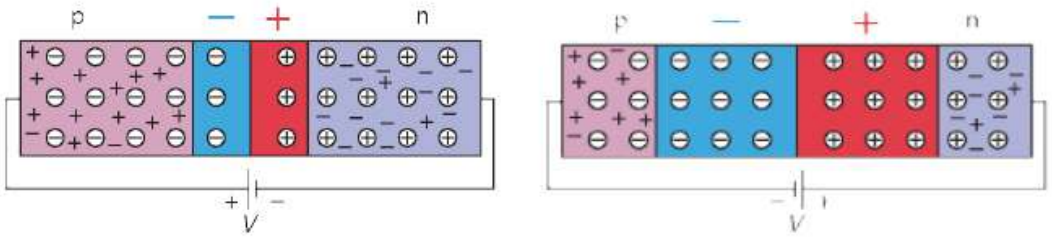

FIGURE 1.4: (**a**) Picture of the PN junction in direct polarization - (**b**)] Picture of the the PN junction in reverse polarization.

In a diode made with a PN junction the P side is called an anode and the area corresponding to the N side is called a cathode. In a junction used as detector, the depletion voltage is defined as the minimum voltage at which the device is completely depleted.

1.2 SDD and its working principle

The Silicon Drift Detector is a semiconductor detector invented by E. Gatti and P. Rehak in 1983 exploiting the planar technology for the production of

silicon detector, started in 1980s, and the idea of sideway depletion. The SDDs are proposed for the detection of ionizing radiation and particles, and for spectroscopy because they have a good energy resolution, and they can also be designed to provide high accuracy in the determination of the interaction position [45, 47, 51, 19].

The operating principle of SDDs for radiation detection is similar to that of a PN diode [Fig. 1.5] [80, 57, 79]. The silicon bulk constitutes the active volume of the sensor. A completely fully depleted part of the device is used, therefore without free charge carriers. Radiation incident on the device looses energy via ionization of the silicon atoms releasing, directly or by secondary interactions, electron and hole pairs. The amount of charge liberated in the crystal, proportional to the energy loss, is the signal to be measured. Electron-hole pairs are collected and converted into a measurable signal. When an electron - hole pair is created, there is a coupling between electrodes and charges (both positive and negative). As soon as the charges move, the charge induced to the electrodes changes and the induced current (expressed mathematically by the Branch theorem) that depends on this coupling changes continuously while the charges move in the junction. [80, 53, 57].

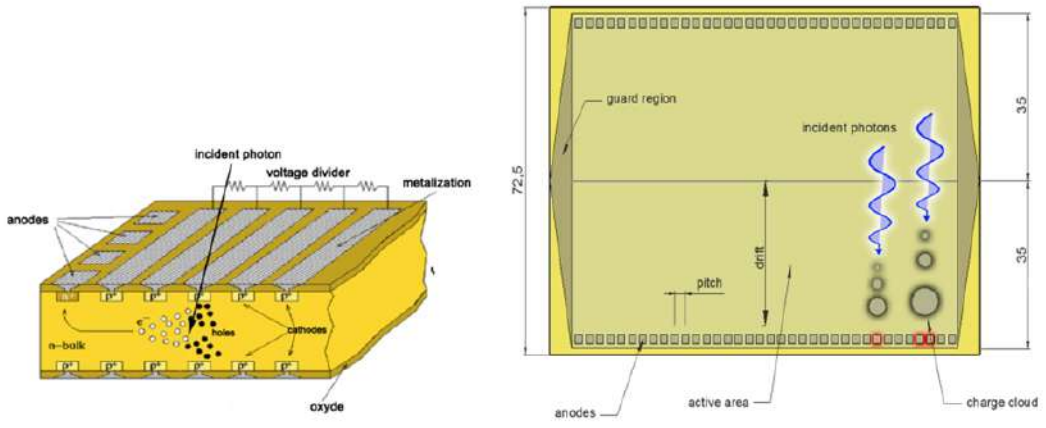

FIGURE 1.5: SDD working principle [10].

The drift chamber is generally built on a doped silicon substrate n. On both sides are implanted into the surface of the p+ electrodes, commonly called cathodes, which are used to deplete the detector and impose an electric field inside it. On one side of the device (commonly called the n side) one or more of the following are implanted n+ electrodes that act as anodes for collecting the charge generated within the emptied region. A fairly high negative voltage is applied to the cathodes so as to completely depleted the substrate n [Fig. 1.6] and create an electric field that directs the electrons towards anodes and

captures on the cathodes the holes created by the arrival of a photon X. The number of electrons collected by the anode is proportional to the energy of the incident photon [46, 57, 26].

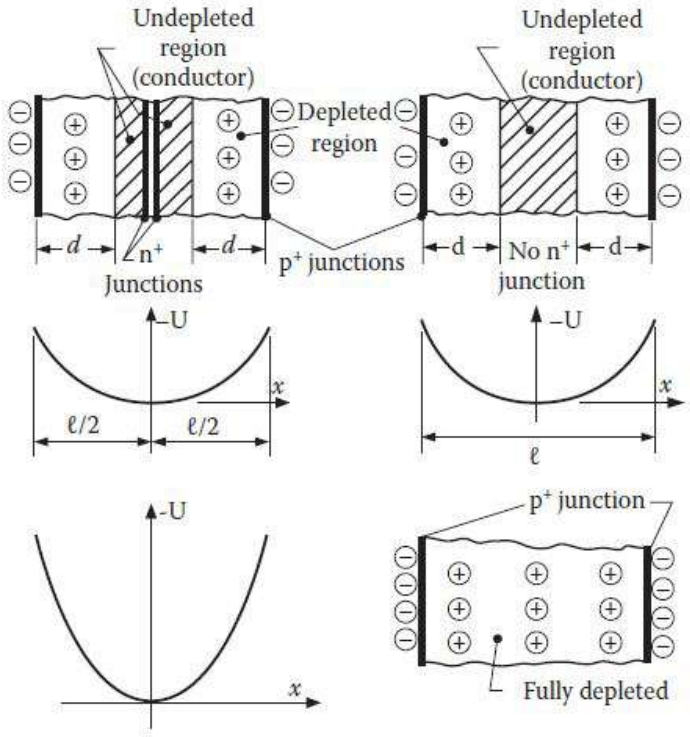

FIGURE 1.6: Depletion in an SDD: scheme of the situation in the diodes and of the corresponding potential energy of the electrons [46, 56].

The electrons are guided to the collection anodes through the potential: in fact, the minimum of the potential is located right at these collection electrodes. It is possible to both change the collection speed by changing the voltage [Fig. 1.7].

1.2.1 Readout chain, noise and energy resolution

A typical readout chain includes: a preamplifier, a pulse-shaping filter, a peak detector, an analog-to-digital (ADC) converter, and an acquisition system.

Silicon Drift Detectors are readout with Charge Sensitive Amplifiers (CSA) followed by a shaping circuit to optimize noise performance.

SIRIO preamplifier

SIRIO charge preamplifiers is an Ultra Low Noise CMOS Charge Sensitive Preamplifier. It has been specifically designed by Politecnico of Milano for high resolution X-ray spectrometry with SDDs. The front-end integrated circuit is

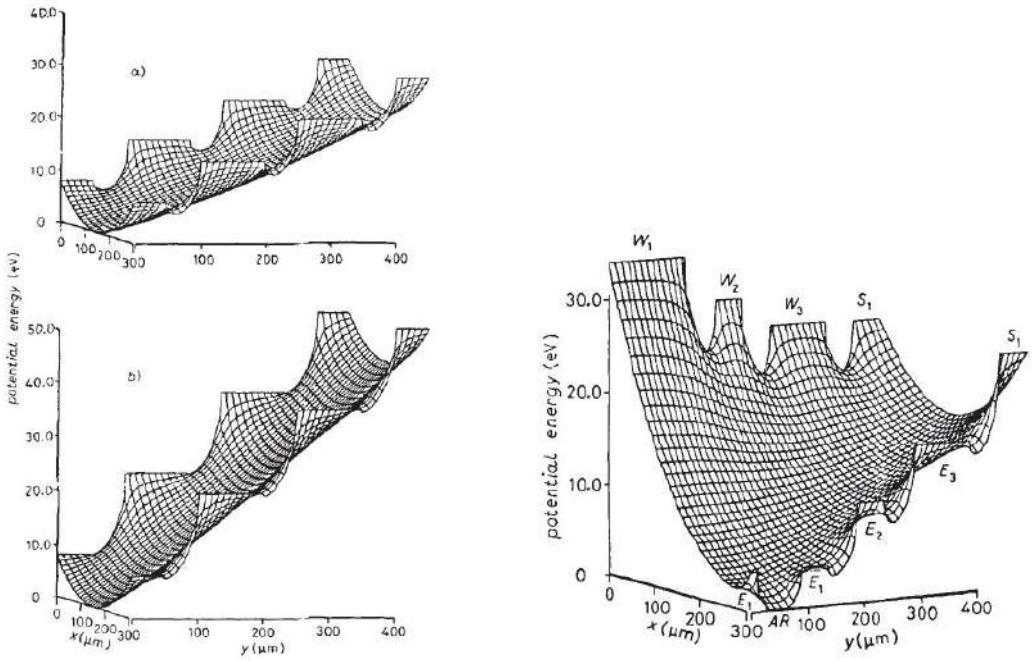

FIGURE 1.7: Gutter-shape potential energy of the electrons (**a**) with voltage differences between two neighboring cathodes of 7.5 V and 15 V in the upper and lower image respectively (**b**) in the region of anode (AR) [45].

built in 0.35 μm AMS CMOS technology and represents the state-of-art in low-noise FE electronics. SIRIO has an Equivalent Noise Charge (ENC) down to 1.2 and 0.9 electrons r.m.s. at room and at -30 °C respectively [19, 20, 23].

This preamplifier is designed to reduce 1/f noise and noise when coupled to a low capacity detector. SIRIO works with pulse reset: an impulse is generated from the control electronics that periodically downloads the feedback capability [26].

Various versions of SIRIO have been designed, in this way each SIRIO adapts best to the characteristics of the detector system and its user requirements.

Contribution to noise

The noise in a semiconductor detector system depends on various parameters: geometry of the detector, the biasing scheme, the readout electronics. The performance of a system is typically expressed as Equivalent Noise Charge (ENC), which is the charge delivered by the detector at which the signal-to-noise ratio (SNR) is unitary.

The noise in a system composed by SDDs and CSA can impact on energy resolution, for this reason is important to model it. The ENC of the system is represented by three terms: series (or voltage noise, consisting mainly of the electronic noise of the preamplifier), parallel (or current noise, consisting

mainly of current noise placed in parallel to the CSA and related to the detector leakage current or noise on the bias), and 1/f noise (or flicker) contributions [Fig. 1.8]. Understanding the source of the noise helps you understand what the optimal peaking time is for the system features. Usually in detectors with low leakage current or working at low temperature the parallel noise component becomes negligible, so the optimal peaking time is the longer one. However, it is important to remember that long peaking times increase the chances of pile-up, so it is useful to find a compromise between the energy resolution and the count-rate of the system [26].

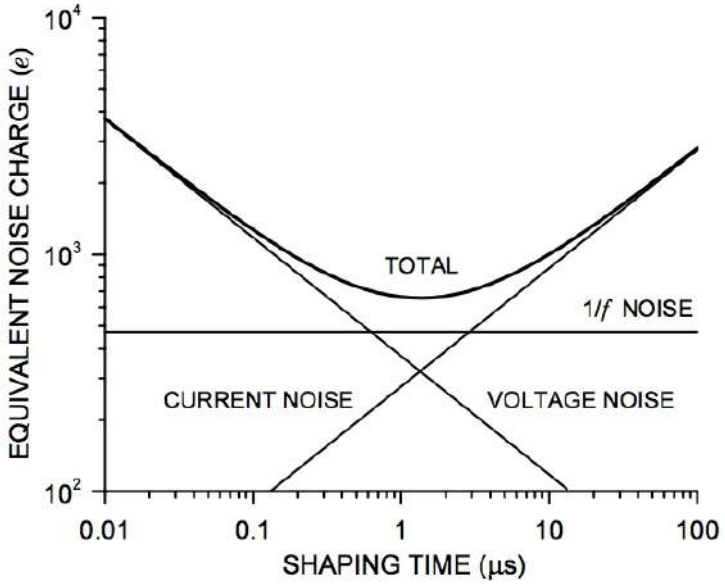

FIGURE 1.8: Graph of the ENC trend of the system as a function of shaping time.

Energy resolution

Energy resolution is one of the main parameters in an energy dispersive detector. The objective is in fact to try to minimize this value in order to obtain the best possible results. The energy resolution is usually referred to the Full Width Half Maximum (FWHM) value of a Gaussian distribution (FWHM=2.355σ).

The factors influencing energy resolution are: fluctuations in the signal charge and fluctuations in the readout electronics

$$\Delta E = \sqrt{\Delta E_{sig}^2 + \Delta E_{elec}^2}$$

.

For state detectors the first term is a theoretical limit and is due to statistical fluctuations in the charge generation process (fluctuations in the number of electron-hole pairs that are produced when the semiconductor is hit by radiation). It can be calculated as

$$\Delta E_{sig}^2 = FWHM_{stat} = 2.355\sqrt{FE_0\varepsilon}$$

where F is the Fano Factor (0.115 for Silicon), E_0 is the energy of photon and ε is mean energy required to extract an electron-hole pair (in silicon is about 3.62 eV). For the Mn-Kα line this term is 119 eV, and it is called Fano limit.

The second term it is due to the intrinsic noise in the detector and preamplifier, and it is:

$$\Delta E_{elec}^2 = 2.355ENC\varepsilon$$

This term cannot be eliminated but only reduced [14].

1.3 Main features of SDD and different geometries

The characteristics of the SDDs lead them to have an excellent signal to noise ratio due to the small size and capacity of the readout anode, and coupled to a low noise FFE can be used for fast high precision X spectroscopy. They have some important features that can be exploited. Thanks to their remarkable versatility, the geometry can be adapted to the needs of measurement: they can have large sensitive area, excellent spatial and temporal resolution, good energy resolution. They also have a good resistance to radiation and a high efficiency at low energy [47, 82, 57, 26, 78, 56].

The versatility and the customizable design specifically for the project certainly remain the special features of these detectors. It is possible to design and realize different types of SDD with different geometries by changing the number and position of the electrode implants and the shape of the potential [47, 82, 57, 26, 78, 56].

1.3.1 Linear Drift Devices

Linear Drift Devices a very simple structure with the collection anodes implanted on the two ends of the n side; the p+ electrodes are in the middle [Fig. 1.9]. The most negative voltage is applied to the central electrode, which decreases towards the anodes, while on the p side of the detector the p+ cathodes

are held at a constant negative potential. The most negative voltage is applied to the central electrode, which decreases towards the anodes, while on the p side of the detector the p+ cathodes are kept at a constant negative potential. The electron-hole pairs created to the left of the central cathode will result on the left anode, those created to the right on the right anode. In addition to making energy measurements they can also make one-dimensional position measurements, where the x coordinate is given by the time of drift of the electrons from the point where the photon hits the detector to one of the two collection anodes [45, 72, 57, 26].

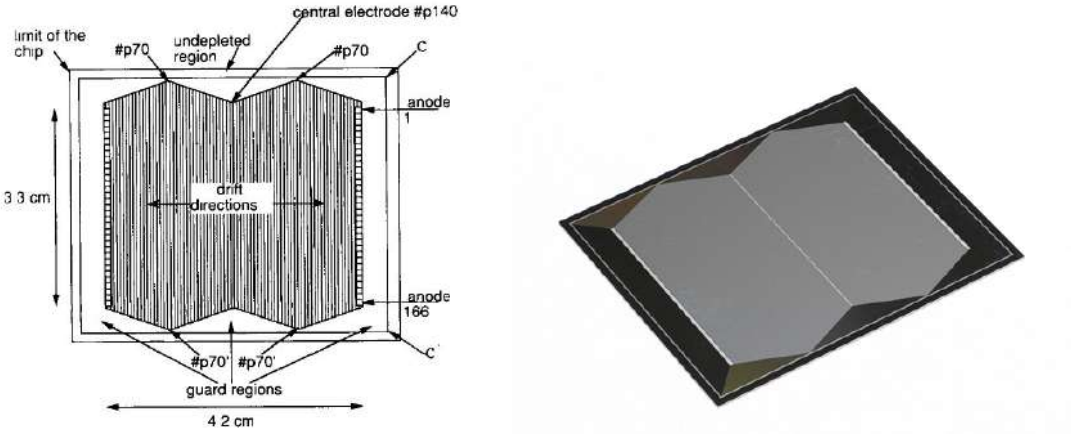

FIGURE 1.9: Linear Drift Devices (**a**) Scheme [81, 45, 57] (**b**) Photograph of the linear SDD [81, 45, 72].

1.3.2 Matrix Drift Devices

Matrix Drift Devices are an evolution of SDDs to drift linear [Fig. 1.10]. In fact, it is obtained by dividing the long anodes of the latter into several pads. The result is a detector with which the position can be measured in a two-dimensional way: where, in addition to the x, always given by the drift time, there is also have information on the y according to the anode that collected the charge [45, 72, 82, 57, 26].

1.3.3 Large Area Devices

The large area semiconductor drift detectors are developed for high resolution measurement of the position of ionizing particles and of the energy deposited in the detector. One original design of large area SDD (with an active area of 7.0 x 7.5 cm^2) was installed and used for 10 years (2007-2017) in the Inner Trackin System of the ALICE experiment at LHC [Fig. 1.11] [69, 81, 70].

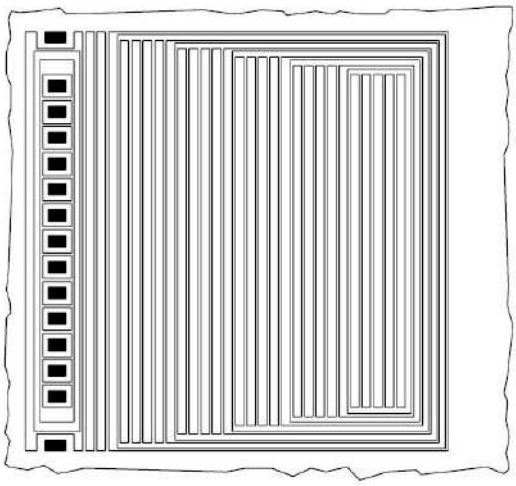

FIGURE 1.10: Scheme of a Matrix Drift Devices [45, 57, 51].

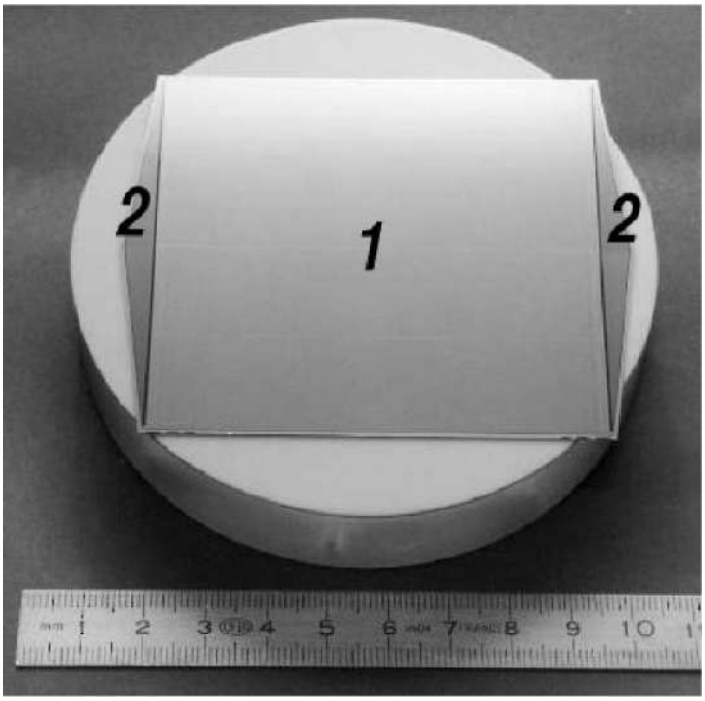

FIGURE 1.11: Photograph of the Large Area SDD of ALICE [69, 81, 70].

A new large area linear multi-anode SDD (with an active area of 12.0 x 7.2 cm^2) has been developed for X-ray astronomy applications [43]. This detector has a sensitive area of 76 cm^2, and an energy range of 2-50 keV with a spectral resolution below 260 eV at 6 keV [10].

1.3.4 Pixel Drift Devices

Pixel Drift Devices are the are the SDDs that most allow you to take advantage of the features. This is useful for applications that predominantly require good

energy resolution rather than spatial one.

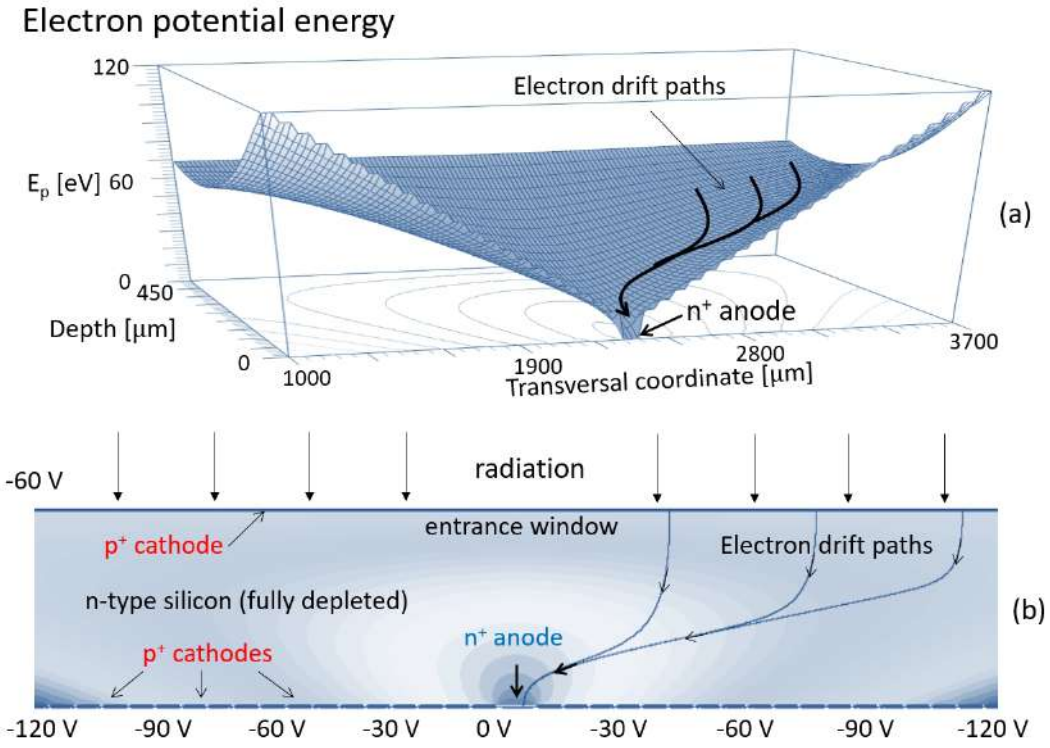

FIGURE 1.12: (**a**) The funnel-shaped potential energy of the electrons inside the cell (**b**) The section of a SDD sensor (1 cell) [19].

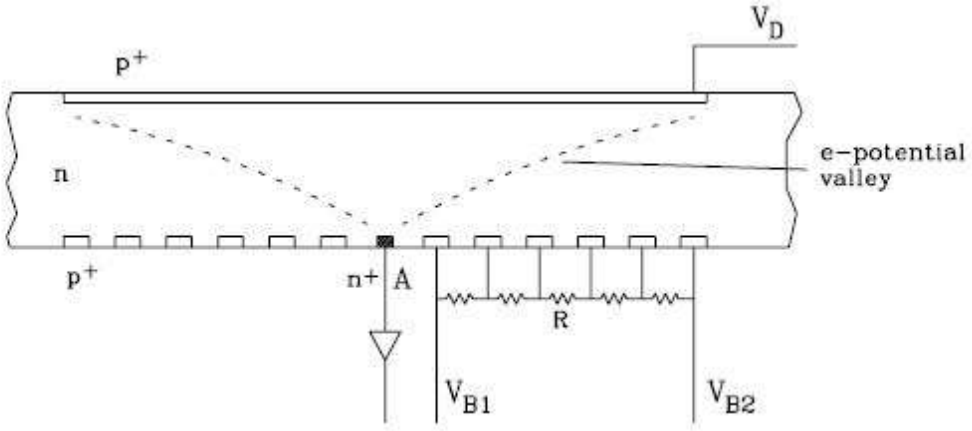

FIGURE 1.13: Section of an SDD with a single-side structure [57].

The pixellated SDD [Fig. 1.13] are built on a doped silicon substrate n. A single p+ cathode is implanted in the window through which the photons enter (called the p-side of the detector) along the entire active surface of the detector, which is supplied with a negative bias voltage. On the n side, a small n+ anode is implanted, surrounded by p+ circular strip cathodes (called drift cathodes) that extend at regular intervals from the anode to the edge of the active cell

surface. The cathodes on the n side are connected together by resistors that act as voltage dividers: a negative voltage is applied to the outermost cathode, it gradually decreases in the direction of the innermost cathode (also called the return cathode) on which a negative voltage of a few volts is usually imposed. This leads to the complete depleting of the substrate n with an electric drift field that guides the charge carriers towards the anode. When a photon penetrates the silicon it creates electron-hole pairs. The holes are almost instantly absorbed by the nearest cathode, while electrons are guided inside the substrate towards the collection anode [47, 57, 56, 66, 26]. In this geometry the electron potential energy has a funnel-shaped distribution that drives the electrons towards the anode, thus ensuring an effective charge collection (holes, instead, are collected by the cathodes) [Fig. 1.12].

The readout anodes of the pixel SDD are wire bonded to a Charge Sensitive Amplifier (CSA). In this way the acquisition, amplification and transformation of the collected signal begins.

These individual cells become the basis to represent the customized geometries that best fit the needs.

1.4 Multipixel monolithic SDD

The possibility of starting from cells of different shapes and being able to design detectors of various shapes and sizes has allowed to optimize, along with production process, also the ability to customize monolithic arrays of SDD for projects in which they will be used.

A small example is provided in Figures 1.14, where a multi-project wafer of the ReDSoX Collaboration is visible. Three of the detectors that will be analyzed in detail are present in this photo: the basic sensor (called strip) the XAFS-SESAME Detector System (analyzed in detail in Chapter 4), the trapezoidal detector for the TwinMic beamline (described in Chapter 5), and that of the type on which the mapping was made in the chapter **??**.

1.4.1 Some additional details about multipixel monolithic sensors

The multipixel monolithic sensor has been designed to be able to detect low energy X-rays with good sensitivity down to few hundreds of eV by minimizing the passive materials encountered by the radiation before reaching the bulk (entrance window): a thin dielectric layer, a protective thin layer of oxide,

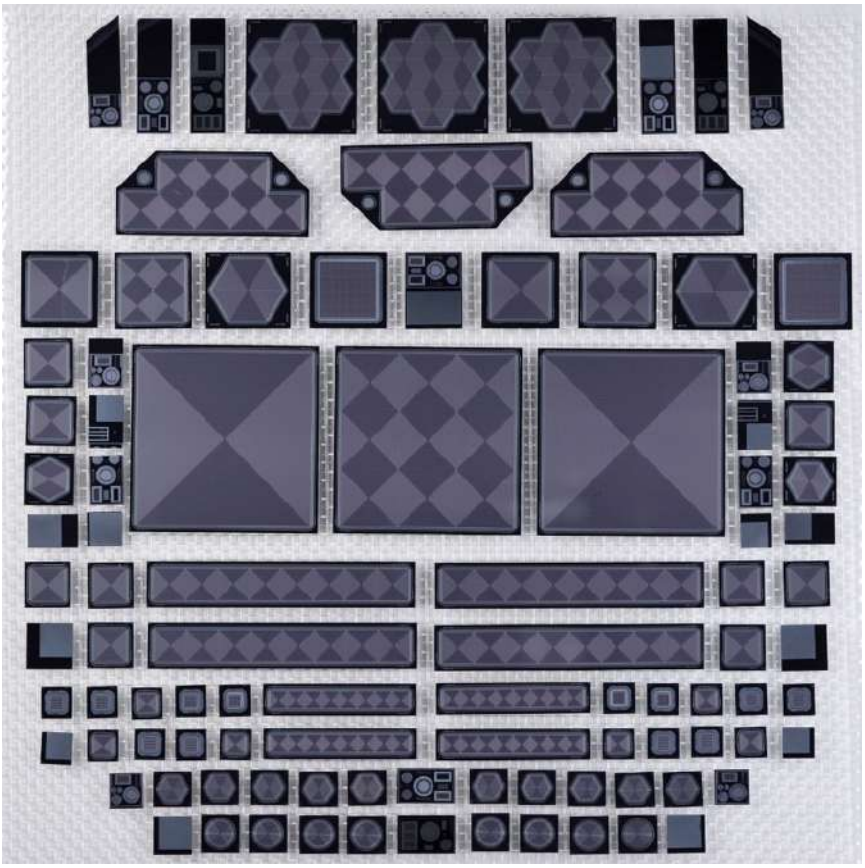

FIGURE 1.14: Multi-project wafer of ReDSoX Collaboration: the sensors were simulated and designed by INFN-Trieste and produced by FBK-Trento.

covering a shallow uniform junction, assuring efficient radiation transmission and collection of carriers generated close to the detector surface, specifically produced at FBK with a proprietary technology[1], assuring efficient radiation transmission and collection of carriers generated close to the detector surface. No aluminum layer is covering the entrance window. The expected overall dead layer is in the order of few tens of nm. The thin detector entrance window the detection efficiency at the C Kα line is at least 60% (based on Geant4 Monte Carlo simulations [17]) [28]. On the other side, at the center of each cell is located an anode surrounded by several concentric cathodes, the most external of which (the HV bias cathode) being in common to all the cells. Surrounding the cells, on both sides, several floating p+ rings (guard cathodes) gently degrade the electrostatic potential to ground before reaching the edge of the structure.

[1]The specific details of the FBK technology cannot be disclosed, the approach adopted is similar to the one reported in [36].

Chapter 2

Sensor optimization

In the chapter 1 it has been presented the main uses currently being made of SDDs. It is important to evaluate the quality of current detectors and implementing improvements, where necessary. In this regard, to improve the performance of the detectors, one can act on several fronts: to deepen the knowledge of the critical issues of one's own detectors, so as to improve them, and modify them in order to try to make them more suitable for others future developments and uses.

2.1 Mapping of 3 x 3 mm^2 SDD

To evaluate and improve the performance of the detectors and to find future optimizations, an accurate characterization of the detectors and a detailed mapping campaign was carried out. In particular, the main purpose is to map the efficiency and uniformity of charge collection as the polarization voltage of the sensor changes. This analysis was done on a Silicon Drift Detector with 3 x 3 mm^2 sensitive area designed by INFN of Trieste and built by FBK-Trento [37]. It represents a single-pixel precursor of a monolithic matrix of multipixel Silicon Drift Detectors and, at the same time, a model of one cell Fluorescence Detector System (XAFS) for SESAME.

The point-by-point mapping tests of the detector were carried out in the X-ray facilities at INAF-IAPS in Rome, equipped with a motorized two-axis micrometric positioning system. High precision characterization of this detector was done with a radioactive ^{55}Fe source and a collimated monochromatic X-ray beam.

The mapping in different positions and bias condition was specifically-aimed to the detailed analysis of the charge collection efficiency at the edge of the detector. We compare it with a mapping performed by F. Ceraudo [35] on a previous version of SDD, using the same analysing software.

The result lead to understand and verify the aspects related to the collection of the signal with respect to the position of interactions of the photons, especially in consideration of the new design and development of monolithic multipixel detectors.

2.1.1 Detector and experimental setup

The detector mapped is a not-collimated single-pixel Silicon Drift Detector (SDD), with nominal 3.0 x 3.0 mm^2 [Fig.2.1] sensitive area, designed by INFN of Trieste and built by FBK-Trento. The SDD, consists of 450 μm-thick fully depleted n-type Silicon bulk, with an entrance window (with bias voltages V_{WIN}) in the front side. In the backside, the drift p+ cathodes (bias voltage V_{OR} and V_{IR} is applied respectively to the outer and inner drift cathodes) and the small, very low capacitance central, n+ anode, connected with the readout by the ultra-low noise SIRIO [19, 23] charge sensitive preamplifier. The potential energy of the electrons in the SDD has the shape of a funnel [19].

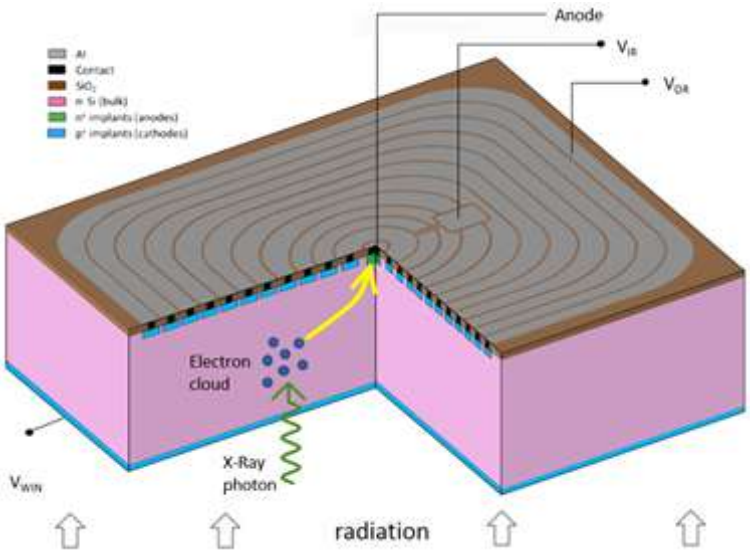

FIGURE 2.1: Working principle and structure of the detector.

The detector mapping [34, 35] were carried out in the X-ray facilities at INAF-IAPS in Rome, equipped with a motorized two-axis micrometric positioning system. The sources used for these measurements were: a radioactive ^{55}Fe source and a collimated Ti X-ray tube with a Bragg crystal monocromator. The measurements were carried out in an air-conditioned room with a constant ambient temperature of 18 °C.

Experimental setup

The detailed description of the experimental setup used for the measurement is shown in Figure 2.3 and described below.

The measuring room with all the setup is at a controlled temperature of 18 °C for all measurements.

A closed and darkened metal box [Fig. 2.3 (1)] contains the QuadSDD [Fig. 2.2] composed by the sensor and the SIRIO amplifier, whose output is then directly digitized and processed by a Multi-Channel Analyzer (MCA). Nitrogen is fluxed in the box in a constant way for all measurements [Fig. 2.3 (14)].

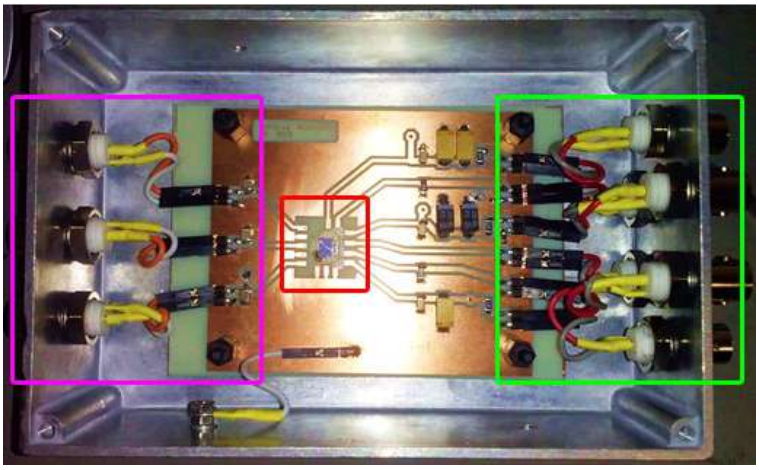

FIGURE 2.2: Picture of the QuadSDD circuit: SDD and SIRIO preamplifier (boxed in red), high-voltage supply (boxed in pink), and low-voltage supply and scientific signals (boxed in green) [35].

A power supply was used for depletion voltage (window, V_{WIN}) and the anode (inner ring, V_{IR}) of the detector [Fig. 2.3 (4)], and another power supply was used for powering the detector cathode (outer ring, V_{OR}) [Fig. 2.3 (5)]. An high voltage filter was applied to the detector [Fig. 2.3 (13)].

Another power supply was needed to power the SIRIO preamplifier [Fig. 2.3 (6)] and the relative low voltage filter [Fig. 2.3 (12)].

Connected to the system there are the amplifier and its power supply, and the reset pulser [Fig. 2.3 (11)(7)(8)].

To complete the acquisition was used a DP5 digital pulse processor [Fig. 2.3 (9)] connected with the acquisition computer, located outside the experimental room.

QuadSDD circuit, the closed box with the sensor, was placed on two motorized micrometric rails for two-dimensional positioning [Fig. 2.3 (3)]: in this way it was possible change the position of the sensor to do the mapping measurements.

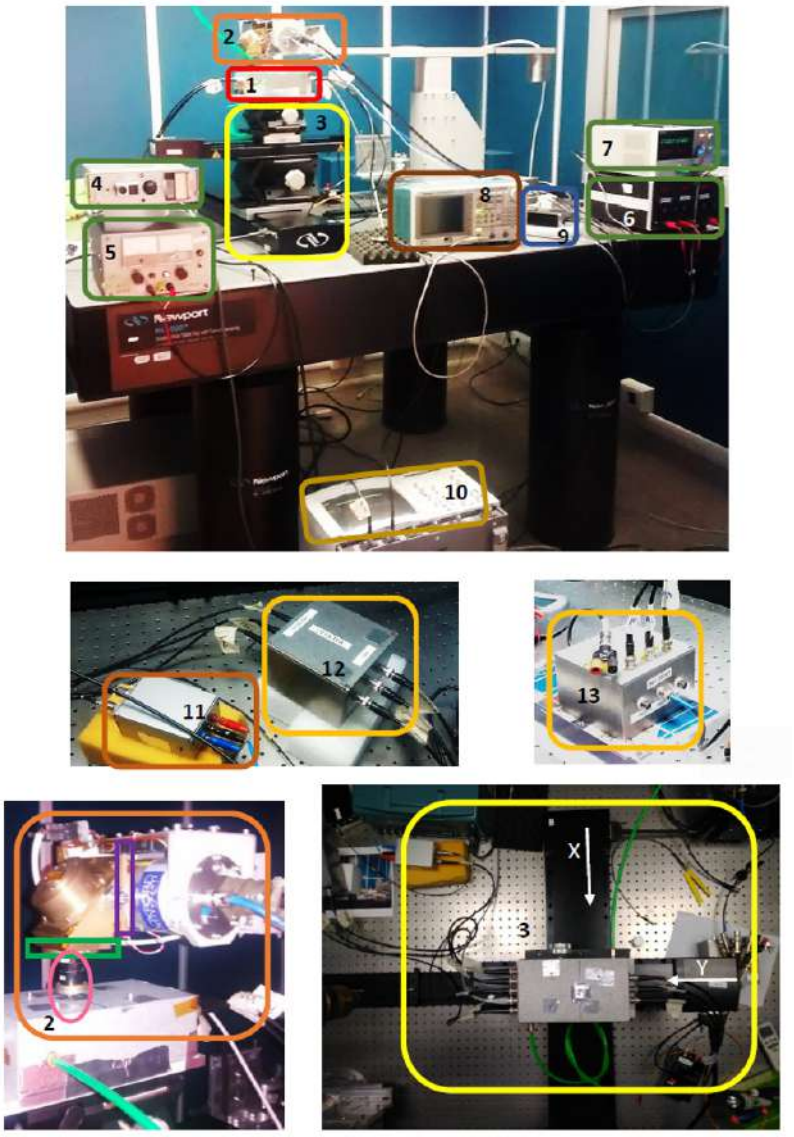

FIGURE 2.3: Experimental setup: 1. Sensor and SIRIO amplifiers (QuadSDD circuit) - 2. Ti anode X-ray tube equipped with a Bragg diffractor to select the Ti Kα line (4.5 keV), crystal: Fluorite CaF^2 (220), The X-ray tube was configured at 35 kV and 0.6 mA. A 1/40-ratio diaphragm (purple box in 2) is between the tube and the diffractor, the diaphragm between the diffractor and the detector is composed of: a second 1/40-ratio diaphragm (green box in 2), a 34 mm length diaphragm and a diaphragm with 100 μm hole size (pink box in 2) - 3. Two motorized micrometric rails for two-dimensional positioning - 4. Supply voltage needed for depletion voltage (window, V_{WIN}) and the anode (inner ring, V_{IR}) for the detector - 5. Supply voltage needed for the cathode (outer ring, V_{OR}) for the detector - 6. Supply voltage needed for the SIRIO preamplifier - 7. Supply voltage needed for the amplifier - 8. Reset pulser - 9. DP5 digital pulse processor - 10. Oscilloscope - 11. Amplifier - 12. Low voltage filter for the SIRIO preamplifier supply voltage - 13. High voltage filter for the detector - 14. Nitrogen.

An Ti anode X-ray tube, model Oxford series 5000, was used as the main source for the measurements [Fig. 2.3 (2)]. The X-ray tube was equipped with a Bragg diffractor to select the Ti Kα line (4.5 keV), crystal: Fluorite CaF^2 (220), The X-ray tube was configured at 35 kV and 0.6 mA. A 1/40-ratio diaphragm (purple box in 2) is between the tube and the diffractor, the diaphragm between the diffractor and the detector is composed of: a second 1/40-ratio diaphragm (green box in 2), a 34 mm length diaphragm and a diaphragm with 100 μm hole size (pink box in 2).

2.1.2 Measurements and analysis

The main purpose is to map the efficiency and uniformity of charge collection as the polarization voltage of the sensor changes.

Beam shape

Before performing the mapping, we have to estimate the dimension of the beam. The way to do it was to take measurements with a commercial detector, instead of the QuaddSDD, using it as a counter. The detector used was the XR-100CR of Amptek: it is an high performance thermoelectrically cooled Si-PIN X-ray detector and preamplifier [15]. To perform the measurement of the beam size we assume that the beam is a Guassian shape. To determine its FWHM we used a diaphragm on the XR-100CR detector and we moved the detector from x1, near to one edge of the detector, to x2 near to its second edge with a speed of 1μm/s [Fig.2.4 (a)]. As a result we obtained light-curve of the beam shape [Fig.2.4 (b)].

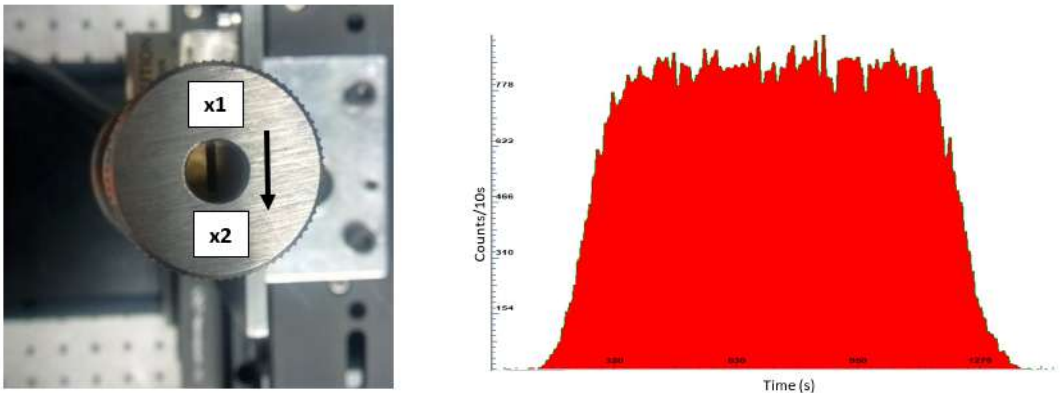

FIGURE 2.4: (**a**) XR-100CR and the diaphragm used for to determine the beam shape - (**b**) Light-curve using the XR-100CR detector. The velocity of the movement is 1μm/s and the light-curve binning is 10s.

We fit the beam shape with a Gauss error function and a complementary error function, we found the σ and we calculated the FWHM of the beam. For the X axis the FWHM of the beam is 165.48 μm and for the Y axis is 128.83 μm.

Beam positioning

An essential requirement for further measurements is to identify the centre position as precisely as possible. To align the detector QuadSDD with the X-Ray tube, we searched for the center position by acquiring a Light-curve. We consider that a constant signal value corresponds to a position inside the sensor and a zero signal value corresponds to a position outside the sensor. The positions where the signal was half of the average were chosen as the limits of the sensor. Simultaneously, one of the motorized rails was moving from one approximate edge to the other. Given that the rail was moving at a known and constant velocity (1μm/s), the light-curve binning is 10 s and knowing the start and the end positions, we can relate the number of channels to the position. In this configuration, the center position was (243.37, 7.955).

Calibration

For the calibration, we acquired, in the central position of the detector previously found, two spectra: one using the ^{55}Fe source [Fig.2.5 (a)] and one using the Ti X-ray tube [Fig.2.5 (b)].

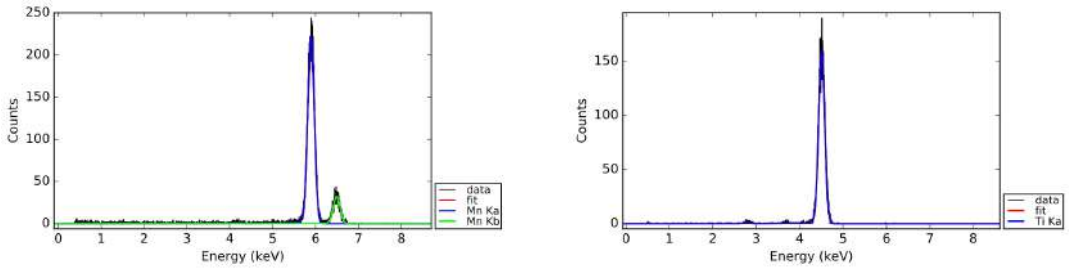

FIGURE 2.5: Calibration acquisitions (**a**) Spectrum of Mn [FWHM 173 eV at 5.9 keV, Shaping Time 2.4 μs, V_{OR} 124.4 V, Temp 231 K, ΔT 240 s] (**b**) Spectrum of Ti [FWHM 165 eV at 4.5 keV, Shaping Time 2.4 μs, V_{OR} 124.4 V, Temp 231 K, ΔT 240 s].

Mapping

The mapping procedure is controlled by a LabView interface named BabylonTower, which allows to move the detector through the micrometric rails

according to the coordinates chosen, respect to the center of the sensor, and programmed for the measurement.

For the point-by-point mapping, we used the collimated Ti X-ray tube and we have acquired data at coarse steps in the central zone (500 μm) and at finer steps (100 μm) near the edges of the detector [Fig.2.6 (a)]. In order to have a better view of the results, and to obtain a square representative of all the detector area, the acquired points have been mirrored. The measurements have been repeated for 4 different outer ring voltages [Fig.2.6 (b)], keeping the values of the other detector voltages as constant as possible. We have chosen to vary the V_{OR} in a range that would guarantee us a uniform spacing between the voltage values, a number of measurements compatible with the times reserved for the test beam, the minimum voltage that would allow us to have a detector correctly polarized, and a maximum voltage equal to that used for the mapping previously made on the previous version of the sensor.

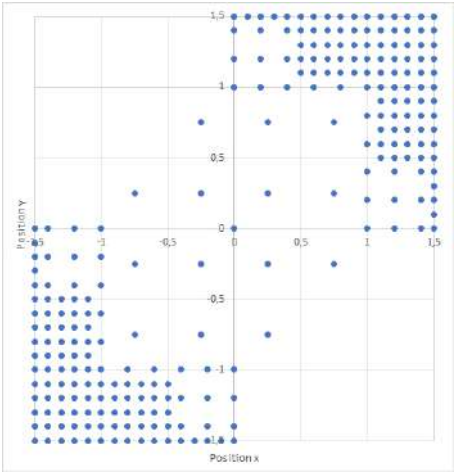

Outer ring voltage (V_{OR})	Windows voltage (V_{WIN})	Inner ring voltage (V_{IR})
-144.6 V	-85.10 V	-23.8 V
-124.4 V	-80.66 V	-21.13 V
-104.06 V	-80.85 V	-19.81 V
-84.1 V	-80.97 V	-18.59 V

FIGURE 2.6: (**a**) Scheme of the grid used for the automatic acquisitions with different steps for the central region and the edge of the detector (**b**) Table showing the four different bias conditions used for the measurements.

Each spectrum acquired, in each point of the grid for each of the 4 power supply configurations, was analysed in the same way. We compare it with the one done on a previous version of SDD. In order to make this analysis comparable with the measurement campaign carried out on an earlier version of the detector we used the same analysis software. The software was written in Python by F. Ceraudo [35].

The analysis process carried out by the software is the following: search for the maximum of the analysed spectrum (which is supposed to be the Ti Kα line). If the number of peak counts is less than 25, the spectrum is discarded, because it is less than that required by Gaussian statistics, and no further

analysis will be carried out on it. If the peak count is higher than 25 we proceed with the estimation of the position of the center of the line and its width through an iteration of 2 Gaussian fits, to improve accuracy. Then energy calibration is performed (was not carried out earlier so as not to influence the values of FWHM), using previously acquired calibration data (under the same measurement conditions). Finally, the plots and results are saved.

From the analysis, 3 parameters are evaluated [Fig.2.7]:

- FWHM - The Full Width Half Maximum of the Ti Kα line
- Relative (than the one obtained for the central point) Ti Kα line position
- Relative (than the one obtained for the central point) Ti Kα line counts, of the data between -1.5σ and 4σ

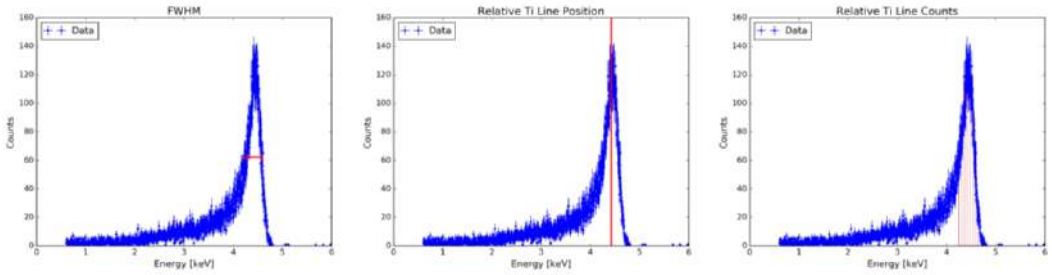

FIGURE 2.7: FWHM - The Full Width Half Maximum of the Ti Kα line (**b**) Relative (than the one obtained for the central point) Ti Kα line position (**c**) Relative (than the one obtained for the central point) Ti Kα line counts.

2.1.3 Results and conclusions

Results of the analysis are the maps, with relative errors, of the trend of the 3 parameters evaluated. In these maps: the squares represented the points of the grid having more than 25 counts for the Ti Kα line, which were processed; the triangles represented the discarded measurements with less than 25 counts for the Ti Kα line. Values between the experimental points were obtained through linear interpolation.

Below are the maps obtained from the analysis:

- FWHM - The Full Width Half Maximum of the Ti Kα line [Fig.2.8] and relative errors [Fig.2.9]
- Relative (than the one obtained for the central point) Ti Kα line position [Fig.2.10] and relative errors [Fig.2.11]

- Relative (than the one obtained for the central point) Ti Kα line counts [Fig.2.12] and relative errors [Fig.2.13]

The value of the spectral resolution of the detector, considering the associated error, remains constant under all measurement conditions. However, there is greater uniformity for a voltage V_{OR} higher than 124 V. Further, the outer ring voltage changes the efficient area of the detector.

The analysis of the results shows that this detector has an effective area of 2.7 x 2.7 mm^2 [Fig.2.8 and Fig.2.14]. In the previous version of the tests carried out in 2016, with the same voltage V_{OR}, on the previous sensor design, by Ciraudo [35], there was a collection area of 2.5 x 2.5 mm^2. If we compare these results we can see that the collection area of the second sensor version is larger than that of the previous sensor, but still less than the nominal 3.0 x 3.0 mm^2 area.

From the analysis and comparison of the data it can be seen that the further we are from the centre, the lower the counts below the peak, the more asymmetric the peak is and the more the centroid moves towards a lower energy [Fig.2.14].

This mapping allows to verify aspects related to the charge collection to the detector's edge. Furthermore, the mapping allows the cross check of the device simulation and fosters the progress in the design and development of new monolithic matrix of multipixel Silicon Drift Detectors for applications in astrophysics and advanced light source.

In the new version of the sensor, INFN-Ts has taken these results into account to improve the design and optimize the collection area. Further comparison mappings on the brand new version of the sensor will be carried out in the coming months.

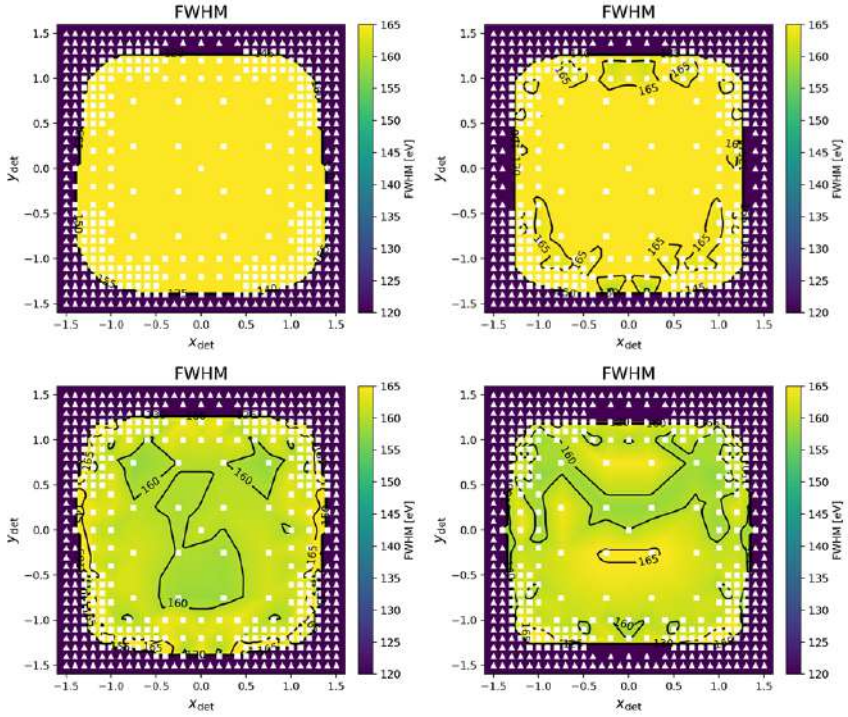

FIGURE 2.8: (**a**) Maps of FWHM - The Full Width Half Maximum of the Ti Kα line - Top row: Right: V_{OR} = 144.6 V, Left : V_{OR} = 124.4 V. Bottom row: Right: V_{OR} = 104.06 V, Left: V_{OR} = 84.1 V.

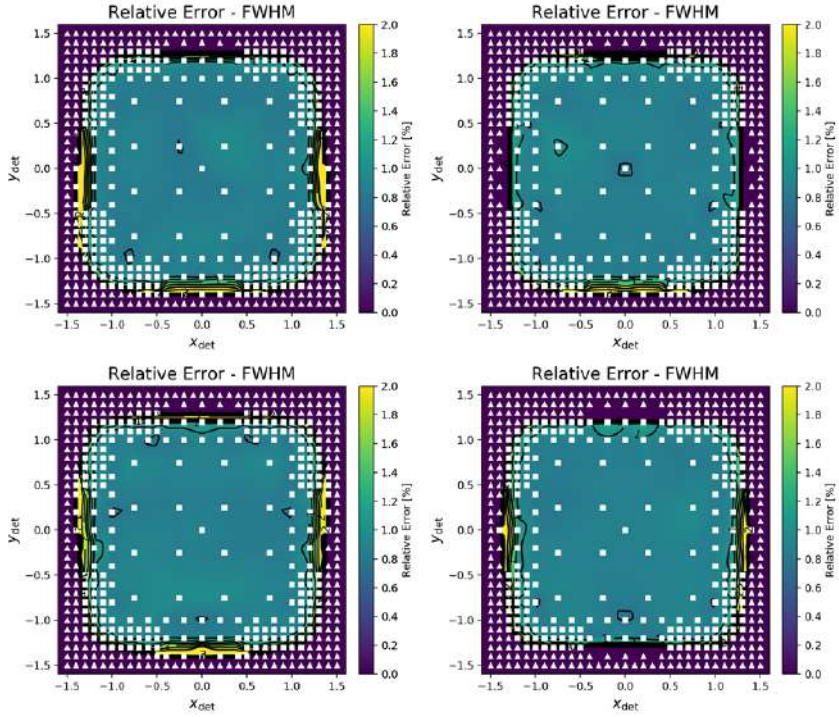

FIGURE 2.9: Maps of the relative error FWHM - Top row: Right: V_{OR} = 144.6 V, Left: V_{OR} = 124.4 V. Bottom row: Right: V_{OR} = 104.06 V, Left: V_{OR} = 84.1 V.

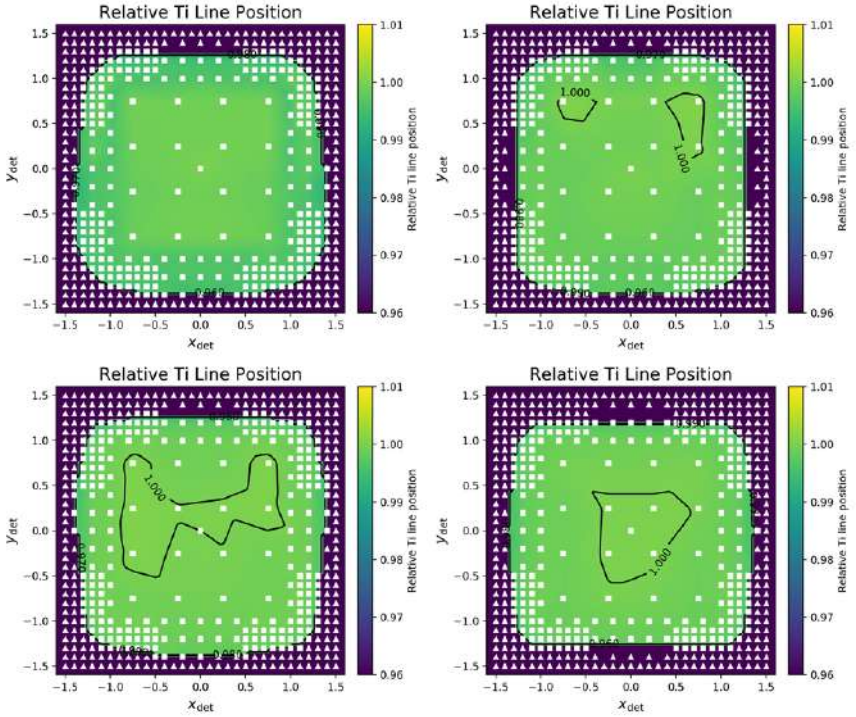

FIGURE 2.10: (**a**) Map of Ti Kα line position - Top row: Right: V_{OR} = 144.6 V, Left: V_{OR} = 124.4 V. Bottom row: Right: V_{OR} = 104.06 V, Left: V_{OR} = 84.1 V.

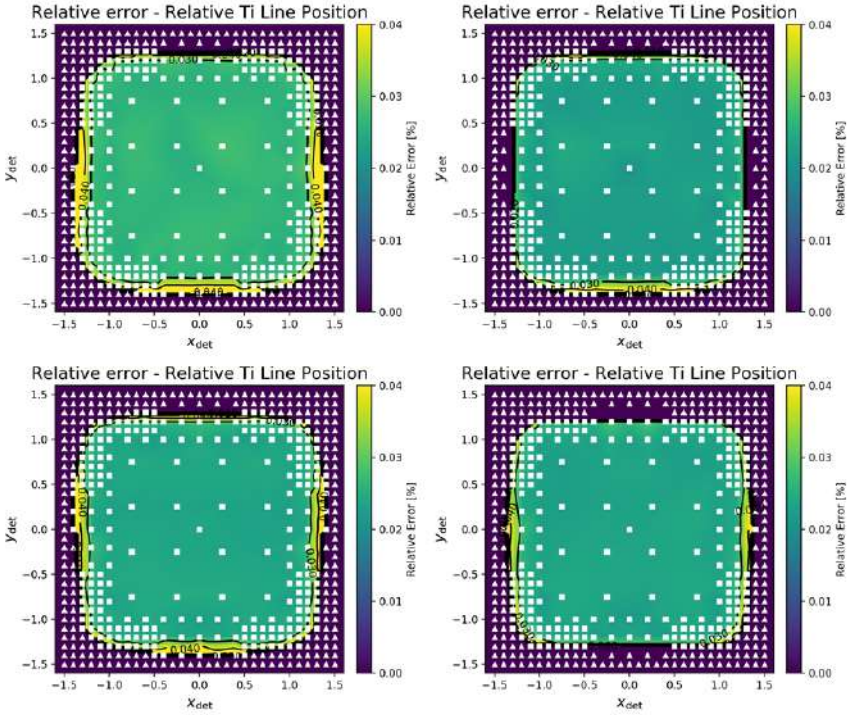

FIGURE 2.11: Map of the relative error Ti Kα line position - Top row: Right: V_{OR} = 144.6 V, Left : V_{OR} = 124.4 V. Bottom row: Right: V_{OR} = 104.06 V, Left: V_{OR} = 84.1 V.

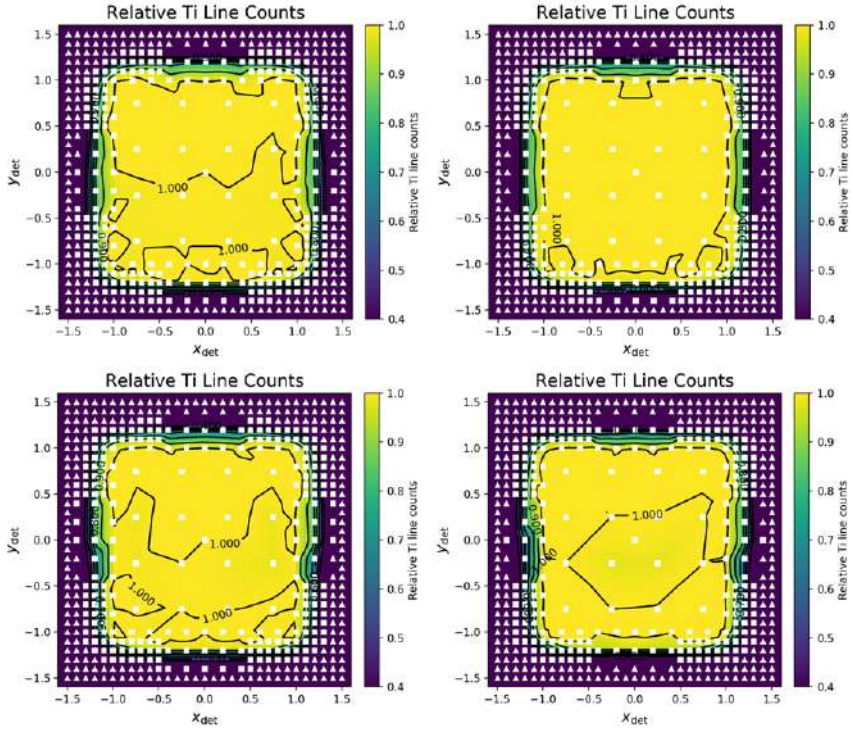

FIGURE 2.12: (**a**) Map of Ti Kα line counts - Top row: Right: V_{OR} = 144.6 V, Left: V_{OR} = 124.4 V. Bottom row: Right: V_{OR} = 104.06 V, Left: V_{OR} = 84.1 V.

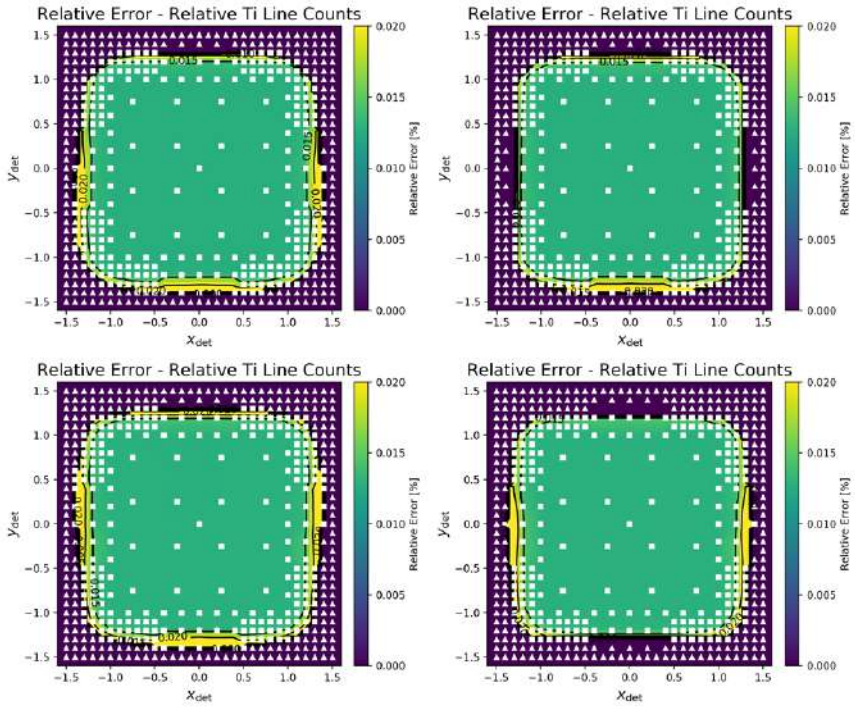

FIGURE 2.13: Map of the relative error Ti Kα line counts - Top row: Right: V_{OR} = 144.6 V, Left: V_{OR} = 124.4 V. Bottom row: Right: V_{OR} = 104.06 V, Left: V_{OR} = 84.1 V.

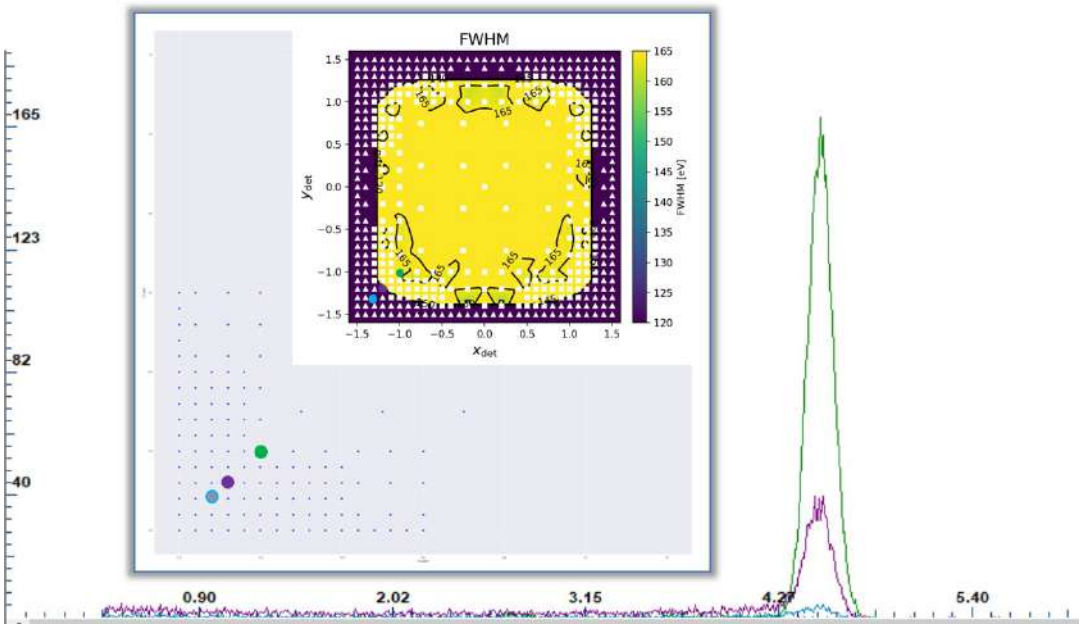

FIGURE 2.14: Spectra (Ti Kα line) at points: green (-1.0, -1.0), purple (-1.2, -1.2) and blue (-1.3, -1.3) with V_{OR} = -124.4 V. The centroid of the peak is, respectively, at 4.51, 4.50 and 4.47 keV, the mismatch is due to the progressive growth of the left shoulder of the peak caused by truncated events where a part of the signal charge is lost to the periphery of the detector.

Chapter 3

Customized detector system for synchrotron radiation applications

Electromagnetic radiation is a basic instrument of investigation for our knowledge of the world. Depending on the energy of the radiation, it is possible to see objects or phenomena characterized by different dimensions. But energy is not the only discriminating factor for the selection of a source: intensity, polarization, coherence and collimation are also very important. Among the sources we have available light or synchrotron radiation is one of the most useful and versatile for its characteristics. It has a number fields such as material science, physics, chemistry, biology, cultural heritage, etc. Also it needs always new and advanced scientific and technological developments both in terms of acceleration technology and in terms of the last step, the beamline detectors [24, 58, 61].

In this context, off-the-shelf detection systems severely constrain the achievable results. Then the main goal of the project was to develop novel versatile detection systems able to cover a large photoemission solid angle, being easily adaptable to the needs of different X-ray spectroscopy beamlines and ready to cope with high photon count-rates in order to exploit all the power of new light sources [28].

3.1 Synchrotron

Synchrotron radiation (or synchrotron light) is now well known as a powerful scientific investigation tool. The phenomenon of the radiation emitted by an electron on a circular orbit has been known since the end of 1800, but only with the construction of the first particle accelerators, after 1940, its potential was realised. [61, 58, 24].

In particular, synchrotron radiation is the electromagnetic radiation emitted by a lightly charged particle (usually electrons or positrons) accelerated radially. When the particle moves with a non-relativistic speed we speak of cyclotron radiation, when instead the particle has a relativistic speed we define synchrotron radiation. The radiation is emitted in the direction of the particle motion, in a narrow cone (the narrower the more the energy of the particle in motion) tangent to the orbit [61].

The synchrotron light source [Fig. 3.1] is a circular accelerator (therefore with fixed radius), in which the electrons are confined in a ring in which the ultra high vacuum is made. Inside this ring, the electrons are accelerated by electric fields, and deflected, to make the circular orbit, by magnetic fields. The radiation thus produced by electrons is very intense, collimated and with a wide emission band that can range from infrared to hard X-rays [Fig. 3.2]. This makes it possible to study all phenomena or things that have a dimension or energy comparable to that of the synchrotron radiation produced. The flux and brilliance of the radiation can be increased by inserting in the straight sections of the ring (placed between the bending magnets) of wigglers or undulators [61]
.

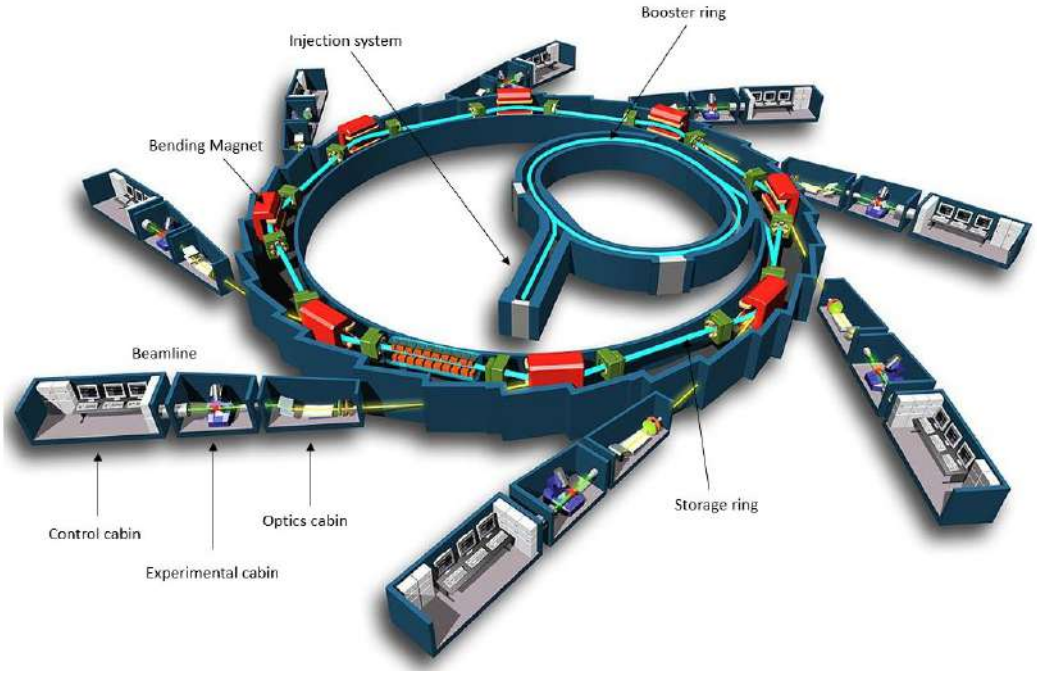

FIGURE 3.1: General diagram of a Synchrotron light source - Copyright EPSIM 3D / JF Santarelli, Synchrotron Soleil [4].

The first facilities of the 60s, defined as first generation, were not instruments dedicated to synchrotron radiation, but physics experiences that were used in a parasitic way. Consequently there was the construction of the first

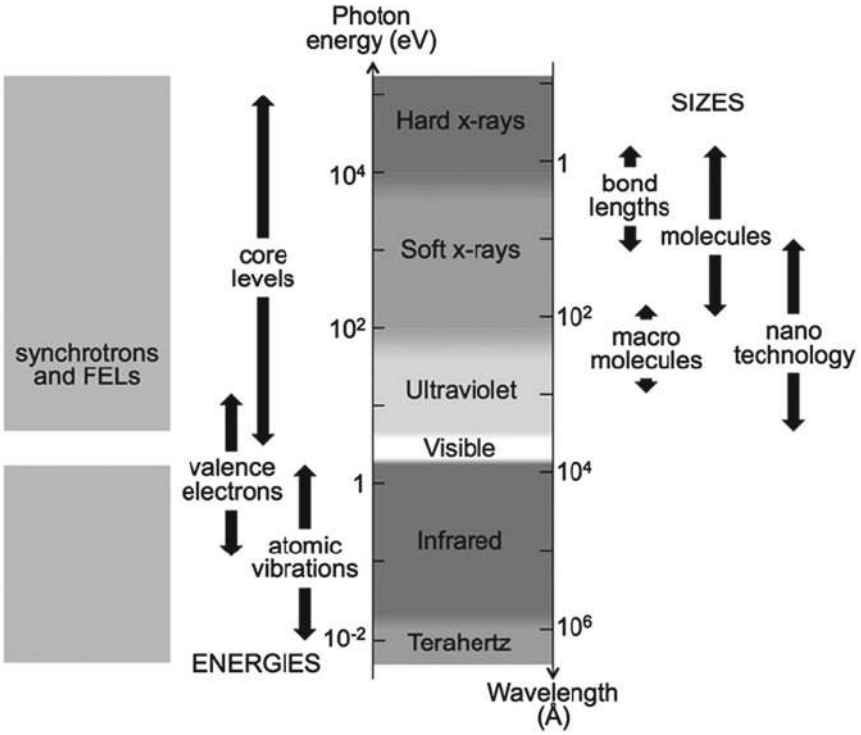

FIGURE 3.2: Scheme comparing the energies, and corresponding wavelengths, of the synchrotron radiation produced with the phenomena or things that can be analysed [61].

facilities dedicated to synchrotron radiation, defined as second generation, and its uses only with the development and use of the first wigglers. A further development, with the passage to the third generation facilities, took place with the development of the undulators. The technological development led to an increase in radiation brightness and thus to the increasing potential of advance light sources. In the 21st century we see the improvement of third generation sources and, together, the development of fourth generation sources based on free electron lasers (FELs) [61] [Fig. 3.3].

Third and fourth generation light sources have revolutionized research in many scientific and technological disciplines. New scientific challenges require the construction of cutting-edge performance machines and experimental stations.

3.2 Some applications: X-ray spectroscopy

X-ray spectroscopy is a technique that uses radiation in the X-ray of the spectrum to investigate matter. The synchrotron radiation plays a very important role in order to investigate matter, and with the X-Ray Spectroscopy is possible to probe composition, particles, bonds of matter [2, 61].

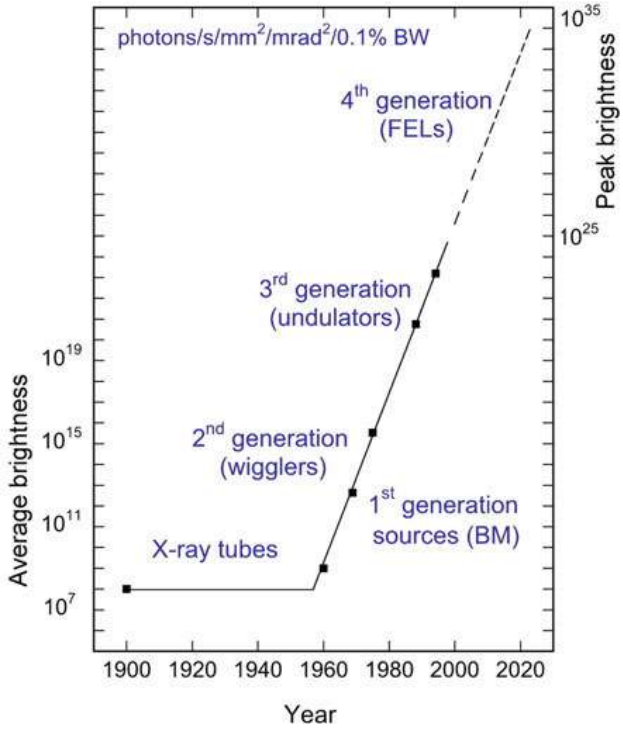

FIGURE 3.3: Comparison between the average brightness of storage rings of different generations [61].

The physical phenomenon can be schematized as follows: the atom, when hit by X-ray, excites an electron from the inner shell. For this to happen the energy of the incident photon must be greater than the bonding energy of the electron. When this electron returns to low energy level it emits a photon that has the characteristic wavelength for the element. From the analysis of the spectrum it is therefore possible to identify the chemical composition of the sample [18].

In order to have optimal spectroscopic measurements, certain characteristics are required from the detectors. Many of these specifications are the main features of the SDD (described in the paragraph 1.3).

Several spectroscopic techniques using X-Ray, those relevant to the detectors analyzed and the measurements performed are as follows.

3.2.1 XRF - X-Ray Fluorescence

X-Ray Fluorescence (XRF) is a spectroscopy in which the incident energy is fixed and the energy dependence of the secondary photons is measured. XRF analysis is a non-destructive technique. The physical phenomenon can be schematized as follows: when an atom that has been excited because it has been hit by X-rays (a photon guides an electron out of the bound state), regains

balance and the sample emits X-ray fluorescence. In this case every element with an edge (whose positions correspond to the bonding energies) below the incident energy will fluoresce. When the energy of the X-rays is sufficient to excite an electron in state 1s we refer to edge K. It is possible from the XRF spectrum to analyse the composition of the sample [Fig. 3.4 and 3.5]. With this type of measurement element concentrations can be quantified [2, 11, 76, 63]. The source can be a radioactive source, an X-ray tube or synchrotron radiation.

This analysis will be performed using the PyMca X-ray Fluorescence Toolkit [77].

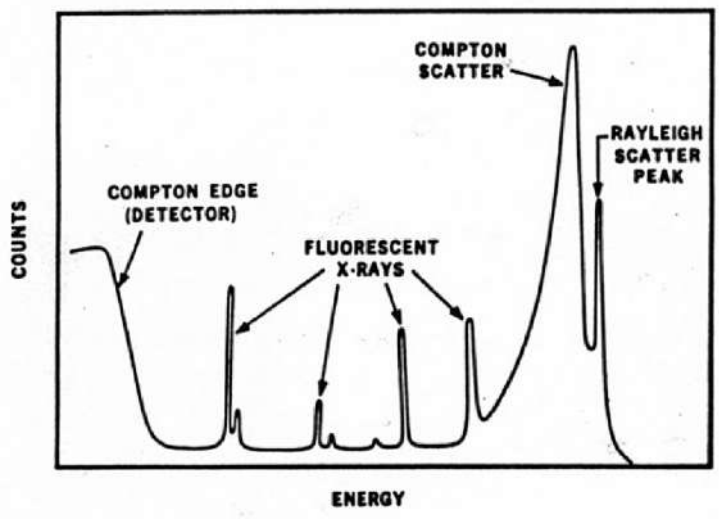

FIGURE 3.4: An example of XRF spectrum [11].

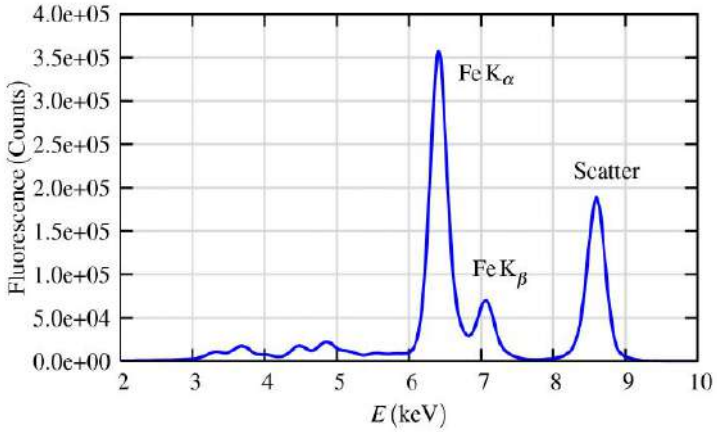

FIGURE 3.5: An example of XRF spectrum showing the Fe Kα and Kβ emission lines, and the elastic scattered peak [63].

3.2.2 XAFS - X-ray Absorption Fine Structure

In general XAFS is the modulation of the X-ray absorption coefficient at energies near and above an X-ray absorption edge.

X-ray Absorption Fine Structure (XAFS) analysis is a non-destructive technique. Usually XAFS spectrum is divided in two regime (with the same physical origin but with different specific interpretation): X-ray Absorption Near-Edge Spectroscopy (XANES) and Extended X-ray Absorption Fine Structure (EXAFS) [Fig. 3.6].

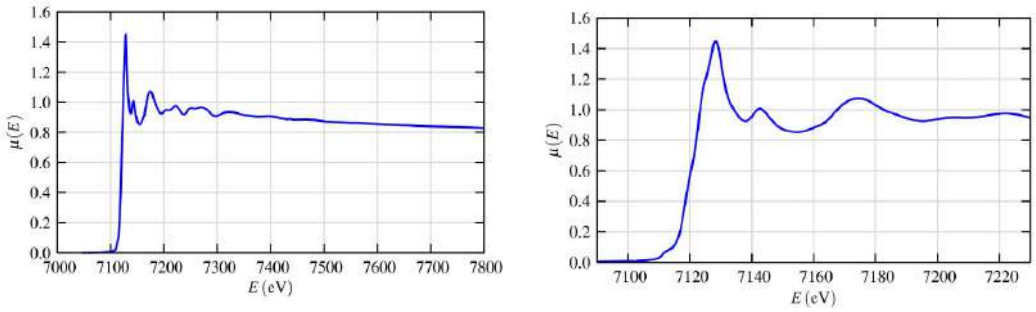

FIGURE 3.6: Example of acquisition for the same sample of (**a**) XAFS spectrum (**b**) XANES spectrum [63].

The physical phenomenon of XAFS spectroscopy can be schematized as follows: when an atom that has been excited because it has been hit by X-rays (a photon guides an electron out of the bound state), regains balance and the sample emits X-ray fluorescence [Fig. 3.7]. This emitted wave propagates and is diffused by the other atoms nearby, from the sample then emerges, and is detected, the interference of these two [Fig. 3.8] [63]. During an XAFS measurement, the energy of the incident beam is changed continuously and over a wide energy range; synchrotron radiation is required as a string to carry out this type of measurement.

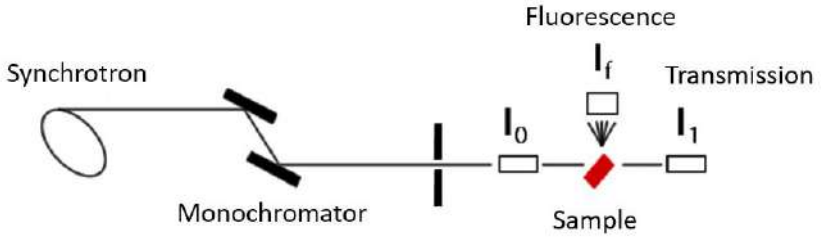

FIGURE 3.7: Scheme of an X-ray Absorption Spectroscopy Spectroscopy experience in transmission or fluorescence. The intensities of the incident and transmitted radiation are measured by ionisation chambers [12].

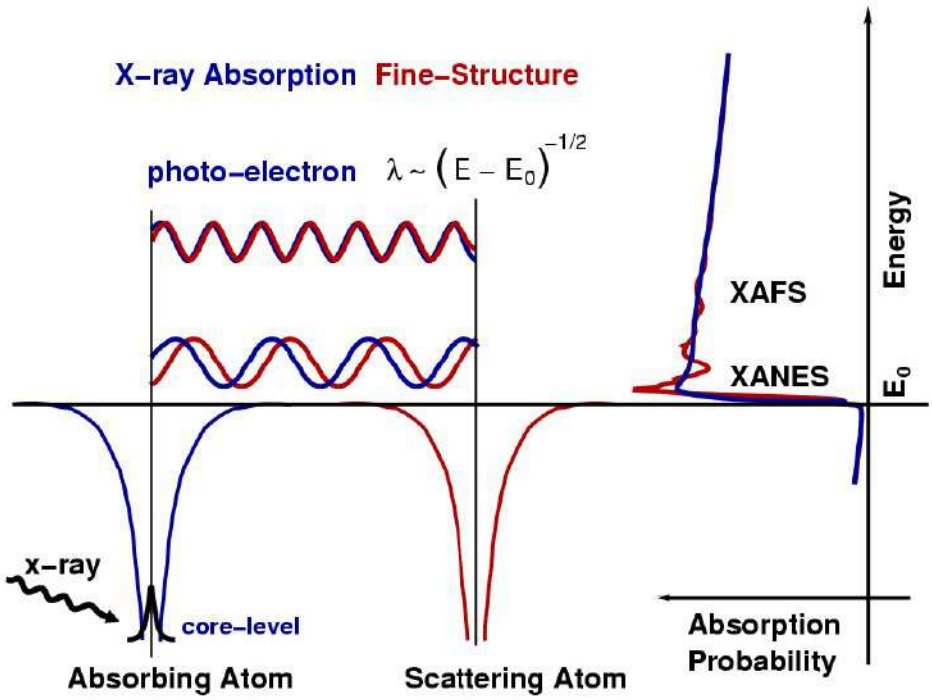

FIGURE 3.8: Physical origin of the XAFS or XANES spectrum [12, 63].

The XAFS technique allow to study the position of atoms within the crystal lattice and to determine the distance, coordination number and species of the neighbours of the absorbing atom. When an atomic species is selected from the sample to be analysed, XAFS spectroscopy then gives information on the chemical state and local atomic structure [63].

This type of analysis are usually performed using the Demeter, a system for processing and analyzing X-ray Absorption Spectroscopy data [71].

3.2.3 XANES - X-ray Absorption Near Edge Structure

X-ray Absorption Near Edge Structure (XANES) spectroscopy results from a physical phenomenon equal to that of XAFS spectroscopy seen previously. But but unlike this last one, XANES analyses the zone closest to the edge [Fig. 3.6 and 3.9]. The same considerations made on the usable sources as for the XAFS measurements can also be made for the XANES measurements.

The XANES technique allow to study the oxidation state and the coordination chemistry of the absorbing atom, for example the valence state. This is possible interpreting the data by comparison with standard samples and peak fit [63, 71].

This type of analysis are usually performed using the Demeter, a system for processing and analyzing X-ray Absorption Spectroscopy data [71].

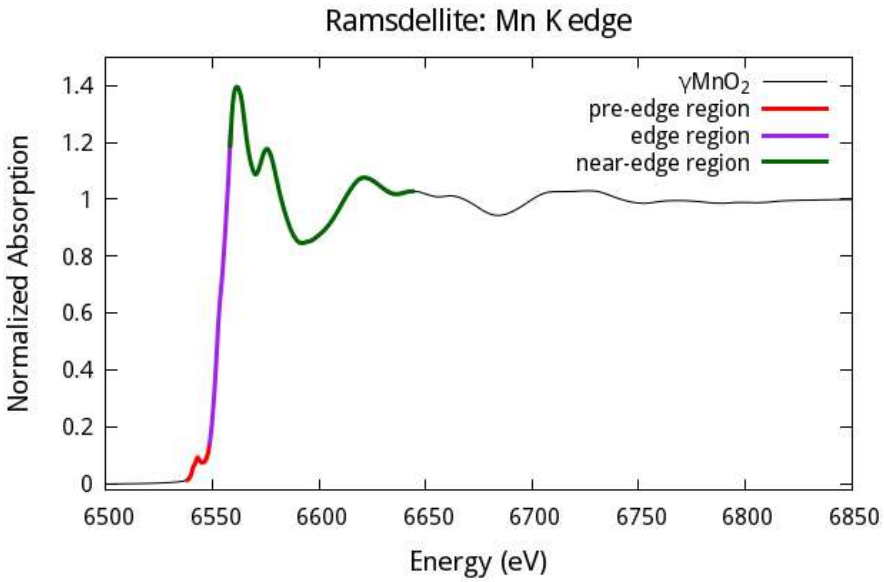

FIGURE 3.9: An example of XANES spectrum (Mn K edge): specific parts of the spectrum are highlighted: pre-edge (red line), edge (purple line), and near-edge (green line) [2].

3.3 SDD for two setups with two different experimental needs

The Silicon Drift Detectors (SDD) are among the most widely used devices in energy dispersive spectroscopy. SDDs have evolved considerably since the first prototype was produced and tested in 1984 [46] and the first large area detector was introduced [82]. Technological advancements contributed to a substantial decrease of the detectors leakage current and to design highly customized ultra low-noise front-end electronics, allowing the operation of large area detectors with good performances even at room temperature [20, 19]. In order to manage high count-rates without saturating the acquisition chain, it is necessary to distribute the charge collection among several electrodes (anodes) and processing channels, thus mitigating the pile-up and dead time phenomena. Since the leakage current is split between several anodes, and since different elements can be assembled in custom configurations, the production of large area multi-element detectors covering a wide solid angle is possible. This is of paramount importance for applications where the events to be measured are rare.

The multi element approach made possible to build custom detector configurations according to the specific experimental requests, paying particular

attention to the maximum expected count-rate and to the operation temperature, while maximizing the collection solid angle. And although the whole system consists of several independent detectors, it is highly integrated in terms of both back-end electronics, and acquisition software, which is unique for the entire instrument. This allows operating the device as a single, large area detector, thus providing a total aligned and calibrated spectrum, while maintaining the possibility to control every single element separately for advanced spatial and morphological studies [25].

There are no universal detectors suitable for all purposes and the off-the-shelf detection systems severely constrain the achievable results. For this reason, the specific needs of two typical realities in which SDDs are mainly used were considered: soft X-ray spectroscopy, where high solid angle acquisition and energy resolution are of paramount importance, and X-ray absorption fine structure (XAFS) analysis, where the detectors have often to cope with very high count-rates. Taking into account the requirements on count-rate, energy resolution as well as the photon energies used at the TwinMic [49] and XAFS [38] beamlines of Elettra synchrotron (Italy) and XAFS beamline of the SESAME Middle Easts light source (Jordan), two detection systems based on multi-element SDDs were developed [28]. The first detector consists of a matrix of 64 SDD elements disposed on 8 monolithic arrays covering an overall non-collimated active area of 576 mm^2 and operating over an energy range between 4 and 30 keV. The second system is composed of 32 SDD elements arranged on 4 monolithic sensors and covers a total non-collimated area of 1230 mm^2. Such device is optimized for detecting low-energy photons in the 200 – 4000 eV energy range. Both systems are highly integrated and can either be operated as an apparent large area single detector or as a multi-element detector, collecting information separately from each single element in order to enable spatially and angularly resolved advanced studies. The performances of the two detector systems have been studied at the XAFS and TwinMic beamlines (Elettra Sincrotrone Trieste, Italy), respectively [28]. In the next two chapters the two detector systems will be described in detail and will present the tests and characterizations carried out.

3.4 Elettra Sincrotrone Trieste

Elettra is the third-generation Italian synchrotron radiation facility in Trieste operating since 1993, provided with 28 beamlines [Fig. 3.10]. This synchrotron produces beams with energy of 2-2.4 GeV, and provides photons in the energy range from a few to several tens of KeV. It is available for experiments

in many fields of physics, chemistry, material engineering biology, medicine, forensic science, and cultural heritage. All the relevant X-ray based techniques are present in the areas of spectroscopy, spectromicroscopy, diffraction, scattering and lithography, together with structures for infrared microscopy and spectroscopy, ultraviolet inelastic scattering and band mapping [3].

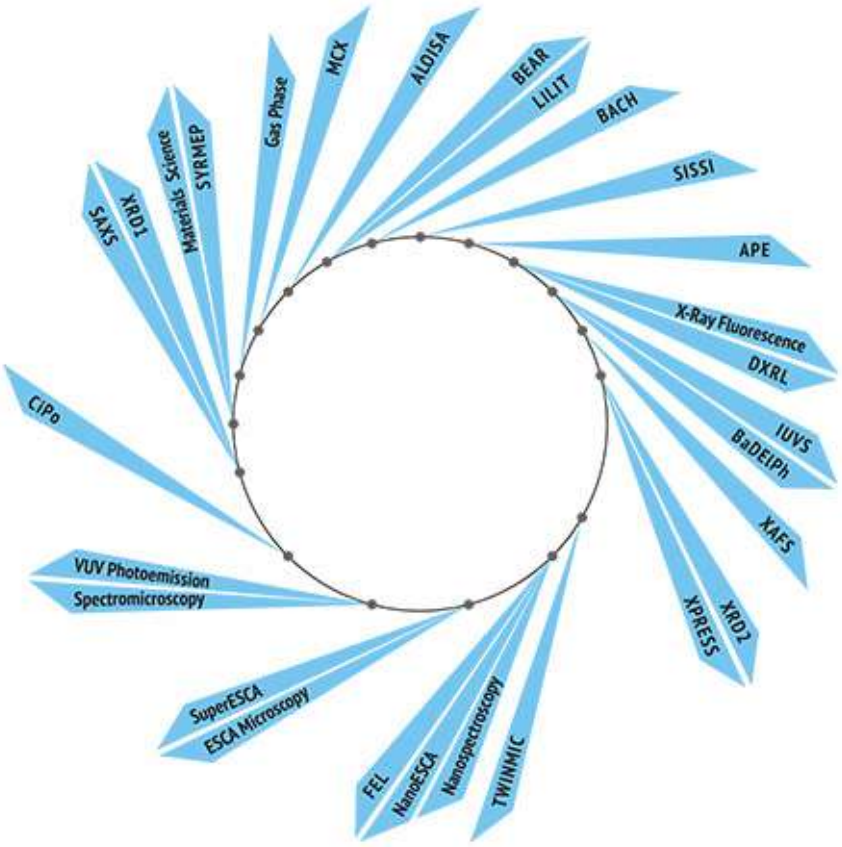

FIGURE 3.10: Sketch of the 28 beamlines of Elettra Sincrotrone Trieste [3].

Elettra Sincrotrone Trieste is a partner of the ReDSoX collaboration[1] and actively participates in the development and testing of new detector systems. Its participation is very important because thanks to the collaboration with the beamline scientists the detectors can be designed and engineered to be suited for their needs increasing therefore the performance of activities at the beamline. In addition, it was crucial the ability to test and optimize the detectors made at the Optical X-ray laboratory, and the beamline XAFS and TwinMic of Elettra Sincrotrone Trieste.

[1]For more details see Appendix A.

3.4.1 XAFS Beamline at Elettra Sincrotrone Trieste

The XAFS beamline at Elettra Sincrotrone Trieste covers an energy range from 2.4 to 27 keV. It combines X-ray Absorption Spectroscopy (XAS) with X-ray diffraction (XRD) to give important physical and chemical information to characterize the atomic structure of the samples under test. As in a typical XAFS beamline, the radiation is diffracted by a double monochromator crystal and hits the sample, which is positioned between two ionization chambers. These measure the intensity of the incident and outgoing beam (transmission measurement). In this way it is possible to study the trend of the absorption coefficient when the energy changes near the absorption edge of an atomic element (typically in an energy range of 1-2 keV around the energy of interest).

When the sample is optically thick or too diluted, the fluorescence technique is used instead of transmission. In this case only a small fraction of the emitted fluorescence radiation generated by the elements under test reaches the detector and it is important for the detector to have a large acceptance to reduce the measurement time. The detector has to be able to cope with a a high count rate maintaining a good energy resolution to resolve the peaks of interest from the surrounding spectrum features [42, 41, 38].

Current detector

The XAFS beamline at Elettra Sincrotrone Trieste uses for its experiments a KETEK GmbH AXAS-M Silicon Drift Detector. It is composed of a single SDD cell of 100 mm^2 (80 mm^2 of effective collimated area) and has an energy resolution of about 170 eV for the Mn Kα line at 5.89 keV at a peaking time of 1.32 μs and cooling at -70 °C. This detector is limited at high count rates by dead time because the use of a large SDD cell (50% of dead time at an OCR of 1.3 x 10^5 counts s^{-1} of output) [8, 7].

3.4.2 TwinMic Beamline at Elettra Sincrotrone Trieste

The TwinMic beamline at Elettra Sincrotrone Trieste covers an energy range from 400 to 2200 eV. TwinMic is a microscope that combines a full-field imaging and a scanning X-ray microscopy in a single instrument: allows you to do X-ray imaging for morphological characterization, dynamic studies and morphology, and also spectromicroscopic analysis with recognition of chemical elements and sample maps. The Low-energy XRF (LEXRF) systems works in vacuum and in the range of the soft X-ray and therefore it allows the mapping of light elements

like C, N, O, Mg, Na, that are the main constituents of the life matter, and then it can supply important information for the study of the biochemical processes [50, 49].

Current detector

The TwinMic beamline at Elettra Sincrotrone Trieste uses for its experiments the Low Energy X-ray Fluorescence (LEXRF) system that is composed of 8 large area Silicon Drift Detectors (SDDs) from company PNsensor disposed circularly [Fig. 3.11]. The 8 SDDs are installed on a copper support that through a water cooling system and Peltier cells allows to have a working temperature of -15 °C. Each SDD has an active area of 30 mm^2 (for a total system active area of 240 mm^2) and an FWHM of 135 eV at the Mn Kα line, and 69 eV at the C kα line. The detectors are windowless in order to reduce the absorption of the most light elements. The solid angle covered by this detector system is about 4° [50].

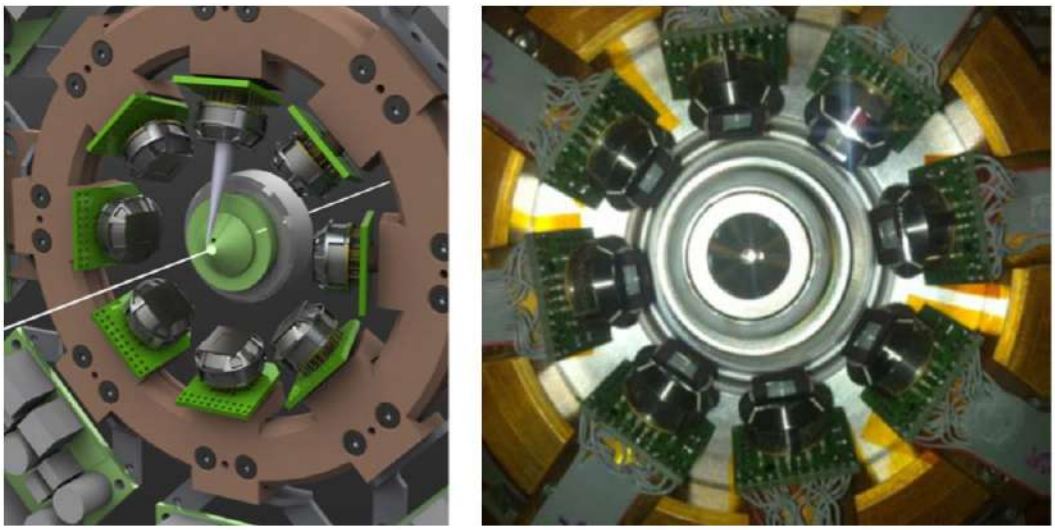

FIGURE 3.11: (**a**) Sketch of the LEXRF detector system on the beamline TwinMic [27] (**b**) Picture of the current LEXRF detector system on the beamline TwinMic [48].

3.5 Synchrotron-light for Experimental Science and Application in the Middle East (SESAME)

The Synchrotron-light for Experimental Science and Application in the Middle East (SESAME) is a project born to help in improving the delicate situation in the Middle East. It is inspired by the CERN model: to promote technology and science in the Middle East to increase cooperation reducing tensions through the front-edge scientific work. The main idea is that scientists with different religion, traditions, political system could work together in an international laboratory.

SESAME is a 2.5 GeV third Generation synchrotron light source located in Jordan, more precisely in Allan, 30 km North-West of Amman. It was officially founded in 2003 as a resource of all the Middle East and North Africa (MENA). The Members (all from MENA) of SESAME are currently Cyprus, Egypt, Iran, Israel, Jordan, Pakistan, the Palestinian Authority and Turkey. The Observer countries, from outside the MENA, are: Brazil, China, France, Germany, Greece, Italy, Japan, Kuwait, Portugal, the Russian Federation, Spain, Sweden, Switzerland, the United Kingdom and the United States of America.

The scientific interdisciplinary program includes: chemistry, physics, biological science, materials science, environmental applications, medicine, agriculture, molecular biology and cultural heritage.

SESAME has the capacity to host about 28 beamlines [Fig.3.12]. The initial beamlines are seven: XAFS/XRF (X-ray Absorption Fine Structure/X-ray Fluorescence) spectroscopy, IR (Infrared Spectromicroscopy), MS (Materials Science), MX (Macromolecular Crystallography), Soft X-ray Beamline, SAXS/WAXS (Small Angle and Wide Angle X-ray Scattering) and Tomography Beamline [13, 39, 75, 1].

Italy, one of the Observer countries, has allocated, through the Ministry of Education, University and Research (MIUR), an ad hoc financing. This significant contribution to its implementation is managed by the Istituto Nazionale di Fisica Nucleare (INFN) in collaboration with Elettra Sincrotrone Trieste. One of such contributions, realized within the ReDSoX (Research Drift detectors for Soft X-ray) Collaboration[2] by INFN-Trieste and Elettra, was the production of a multi-channel silicon detector for X-ray Fluorescence measurements to be used at XAFS/XRF beamline at SESAME, which will be described in the construction and characterisation details in the next chapter.

[2]For more details see Appendix A.

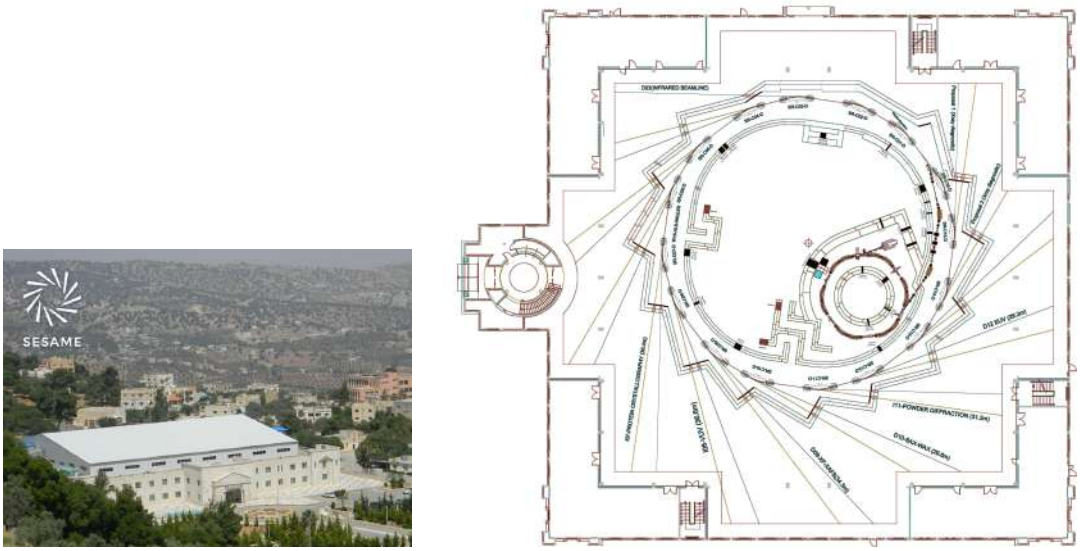

FIGURE 3.12: SESAME: the Synchrotron-light for Experimental Science and Application in the Middle East: (**a**) The building housing the synchrotron and logo [13]. (**b**) SESAME beamlines layout showing the location of the seven Phase I beamlines on the storage ring [1].

In the realization and optimization of the XAFS detector system were crucial conversations with the beamline scientists of the beamline XAFS/XRF of SESAME and Elettra, in order to understand their demands and their needs. In fact, thanks to this synergy between developers and user the detector system has acquired a great added value compared to a commercial detector.

Chapter 4

Detector System for XAFS Beamline

A Fluorescence Detector System for XAFS (X-ray Absorption Fine Structure) composed of 8 monolithic arrays of Silicon Drift Detectors, each having 8 cells of 9 mm^2 area, is being realized within the INFN ReDSoX Collaboration[1]. It will be used for X-ray absorption spectroscopy at the Jordanian synchrotron light source SESAME that provides a photon beam with an energy range between 3 and 30 keV. This detector system has been designed specifically for the beamline requirements, and is equipped with a segmented sensor with 64 cells of smaller area coupled with fast and low-noise electronics with independent read out circuitry, allowing to operate with a low dead time at high count rates. Detailed characterization tests at Elettra Sincrotrone Trieste have demonstrated an energy resolution at the Mn 5.9 keV Kα line, for the monolithic array, below 170 eV FWHM at room temperature.

An infographic timeline of the project's activities over the last 3 years is provided in Appendix B.

The personal contribution for the SESAME project was to carry out the operational coordination with the step-by-step testing and integration of the detector system.

4.1 The novel detector system: XAFS-SESAME Detector System

The detector system was designed and implemented for X-Ray Fluorescence (XRF) and X-ray Absorption Fine Structure (XAFS) experiments. It is based on the state-of-the-art technology both for the sensor and for the readout electronics. It is composed of 8 rectangular monolithic arrays of SDDs, with a total

[1]For more details see Appendix A.

sensitive area of 570 mm^2. It is specially designed from the XAFS beamline scientists' requests and optimized to work in an energy range of 3-30 keV.

The detection system, shown schematically in Figure 4.1, is a modular system consisting of eight planes arranged in an aluminum case. Every plane is composed of an array of SDDs (1) coupled with ultra low-noise Front End Electronics mounted on a PCB (2) connected with the Front End (FE) PCB (3), mounted at 90°. Above the latter there is a brass profile for the cooling system (4). Every plane is inserted in the instrument case as a drawer by means of two sets of frame guides (5-6) and connected to the power supply and filter (7) and Back-End (BE) (8) PCBs. Under the modules, in the back side of the system, there are inlet (9) and outlet (10) cooling distribution. The rear panel supports the Ethernet PCBs (11) and the power supply connectors (12) [66].

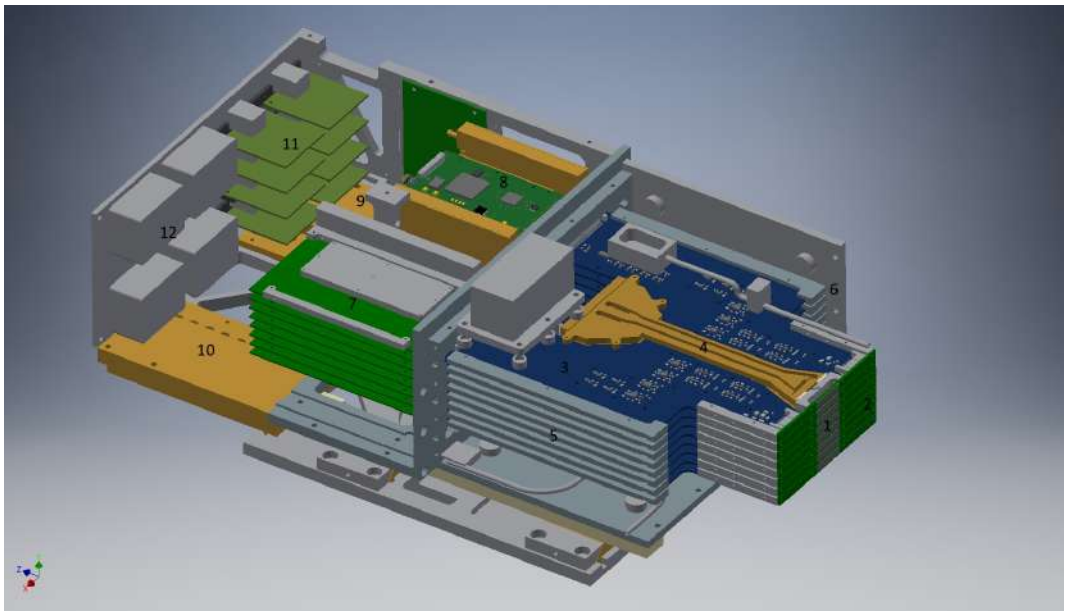

FIGURE 4.1: Detector system: (1) detectors, (2) detector PCB, (3) front-end PCBs, (4) brass profile with cooling liquid flowing inside, (5) insertion guides at flanks of detecting heads, (6) rails for eight detection heads, (7) power supply and filters PCBs, (8) back-end PCBs, (9) inlet cooling distribution, (10) outlet cooling distribution, (11) ethernet PCBs, (12) power supply connectors [66].

Before this final version of the detection system, two different prototypes have been built and tested in the laboratory and on the beamline at Elettra Sincrotrone Trieste [42, 41].

Figure 4.2 shows the first part of the detector system: without the external aluminum case, it is possible to see two of the eight planes mounted inside the system. During operation, the system is completely closed and darkened (with a Mylar window) on the left side, in which there are the SDDs, FE electronics and the first part of the cooling system (an aluminum prototype is visible in the

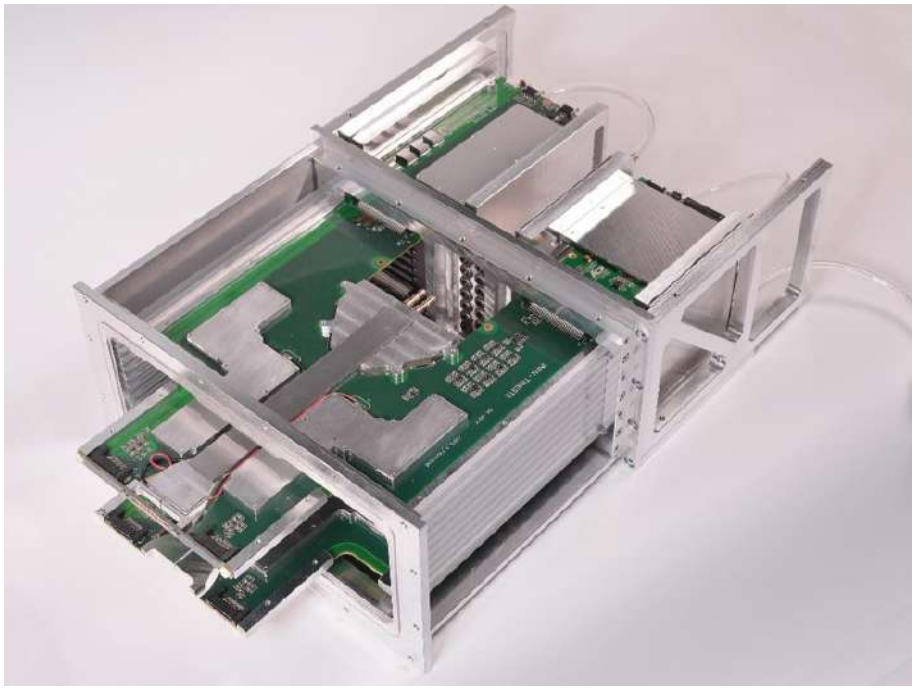

FIGURE 4.2: The first part of the detector system: without the external case, it is possible to see two of the eight modules mounted inside the system.

picture). Moreover, this part of the case is subjected to a moderate nitrogen fluxing in order to avoid dew condensation.

In Figure 4.3 two images of the complete detector system from two different angles. In Appendix C the XAFS-SESAME Detector System Datasheet is given. It contains the main descriptions of the detector system and the instrumentation supplied.

4.1.1 The sensor

The sensors of this detector system, Figure 4.4, consist of SDDs designed by INFN-Trieste and built by FBK-Trento. They are obtained from a high purity, 450 μm thick n-type silicon wafer with a resistivity of 9 kΩ·cm. The sensor is composed of 8 rectangular monolithic arrays of SDDs, each having 8 square cells of 9 mm^2 (called strip) [Fig. 4.4] [66, 41, 19]. The sensors used for this detector system have been designed taking into account the results obtained from the mapping of the chapter 2 and therefore optimized for charge collection. Hence the effective area of these sensors is very similar to the nominal value of active area. Collimation would help define the sensitive area and minimize the partial charge collection of events arising from the detector edge. In the first complete layout collimators have not been installed because the need of progressive characterizing integration of the latter whose test is in progress.

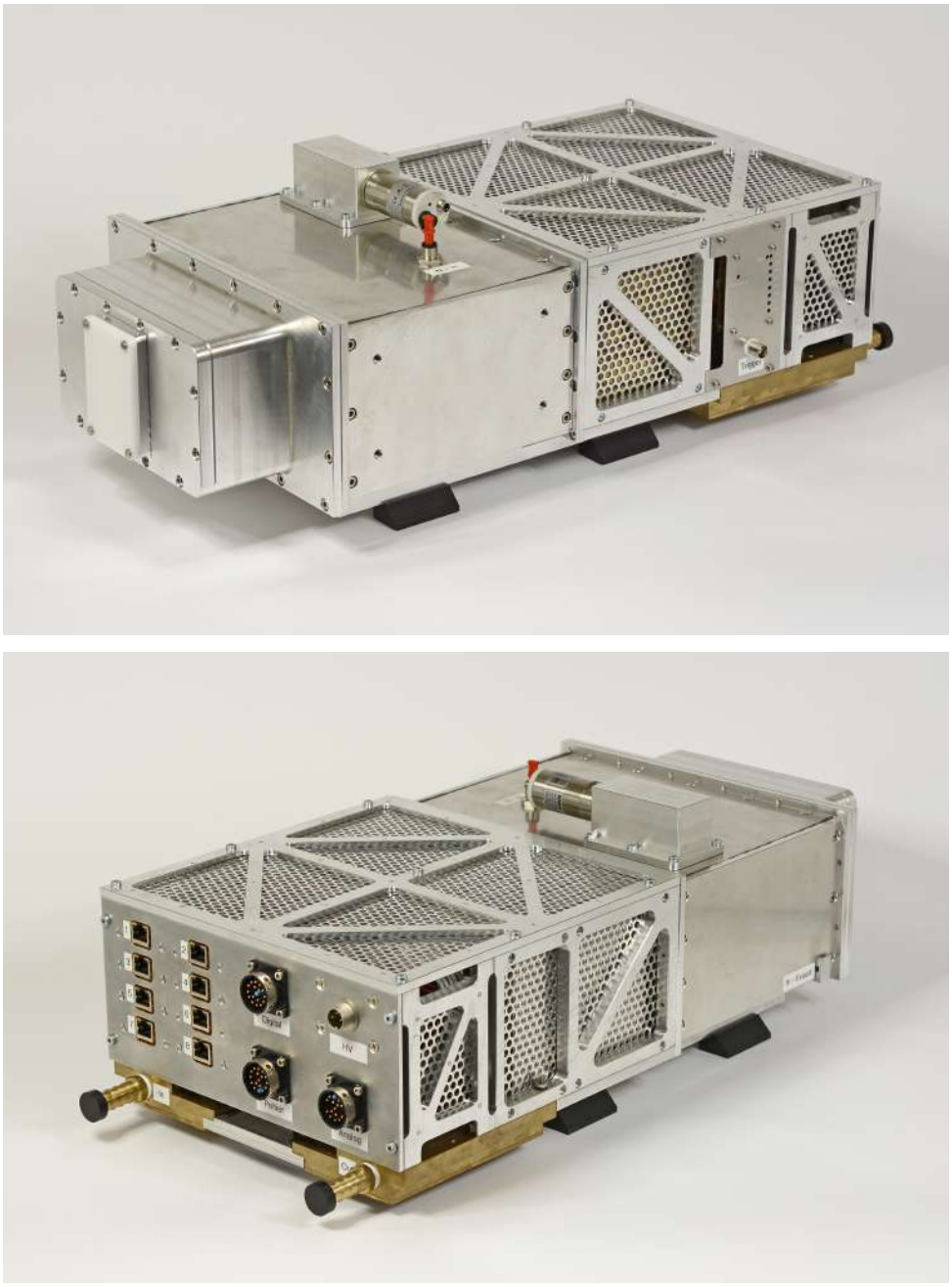

FIGURE 4.3: (**a**) Upper, front and right side of the detector system (**b**) Upper, back and left side of the detector system.

As previously described in chapter 1, the silicon bulk constitutes the active volume of the sensor. The sensor has been designed to be able to detect low energy X-rays with good sensitivity down to few hundreds of eV. This is also possible for the use of a thin entrance window: a shallow uniform p+ implant, common to all the eight cells, covered by a protective thin layer of oxide.

The FBK process technology coupled to the sensor design allowed the construction of devices featuring an anode capacitance of about 40 fF and a leakage current below 100 pA/cm^2 at 20 °C [66].

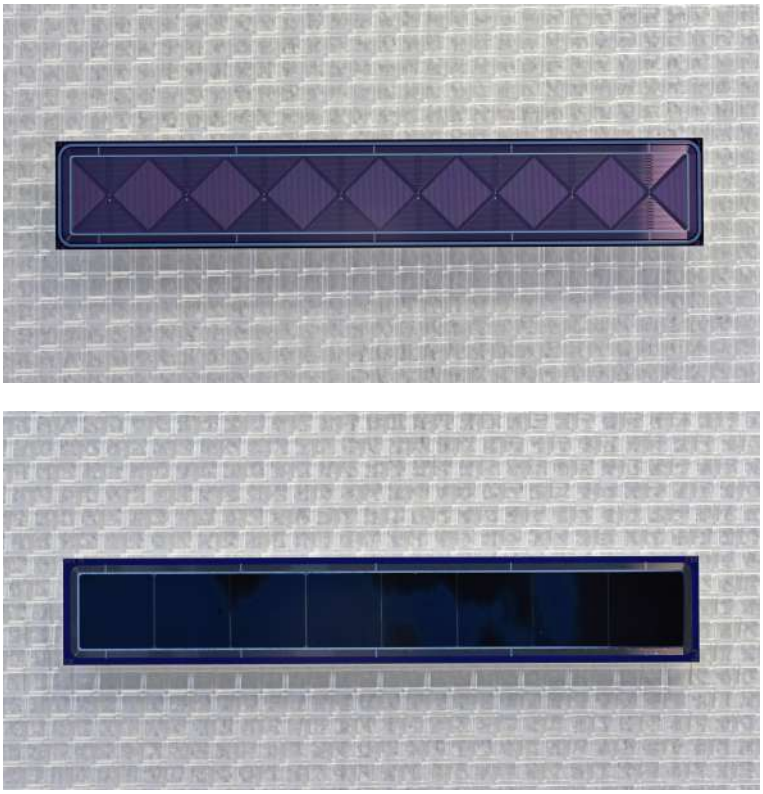

FIGURE 4.4: SDD linear array comprising 8 square cells with a 3 x 3 mm^2 active area. Anode (top) and entrance window (bottom) sides.

Each SDD has an on-board thermistor that, once calibrated in a climatic chamber, allows to determine the temperature of the sensor.

The monolithic array of 8 SDDs is mounted (by means of a thermally conductive and electrically insulating glue) on a detector PCB, onto which 8 SIRIO charge preamplifiers [19, 20] are glued. This detector board also contains bias filter capacitors, connectors to the FE PCB (that is mounted at 90°) and provides anchor points for the coupling to the cold side of the cooling system [Fig. 4.5].

4.1.2 Electronics

The readout anodes of every SDD cell are wire bonded to SIRIO [19, 20, 23] charge preamplifiers [Fig. 4.5 (b)]. This Ultra Low Noise CMOS Charge Sensitive Preamplifier has been specifically designed by Politecnico of Milano for high resolution X-ray spectrometry with SDDs. The front-end integrated circuit is built in 0.35 μm AMS CMOS technology and represents the state-of-art in low-noise FE electronics: it has an Equivalent Noise Charge (ENC) down to 1.2 and 0.9 electrons r.m.s. at room and at -30 °C respectively.

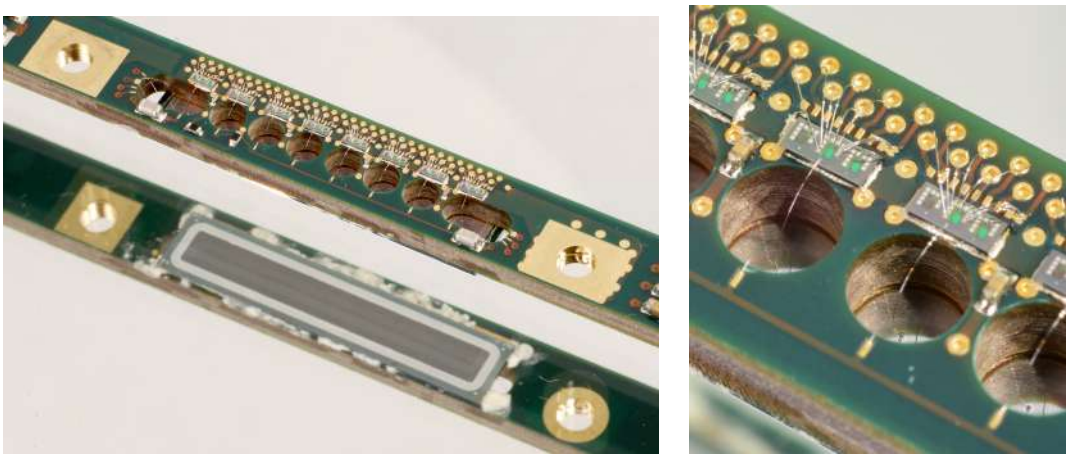

FIGURE 4.5: (**a**) The front and back side of one strip: monolithic SDD with 8 cells installed on PCB and connected with SIRIO charge preamplifiers. (**b**) Detailed view of the SIRIO-SDD connection.

As shown in Figure 4.6, the signal conditioning is divided in: FE, BE, power supplies and filter and ethernet interface (not shown in the Figure 4.6). The Front-End PCB includes eight fast RC-CR^2 analog shaping filters with a selectable time constant, the the logic circuitry that signals the FPGA when to reset the SIRIO preamplifiers and single-ended to differential buffers to drive the ADC inputs.

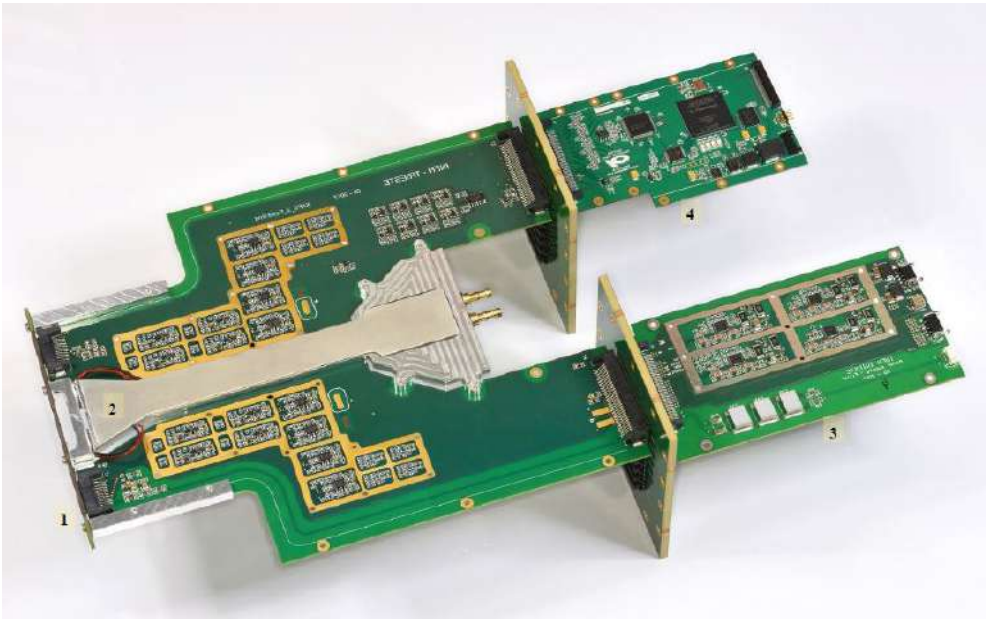

FIGURE 4.6: Signal Conditioning electronic system: (1) Front-End PCBs, (2) cooling profile on FE PCB, (3) Back-End PCB, (4) power supply and filters PCB.

Connected to the FE PCB, the Back-End PCB includes an 8-channel, 12

bit ADC and an FPGA. Here the pre-shaped signals are sampled at a rate of 40 MHz and are filtered with an optimized finite impulse response (FIR) filter of variable length by the FPGA. The selectable peaking times for the acquisition are 0.4, 0.7, 1.0 and 1.45 μs.

After the digital elaboration, the data are transmitted through the ethernet PCB via TCP/IP to a host computer in which there is a dedicated software for the control and the acquisition [41, 66, 28].

4.1.3 The cooling system

The cooling system is meant to stabilize the temperature of the detectors cooling them down moderately (0-10 °C). Toward this purpose we use two systems that complement one another, shown in Figure 4.7 and 4.8: a cooling fluid and Peltier cells. Preliminarily, nitrogen is lightly fluxed inside the aluminum case in order to lower the dew point and prevent water condensation on the FE PCB.

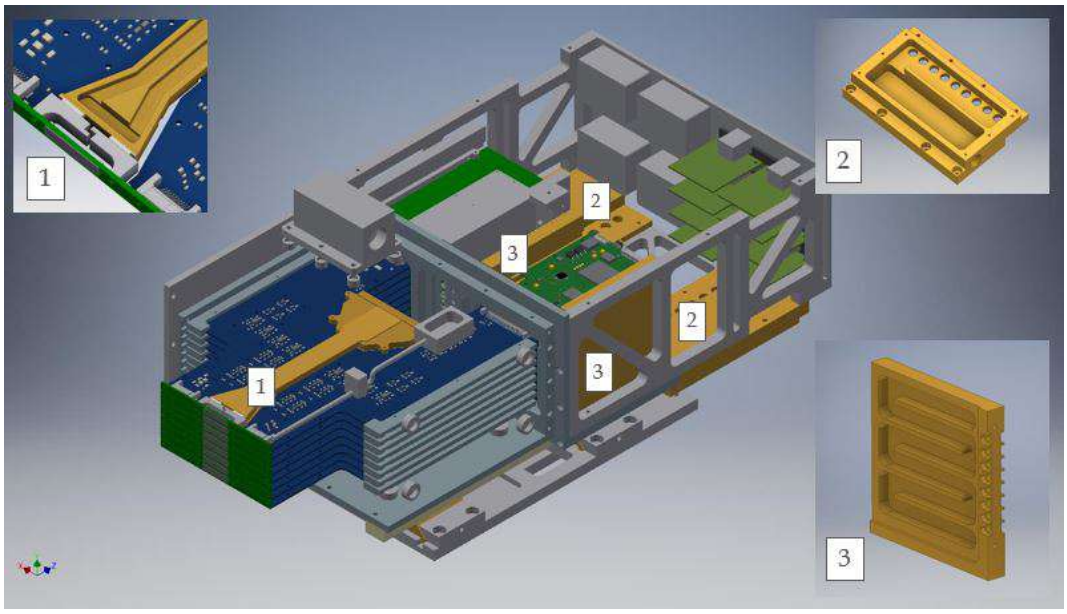

FIGURE 4.7: Cooling system: (1) Peltier cells connected to the PCB and to the Brass profile, (2) inlet and outlet cooling distribution, (3) BE heat exchangers.

The detector PCB on which the SDD array is mounted is in thermal contact with the cool side of a Peltier cell, which is glued to the structure.

Water cooled to 18 °C by an external chiller is circulated through the brass profile on the FE board, the BE heat exchangers and the input and output collectors that together constitute the cooling fluid distribution. In this way it is possible to cool down the temperature of the BE boards. Moreover, the heat from the hot side of the Peltier cell is also removed by the brass profile mounted on the FE PCB [41, 66].

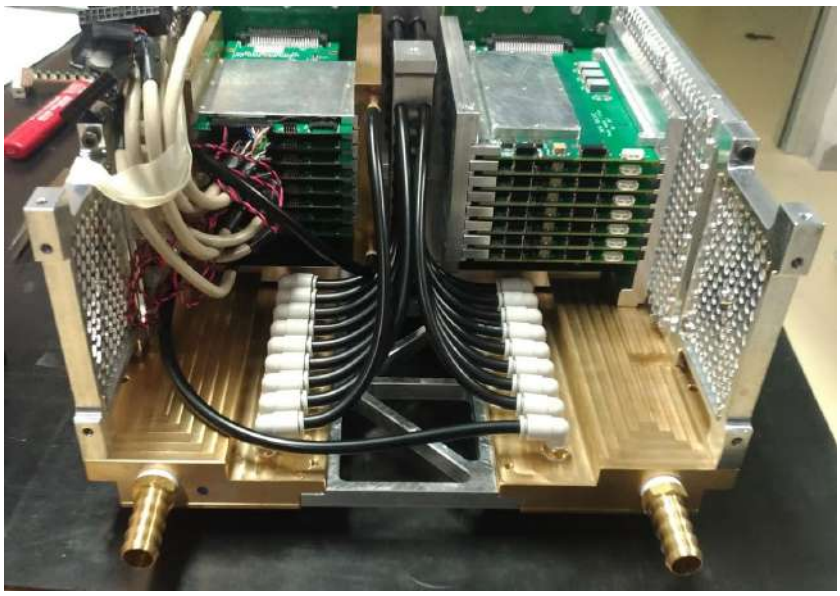

FIGURE 4.8: Detail photo of the cooling system of the detector system (system being assembled). It is possible to see: inlet and outlet cooling distribution, BE heat exchangers, and the tubes through which the refrigerated fluid flows.

In the first version of the cooling system one Peltier cell was used for each FE board, and the metallic profiles of the cooling system were built from aluminum. In the latest version of the cooling system two smaller Peltier cells are used for each FE board, and the metallic profiles, now made in brass, have been modified to optimize the thermal interface with the Peltiers and the detector board. This new configuration allows to reduce power consumption and provides longer durability to the water circulation system while improving the cooling performance.

4.1.4 Software

A custom software was specifically designed, following the beamline requirements, for the tasks of data acquisition and instrument management: FICUS (Fluorescence Instrumentation Control Universal Software) [Figure 4.9]. In Appendix C the the first version of the FICUS software manual is included.

The FICUS software is an integral part of the detector system: it has been designed to complete the instrument according to the requests and needs that have emerged from the continuous consultation with beamline scientists and users. The software has 3 different levels: each level corresponds to a different subject who uses it and, consequently, a different choice of options available. In particular, three levels are available:

- Detector Expert: dedicated to detector and software developers, allows the maximum degree of variation of the available parameters and the display of screens useful for development and debugging;
- Beamline Staff: dedicated to the staff of the beamline, allows an intermediate degree of variation of the parameters for the setting and the measurement;
- User: dedicated to all possible users of the beamline, allows a low degree of parameter variation for data collection and pre-analysis.

FICUS has been tested and used in during all the acquisitions made. This has allowed to verify its performance and to further optimize it. It is also integrated with the line control software, so it can be synchronized with the normal measurement cycle of the line.

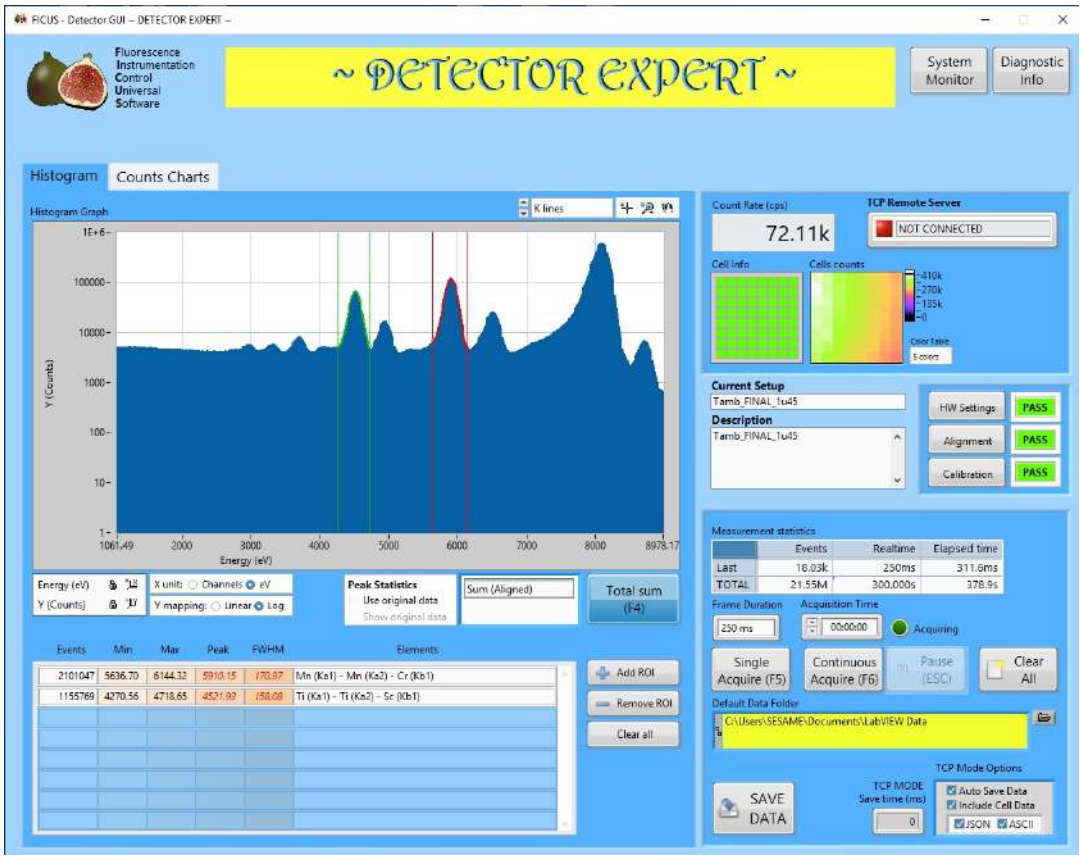

FIGURE 4.9: The windows of the last version of FICUS software acquisition (Histogram), Detector Expert level, after the measurement by five minute with the calibration sample.

Using this software, after a preliminary selection of measurement parameters, it is possible to perform the following tasks: data alignment of the cells, energy calibration, and selection of the Region Of Interest (ROI). During the

measurement it is possible, for example, to obtain a spectrum in real time with some information such as FWMH and peak centroid (in ADC channels and in eV), count rate and dead time.

4.2 Test on the XAFS-SESAME Detector System

To obtain the XAFS-SESAME detector system a detailed and progressive work has been carried out from the selection of the sensors, through testing and assembly of the system. To get to the complete system it was necessary an iterative test and development procedure to solve some hardware, firmware and software bugs. The most relevant logical and chronological steps of this method will be described below.

After the SDDs have been characterized with a probe station, they are glued and bonded on the PCBs and tested at different assembly stages. After these preliminary tests, every strip was mounted on-board into the system and characterized in laboratory with radioactive sources. To carry out more detailed tests at higher energies and rates, the detection system has been brought to the optical X-ray laboratory and on the XAFS beamline at Elettra Sincrotrone Trieste.

4.2.1 Characterization of detector strips

The first test done on a strip (and, consequently, a complete plane) is the acquisition with both a pulser and a ^{55}Fe source to analyze the correct functioning of the cells, uniformity and resolution of the SDDs. In a second moment the calibration of on-board the temperature sensor of the SDD arrays is carried out, which allows the determination of its operating temperature during the experimental measurements. The characterization tests were made for all the strips of the detector system. Only a representative graph of the sum of the 8 channels of the strip21 is shown in Figure 4.10.

In laboratory [Fig. 4.11], we tested also the performance by changing the power supplies (and using batteries to power the system), the digital filter applied and the waiting time after reset. These test lead to the best measurement parameters. We noted that, despite the many changes, the system was robust enough not to present sizable performance variations.

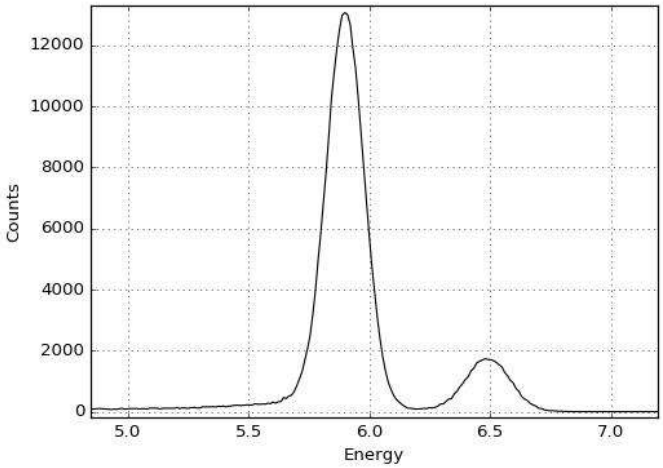

FIGURE 4.10: Acquisition with all the 8 channel of strip21 and ^{55}Fe source at room temperature. The resolution is 170 eV at Mn Kα line at room temperature for a peaking time of 0.9 μs.

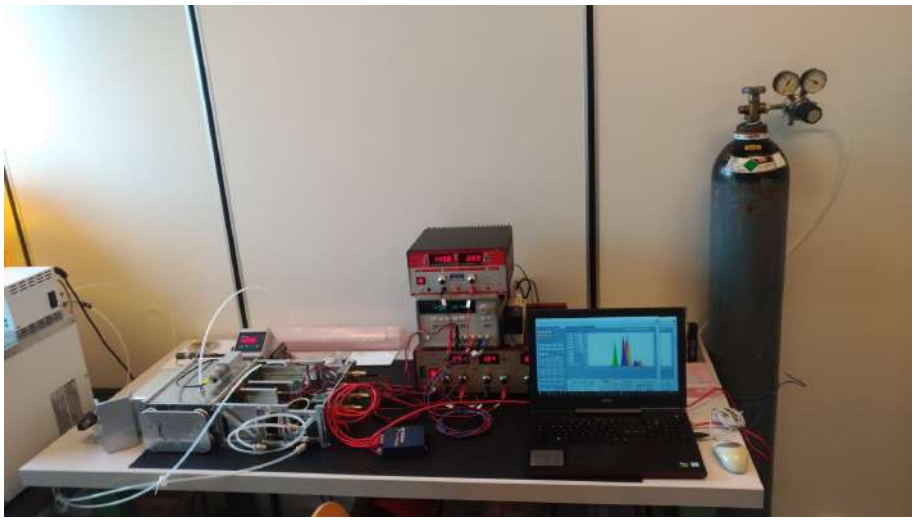

FIGURE 4.11: Detector system at the INFN Trieste laboratory. From left to right: chiller, ^{55}Fe source, detector system, power supplies, laptop with acquisition software (previous version of FICUS), nitrogen bottle.

For the preliminary test we used the X-ray optical laboratory of Elettra Sincrotrone Trieste. In particular we used an X-ray tube with an Ag anode as source and the detector system with only one module.

The first measurement was done to characterize the spectrum of the beam scattered by a plastic sheet since this was used to perform the successive tests.

The next test of the detector system was the characterization of the materials used in the instrument to check if they can interfere with the measurements the detector is designed for: we analyzed the detector PCB, including its components, the Peltier cell, and the glue used to mount detector, ASIC and Peltier.

By comparing the acquired data with the spectrum of the scattered beam, the analysis showed that none of the materials that make up the measurement system produced relevant peaks in the scattering spectrum, confirming therefore that they do not affect the measurements [Fig. 4.12]. It is underlined however that for this test the system (detector, software, firmware, filters, cooling system) was in a prototype state.

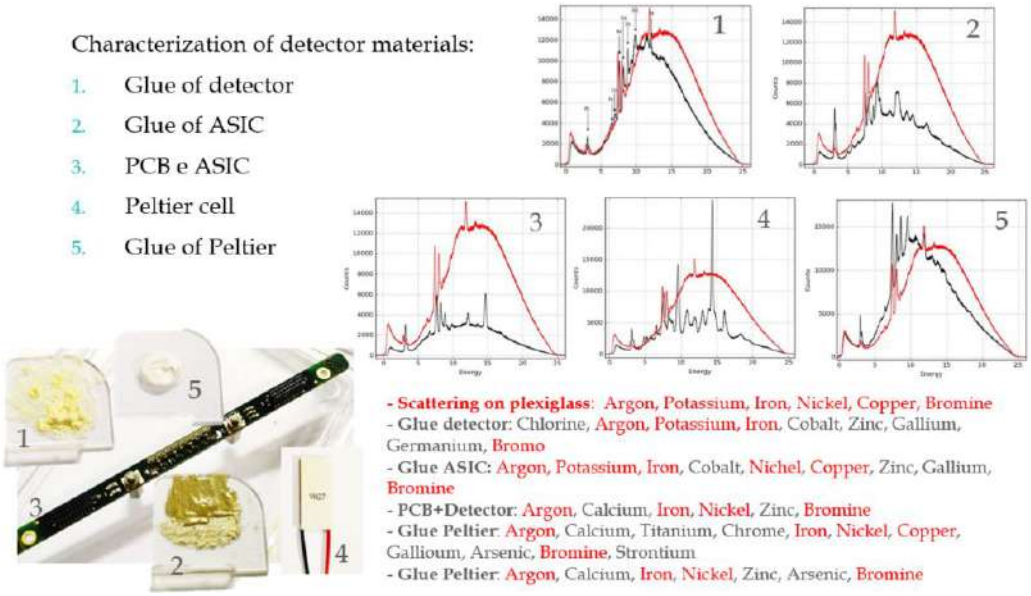

FIGURE 4.12: Characterization of the detector materials: analysis of the detector PCB (including its components), the Peltier cell, and the glue used to mount detector, ASIC and Peltier. All the spectra are compared with the spectrum of the scattered beam (in red).

A sample was prepared and subsequently used to test the detector system. This sample was composed of Ti, Zn, and Mo; in this way we made an energy calibration in a large energy range, from 4 to 20 keV, and analyzed the performance of the detector in detail. This task was performed using the PyMca X-ray Fluorescence Toolkit [9, 77]. Figure 4.13 presents the spectrum and the peak energy of the elements present in the calibration sample; this acquisition was done at room temperature. Table 4.1 shows the analysis of the FWHM of the elements present in the calibration sample.

The high flux provided by the X-ray tube allowed us to design and test a digital pile-up rejection circuit, within the FPGA, that enabled us to improve the detector performance and to measure the Output Count-Rate (OCR) as function of the Input Count-Rate (ICR) [Fig. 4.14]. To perform the OCR vs ICR scan we irradiated a Zn target (fluorescence lines Kα = 8639 eV and Kβ = 9572 eV): using a peaking time of 0.9 μs, a single module produces an OCR

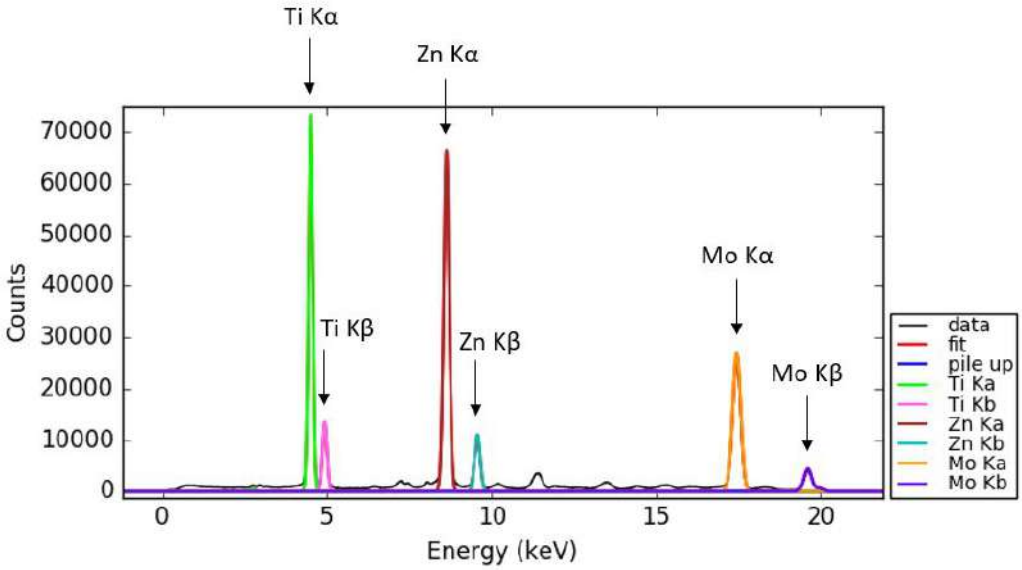

FIGURE 4.13: Analysis of the sample (Ti, Zn, Mo), acquisition with strip8 at room temperature at the Optical X-ray laboratory of Elettra Sincrotrone Trieste.

TABLE 4.1: The analysis of the FWHM of the elements present in the sample (Ti, Zn, Mo).

Line	**Energy [eV]**	**FWHM [eV]**
Ti Kα	4509	155
Ti Kβ	4932	159
Zn Kα	8639	193
Zn Kβ	9572	201
Mo Kα	17479	257
Mo Kβ	19607	270

of 1600 kcounts/s·cm^2, hence the complete detection system with 64 cells is expected to be able to operate up to 10 Mcounts/s [66].

Another test was performed with two test strip mounted in the central position of the case (strip1 with only 5 cells active and the strip8 with all the cells active, for for a total of 13 active cells) to confirm the ability of the new system to work at high input count-rates (ICR) while maintaining low dead time and a good energy resolution. Experimental results confirmed the targeted design parameters, reaching a maximum acquisition rate of 3.1 Mcounts/cm^{2}s with a peaking time of 0.4 μs [Fig. 4.15]. This translates into an output count-rate (OCR) of 15.5 Mcount/s for the entire 64 elements collimated detector [28].

There is obviously a trade-off between energy resolution and short signal

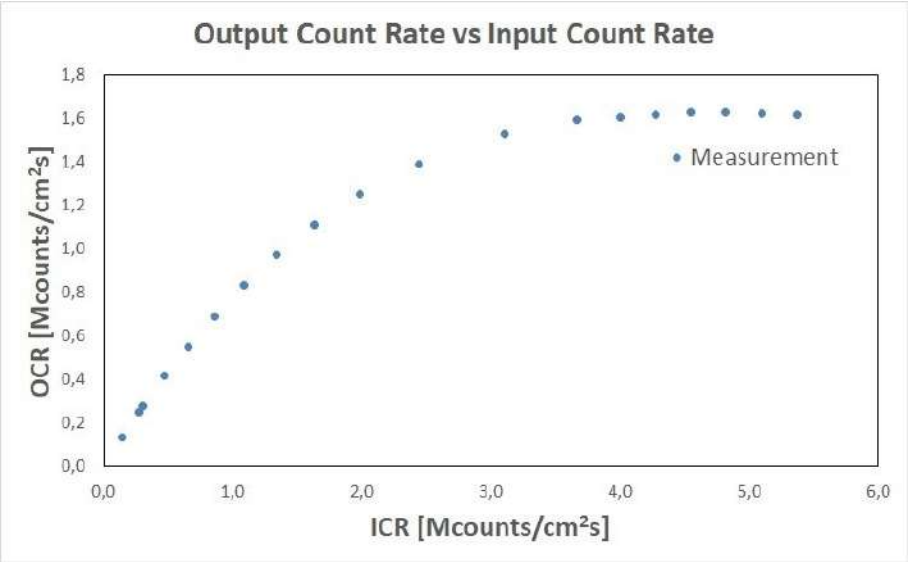

FIGURE 4.14: Output count-rate (OCR) was measured with a single module as a function of Input count-rate (ICR) [66].

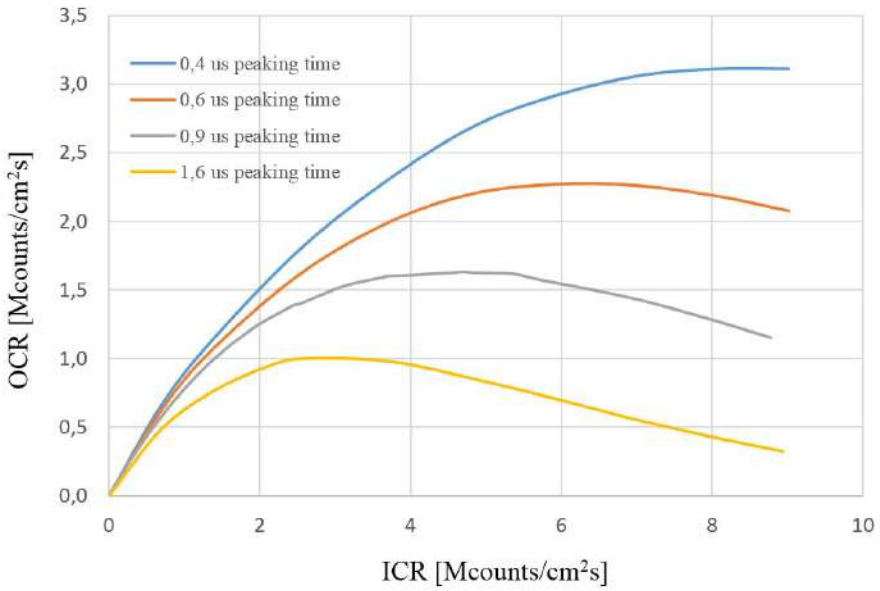

FIGURE 4.15: Output count-rate (OCR) versus input count-rate (ICR), obtained with different peaking time ranging from 0.4 to 1.6 μs [28].

process time (which permits high throughputs). The maximum OCR was obtained with a peaking time of 0.4 μs; the energy resolution was around 175 eV FWHM at Mn Kα. The longer is the shaping time, the lower is the white voltage noise (for this reason, and analyzing the resolution measures depending on peaking time, for the following measures it has been chosen to consider optimal and to use a peaking time of 1.45 μs). Being the leakage current for a single XAFS 9 mm^2 SDD element as low as 10 pA at 20 °C, the energy resolution is improved by increasing the shaping time towards some microseconds. An

energy resolution below 150 eV FWHM at Mn Kα line was measured using 1.6 μs peaking time. With this peaking time the maximum achievable OCR results around 1 Mcounts/cm^{2}s, however with a slightly worse energy resolution (155 eV FWHM at Mn Kα) a maximum OCR of 1.6 Mcounts/cm^{2}s was obtained with 0.9 μs peaking time [28].

4.2.2 First test on the XAFS beamline at Elettra

In February 2018 the detector system using two SDD modules (strip8 with 8 channels and strip1, a first prototype in which only 5 channels work properly) was tested on the XAFS beamline [66]. The detector system (working at room temperature and with a peaking time of 0.9 μs) was installed in two different position: normal position [Fig. 4.16 (a)] and parasitic position [Fig. 4.16 (b)]. In parasitic position the detector is 2-3 times further away from the sample than the KETEK SDD.

FIGURE 4.16: The detector system during the test at the XAFS beamline: (**a**) our detector system and the KETEK SDD are both in normal position. (**b**) the KETEK sensor is in normal position while our detector system is in parasitic position.

Preliminary to the measurements a new calibration sample was prepared and subsequently used to test the detector system. This sample was composed of K, Ti, Mn, Zn, Br, Zr; in this way we could make energy calibration in a large energy range, from 4 to 18 keV, and analyze the performance of the detector in detail. To deploy this analysis we used PyMca X-ray Fluorescence Toolkit [9, 77]. Figure 4.17 presents the spectrum and the peak energy of the elements present in the calibration sample; this acquisition was done at room temperature in normal position. Figure 4.18 (a) shows the comparison between the sum spectrum of the 13 channels (strip8+strip1, in black) and that of a single channel (ch1 of strip8, in red); figure 4.18 (b) shows the analysis of the FWHM of the elements present in the calibration sample for the same data sets.

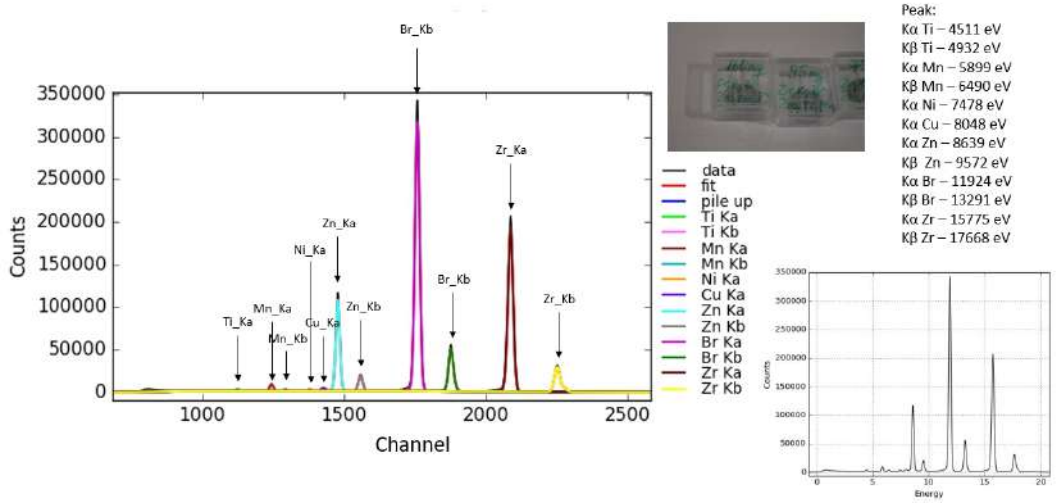

FIGURE 4.17: Analysis of the calibration sample (K, Ti, Mn, Zn, Br, Zr), acquisition with strip1 and strip8 at room temperature at Elettra Sincrotrone Trieste with detector in normal position. The beam energy was 20 keV.

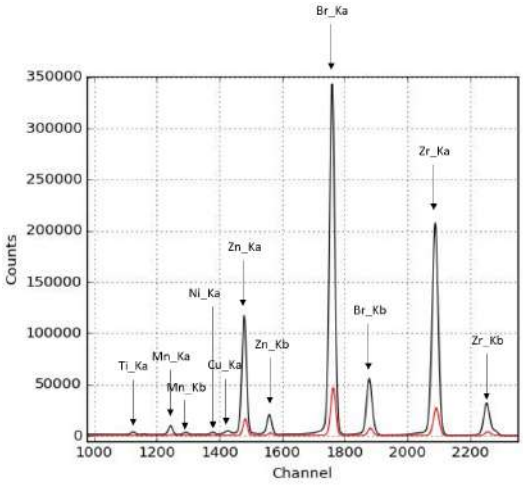

LINE	FWHM [eV] strip8_ch1	Chi square strip8_ch1	FWHM [eV] strip8+strip1	Chi square strip8+strip1
Ti_Ka	147	1.17	163	12.44
Ti_Kb	151	0.86	167	4.11
Mn_Ka	159	0.82	175	26.68
Mn_Kb	164	6.13	179	47.05
Ni_Ka	172	2.12	187	11.88
Cu_Ka	176	8.44	191	85.87
Zn_Ka	180	3.66	195	175.64
Zn_Kb	187	3.17	202	47.66
Br_Ka	203	4.57	218	626.60
Br_Kb	212	2.09	227	131.14
Zr_Ka	226	1.98	241	467.27
Zr_Kb	237	1.46	252	75.80

FIGURE 4.18: (**a**) Analysis of the calibration sample (K, Ti, Mn, Zn, Br, Zr), acquisition with strip1 and strip8 at room temperature at Elettra Sincrotrone Trieste with detector in normal position, beam energy of 20 KeV - comparison between acquisition with one channel (in red) and with 13 channels (in black) (**b**) The table at the right shows the energy resolution at the different lines of the calibration sample for 1 channel and for the sum of 13 channels.

After these preliminary measurements, a simultaneous acquisition of a sample containing Selenium was performed with the KETEK SDD in normal position and the new detector system (with active only the strip8) in parasitic position.

The results of this test allow us to compare the two detectors (the KETEK SDD against one 8-SDD module), whose normalized spectra are plotted in Figure 4.19:

- The energy resolution is comparable;
- KETEK SDD stops working effectively at a maximum OCR just above 100 kcounts/s with a dead time of 50%;
- One module of 8 SDDs have an OCR of 1600 kcounts/s·cm^2 (that is higher than 10 Mcounts/s for the complete system of 8 modules).

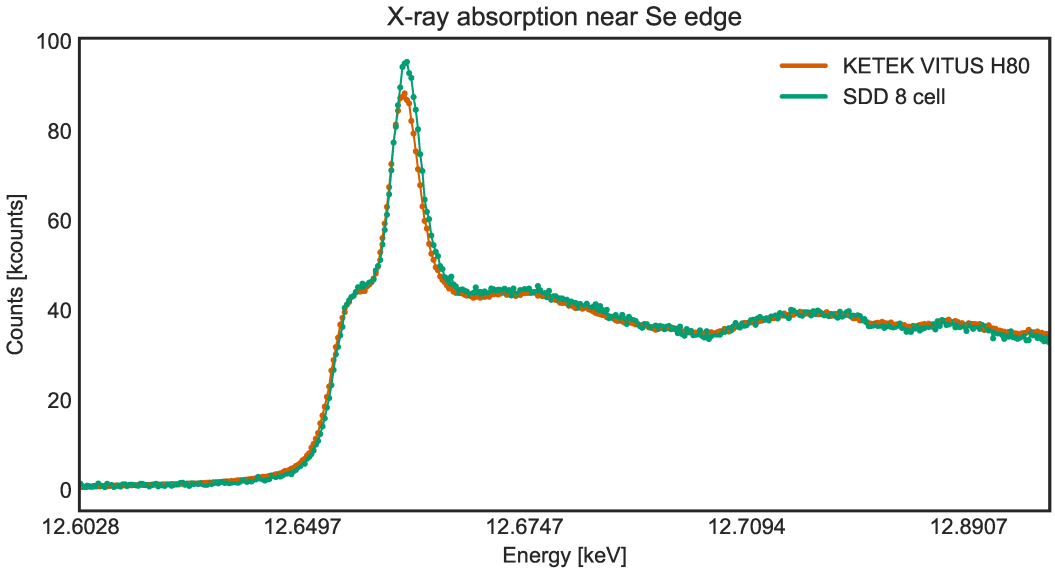

FIGURE 4.19: Normalized XAFS spectra measured by the two detectors near the Selenium edge (single module of 8 SDDs vs standard single element SDD (KETEK VITUS H80) [66].

4.2.3 Development of the eight-strip detector system

After this encouraging first measurement on the XAFS beamline the work of development and optimization of the detector proceeded towards the complete system.

One of the steps was to install the previously described cooling system on the case. subsequent measures will have the advantage of stabilization of the temperature of the system. Before the cooling system was permanently and permanently installed, it was kept in operation and monitored for weeks.

The improved version of SDDs to maximise the active area was pre-tested in order to find the strips that showed uniform behaviour and with the desired characteristics.

The new SIRIO (SFS3) preamplifiers in an optimized version from PoliMI have been used to improve the performance of the detector system. Elettra

proceeded with the implementation of the FICUS software. The firmware of the BE and communication boards has also been improved. Digital filters have been created for each channel of the detector.

The selected SDDs were glued and mounted, and tests were carried out on them to assess their stability and repeatability characteristics. Only the strips that have passed all these tests on bench setup were selected to be part of the detector system. Based on the test results, the mounting position was chosen. The selected SDD strips, their position and characteristics are shown in Table 4.2.

TABLE 4.2: Information of the SDDs installed in the XAFS-SESAME Detector System.

Position	Strip Name	Production Lot	Wafer	ID
1	strip12	SESAME	W2	NNS-12
2	strip20	SESAME	W5	NNS-8
3	strip16	SESAME	W2	NNS-4
4	strip14	SESAME	W3	NNS-2
5	strip15	SESAME	W3	NNS-4
6	strip21	SESAME	W4	NNS-9
7	strip22	SESAME	W5	NNS-3
8	strip18	SESAME	W3	NNS-8

All these steps have led to the final assembly of the XAFS-SESAME Detector System [Fig. 4.20]. The appearance of the complete system is that shown in Figure 4.4.

FIGURE 4.20: The SDDs installed in the XAFS-SESAME Detector System.

To complete the tests, the system was again installed in the Optical X-ray laboratory [Fig. 4.21] to use the source with rotating Cu anode.

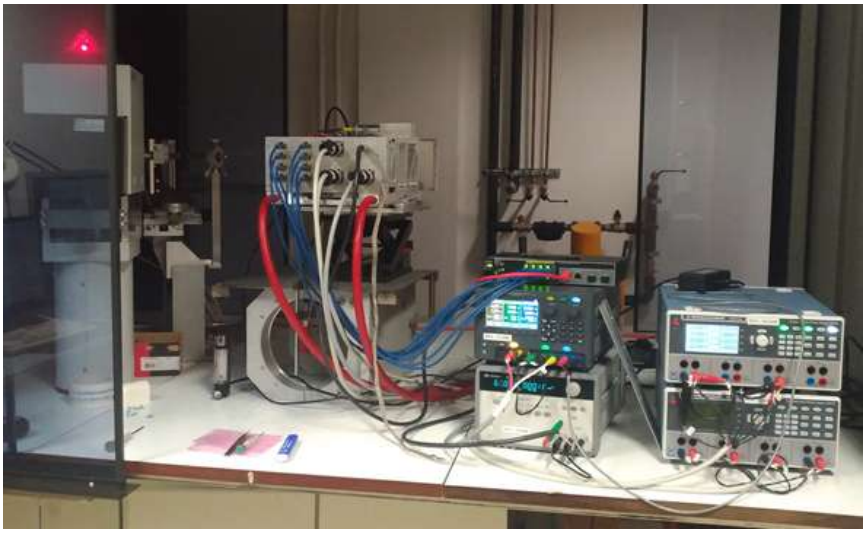

FIGURE 4.21: The XAFS-SESAME Detector System installed in the Optical X-ray laboratory.

FIGURE 4.22: FICUS software screenshot of the simultaneous live acquisition of the 64 channels of the Detector System of the signal coming from the calibration sample: all channels work properly.

Several tests have been performed using this source and the calibration sample, previously used, to better optimize the system, firmware and FICUS software. An example of the simultaneous acquisition of the 64 channels of the Detector System is shown in Figure 4.22.

In Figure 4.23 (a) it is possible to see the typical values of the temperatures in the condition at room temperature (Tamb), obtained with the ignition of the chiller only, and in the condition of cooled system (Tcool), obtained with the

ignition and complete supply also of the Peltier cells. It is also possible to see the progressive trend of the temperatures during the gradual feeding phase of the Peltier cells [Fig. 4.23 (b)].

Mode select
Last value

Detector	LDO	FPGA	ADC
Detector 1	28.06 °C	48.25 °C	38.31 °C	33.87 °C
Detector 2	28.62 °C	47.62 °C	38.19 °C	34.87 °C
Detector 3	27.44 °C	44.19 °C	37.94 °C	34.25 °C
Detector 4	25.44 °C	48.50 °C	38.06 °C	34.50 °C
Detector 5	26.69 °C	46.75 °C	36.75 °C	34.06 °C
Detector 6	27.37 °C	47.31 °C	37.56 °C	33.44 °C
Detector 7	26.12 °C	46.37 °C	38.44 °C	33.87 °C
Detector 8	25.87 °C	46.75 °C	37.69 °C	34.62 °C

Mode select
Last value

Detector	LDO	FPGA	ADC
Detector 1	7.81 °C	48.06 °C	38.31 °C	33.69 °C
Detector 2	8.00 °C	47.50 °C	38.19 °C	34.75 °C
Detector 3	5.19 °C	44.06 °C	37.69 °C	34.12 °C
Detector 4	3.94 °C	48.75 °C	38.12 °C	34.50 °C
Detector 5	4.50 °C	47.31 °C	37.37 °C	34.19 °C
Detector 6	3.50 °C	47.62 °C	38.12 °C	33.75 °C
Detector 7	5.12 °C	46.87 °C	38.94 °C	34.06 °C
Detector 8	5.12 °C	47.69 °C	38.25 °C	34.94 °C

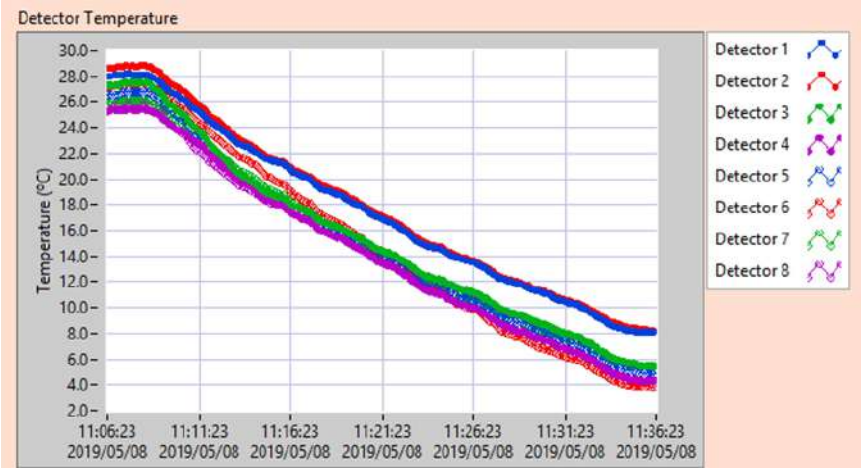

FIGURE 4.23: (**a**) Typical values of the temperatures in the condition at room temperature (Tamb) and in the condition of cooled system (Tcool) (**b**) The progressive trend of the temperatures during the gradual feeding phase of the Peltier cells.

Among the tests carried out in the Optical X-ray laboratory, with different samples in addition to the calibration sample [Fig. 4.24], for example an acquisition with all the 64 channels was made with a sample of iron at room temperature. The resolution is 196 eV at Mn Kα line at room temperature for a peaking time of 1.45 μs [Fig. 4.25]. This analysis was also performed using the PyMca X-ray Fluorescence Toolkit [9, 77].

Complete system was carried out to verify that the gradual integration had been successful and that the detector system worked properly. In this way it was possible to debug the software and verify the performance of the system before mounting it on the XAFS beamline for tests with synchrotron radiation.

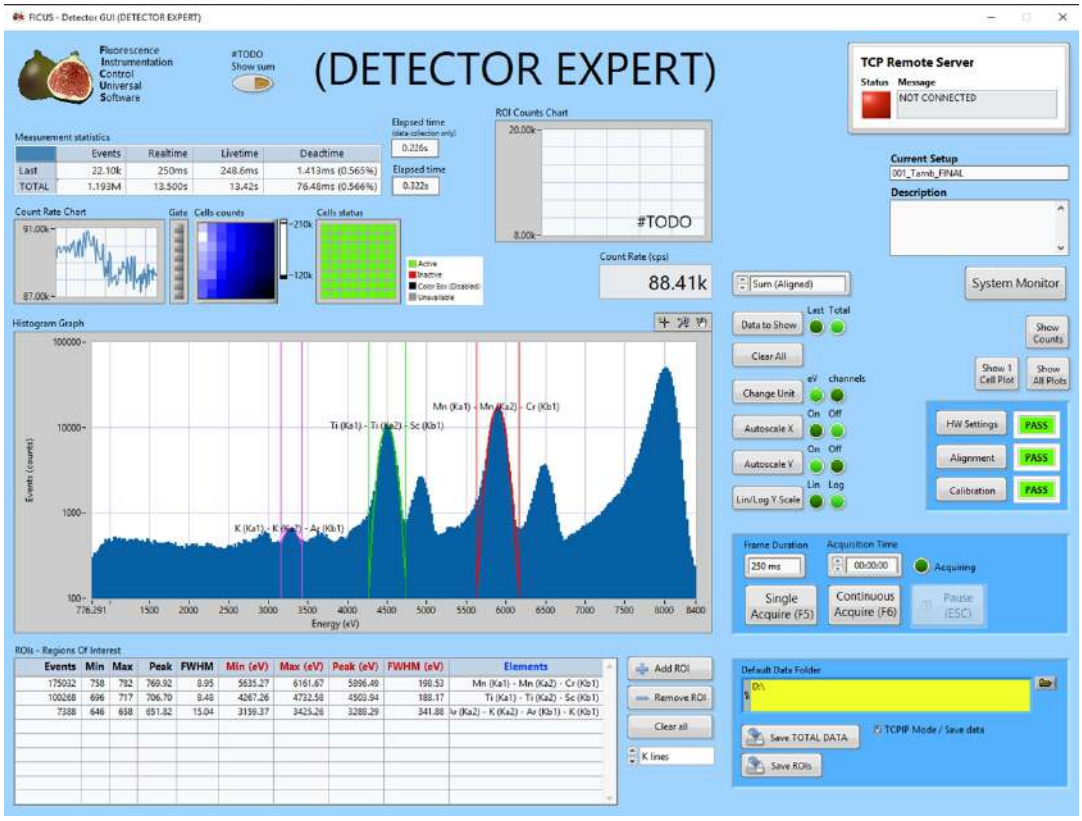

FIGURE 4.24: Acquisition window of the old version of the FICUS software during test acquisitions with the calibration sample at room temperature in the Optical X-ray laboratory.

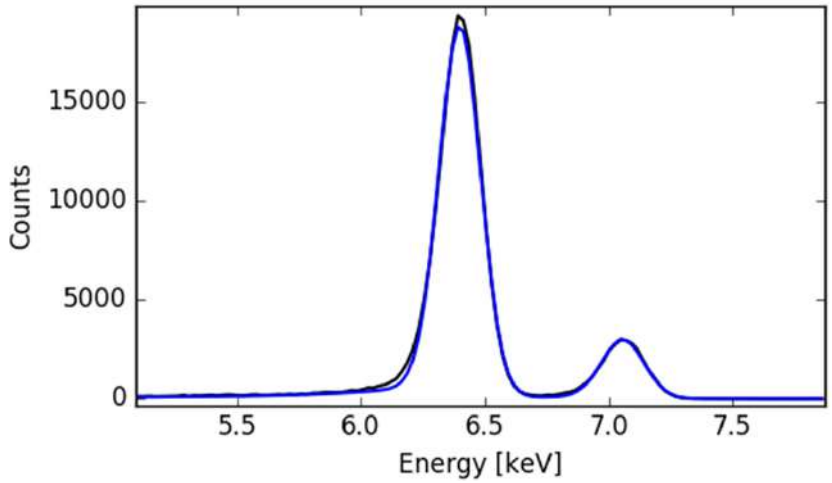

FIGURE 4.25: Acquisition with all the 64 channel of the Detector System with Fe sample and X-ray tube at room temperature. The resolution is 196 eV at Mn Kα line at room temperature for a peaking time of 1.45 μs.

4.2.4 Final detector system on the XAFS beamline at Elettra

In March 2019 and May 2019 the complete detector system was tested on the XAFS beamline. It was installed in the normal position in order to test the acquisition and verify the integration with the acquisition system of the beamline and optimize performance.

Beamtime March 2019

During the tests in March 2019, samples specially prepared by beamline scientists were analysed to test the performance of the detector system. For example, a sample composed mainly of Cr with traces of Fe; samples with different percentages of Fe were prepared and analysed. The one presented in Fig. 4.26 is the sample A with 0.09% in moles. A full EXAFS spectrum to the line of the Fe was acquired. Below is the first (in black, with the beat at 6.7 keV) and last (in red, with the beam at 8.5 keV) XRF spectrum of the acquisition, each lasting 5 seconds at room temperature for a peaking time of 1.45 μs. The black spectrum was acquired with beam energy below the iron edge and therefore only the fluorescence of chromium appears. The spectrum in red instead has been acquired with beam energy above the iron edge and therefore the fluorescence lines of chromium and iron are present.

Once this challenge had been overcome, 3 samples of mushrooms with about 200 ppm of Fe were analysed [Fig. 4.27]. For all 3 mushroom samples complete EXAFS spectra were acquired at the Fe line (4 for mushroom1 and mushroom2 and 3 for mushroom3) each with single acquisition lasting 5 seconds at room temperature for a peaking time of 1.45 μs. The repeatability of the measurements and the stability of the system were proven: in fact, the EXAFS spectra were perfectly superimposable in the examination carried out by the beamline scientist [Fig. 4.28].

Beamtime May 2019

During the tests carried out during the beamtime in May 2019 [Fig. 4.29], real samples specially carried by the scientist Carlo Meneghini were analysed to test the performance of the detector system with a real scientific problem. In particular, we analyzed samples of mussel shells, in search of possible pollutants, and geological samples to do in-depth research of their content of heavy metals [Fig. 4.30].

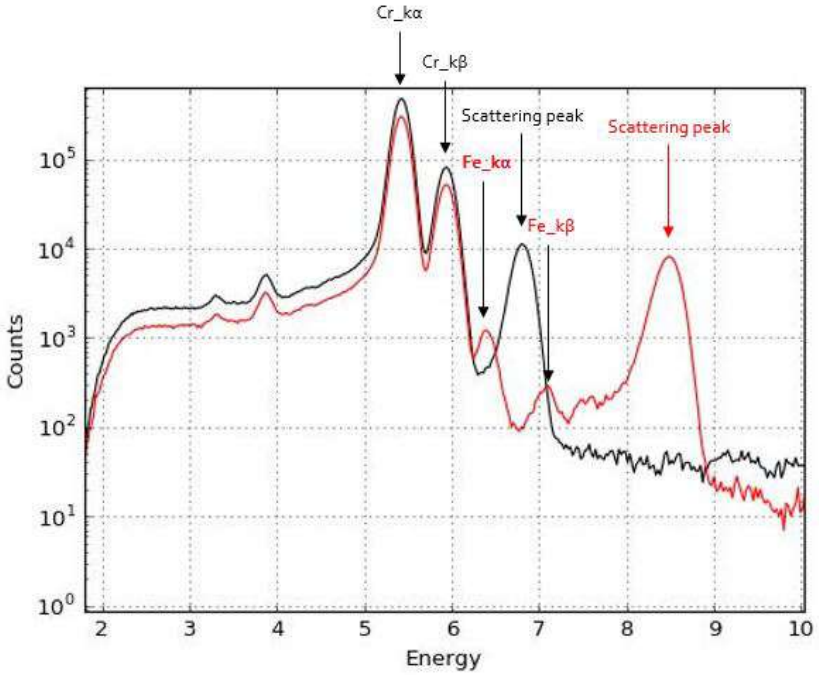

FIGURE 4.26: Spectrum of a sample with Cr and Fe (in 0.09% in moles). The first (with the beam at 6.7 keV, in black) and last (with the beam at 8.4 keV, in red) XRF spectrum of the acquisition, each lasting 5 seconds at room temperature for a peaking time of 1.45 μs. The black spectrum was acquired with beam energy below the iron edge and therefore only the fluorescence of chromium appears. The spectrum in red instead has been acquired with beam energy above the iron edge and therefore the fluorescence lines of chromium and iron are present.

FIGURE 4.27: Three different samples of mushrooms.

Acquisitions of XANES spectra of the samples in the number and lines shown in the Table 4.3 were carried out. For the mussel sample, which contains about 100-120 ppm of Cu, each acquisition has a total duration of about 2 hours. For the geological samples each acquisition has a total duration of about 50 minutes.

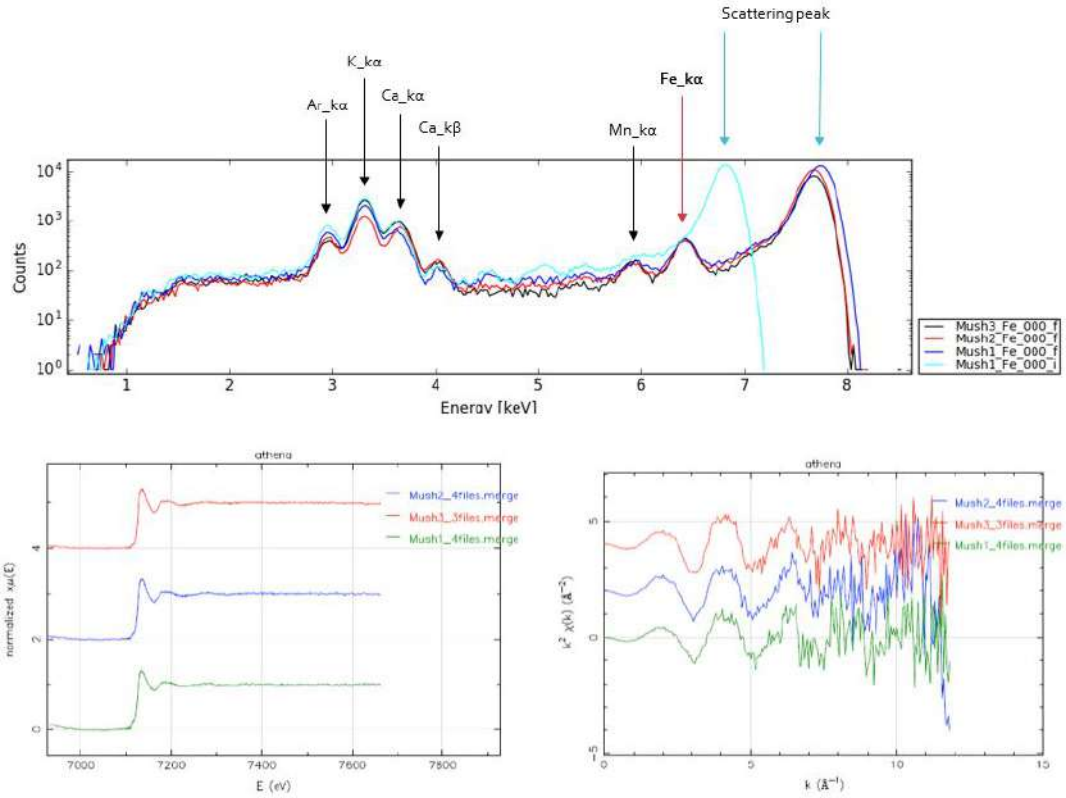

FIGURE 4.28: (**a**) The XRF spectra of the samples of mushrooms from single acquisition (64 channels summed) of XAFS spectrum (lasting 5 seconds at room temperature for a peaking time of 1.45 μs): the first (in blue) and last (in blue) acquisition of mushroom sample 1, the last acquisition of mushroom 2 (in red), and the last acquisition of mushroom 3 (in black) (**b**) The EXAFS spectra of the sum of the acquisitions for each of the three samples compared.

In both cases, each acquisition has been carried out with a cooled system and with a peaking time of 1.45 μs. The results of the preliminary analysis will be presented in the next paragraph.

4.2.5 First scientific results of the XAFS-SESAME Detector System

Thanks to these tests, we have tried to verify the performance and reliability of the XAFS-SESAME Detector System both from a technological and a scientific point of view.

Detailed analyses of the data acquired are in progress. The following are the preliminary analyses that have already been carried out.

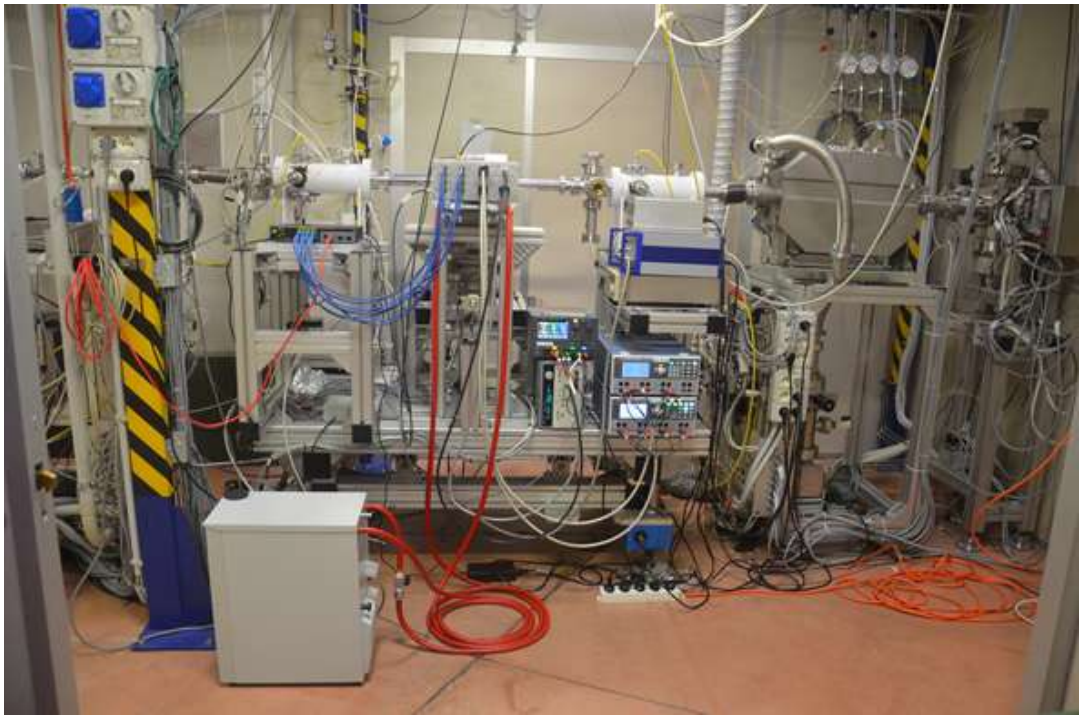

FIGURE 4.29: The XAFS-SESAME Detector System installed in the XAFS beamline in May 2019.

FIGURE 4.30: Real samples carried by the scientist Carlo Meneghini (**a**) Geological samples from Appennine (**b**) Mussel from Sardinia.

Mussel

The analysis of the mussel sample will be reported first. The principal objective of the scientific analysis is to discover the composition of the sample in order to investigate the presence of heavy metals; this possible presence may be related to the characteristics of the place where the mussel was harvested.

The XRF analysis concerns the last acquisition made for the XANES spectrum on the Fe line: an acquisition of 5 seconds with cooling system for a

TABLE 4.3: Information about the XANES acquisitions carried out during the May 2019 beamtime.

Sample	**Line**	**Number of acquisition**	**Time duration each [min]**
Mussel	Cu Kα	2	60
Mussel_b	Cu Kα	2	60
Geological_Sample_c9	Cr Kα	12	30
Geological_Sample_c9	Fe Kα	1	40
Geological_Sample_c9_1a	Cr Kα	4	30
Geological_Sample_c9_1b	Cr Kα	2	30
Geological_Sample_c9	V Kα	1	30
Geological_Sample_c9	Mn Kα	1	15
Geological_Sample_c9	Mn Kα	5	30
Geological_Sample_c9	Mn Kβ	1	30
Geological_Sample_c11	Fe Kα	1	40
Geological_Sample_c11	Mn Kβ	4	30
Geological_Sample_c13	Fe Kα	1	40
Geological_Sample_c13	Mn Kβ	4	30
Geological_Sample_c20	Fe Kα	1	50
Geological_Sample_c20	Mn Kβ	8	30

peaking time of 1.45 μs. The spectrum [Fig. 4.31] shows the presence in the sample of Ca, Mn, Fe, Co, Ni, Cu.

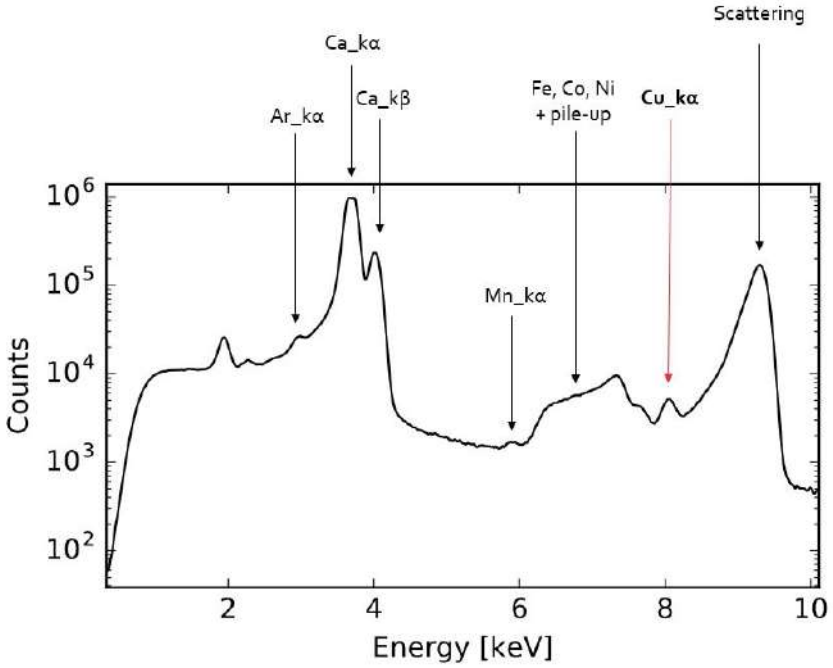

FIGURE 4.31: The XRF spectrum of the mussel sample since the last acquisition made for the XANES spectrum on the Fe line; acquisition of 5 seconds with cooling system for a peaking time of 1.45 μs.

First of all, it should be noted that the spectra of the two successive acquisitions are perfectly superimposable, a sign of the repeatability of the measurements taken. We also notice the presence of saturation effects on the signal (a problem that has been solved in the acquisitions with the following samples, moving the detector away from the sample by a few cm and making sure, before acquisitions, that the spectrum XRF was not saturated for any of the channels).

Preliminary analyses of XANES spectra of mussel samples, which contains about 100-120 ppm of Cu, were done. The Figure 4.32 shows the results: the comparison with the standard samples gives the information that 46 % of $Cu(I)_2O$ and 54 % of Cu(II)O seem to be present in the sample.

Also with regard to geological samples, the main scientific aim is to investigate the composition of the samples, the nature of the links between the constituents and to investigate the strange composition of these samples.

The Table 4.4 shows the composition of the geological samples we have analysed. The data relating to the elements analysed with the acquisitions made are highlighted: Cr in fuchsia, Mn in blue, and Fe in green.

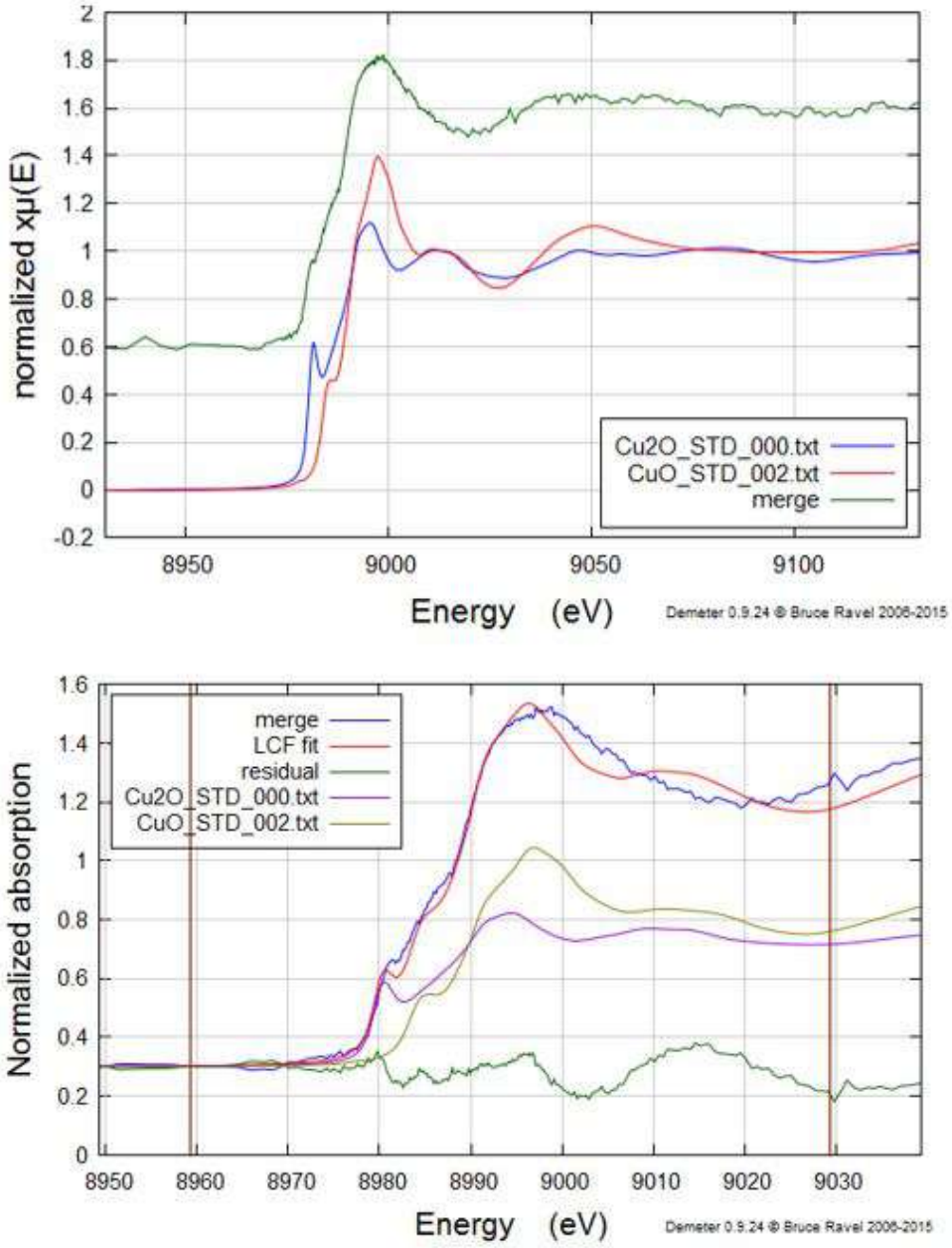

FIGURE 4.32: Preliminary analysis of XANES spectra of mussel samples, which contains about 100-120 ppm of Cu, (**a**) Are represented: (in green) the sum of the two acquired XANES spectra (2 scans of two hours each), (in red) the spectrum of a standard sample of CuO, and (in blue) the spectrum of a standard sample of Cu_2O (**b**) Are represented: (in blue) the merge of the two acquired XANES spectra (2 scans of two hours each), (red) the fit obtain the fit obtained by assuming a composition of Cu(I) 46% and Cu(II) 54% present in the mussel sample, (green) the residual, (yellow) the spectrum of a standard sample of CuO, and (purple) the spectrum of a standard sample of Cu_2O.

TABLE 4.4: Information about the composition of the geological samples.

Sample	C09 [mg/kg]	C11 [mg/kg]	C13 [mg/kg]	C20 [mg/kg]
Al	514	300	319	239
V	3.1	2.1	1.2	0.8
Cr	2.90	2.92	3.48	4.48
Fe	397	131	129	212
Mn	38.2	11.9	19.6	12.8
Ni	2.4	1.8	1.6	1.5
Co	1.08	0.58	0.53	0.54
Cu	1.39	0.78	0.82	0.79
Zn	7.3	16.4	11.4	8.4
Rb	0.85	0.52	0.51	0.25
Sr	138	100	105	72
Mo	0.29	0.20	0.16	0.13
Cd	0.18	0.17	0.12	0.34
Ba	6.2	4.2	3.4	3.0
Pb	0.9	2.5	0.8	0.6
U	1.6	1.4	1.3	1.2

As was already evident from the composition, from the analysis of the XRF spectra it can be seen that the spectra relative to the geological samples c9, c11, c13 and c20 are very similar to each other (only one is reported). The lines relating to the elements analysed are highlighted (with the same colors used in the Table 4.4): Cr in fuchsia, Mn in blue, and Fe in green.

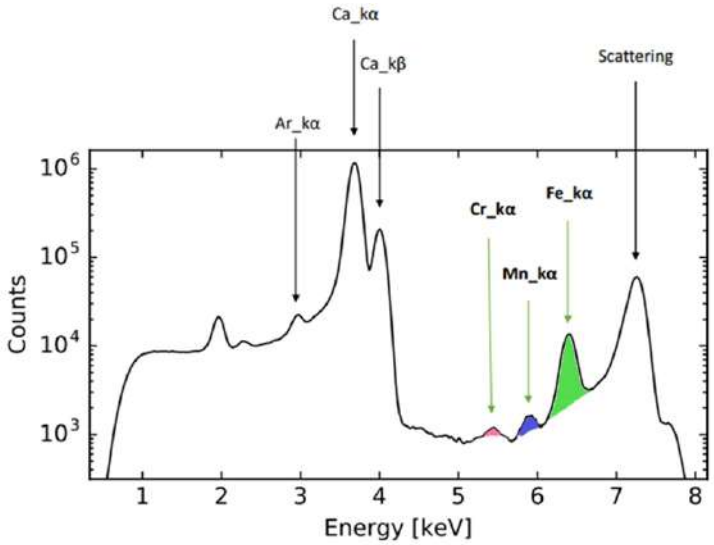

FIGURE 4.33: The XRF spectrum of the geological samples since the last acquisition made for the XANES spectrum; acquisition of 5 seconds with cooling system for a peaking time of 1.45 μs.

The XRF analyses concerns the last acquisition made: an acquisition of 5 seconds with cooling system for a peaking time of 1.45 μs. The spectrum [Fig. 4.33] shows the presence in the sample of Ca, Cr, Mn, Fe.

The first remarkable result is that, although there is a quantity of Cr in the samples between 3 and 5 ppm, this is well detectable in the spectrum in Fig. 4.33 (fuchsia peak).

Also with regard to geological samples, the main scientific aim is to investigate the composition of the samples, the nature of the links between the constituents and to investigate the strange composition of these samples. Each acquisition has an average total duration of about 40 minutes; each one has been carried out with a cooled system and with a peaking time of 1.45 μs. The measurements were all carried out consecutively and some were repeated up to 12 times.

It should be noted that the spectra of the two successive acquisitions are perfectly superimposable, a sign of the repeatability of the measurements take, and it represents the fact that the detector system is reliable.

Preliminary and qualitative analysis of XANES spectra of geological samples were done and are presented below.

Fe in the geological samples

The analysis started from the element between Fe, Mn and Cr of which the geological samples tested are richer: Fe, is present in quantities between 130 and 400 ppm, in particular in 400 ppm in c09, 131 ppm in c11, 129 ppm in c13, and 212 ppm in c20 [Table 4.4]. The Figure 4.34 shows the XANES spectra: in the lower part there are the spectra relative to the sum of the data for each sample (c9 in purple, c11 in blue, c13 in red, and c20 in green); in the upper part the reference sample spectra. A quantitative comparison shows that samples with more Fe (c09 and c20) seem to be composed of Fe^{3+}, while samples with less Fe seem to be composed of Fe^{2+} and Fe^{3+}.

Mn in the geological samples

In the geological samples the Mn is present in quantities between 10 and 40 ppm about, in particular in 38.2 ppm in c09, 11.9 ppm in c11, 19.6 ppm in c13, and 12.8 ppm in c20 [Table 4.4]. Figure 4.35 shows the XANES spectra: in the upper part there are the spectra relative to the sum of the data for each sample (c9 in blue, c11 in red, c13 in green, and c20 in purple); in the lower part the reference sample spectra.

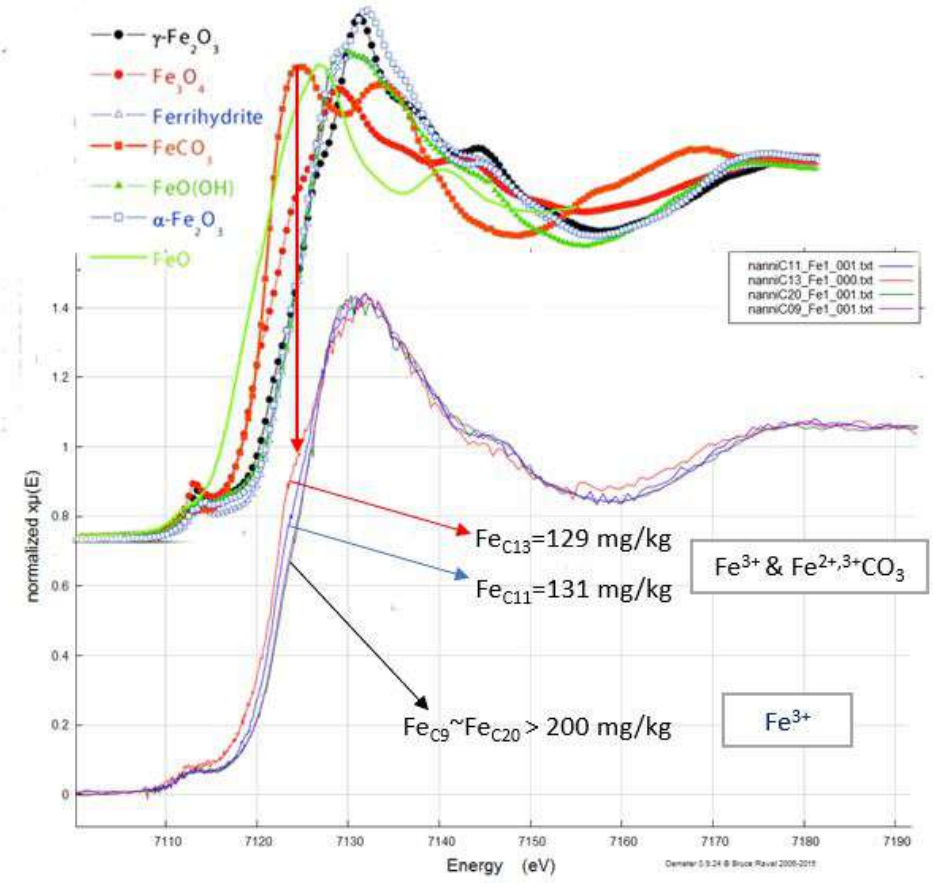

FIGURE 4.34: The XANES spectra of Fe relative to the sum of the data for each sample (c9 in purple, c11 in blue, c13 in red, and c20 in green) in the lower part; they are compared to the reference sample spectra (in the upper part of the figure).

A quantitative comparison shows that all the samples seem to be composed of Mn^{3+} and Mn^{2+}.

Cr in the geological samples

In the geological sample C09 the Cr is present in quantities of 2.90 ppm [Table 4.4]. This is the only geological sample for which this acquisition was made. Figure 4.36 shows the XANES spectra: in the upper part there is the spectrum relative to the sum of all the 12 set of data (in purple); in the lower part the reference sample spectra.

A quantitative comparison shows that the c09 sample seem to be composed mainly of Cr^{3+} and Cr^{2+}.

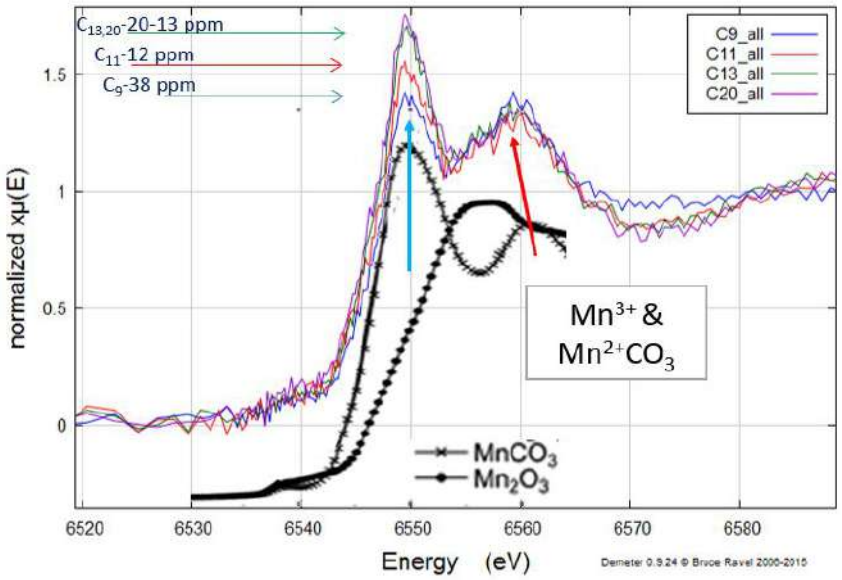

FIGURE 4.35: The XANES spectra of Mn relative to the sum of the data for each sample (c9 in blue, c11 in red, c13 in green, and c20 in purple) in the upper part; they are compared to the reference sample spectra (in the lower part of the figure).

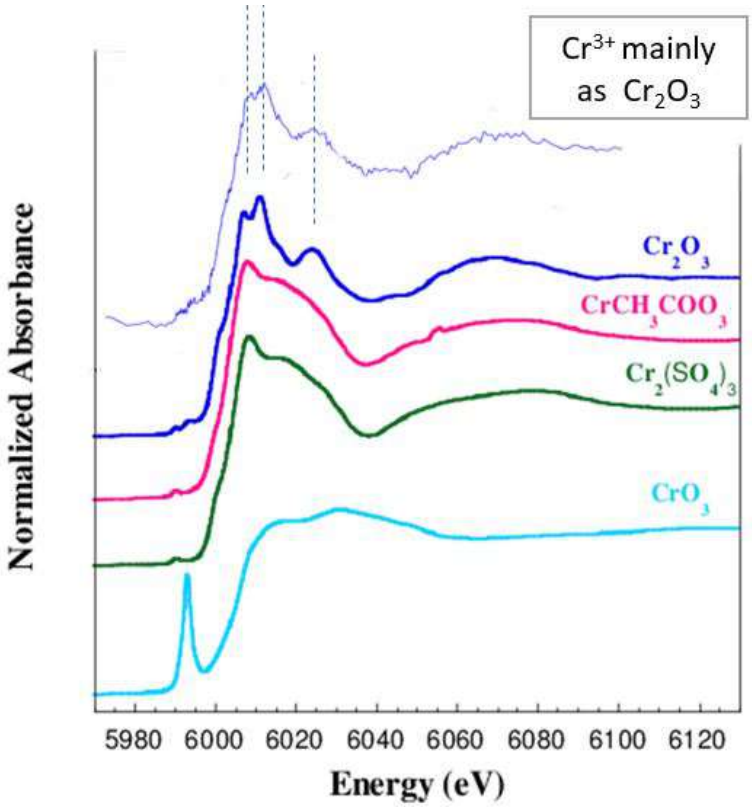

FIGURE 4.36: The XANES spectrum of Cr relative to the sum of the data for the c09 sample (in purple) in the upper part; it is compared to the reference sample spectra (in the lower part of the figure).

4.2.6 Detection System optimization

After testing the XAFS beamline, the system was reassembled in the Optical X-ray laboratory.

Some bugs firmware and software are resolved. Optimized and customized digital filters have been generated for each channel. The optimization of the filters allowed an improved and simplified procedure of alignment of the channels through the software.

Final global setup have been created: for room temperature, (called Tamb, only the chiller is switched on) and cooled system (called Tcool, with maximum power allowed by the system), and for the 4 possible peaking times (0.4, 0.7, 1.0 and 1.45 μs).

Usually the working temperatures of the system are those shown in the tables in Figures 4.37.

Mode select: Last value

Detector	LDO	FPGA	ADC
Detector 1	27.81 °C	43.56 °C	35.81 °C	32.06 °C
Detector 2	28.50 °C	43.12 °C	35.87 °C	33.06 °C
Detector 3	27.12 °C	40.50 °C	35.94 °C	32.75 °C
Detector 4	24.75 °C	44.81 °C	36.25 °C	32.87 °C
Detector 5	26.75 °C	42.81 °C	34.75 °C	32.50 °C
Detector 6	27.50 °C	43.25 °C	35.19 °C	31.69 °C
Detector 7	25.87 °C	42.25 °C	35.94 °C	32.06 °C
Detector 8	26.75 °C	42.94 °C	35.25 °C	33.25 °C

Mode select: Last value

Detector	LDO	FPGA	ADC
Detector 1	7.75 °C	48.00 °C	38.25 °C	33.56 °C
Detector 2	8.37 °C	47.44 °C	38.31 °C	34.69 °C
Detector 3	5.31 °C	44.12 °C	38.12 °C	34.37 °C
Detector 4	3.37 °C	49.00 °C	38.50 °C	34.44 °C
Detector 5	4.94 °C	46.69 °C	36.87 °C	33.81 °C
Detector 6	4.50 °C	47.06 °C	37.75 °C	33.44 °C
Detector 7	5.69 °C	46.25 °C	38.50 °C	33.56 °C
Detector 8	6.56 °C	47.12 °C	37.87 °C	34.75 °C

FIGURE 4.37: Usual temperatures of SDDs: (**a**) when the system works at room temperature (Tamb) with only the system of temperature stabilization through the chiller (**b**) when the system works at cooled temperature (Tcool) with additional cooling with Peltier cells.

At the end of the entire process of testing and optimising the XAFS-SESAME Detector System, the latest acquisitions were made with the calibration sample for each of the global setups (under the relevant conditions). The analyses of the FWHM Mn Kα line relative to the sum of the signal coming from all 64 channels at different peaking times and temperatures are shown in the Table 4.5. These analyses and subsequent ones were also performed using the PyMca X-ray Fluorescence Toolkit [9, 77].

The same values found have been reported in the graph to be able to visualize the trend of the resolution to the variation of the peaking time, to the two different temperatures of work [Fig. 4.38].

Finally we have analyzed in detail the acquisitions at peaking time of 1.45 μs in order to compare the values of the resolutions for each of the 64 channels with the temperature variation. The resolution FWHM Mn Kα line for each channel

TABLE 4.5: Analyses of the FWHM Mn Kα line in acquisitions made with the complete and optimized detector system at different peaking times and temperatures. The values are relative to the sum of the signal coming from all 64 channels. The Peak to Background (P/B) Ratio is calculated as the ratio of Mn Kα peak to the value of the spectrum at 2500 eV.

Temperature Fig. 4.37	**FWHM Mn_Kα [eV]**	**Peaking Time [μs]**	**P/B Ratio**
Tamb	195	0.4	26.5
Tamb	177	0.7	28.5
Tamb	171	1.0	28.0
Tamb	168	1.45	26.6
Tcool	192	0.4	28.7
Tcool	174	0.7	30.1
Tcool	166	1.0	30.9
Tcool	162	1.45	29.2

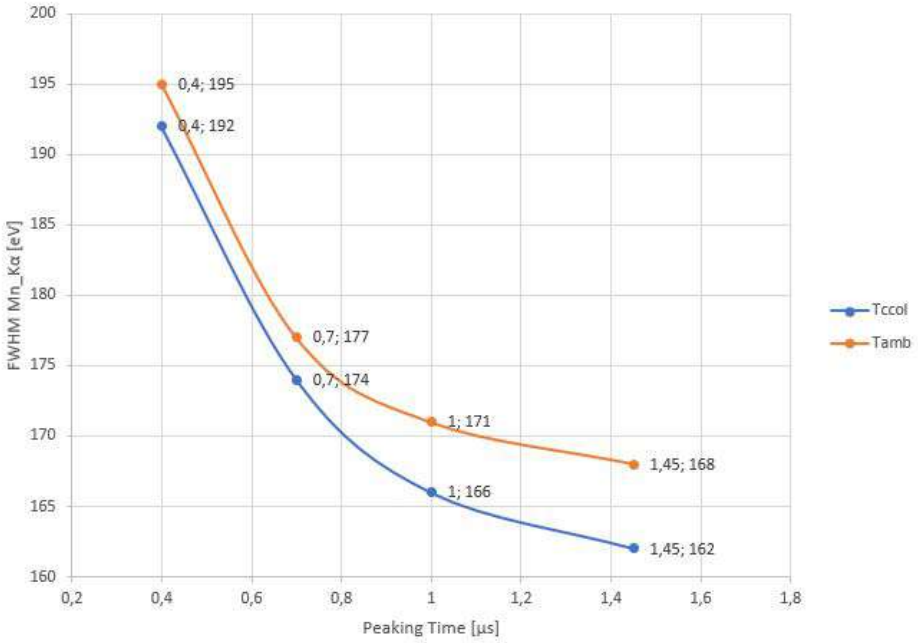

FIGURE 4.38: Analysis of the FWHM Mn Kα line in acquisitions made with the complete and optimized detector system at different peaking times and temperatures (in orange the data acquired at room temperature, Tamb, and in blue the data acquired with cooled system, Tcool).

of measurement at Tamb and Tcool are given respectively in the Table 4.6 and 4.7. The visual comparison between the FWHMs of the channels related to these data sets is shown in Figure 4.39. In order to verify the trend, the difference was calculated and it is shown in Table 4.8.

The most relevant differences between the resolutions at room temperature and those at cooled system are marked in bold.

TABLE 4.6: Analysis of the FWHM Mn Kα line in acquisitions made with the complete and optimized detector system at 1.45 μs of peaking times and at room temperature (Tamb). The values are relative to the signal coming from each single channel. **The mean resolution between channels is 168 eV.** The resolution of the sum of the signal coming from all 64 channels is 168 eV, as seen in Table 4.5.

Strip Position	Strip Name	Ch1 [eV]	Ch2 [eV]	Ch3 [eV]	Ch4 [eV]	Ch5 [eV]	Ch6 [eV]	Ch7 [eV]	Ch8 [eV]
1	**strip12**	166	186	166	166	168	167	162	169
2	**strip20**	167	168	170	161	166	176	167	167
3	**strip16**	162	163	168	166	172	163	164	161
4	**strip14**	162	164	169	169	164	163	170	166
5	**strip15**	165	170	164	169	166	161	163	164
6	**strip21**	170	167	163	170	165	167	167	165
7	**strip22**	175	172	170	173	167	168	165	165
8	**strip18**	180	167	169	174	173	179	168	175

TABLE 4.7: Analysis of the FWHM Mn Kα line in acquisitions made with the complete and optimized detector system at 1.45 μs of peaking times and with cooled system (Tcool). The values are relative to the signal coming from each single channel. **The mean resolution between channels is 161 eV**. The resolution of the sum of the signal coming from all 64 channels is 162 eV, as seen in Table 4.5.

Strip Position	Strip Name	Ch1 [eV]	Ch2 [eV]	Ch3 [eV]	Ch4 [eV]	Ch5 [eV]	Ch6 [eV]	Ch7 [eV]	Ch8 [eV]
1	**strip12**	160	169	159	158	163	162	155	164
2	**strip20**	159	164	160	156	162	167	165	160
3	**strip16**	157	156	160	158	164	156	160	155
4	**strip14**	156	160	164	165	158	156	158	159
5	**strip15**	162	166	159	158	161	159	156	158
6	**strip21**	159	158	158	160	161	165	162	160
7	**strip22**	161	162	161	174	161	162	160	160
8	**strip18**	173	165	164	167	166	170	162	171

To complete the analysis, Table 4.8 was compared with the anode current values [Table 4.9] measured cell by cell before the SDDs were mounted. Current values above 10 pA are highlighted in bold. To better visualize the correlation between the value of the difference of FWHM at different temperatures and the anode current the values in Tables 4.8 and 4.9 are shown in the Figure 4.40 and 4.41.

There is a perfect correspondence between the channels that already had a current greater than 10 pA before the installation and the channels whose resolution improves more with the lowering of the temperature, which leads to

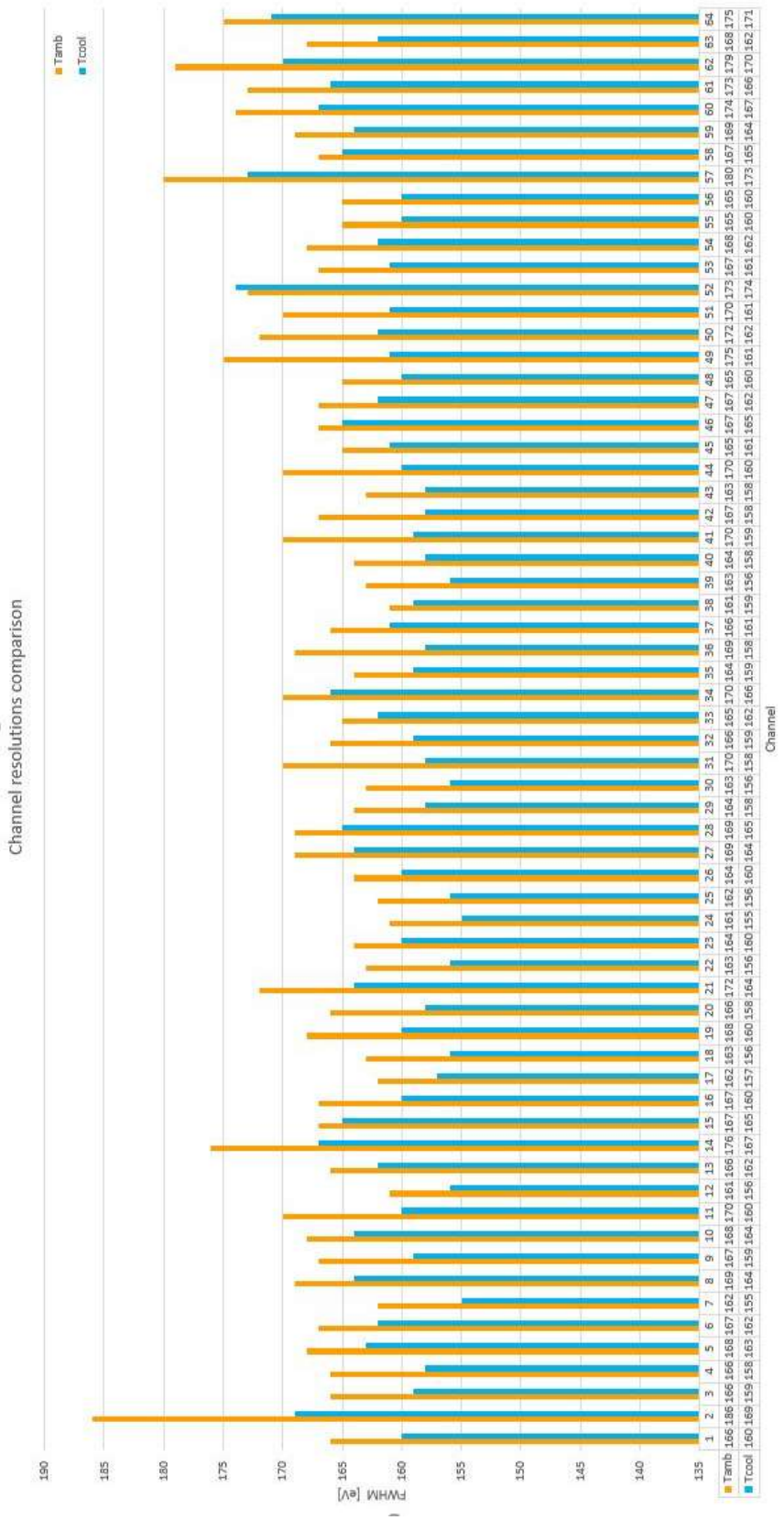

FIGURE 4.39: Comparison between FWHM of Tamb (orange) and Tcool (blue) channels related to the data respectively in the Tables 4.6 and 4.7.

TABLE 4.8: Differences between the FWHM values of the Mn Kα line measured at Tamb and Tcool (the exact values of the temperatures on the strips are those present in Figure 4.37). The mean value of the differences is 6.4 eV. The most relevant differences between the resolutions at room temperature and those at cooled system are marked in bold.

Strip Position	**Strip Name**	**Ch1 [eV]**	**Ch2 [eV]**	**Ch3 [eV]**	**Ch4 [eV]**	**Ch5 [eV]**	**Ch6 [eV]**	**Ch7 [eV]**	**Ch8 [eV]**
1	**strip12**	6	**17**	7	8	5	5	7	5
2	**strip20**	8	4	**10**	5	4	**9**	2	7
3	**strip16**	5	7	8	8	8	7	4	6
4	**strip14**	6	4	5	4	6	7	**12**	7
5	**strip15**	3	4	5	*11*	5	2	7	6
6	**strip21**	**11**	**9**	5	**10**	4	2	5	5
7	**strip22**	**14**	*10*	9	-1	6	6	5	5
8	**strip18**	7	2	5	7	7	**9**	6	4

TABLE 4.9: Anode current values (in pA) of individual strip channels measured before bonding and mounting operation. Current values above 10 pA are highlighted in bold.

Strip Position	**Strip Name**	**Ch1 [pA]**	**Ch2 [pA]**	**Ch3 [pA]**	**Ch4 [pA]**	**Ch5 [pA]**	**Ch6 [pA]**	**Ch7 [pA]**	**Ch8 [pA]**
1	**strip12**	5.15	**24.30**	4.95	4.85	4.80	4.75	4.80	5.05
2	**strip20**	9.55	7.85	**20.45**	7.75	7.65	**18.75**	7.50	7.65
3	**strip16**	6.40	6.60	6.55	6.80	8.70	7.05	7.25	7.30
4	**strip14**	7.00	6.95	6.90	6.90	6.95	6.90	**15.00**	6.90
5	**strip15**	7.10	7.05	7.15	7.05	7.05	6.95	6.95	7.00
6	**strip21**	**11.65**	**10.25**	7.05	**22.55**	7.00	6.65	6.75	6.80
7	**strip22**	**21.65**	6.65	6.75	6.75	6.65	6.75	6.65	6.45
8	**strip18**	7.25	7.20	7.15	7.25	7.25	**18.75**	7.20	7.20

the lowering of the leakage current in the SDD. Only two channels (highlighted in italics), whose current was below 10 pA before mounting, are positively affected by the lowering of temperature; it is thought that it may be due to a small resentment of the anode due to the bonding.

At the end of these tests we can safely say that the XAFS-SESAME Detector System has achieved and exceeded the targets required by the beamline scientists for delivery.

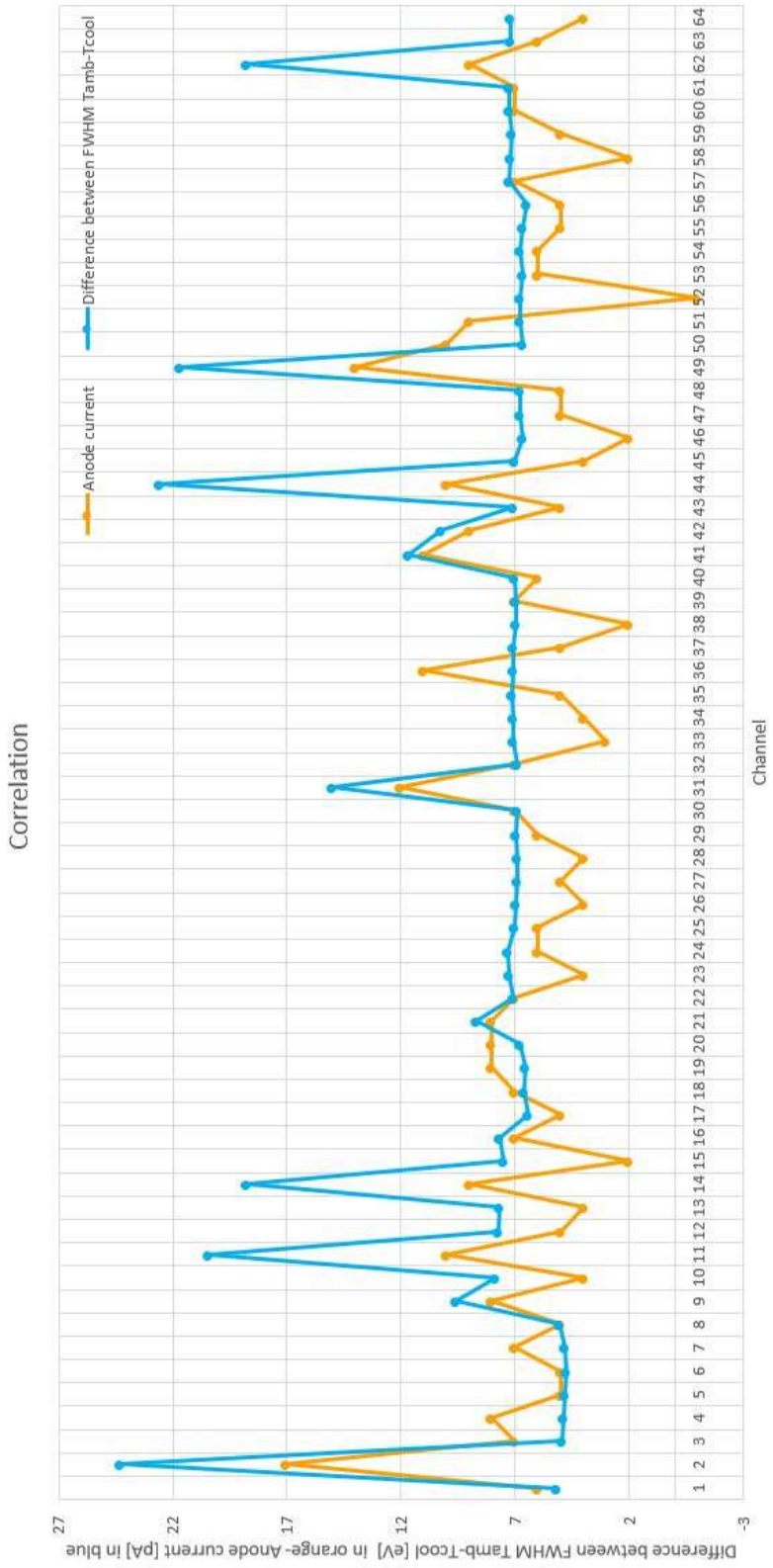

FIGURE 4.40: FWHM at different temperatures and anode current for channels (values in Tables 4.8 and 4.9.

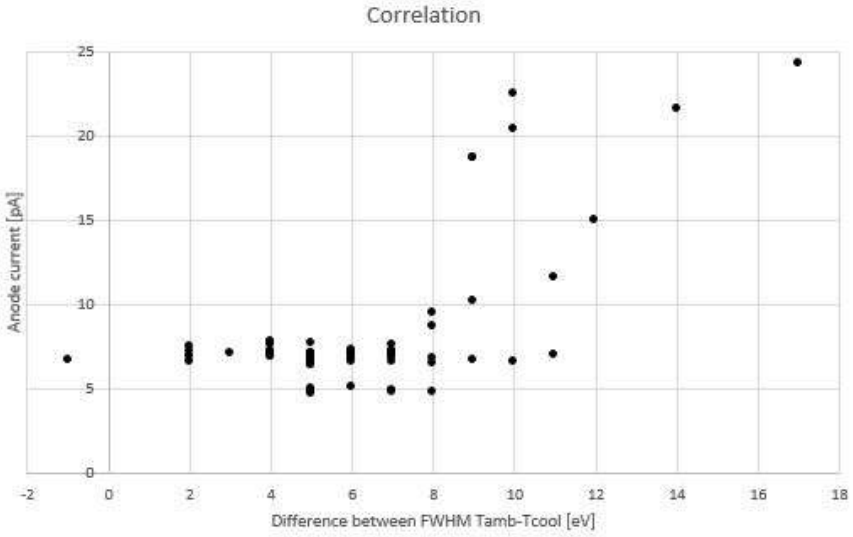

FIGURE 4.41: Correlation between the FWHM difference value at different temperatures and the anode current (the values in Tables 4.8 and 4.9).

4.3 Current status of the XAFS-SESAME Detector System and future perspectives

At the end of the optimization and the last tests, the XAFS-SESAME Detector System was properly packed, with all the instrumentation supplied, and sent to the synchrotron SESAME. The packaging and shipping operation required appropriate precautions to ensure the safety of the equipment during transport [Fig. 4.42]. The documentation to be attached to the detector, i.e. the first version of the instrument manual, the software manual and the datasheet are being completed (the first versions are attached in appendix C to the thesis).

On 31/10/2019 the detector arrived in Jordan. In the following phases will be carried out the work of assembly, commissioning, optimization and commissioning of the instrument on the XAFS beamline of SESAME.

The XAFS-SESAME Detector System has demonstrated in the tests that it can achieve great goals. Now the new challenge for him will be to be tested every day in the field in the hands of beamline scientist and user at the synchrotron SESAME in Jordan, where in a few months will be at the service of the international scientific community.

But it's not over because new challenges can be seen on the horizon, in fact after obtaining these results the demands from the beamline scientist become more difficult: to create a new version of the detector system for the beamline XAFS of Elettra that can wash in vacuum.

FIGURE 4.42: Photographic documentation of the packaging phase and preparation of the detector system and instrumentation provided for shipment.

Note

This work has been made within the ReDSoX-2 INFN research project, supported with the contribution of the Italian Ministry of Education, University and Research within the EUROFEL and SESAME Project.

Chapter 5

Detector System for TwinMic Beamline

Over the last years X-ray Fluorescence (XRF) spectroscopy has become one of the essential analytical techniques in various scientific fields such as life and environmental sciences but also in archaeological, cultural, forensic chemistry and industrial applications, respectively. This technique exploits an X-ray source to excite the emission of fluorescence photons in the sample under examination and allows the elucidation of its chemical composition by analysing the collected fluorescence spectrum. In synchrotron radiation facilities the exciting radiation is often focused on a sub micrometric focal point, which enables high spatial resolution X-ray fluorescence spectro-microscopy, thus 2 dimensional elemental mapping, by scanning the sample over the stationary incident beam. As the illuminated sample emits XRF isotropically in all directions, an ideal detector should entirely encase the sample in order to collect all emitted fluorescence photons. Because of technological limitations in detectors construction and mechanical constraints, which are different for each experimental setup, commercial off the shelf detectors often cover only a small fraction of the solid angle, thus losing a substantial part of the information carried by the fluorescence photons. This can be counterbalanced by increasing the dwell time per scan point, which subsequently leads to a dilation of the measurement time per samples and subsequently reduces the number of possible experiments for any given beamtime. Moreover, the prolonged exposure to an intense X-ray beam increases the possibility of radiation damage, especially in fragile biological samples. These motivations have prompted the research to explore new solutions related to silicon drift detectors, which are the most commonly used detectors in X-ray fluorescence spectroscopy. Below we introduce a new multi-element detector system able to match the aforementioned requirements for low energy XRF (LEXRF) spectroscopy and we present the recent results obtained at the TwinMic beamline of Elettra Sincrotrone Trieste [30].

5.1 The novel detector system

Low-energy X-ray fluorescence (LEXRF) is an essential tool for bio-related research of organic samples, whose composition is dominated by light elements. Working at energies below 2 keV and being able to detect fluorescence photons of lightweight elements such as carbon (277 eV) is still a challenge, since it requires in-vacuum operations to avoid in-air photon absorption. Moreover, the detectors must have a thin entrance window and collect photons at an angle of incidence near 90 degrees to minimize the absorption by the protective coating. Considering the low fluorescence yield of light elements, it is important to cover a substantial part of the solid angle detecting ideally all emitted X-ray fluorescence (XRF) photons. Furthermore, the energy resolution of the detection system should be close to the Fano limit in order to discriminate elements whose XRF emission lines are often very close within the energy spectra. To ensure all these features, a system consisting of four monolithic multi-element silicon drift detectors was developed. The use of four separate detector units allows optimizing the incidence angle on all the sensor elements. The multi-element approach in turn provides a lower leakage current on each anode, which, in combination with ultra-low noise preamplifiers, is necessary to achieve an energy resolution close to the Fano limit. The potential of the new detection system and its applicability for typical LEXRF applications has been proved on the Elettra TwinMic beamline.

The difficulties encountered at TwinMic [49] are typical for all the low-energy fluorescence synchrotron radiation beamlines. Even if working in vacuum suppresses the in-air photon absorption, the overall photon count-rate in LEXRF is limited by the low fluorescence yield in comparison to the Auger-probability and by an unavoidable photon absorption in the detector entrance window or other window protection layers. It is therefore essential to increase the solid angle seen by the detector in order to collect almost all emitted fluorescence photons. This can be achieved only with custom-made detectors, specially designed for the requirements of a particular beamline.

For applications in which large solid angle and an energy resolution close to the Fano limit are paramount, a multi-element structure is undoubtedly the most suitable geometry for silicon drift devices [46]. In multi-element SDDs electrons generated by photon absorption in the depleted volume are conveyed by a suitable electric field towards several small anodes, each collecting the charge from a separate region of the detector. The technique of dividing the detector into macro-pixels has numerous benefits, including:

- A smaller area of the single element ensures a proportionally smaller leakage current on the anodes, which means that a multi-element detector can operate with the same noise characteristics at higher temperature than a single-element SDD with the same active area.
- As it is less likely that multiple events will occur simultaneously on a smaller area, a multianode structure permits better operation at higher photon fluxes than a single SDD possessing the same active area, thus reducing the pile-ups in a single element.
- A multi-element structure allows to easily configure suitable geometries for a particular experimental setup, "assembling" various elements of the detector in order to cover a substantial portion of the solid angle while matching the clearance constraints of the experimental chamber.

5.1.1 Detectors characteristics and architecture

The detector system presented in this work is an evolution of the sensors described in [27, 67, 48, 29]. With some essential upgrades, the improved new setup renders the detector competitive with state of the art off the shelf devices.

Regarding spatial constrains of the experimental chamber of the TwinMic beamline, simulations based on Geant4 software toolkit [17] showed that the most suitable configuration is a compound of 4 trapezoidal-shaped detectors, assembled as sides of a pyramidal frustum, where the synchrotron beam transverses the minor base and impinges on the sample placed in the centre of the major base [Fig. 5.1]. The new detector consists of four monolithic SDD arrays covering a total non-collimated active area of 1232 mm^2, and a total collimated active area of 1113 mm^2. Each trapezoidal-shaped sensor is composed of 8 square cells of 6.2 x 6.2 mm^2.

Owing to previous experiences, in this experiment the 4 detectors were tilted by 45° in order to minimize the path of photons in the inactive detector entrance window (the photons penetrate the detector at an angle of incidence close to 90°). In this configuration the total collection solid angle results in 0.54π steradians, which means about 27% of the hemisphere on which the sample emits XRF. This is approximately 7 times higher when compared to the solid angle covered by the 8 commercial SDDs currently used on the beamline [49].

In the low-energy regime the angle of incidence is a very important qualifying parameter because of photon absorption in the entrance window. To ensure optimal collection efficiency at low energies it is therefore necessary to divide

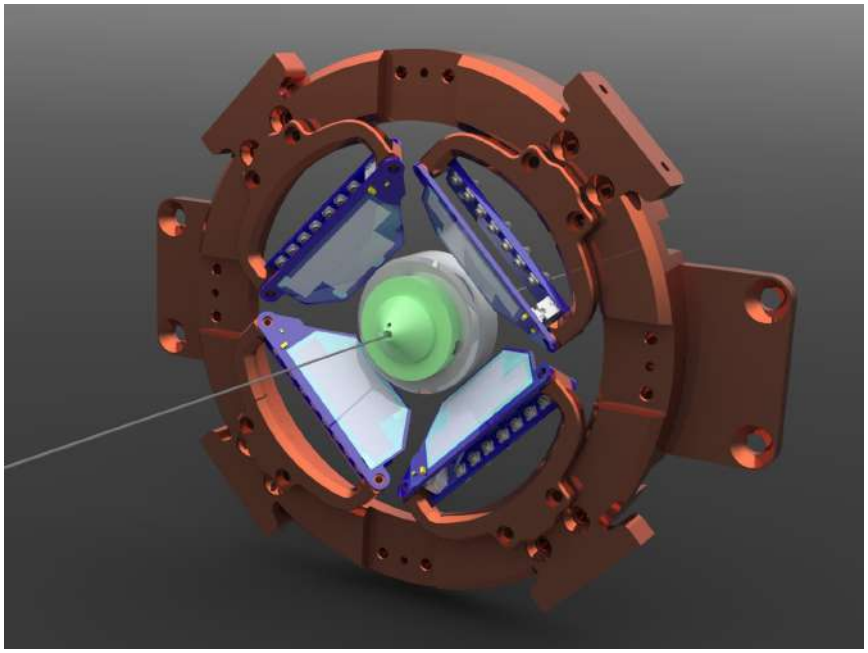

FIGURE 5.1: Sketch of new detector system of the beamline TwinMic. The new detector system consists of 4 monolithic SDD sensors composed of 8 elements each. The focused synchrotron beam exits from the centre of the detector system and hit the specimen placed just above the detectors. [28, 30].

the entire detector assembly into several separate SDDs and orient them independently, avoiding the use of a single monolithic SDD, as proposed in some work [55], which entails a very unfavourable angle of incidence.

The trapezoidal SDDs [Fig. 5.2] were fabricated on a 450 μm thick n-type silicon substrate with a resistivity of 9 kΩcm. The long base of the sensors measures 33.6 mm, the short base 20.3 mm and the height 15 mm. In order to minimize the dead space the lower wings of the trapezium are cut to allow placing the detectors closer to each other. The active area of each sensor is subdivided into 8 square elements, with a leakage current of less than 100 pA/cm^2 at room temperature. The anode capacity is about 30 fF.

The new features introduced in this setup resulted in a fivefold improvement of the collection efficiency, with respect to the standard measurement system of the TwinMic beamline, while preserving the excellent energy resolution (as reported in the experimental results section).

5.1.2 The cooling system

One of the challenges of this detector system has been that of the in-vacuum cooling. To obtain this the cooling ring already present in the experimental

FIGURE 5.2: The multipixel SDD with trapezoidal shape for the detector system TwinMic. The active area of each sensor is divided into 8 square elements; the long base of the detector measures 33.6 mm, the short base 20.3 mm and the height 15 mm [30].

chamber was used. The chiller, which circulates a mixture of water and alcohol, brings the system to 10 °C [27].

The new SDDs are equipped with implants for temperature monitoring and are actively cooled down to a desired operating temperature by Peltier cells. The temperature measurement is carried out by providing a small current on silicon resistors implanted on the edge of the detector, outside its active area. The resistance of the resistors decreases lowering the temperature, guaranteeing an accuracy of around 1 °C following an appropriate calibration. Eventually the temperature is stabilized by using a suitable PID controller.

5.1.3 Acquisition system

A readout complete scheme for a single trapezoidal detector is shown in Fig. 5.3.

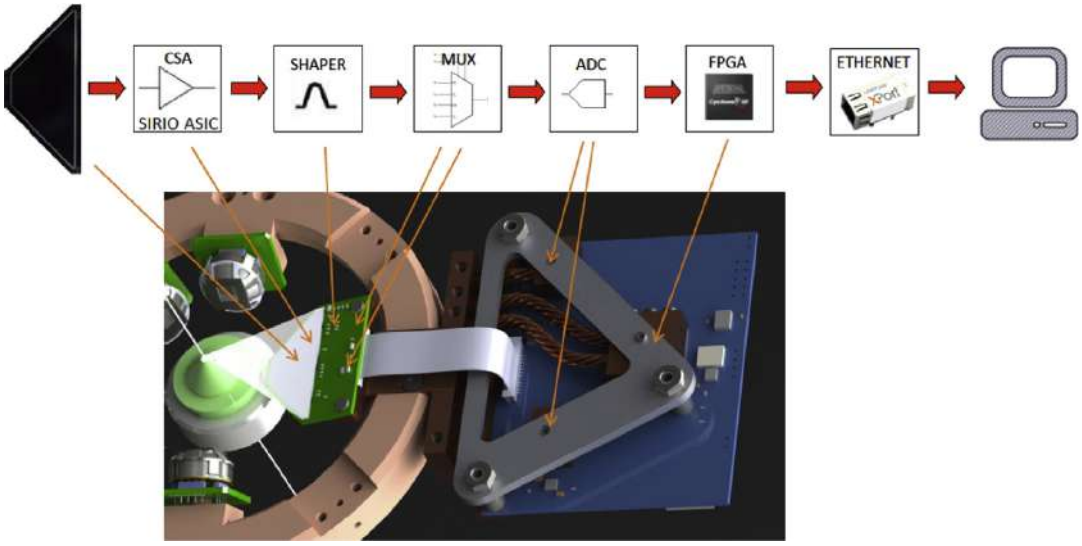

FIGURE 5.3: Scheme of the acquisition system of the detector system [48].

The electrons collected on the SDD anodes are converted into a voltage signal by a dedicated electronics. Since each single photon induced charge pulse consists of a few hundred electrons only, the first amplification stage is one of the most critical elements for preserving the energy resolution in the read-out chain. All tests described here have been carried out with the SIRIO preamplifier—a charge sensitive amplifier (CSA) developed at the Polytechnic of Milan [21]. It is a charge preamplifier built in 0.35 μm AMS CMOS technology, the result of years of research mainly aimed to reduce the electronic noise at its ultimate limits [22]. The third-generation SIRIO-3G ASIC has an intrinsic equivalent noise charge (ENC) of 1.3 electrons r.m.s. at room temperature and even less than 1 electron at -30°C [23, 19]. Owing to its excellent noise characteristics and the fact that the ASIC has been designed and developed specifically for the SDD designed at INFN in Trieste and produced by FBK, SIRIO is the optimal read-out for the multi-element sensors described here.

In order to increase the signal-to-noise ratio, the output signal from the CSA (a voltage step of a few mV) is filtered and further amplified by CR-RC^2 analogue pre-shaper with a peaking time of 0.4 μs before being sampled and digitized by the back-end electronics. The shaper must be designed to optimize the ENC and to amplify the signal in order to cover the full range of the analog to digital converters (ADCs) minimizing the quantization noise.

Another advantage of the new X-ray detection systems is its real-time sampling and processing stage based on ADC and field programmable gate array (FPGA) placed close to the front-end in the vacuum environment of the experimental chamber. This approach decreases the length of connections carrying delicate analog signals before their conversion into robust digital signals and also allows maintaining a fixed and limited number of vacuum feedthroughs, regardless of the number of detector elements.

The analog pre-shaper allows filtering a large part of the noise; however, it consists of discrete electronics components and it is not configurable. During previous tests we noticed that, beside finding the optimal peaking time based on the series/parallel noise, it is also essential to take into account the specific noise of the given work environment (disturbances of step motors, vacuum pumps etc.). In order to allow configurable filtering based on different acquisition requirements it was decided to implement further digital filtering on the sampled data based on finite impulse response (FIR) filters. The FPGA can manage independent fully parameterized trapezoidal filters (one per detector element) that can be programmed by the user even during the acquisition. By analyzing the raw signals it is possible to configure the coefficients in order to attenuate

any noise present at certain frequencies and adjust the output peaking time to reach the optimal value.

The data collected and processed by the 4 FPGAs (one for each trapezoidal sensor) are transmitted via TCP-IP protocol to a control PC running a specially developed software. In order to obtain one comprehensive spectrum from all single SDD elements, this software is capable to offset and gain correct the spectra of each detector element in real time. Further data analyses are facilitated by providing suggestions of the elements found in the obtained spectrum. At the same time, the software can be remotely controlled through a TCP-IP connection, so that the whole system can be easily included in a pre-existing integrated measurement environment.

5.2 Experimental results and future perspective

After initial tests and characterizations in the laboratory with conventional X-ray sources the performances of the detector were studied at the TwinMic beamline [26, 27, 29].

As far as the solid angle coverage and the count-rates are concerned the system satisfies the main design target by a fivefold increase of the integrated count rate compared to the TwinMic standard detection system [50]. With the new cooling system also the energy resolution has been substantially improved with respect to the first prototypes. The most common method for evaluating the energy resolution of SDDs consists in measuring the radioactive isotope ^{55}Fe, which emits photons of substantially two different energies: Mn Kα at 5.90 keV and Mn Kβ at 6.49 keV. An average trapezoidal SDD shows a fairly uniform energy resolution on all the detector elements. In particular the energy resolution on Kα (5.9 keV) taken at -20 °C with a peaking time of 4 μs shows a FWHM ranging from 125 eV to 132 eV [Fig. 5.4] with an average resolution of 129 eV FWHM thus very close to the Fano limit.

The new detection system shown in Figure 5.5 was then tested at the low energies, exciting with a monochromatic photon beam of 2 keV a standard sample of 550 nm thick MgF_2 layer deposited on a 100 nm thick silicon nitride window. The spectrum [Fig. 5.6 (a)] shows the K emission lines of F, Mg, Si and a small elastic peak at 2 keV. The energy resolution is of about 93 eV FWHM on the Mg Kα emission line (1253.6 eV) with a count-rate of $2.10 \cdot 10^5$ counts/s, whereas the flux of the incident beam was 109 photons/s. The collection efficiency on

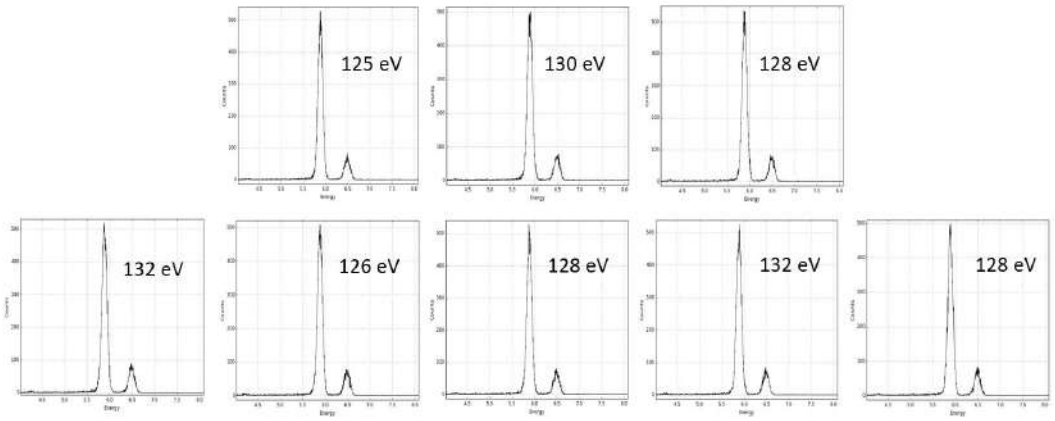

FIGURE 5.4: Energy resolution (FWHM) at 5.9 keV of an average trapezoidal SDD taken at -20 °C with a peaking time of 4 μs. [30].

the same specimen using the same incident photon flux was then compared with that of the standard TwinMic detection system. For the same dwell time one of the 4 trapezoidal SDD sensors already acquires more photons than the entire TwinMic standard setup [Fig. 5.6 (b)], so that the complete system increases the detection efficiency by 550%.

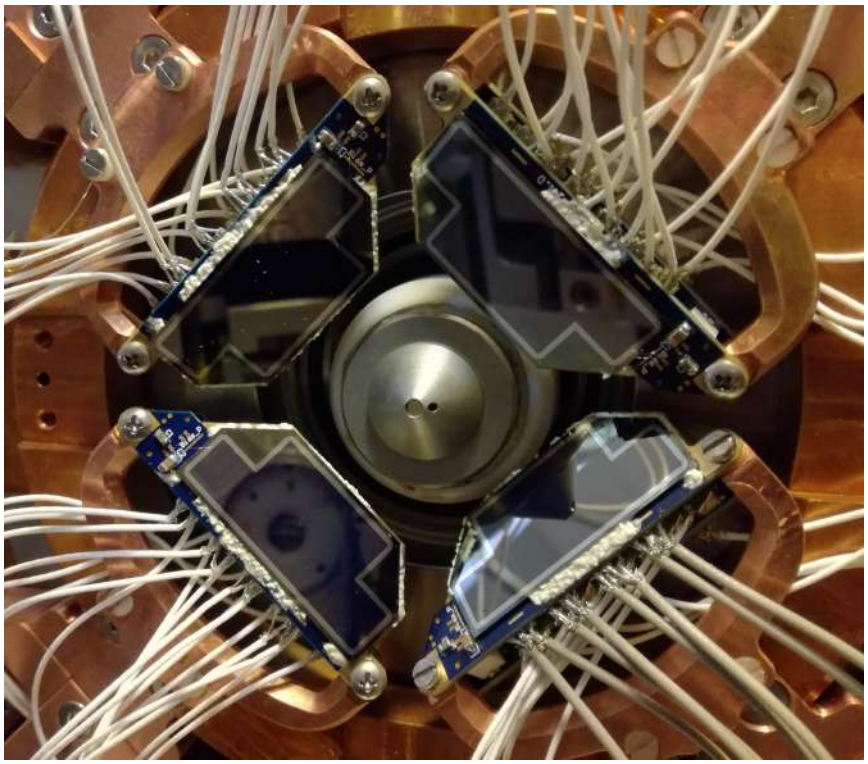

FIGURE 5.5: The detector system for TwinMic beamline at Elettra Sincrotrone Trieste: it is composed by 4 trapezoidal SDD sensors. In this picture the system detector is installed in the experimental chamber of the TwinMic beamline at Elettra [30].

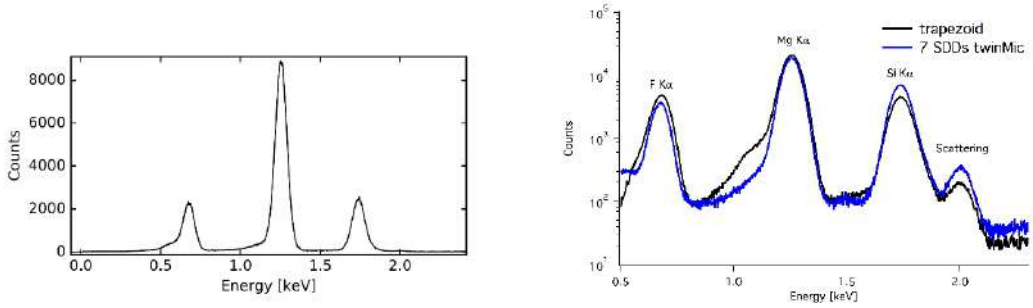

FIGURE 5.6: (**a**) K emission lines of F, Mg, Si and elastic peak at 2 keV. The energy resolution is of about 93 eV FWHM at 1254 eV with a count-rate of $2.10{\cdot}10^5$ counts/s. (**b**) A comparison with the standard TwinMic detection system, where the clearly visible low energy tails on the left of the XRF peaks on the trapezoidal multi-element SDD are due to the lack of collimation [30].

Further measurements were carried out on a biological sample, a slice of human lung tissue of a patient exposed to asbestos fibres, representing a typical case study performed at the TwinMic beamline [65, 64]. The XRF mapping was acquired at 2 keV by scanning the sample with 0.5 μm step size. The elemental distributions are shown in figure 7 where a comparison between one trapezoid [Fig. 5.8 (a)] and the standard LEXRF setup of TwinMic [Fig. 5.8 (b)] are depicted. Even if the mapped areas are not exactly coincident the overall counts proof the previous finding of a fivefold increase with respect to the 8 SDDs TwinMic system.

As transpires from the Figure 5.8 (c) there is still an important issue to be addressed. All the previous measurements were performed without a collimation system and this causes extended tails towards lower energies left of the XRF peaks that particularly worse the XRF lines below 1 keV, especially in complex spectra with multiple peaks in a narrow energy range. These tails are due to partial charge collection from X-rays impinging at the periphery of the multi element SDDs and can be avoided by utilizing suitable collimators as demonstrated in Figure 5.7.

To confirm the above-mentioned hypothesis one element of the monolithic trapezoidal sensor was equipped with a 100 μm thick Mo collimator. A comparison carried out with ^{55}Fe reveals that the presence of the collimator greatly reduces the low energy background and the left tail of the XRF peaks. For the collimator setup the peak-to-valley ratio can be quoted as 15600:1 [Fig. 5.7].

The experimental data acquired with the new detector system using laboratory sources and the TwinMic beamline confirmed the targeted design parameters; sensitivity to low energies has been proved acquiring Carbon (C) fluorescence X-ray photons (277 eV) and a count-rate gain of 5 times compared

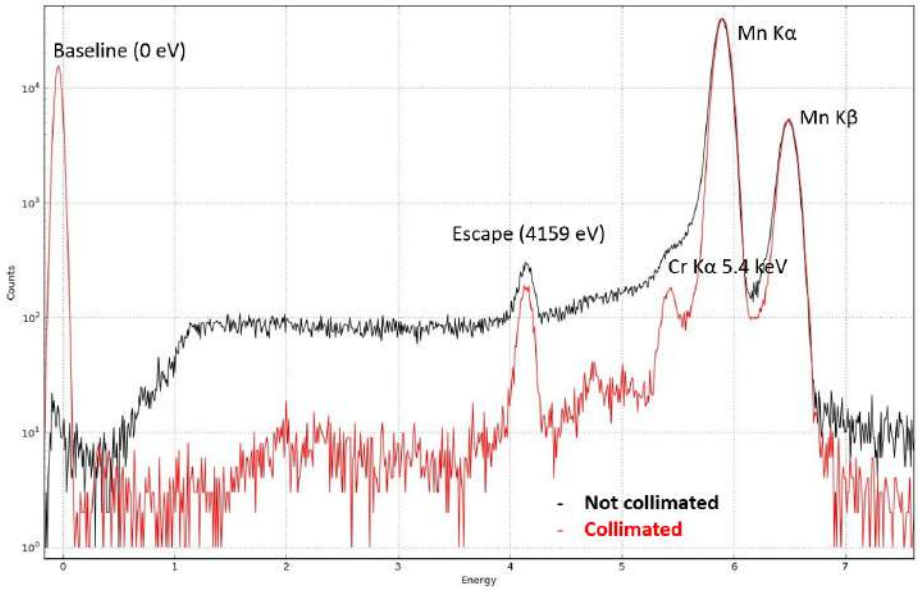

FIGURE 5.7: Comparison between not-collimated (black) and collimated (red) ^{55}Fe spectra of one trapezium element. The peak-to-valley ratio of the correctly collimated detector, i.e. the Mn Kα peak counts divided by the average number of counts around 1 keV, results in 15600:1 [30].

to the standard TwinMic detectors has been observed. To collect a typical map of 60 x 140 pixels, the standard system usually works with a dwell time of 5 s/pixel for a total acquisition time of approximately 11.6 hours. With the new detection setup the same measure would be reduced to less than 2.3 hours, thus allowing a greater number of experiments and better preservation of the sample.

The energy resolution is comparable with that of the 8 standard SDDs, although we note the lack of a collimator, which has already been produced and will be implemented for the next test campaigns.

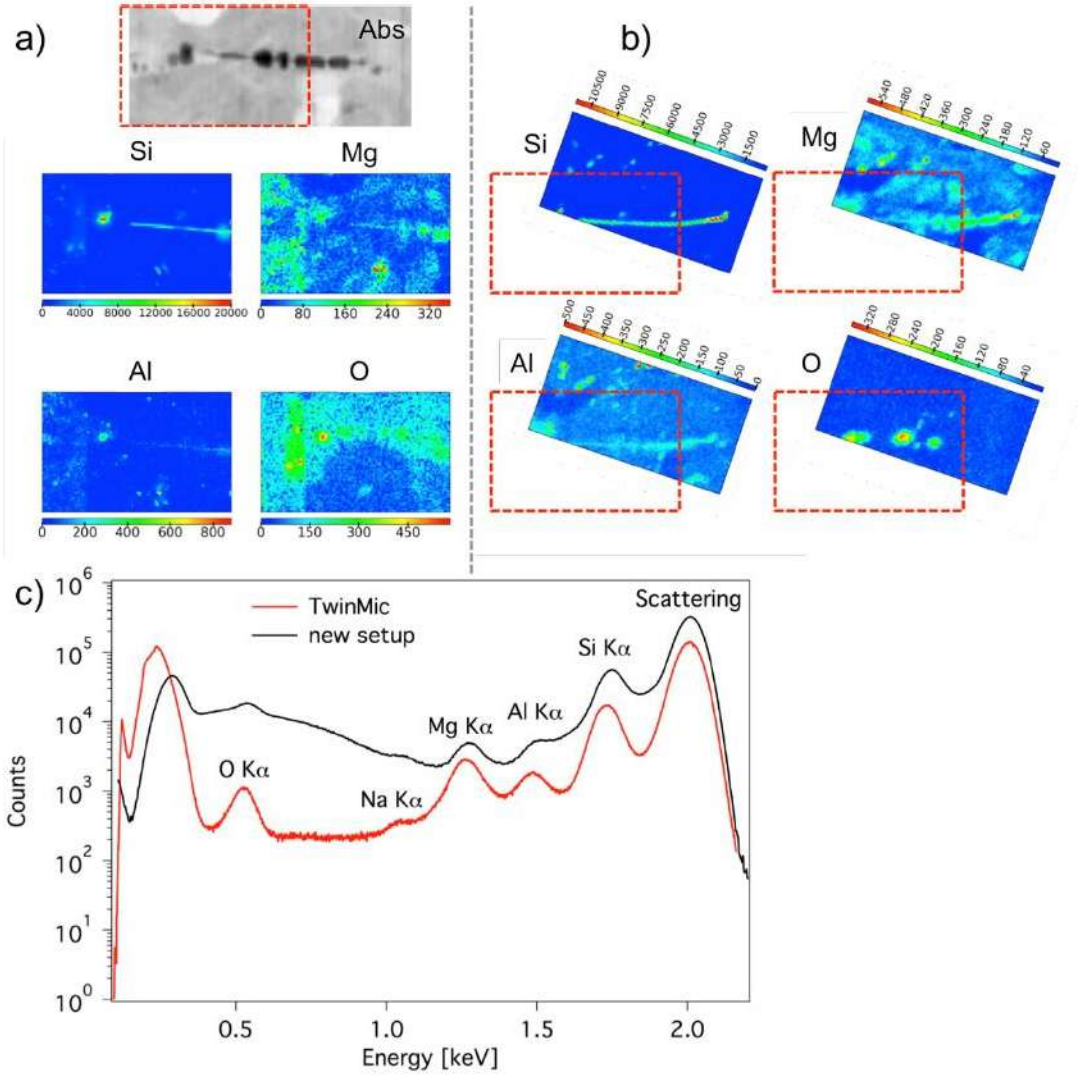

FIGURE 5.8: Elemental distributions of Si, Mg, Al and O in a slice of human lung tissue containing an asbestos fibre, together with the corresponding absorption image (Abs), where a comparison between 1 trapezoid (**a**) and the standard LEXRF setup of TwinMic (**b**) is depicted. In (**c**) are shown the sum spectra of the current collimated TwinMic system and one non-collimated trapezoid of the new setup. [30].

5.3 XRF topography

Synchrotron based Low Energy X-ray Fluorescence (XRF) spectroscopy is one of the most widely used non-destructive techniques for elemental analysis in many fields; from biomedical to electrochemical. The XRF emission is an isotropic phenomenon. Despite the known angular dependence of XRF detection, artefacts remain an issue especially when using micro- or nano-X-ray beams and detectors located at small angles with respect to the sample's surface. This angular dependence may be an advantage in some cases but for inhomogeneous samples with non-flat surfaces such as biological specimens, the sample

topography and roughness play an important role and may cause misleading interpretation [25]. Below we present the results obtained with a new detector system based on 4 trapezoidal sensors, each containing 8 SDD elements [48, 28, 29] recently developed at the TwinMic beamline of Elettra Sincrotrone Trieste [49, 54].

5.3.1 Materials and methods

During the measurement with the new detector system, TwinMic microscope was operated in scanning mode [49] with 2 KeV incident photon beam energy, a spot of 500 nm and a dwell time of 5 s per pixel. The scan was acquired line by line. The sample consisted of 2 crossing 25 μm diameter Al wires over a uniform 50 nm thick NiFe layer [Fig.5.9 (a)].

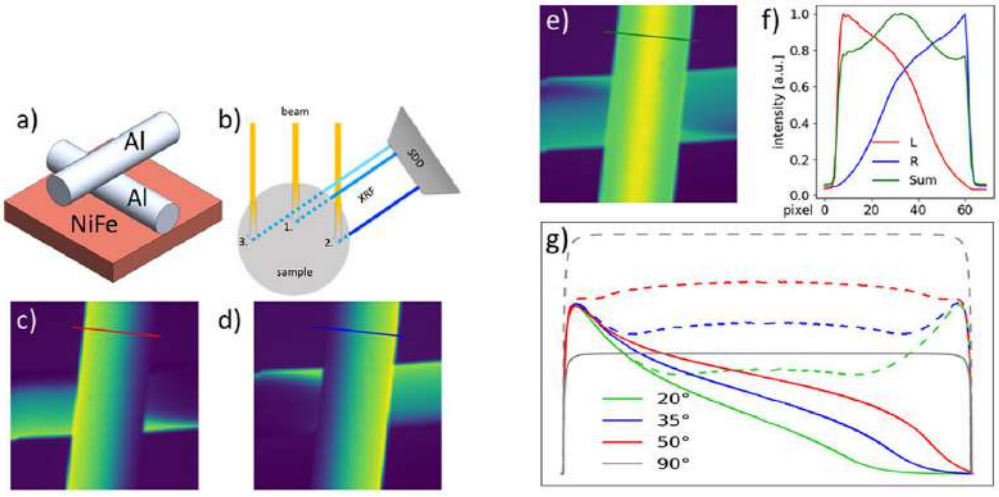

FIGURE 5.9: (**a**) Sample schematic view (**b**) Schematic view of incoming and detected X-ray beams (**c**) and (**d**) XRF Al maps of the wires acquired by the left and right detectors respectively (**e**) sum of panels c and d (**f**) lines profiles across the lines marked in panels c, d and e (**g**) simulated XRF intensity across the wires for different detector inclinations (20°, 35°, 50°, 90°) of a detector on one side of the wire (continuous lines) and for 2 opposite ones (dashed lines).

5.3.2 Results and conclusions

The XRF maps and their corresponding line profiles [Fig.5.9 (c) (d) (e) (f)] other than the expected shadows, exhibit a much higher intensity on the borders facing the specific detector. While a uniform Al XRF detection intensity would be desirable, this holds true mostly for detectors located perpendicularly to the sample's surface (continuous grey line in Fig. 5.9 (g)). However, when the detector axis forms a smaller angle compared to the samples' surface, as

in this study, the sum shows a different trend (Fig. 1e with corresponding green line profile in Fig.5.9 (f)). This is not surprising if we take into account the overall sample–detector geometry with their relative dimensions. With a uniform composition of the wire, while the primary beam penetration depth (yellow arrow in Fig.5.9 (b)) is the same in each position of the scan, the XRF photons emitted by a small volume inside the wire are more re-absorbed on the top of the wire (case 1), compared to the side facing the detector (case 2), since for the latter their path inside the sample becomes shorter (dashed lines). Thus the sample geometry clearly affects XRF intensity. When using a multi detector system, however, often the response of all detectors is summed to maximise statistics and count rate. This example shows that even by summing the XRF counts of two opposite detectors [Fig.5.9 (e)] the final map is not as the expected one. The green line profile of Fig.5.9 (f) should in fact look like the grey dashed line profile of Fig.5.9 (g). Interestingly Fig.5.9 (g) shows that the higher is the angle between incoming beam and detector axis, the more pronounced are the misleading border effects on the sum maps (dashed lines).

Often micro-beam setups are prone to produce artefacts in XRF maps sometimes yielding misleading results [25]. This is more likely for morphologically complex samples. The topographical information can be used not only to correct artefacts (red dashed line in Fig.5.9 (g)), but also to provide additional information about the morphology of the sample [Fig.5.9 (c) (d)]. Finally, the obtained results suggest that the detectors geometry by itself can play an important role for optimising the performance with respect to both detection efficiency and extraction of topography data.

New data with specially designed samples are being analysed and new tests are planned for the coming months.

Chapter 6

Silicon Drift Detectors for applications in astrophysics

One of the biggest scientific and technological challenges comes from the space sector. This has always seen scientists from multiple disciplines pushing themselves to the limit of technology to be able to look beyond current knowledge.

In astrophysics, light from various objects allows us to investigate their characteristics, and have a larger and more complete view of the physical phenomena involved.

Astrophysics have marked key points for the development of knowledge. One of these happened on 17 August 2017, when for the first time we witnessed the reception of the gravitational wave coming from the merging of two neutron stars. This phenomenon has awakened a desire for complete knowledge of astrophysical phenomena that has certainly opened the door to a new way of approaching observations of the sky. It has led to what is called multi-messenger astronomy, which represents the future for a greater and deeper knowledge of astrophysical phenomena. Driven by this new stimulus, new ways of observing the sky at more wavelengths and with an increasing focus on collaboration and networking are being planned.

Among the many topics still under study, one of the phenomena of astrophysics very intriguing and compelling is certainly linked to Gamma Ray Bursts (GRB). These are intense flashes of light in the gamma band of the electromagnetic spectrum observed since the 1960s. GRBs last between a few seconds and tens of minutes and are among the most energetic phenomena observed. They have an isotropic distribution in the sky and therefore have an extragalactic origin. It is impossible to predict where and when the next GRB will be observed. In order to study and understand them, it is important to try to observe with an all sky monitor in the X and gamma bands of the spectrum. New projects are active or under study to try to do this.

In this context there are some projects that exploit new detector systems. To achieve these goals in high-energy astrophysics you must therefore have a detector that:

- work in the wide energy range (energies between 1 keV and 1 MeV)
- has a good energy resolution
- has a good temporal resolution
- is compact and has a light weight
- has a moderate power consumption

A possible solution to all these requests is in the following description of the detection system for X- and γ-ray, in which we have the combination of using a Silicon Drift Detector with a crystal scintillator.

6.1 A new detector architecture: coupling SDD with crystal scintillator

The silicon drift detectors are mainly used for their good energy resolution and their low intrinsic noise, to detect X-rays of energy between 1 and 30 keV. A different (and complementary) way of using them is to use them indirectly by coupling them to a scintillating crystal. In this way it is possible to use only one detector for the detection of X and gamma ray.

Considering that to use a single detector for the acquisition of very different signals to be able to discriminate well between the two signals is very important. One possible way to discriminate is to use the different temporal properties of the two types of signals: the interaction of the radiation in the silicon creates electron-hole pairs that are quickly collected (about 10 ns of rise time), on the other side, the scintillation process is slower (about a few microseconds) because it is dominated by the fluorescence de-energizing time. therefore with a Pulse Shape Discriminator (PSD) it is possible to discriminate between the two types of signals. PSD can be obtained in several ways [60, 59].

The new detector core architecture (the "siswich" read-out concept [32]) is about how to discriminate between the two types of signals: this is done not through the temporal study of the signal but thanks to a different way of connecting together parts of the detector system. In this new way a single crystal is coupled to two SDD channels. The X-ray radiation affects an SDD

matrix and is detected by it, particularly only in the cell of the SDD that hits. The gamma radiation passes undisturbed through the SDD and deposits its energy on the crystal scintillator, that reemits in visible light and it lights evenly: in this way both SDD cells receive the same signal at the same time. This allows the detection of X-rays and gamma rays to be discriminated with a segmented SDD.

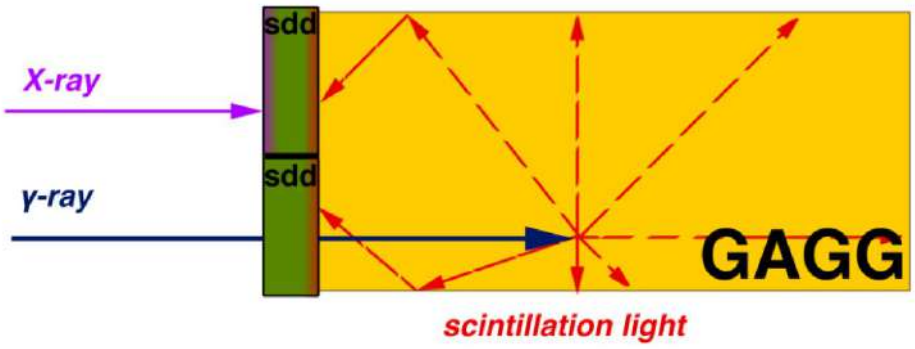

FIGURE 6.1: New detection core architecture in which a single crystal is coupled to two SDD channels. The X-ray radiation affects an SDD matrix and is detected by it, particularly only in the cell of the SDD that hits. The gamma radiation passes undisturbed through the SDD and deposits its energy on the crystal scintillator, that reemits in visible light and it lights evenly: in this way both SDD cells receive the same signal at the same time. This allows the detection of X-rays and gamma rays to be discriminated with a segmented SDD.

This new method of detection is just a relevant piece that led to the project to observe the sky X and gamma with a compact and lightweight detector system, low power consumption, with good energy and temporal resolution. One of the projects based on this new detection method is the HERMES project.

6.2 HERMES project

The *High Energy Modular Ensemble of Satellites* (HERMES) project [44] is aimed to realize a modular X/gamma ray monitor for transient events, to be placed on-board of a nano-satellite bus (e.g. CubeSat). This expandable platform will achieve a significant impact on Gamma Ray Burst (GRB) science and on the detection of Gravitational Wave (GW) electromagnetic counterparts: the recent LIGO/VIRGO discoveries demonstrated that the high-energy transient sky is still a field of extreme interest. The very complex temporal variability of GRBs (experimentally verified up to the millisecond scale) combined with the spatial and temporal coincidence between GWs and their electromagnetic

counterparts suggest that upcoming instruments require sub-microsecond time resolution combined with a transient localization accuracy lower than a degree. The current phase of the ongoing HERMES project is focused on the realization of a technological pathfinder with a small network (3 units) of nano-satellites to be launched in mid 2020. We will show the potential and prospects for short and medium-term development of the project, demonstrating the disrupting possibilities for scientific investigations provided by the innovative concept of a new "modular astronomy" with nano-satellites (e.g. low developing costs, very short realization time). Finally, we will illustrate the characteristics of the HERMES Technological Pathfinder project, demonstrating how the scientific goals discussed are actually already reachable with the first nano-satellites of this constellation. The detector architecture will be described in detail, showing that the new generation of scintillators (e.g. GAGG:Ce) coupled with very performing Silicon Drift Detectors (SDD) and low noise Front- End-Electronics (FEE) are able to extend down to few keV the sensitivity band of the detector. The technical solutions for FEE, Back-End-Electronics (BEE) and Data Handling will be also described.

6.2.1 HERMES mission concept

The High Energy Modular Ensemble of Satellites (HERMES) [5] project aims to realize a new generation instrument for the observations of high energy transients. The proposed approach here differs from the conventional idea to build increasingly larger and expensive instruments. The basic HERMES philosophy is to realize innovative, distributed and modular instruments composed by tens/hundreds of simple units, cheaper and with a limited development time. The present nanosatellite (e.g. CubeSats) technologies demonstrates that off-the-shelf components for space use can offer solid readiness at a limited cost. For scientific applications, the physical dimension of a single detector should to be compatible with the nanosatellite structure (e.g. 1U CubeSat of 10 x 10 x 10 cm^3). Therefore, the single HERMES detector is of course underperforming (i.e. it has a low effective area), when compared with conventional operative transient monitors, but the lower costs and the distributed concept of the instrument demonstrate that is feasible to build an innovative instrument with unprecedented sensitivity. The HERMES detector will have a sensitive area $>$ 50 cm^2, therefore with several tens/hundreds of such units a total sensitive area of the order of magnitude of $\sim$ 1 m^2 can be reached.

By measuring the time delay between different satellites, the localization capability of the whole constellation is directly proportional to the number of

components and inversely proportional to the average baseline between them. As a rough example, with a reasonable average baseline of ∼7000 km (comparable to the Earth radius, and a reasonable number for low-Earth satellites in suitable orbits) and ∼100 nanosatellites simultaneously detecting a transient, a source localization accuracy of the order of magnitude of ∼10 arcsec^2 can be reached, for transients with short time scale (ms) variability.

The current phase of the project, *HERMES Technological Pathfinder* (TP), focuses on the realization of three nanosatellites, ready for launch at mid-2020. The purpose here is to demonstrate the feasibility of the HERMES concept, operating some units in orbit and to detect a few GRBs. The next phase of the project, *HERMES Scientific Pathfinder* (SP) [6], will demonstrate the feasibility of GRB localization using up to 6–8 satellites in orbit. Although in both these preliminary phases reduced ground segment capabilities will be used, i.e. reduced data-downloading with a few ground contacts/day, the complete development of the HERMES detectors is expected. These activities will pave the way to the final HERMES constellation composed of hundreds of nanosatellites. Detailed mission studies, including orbital configuration, attitude control strategy, and sensitive area distribution will be performed, as well as a proper planning of the ground segment allowing to reach the ambitious scientific requirements, i.e prompt diffusion of the transient accurate localization. Thanks to the production approach, the context of a typical Small or Medium-class space mission seems to be compatible with HERMES final constellation, where most of the resources will be devoted to the multiple launches and to the realization of the ground segment.

6.2.2 Payload description

A possible solution for the HERMES payload is allocated in 1U-Cubesat (10 x 10 x 10 cm^3) [Fig. 6.2]. A mechanical support is placed on the instrument topside. The support is composed by two parts to accommodate an optical/thermal filter in the middle. The electronic boards for the Back-End and the Data Handling unit are allocated on the bottom of the payload unit. The detector core is located in the middle: this is a scintillator-based detector in which Silicon Drift Detectors (SDD, [46]) are used to both detect soft X-rays (by direct absorption in silicon) and to simultaneously readout the scintillation light. The payload unit is expected to allocate a detector with >50 cm^2 sensitive area in the energy range from 3–5 keV up to 2 MeV, with a total power consumption <4 W and total weight of <1.5 kg.

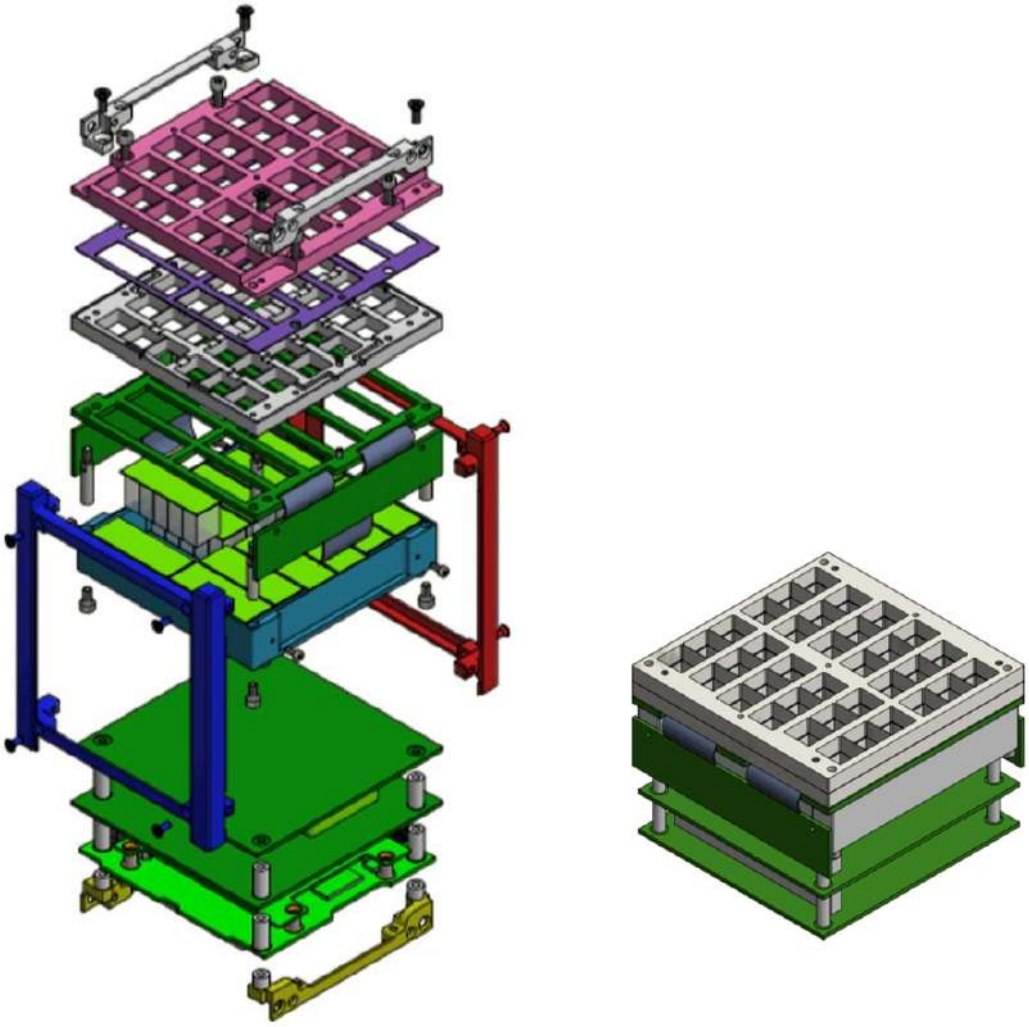

FIGURE 6.2: (**a**) Exploded view of the payload unit (10 x 10 x 10 cm^3) on board the HERMES nanosatellite. From the top are shown the mechanical support composed by top (pink) and bottom (gray) parts, with optical filter (violet) in middle, the FEE board (dark green) allocating SDD matrices (light green), FE-LYRA chips on the top and BE-LYRA chips folded on the side (not shown for clarity), the GAGG crystal pixels (white transparent) and their housing (greenish blue). Mechanical ribs on top (gray) and on bottom (yellow) are also visible, necessary to fix the payload components to the satellite structure (blue and red) (**b**) Compact view of the payload unit (10 x 10 x 10 cm^3) on board the HERMES nanosatellite.

Detector core architecture

Aiming at designing a compact instrument with a very wide sensitivity band, the detector is based on the so-called "siswich" concept [59, 60], exploiting the optical coupling of silicon detectors with inorganic scintillators. The detector is composed by an array of scintillator pixels, optically insulated, read out by Silicon Drift Detectors.

In this concept the SDDs play the double role of read-out device for the optical signal from the scintillator and of an independent X-ray solid state detector. Low energy X-rays are directly absorbed by the SDD, while higher energy X-rays and γ-rays are absorbed in the crystal and the optical scintillation photons are collected by the same detector. Only very low noise readout sensors and front-end electronics allow to reach a low energy scintillator threshold below 20–30 keV. Above these energies the increasing sensitivity of the scintillator is able to compensate the lack of efficiency of thin silicon sensors (450 μm), so a quite flat efficiency in a wide energy band for the whole integrated system is reached. The inorganic scintillators selected for this innovative detector is the recently developed [6] Cerium-doped Gadolinium–Aluminum–Gallium Garnet (Ce:GAGG), a very promising material with all the required characteristics, i.e. a high light output ($\sim$50,000 ph/MeV), no internal radioactive background, no hygroscopicity, a fast radiation decay time of $\sim$90 ns, a high density (6.63 g/cm^3), a peak light emission at 520 nm and an effective mean atomic number of 54.4. All these characteristics make this material very suitable for the HERMES application. Since GAGG is a relatively new material, it has not yet extensively investigated with respect to radiation resistance and performance after irradiation, although the published results are very encouraging [74, 83, 84]. These tests showed that GAGG has a very good performance, compared to other scintillator materials largely used in the recent years in space-borne experiments for γ-ray astronomy (e.g. BGO or CsI), i.e. a very low activation background (down to 2 orders of magnitude lower than BGO), and a minor light output degradation with accumulated dose.

The SDD development builds on the state-of-the-art results achieved within the framework of the Italian ReDSoX collaboration[1], with the combined design and manufacturing technology coming by a strong synergy between INFN-Trieste and Fondazione Bruno Kessler (FBK, Trento), in which both INFN and FBK co-fund the production of ReDSoX Silicon sensors. A custom geometry for a SDD matrix [Fig. 6.3] was designed, in which a single crystal ($\sim$ 12.1 x 6.94 mm^2) is coupled with two SDD channels. Therefore, the scintillator light uniformly illuminates two cells, giving rise to a comparable signal output for both channels. This allows to discriminate scintillator events (higher energy γ-rays) by their multiplicity: lower energy X-rays, directly absorbed in the SDD, are read out by only one channel.

[1]For more details see Appendix A.

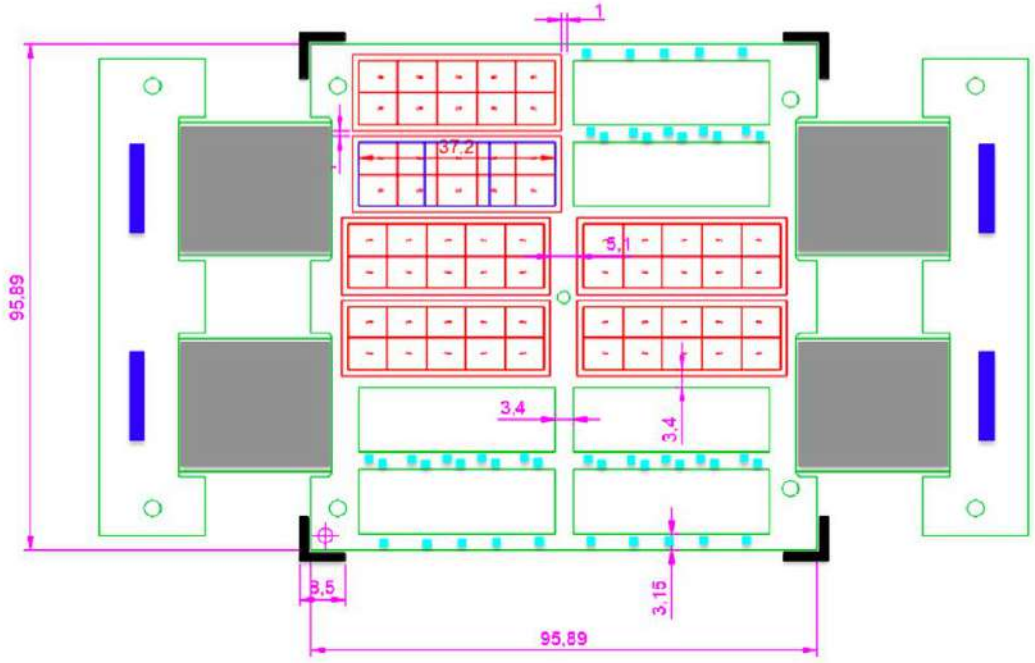

FIGURE 6.3: Sketch of the top view of FEE board for the HERMES nanosatellite. The black corner indicate the overall nanosatellite structure (10 x 10 cm^2). The board will allocate SDD matrices (in red) and FE-LYRA chips (light blue) very close to each SDD anode. The BE-LYRA chips (blue) are allocated on the rigid part that will be folded on the side of the satellite, by means of flex cables (gray).

Readout ASIC: from VEGA to LYRA

The HERMES detector, constituted by 120 SDD cells distributed over a total area of ∼92 cm^2, requires a peculiar architecture for the readout electronics. A low-noise, low-power Application Specific Integrated Circuit (ASIC) named LYRA has been conceived and designed for this task. LYRA has an heritage in the VEGA ASIC [16, 31] that was developed by Politecnico of Milano and University of Pavia within the ReDSoX Collaboration during the LOFT Phase-A study (ESA M3 Cosmic Vision program), although a specific and renewed design is necessary to comply with the different SDD specifications, the unique system architecture and the high signal dynamic range needed for HERMES. A single LYRA ASIC is conceived to operate as a constellation of 32+1 Integrated Circuit (IC) chips. The 32 Front-End ICs (FE-LYRA) include preamplifier, first shaping stage and signal line-transmitter, the single Back-End IC (BE-LYRA) is a 32-input ASIC including all the circuits to complete the signal processing chain: signal receiver, second shaping stage, discriminators, peak&hold, control logic, configuration registers and multiplexer. The FE-LYRA ICs are small (0.9 x 0.6 mm^2 die) allowing to be placed very close to the SDD anodes, in

order to minimize the stray capacitances of the detector-preamplifier connection, maximizing the effective-to-geometric area ratio (∼54 cm^2 vs. ∼92 cm^2). In this configuration [Fig. 6.3], the BE-LYRA chips (∼ 6.5 x 2.5 mm^2 die) can be placed out of the detection plane, allocating SDD matrix and FE-LYRA ICs on a rigid part, by means of embedded flex cables. The flat cables allow also avoiding the additional space required by connectors, offering the possibility to "fold" the boards allocating the BE-LYRA chips (on a rigid part) at right angle with respect to the detection plane, on the external side of the payload unit.

Back-End electronics

The Back-End electronics (BEE) of HERMES includes the BE-LYRA chips, external commercial analog-to-digital (ADC) converters and a FPGA-based control logic. The control logic takes care of the signal handshaking required to read out analogue signals from BE-LYRA chips, synchronizing the digital conversion operations, and time tagging the events based on conventional GPS sensor, combining an atomic clock signal (CSAC) to reduce as much as possible the natural shift/jitter of the GPS sensor ensuring a sub-microsecond timing resolution. Due to the peculiar architecture of the detector core, the BEE will also perform the Event Data Generator functionality, automatically discriminating the location of photon interaction (silicon or scintillator), on the basis of the multiplicity of the readout signals. This fundamental task has to be carried out in real-time to generate the photon lists that include channel address, time of arrival of photons and a raw energy estimation, which are mandatory for scientific data processing based on a suitable on-board logic.

Payload data handling unit

The HERMES Payload Data Handling Unit (PDHU) will be implemented on iOBC, manufactured by ISIS, a commercial on-board computer. This model, with a weight of ∼100 g and an average power consumption of 400 mW, will implement all functionalities required for HERMES, such as telecommands (TCs), housekeeping (HKs), power system commanding (PSU), handling operative modes of the payload (by TCs or automatically), generating the telemetry packets (TMs) and managing the interface with the spacecraft. A custom algorithm making the satellites sensitive X-ray and γ-ray transients, continuously compare the current data rate of the instrument with the average background data rate taken previously. When a transient occurs, the events, recorded on a circular buffer, are then sent to the ground on telemetry packets. Due to the different

families of GRB, ratemeters on different timescales, energy bands and different geometric regions of the detection plane will be implemented.

6.2.3 Conclusion and future perspectives

The HERMES project final aim is to realize a new generation instrument composed by hundreds of detectors onboard nanosatellites. This disruptive technology approach, although based on "underperforming" individual units, allows to reach overall sensitive areas of the order of $\sim$1 m^2, with unprecedented scientific performance for the study of highenergy transients such as GRBs and gravitational wave counterparts. The current ongoing phase of the HERMES project (Technological Pathfinder), focuses on the realization of the three nanosatellites to be launched in mid-2020, that will demonstrate the proposed approach to detector design (Silicon Drift Detectors coupled to GAGG:Ce scintillator crystals) and its performance. In this framework, relevant prototyping activities are currently under development, towards the implementation phase.

Chapter 7

A new development: the Pixel Drift Detector - PixDD

The new scientific objectives to be achieved and the experience that in these years we have accumulated on many fronts with various projects has led us to develop a new pixel silicon drift detectors: the PixDD [40].
This detector is designed to be fast, have good energy and temporal resolution (so you can perform a good spectroscopic and temporal analysis), being able to work at high count rates, and also have a low power consumption (including the one for cooling). This would make them perfect for astrophysical applications, such as being placed at the focal plane of an X-ray telescope.

The design, production and laboratory characterization of a state-of-art pixelated detector prototype — PixDD — based on planar silicon technology is presented. PixDD is aimed at the measurement of X-rays between 0.5 and 15 keV with a nearly "Fano-limited" spectral resolution, a timing resolution of few microseconds and a photon-by-photon fast read-out. The detector system exploits the superior noise characteristics typical of the Silicon Drift Detectors (SDD) and the ultra-low noise performance of a dedicated front-end electronics. The PixDD development builds on the state-of-the-art results achieved in Italy on both SDDs, with the combined design and manufacturing technology of INFN-Trieste and Fondazione Bruno Kessler (FBK, Trento), and the read-out electronics, with the unprecedented noise performance of the SIRIO charge preamplifier [21, 23] developed at Polytechnic of Milan. This high-performance, pixelated silicon detector (<1 mm^2/pixel) has been designed aiming to imaging, timing and spectroscopic studies of astrophysical X-ray sources and will enable the development of a large-area detector with immediate application to spaceborne high-energy astrophysics experiments.

The PixDD detector layout is aimed at reducing the total capacitance of the anode when compared with a classical pixel structure of the same size, thus minimizing the series noise contribution and enhancing the performance. The

detector is composed of a matrix of small drift structures having a common shallow p+ entrance window. On the anode side, two cathodes surrounding the collecting electrode provide a transversal field, which is designed to avoid regions where the potential is slowly varying and the drift velocity is therefore very small. In Figure 7.1 the simplified PixDD detector layout is shown. The two drift cathodes (in grey) are biased from the external circuitry without the need for integrated resistors. This allows to minimize the detector power consumption with respect to the use of an integrated voltage divider for each detector cell. The shallow p+ entrance window (on the bottom in Fig.7.1) is biased at a negative potential with respect to the anodes (-85V $\leq$ Vdep $\leq$ -75V) to ensure the full depletion of the detector bulk. The first PixDD detector prototype [Fig.7.2] has been fabricated by FBK on a 450 μm thick n-type, floating-zone (FZ) silicon substrate with a resistivity of 9 k$\Omega \cdot$ cm. The detector is made of a total of 16 square pixels 500 μm x 500 μm wide, arranged in 4 rows by 4 columns. By design, the anode capacitance is about 30 fF. The shallow p+ implant of the entrance window guarantees a good detector quantum efficiency for low energy photons.

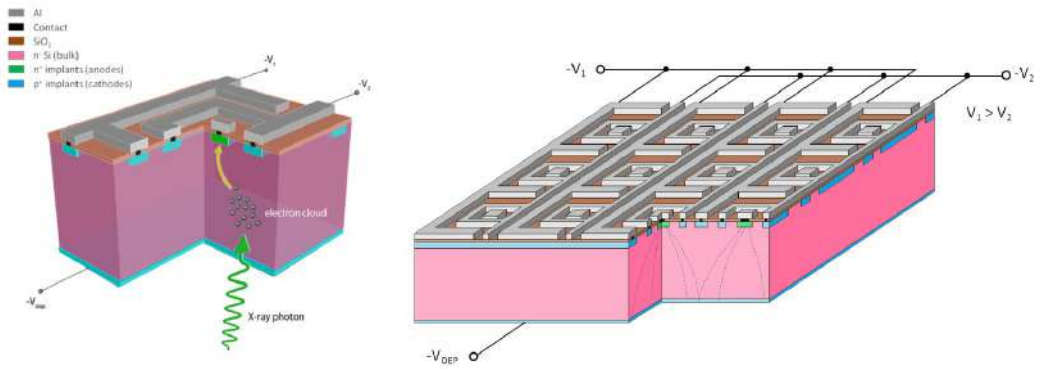

FIGURE 7.1: (**a**) Simplified single pixel layout (**b**) Multi-pixel layout (right) of the PixDD detector.

7.1 PixDD read-out system

In order to characterize the novel PixDD detector an ultra low-noise charge preamplifier has been selected to ensure the minimum contribution of the front-end electronics to the detector noise and energy resolution. All the tests described here have been performed with the SIRIO 3 charge sensitive preamplifier (CSA) developed at the Polytechnic of Milan [23] to achieve a nearly Fano limited resolution performance.

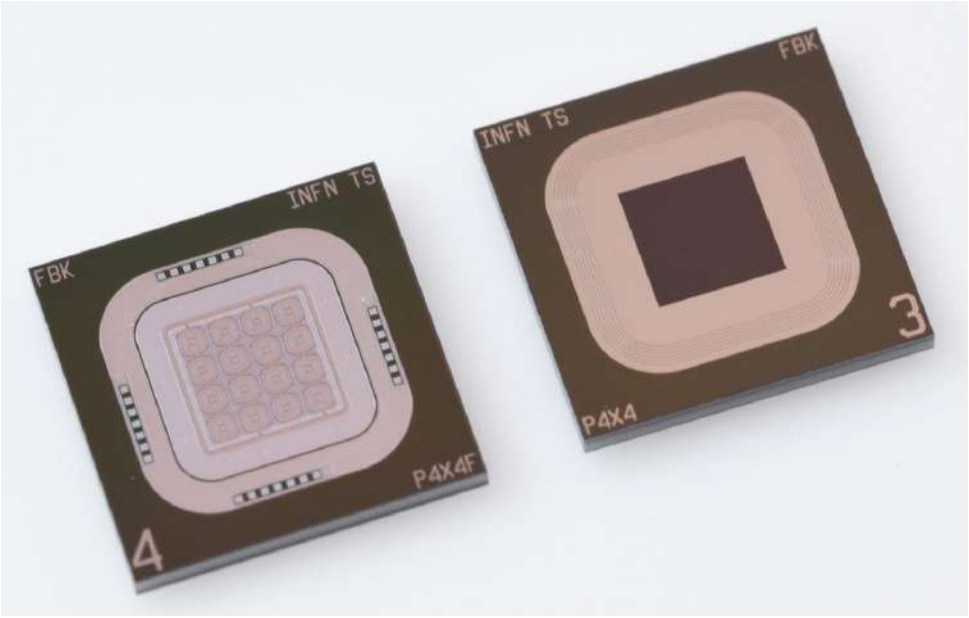

FIGURE 7.2: The first PixDD detector prototype. Left: n-side (anode side), Right: p-side (entrance window side).

To simplify the interconnection scheme between the CSA and the 16 channels of the PixDD detector, a custom 4-channel SIRIO preamplifier (SIRIO 3.4) has been designed and built in 0.35 μm AMS CMOS technology. The four channels share the CSA biases and the reset signals, while the inputs, the test injection pads and the feedback network fine-tuning voltages (V_{ssi}) are individual for each channel. The overall dimensions of the 4-channel preamplifier chip are 2300 μm x 1820 μm.

Two custom PCBs, namely PixDD control board (PixDD-CB) and PixDD detector board (PixDD-DB), have been designed and manufactured by IASF Milano and IAPS Rome to integrate the PixDD detector with the SIRIO 3.4 chips [Fig.7.3]. The PixDD-CB provides bias line distribution for both the detector and the CSA chips and allows for the fine regulation of the 16 feedback network fine-tuning voltages. The setting of the V_{ssi} voltages is performed by means of digital potentiometers (AD5263 by Analog Devices) controlled with I^2C interface. The PixDD-DB provides effective filtering of the bias lines, impedance matching for the reset and test pulse signals, detector and read-out chip mounting and interconnection. Moreover, an analogue temperature transducer (Analog Devices AD590KF) placed in close proximity of the detector die allows for a direct monitoring of the detector temperature. Input and output analogue signals are available through a set of 50 Ω MCX connectors placed on the PixDD-DB perimeter, while the interconnection between the two PCBs is accomplished by means of ribbon flat cables.

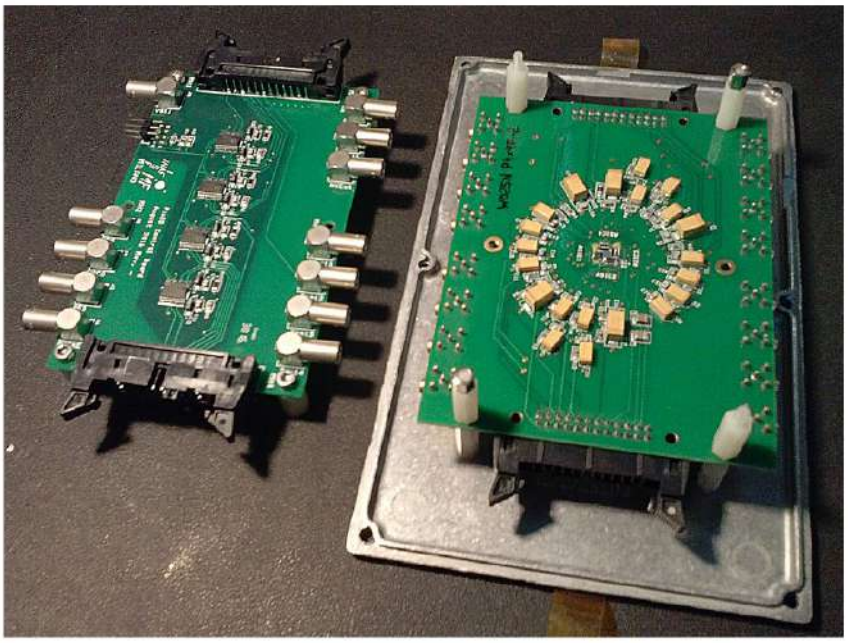

FIGURE 7.3: PixDD control board (PixDD-CB, left) and PixDD detector board (PixDD-DB, right) developed at the Istituto di Astrofisica Spaziale e Fisica Cosmica (IASF) in Milan.

7.1.1 Front-end electronics characterization

The performance of the front-end system (FEE) has been tested and characterized in the INAF-IAPS laboratory after the integration of the SIRIO 3.4 ASICs with the PixDD-DB but before the interconnection of the PixDD anodes with the read-out input pads. The system biases were provided by standard linear power supplies, filtered by 2-stage RC networks and integrated EMI filters. The injection of charge pulses was made by means of voltage steps applied to the SIRIO 3.4 test capacitances and generated by an Arbitrary Function Generator (Rigol DG5251). A passive 40–60 dB attenuator was used to maximize the signal to noise ratio of the injected voltage steps. A second Arbitrary Function Generator (Tektronix AFG3022B) was used to generate the periodic digital signal for the preamplifier reset. After a further amplification ($G_v = 10$), carried out by means of a custom AC coupled amplifier, the SIRIO 3.4 output signals were processed and acquired with a Digital Pulse Processor (Amptek DP5).

In order to characterize each system channel in terms of noise and functionality, the 16 CSAs have been individually stimulated with different test-pulse amplitudes, ranging from 170 eV to 3490 eV (equivalent energy in silicon). An average equivalent noise charge (ENC) of 4.0 ± 0.4 e^- r.m.s. has been measured at +21 °C in the 500 eV–3490 eV energy range (40 dB attenuation applied to the test signal). A significantly better ENC of 2.4 ± 0.2 e^- r.m.s has been

obtained between 170 eV and 500 eV (attenuator set to 60 dB), most likely indicating the presence of a non-negligible noise contribution from the Arbitrary Function Generator. Although the measured ENC at room temperature is still substantially larger than the value of 1.3 e^- r.m.s. measured with the single channel SIRIO [19], the overall FEE performance has been considered very promising to fulfil the energy resolution requirement at room temperature ($\leq$ 150 eV FWHM at 5.9 keV) of the integrated detector system.

7.2 PixDD detector characterization

After the FEE system electrical characterization, the 16 PixDD anodes have been wire-bonded at the INFN Trieste laboratories to the relevant CSA input pads [Fig.7.4 (a) and (b)]. The adopted bonding scheme [Fig.7.4 (c)] was designed to minimize the bonding length and thus the stray capacitance contribution of the wire bondings to the system series noise. Fifteen out of sixteen CSA channels were successfully wire-bonded to the PixDD anodes, while channel number 3 (CH03 hereafter) experienced an interconnection problem during the wire bonding procedure of the SIRIO 3.4 input pad, resulting unusable for all the following measurements.

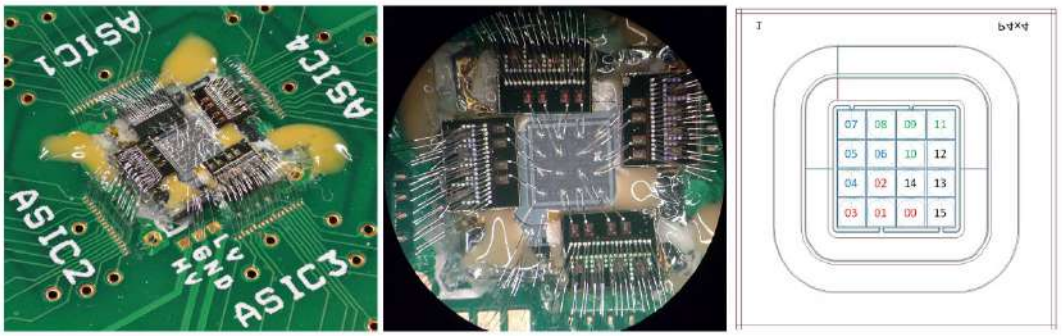

FIGURE 7.4: (**a**) and (**b**) The PixDD detector wire bonded to the 16 SIRIO 3.4 channels. (**c**) Correspondence of SIRIO 3.4 channels with PixDD pixels as seen from the p-side detector window - Different number colours refer to different SIRIO 3.4 ASICs (red: ASIC 1, blue: ASIC 2, green: ASIC 3 and black: ASIC 4).

The integrated detector has been enclosed in a light-tight aluminium box to provide proper shielding. All the measurements have been performed at a detector temperature of +27 $\pm$ 1 °C, with the box continuously exposed to a nitrogen flow in order to maintain a dry atmosphere.

For the test the PixDD detector has been illuminated with a ^{55}Fe radioactive source. The data were acquired and processed individually on all the pixels. The

energy spectra, obtained with a peaking time of 1 μs at +27 °C, are displayed in Figure 7.5. The FWHM energy resolution of all the channels lies between 141 eV and 156 eV.

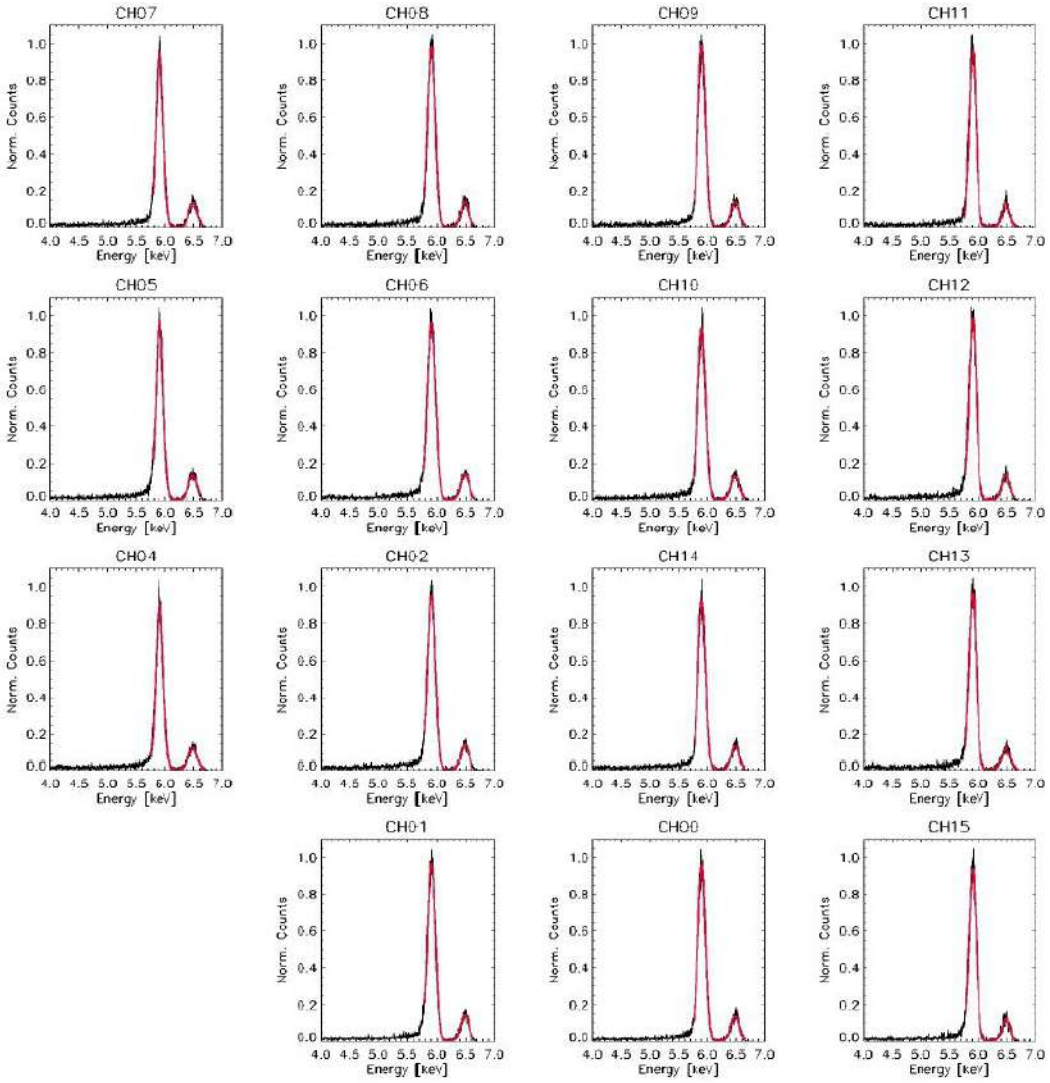

FIGURE 7.5: ^{55}Fe energy spectra acquired with 1 μs peaking time. CH03 (on the bottom-left corner of the detector) has not been acquired due to problems during the CSA–anode interconnection.

The signal conditioning and digitization system used so far for the PixDD characterization is limited to the acquisition of a single channel. To overcome this limitation, a multi-channel digitization system, based on the CAEN DT4750 fast digitizer, has been built. A custom 16-channels interface board has been designed and manufactured to provide proper amplification of the signals and analogue pre-filtering by means of a highpass CR network with 3.4 μs time constant.The signals have been digitized by the CAEN DT4750 digitizer at 62.5 MS $\cdot$ s^{-1} with 12 bit resolution, controlled by a specifically developed LabView

interface. The pulse-height analysis has been performed off-line by means of a digital trapezoidal filter. In presence of a trigger signal, provided by a digital threshold discriminator implemented in the DT4750 firmware, all the connected channels are sampled simultaneously and the waveforms are stored in a FITS binary table. This multi-channel acquisition system allowed for an in-depth characterization of the detector response.

A dedicated measurement campaign was carried out in the X-ray facility of the INAF-IAPS Rome laboratory [62] with the aim of characterizing the noise properties of the integrated PixDD-FEE system. The facility was equipped with a commercial Ti-anode X-ray tube and a custom collimation system to produce a ~ 40 μm FWHM wide X-ray spot on the detector surface. A three-axis motorized linear stage system was used to position the X-ray spot in the centre of each PixDD pixel with micrometric precision.

Each PixDD pixel has been exposed to more than 7.3 x 10^4 counts in the 2–15 keV energy band, with a count rate of about 175 counts $\cdot$ s^{-1} (corresponding to a flux of 7.0 x 10^4 counts $\cdot$ cm^{-2} $\cdot$ s^{-1}), for a total of 1.1 x 10^6 counts collected by all the 15working channels. For each channel, the acquired signal waveforms were digitally shaped with different peaking times ranging from 0.32 μs to 9.6 μs and the resulting energy spectra were fitted with two Gaussian functions centred at 4.51 keV and 4.93 keV (Titanium Kα and Kβ fluorescence lines) to estimate the energy resolution and thus the single-channel noise.

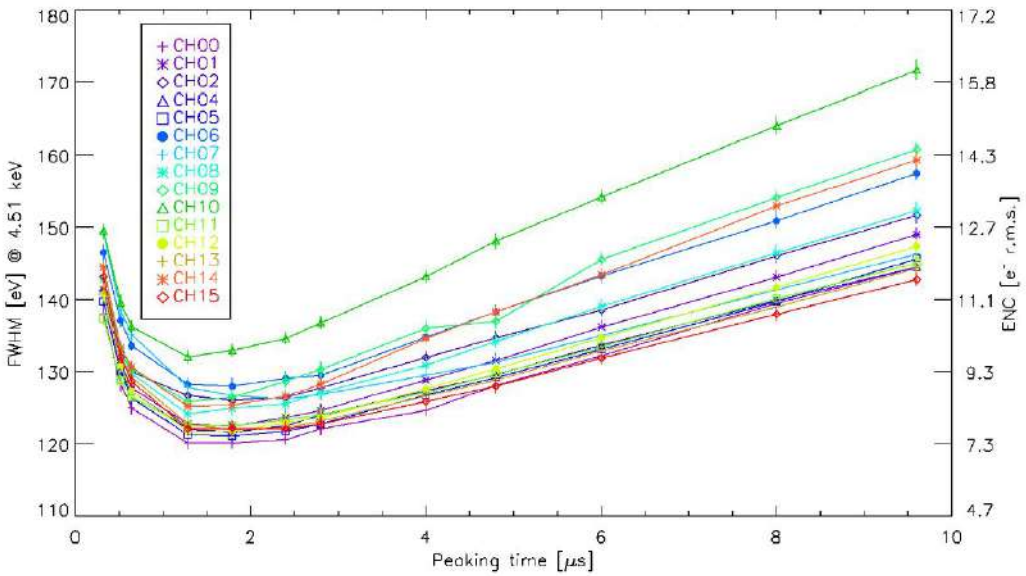

FIGURE 7.6: Energy resolution at 4.51 keV and the corresponding equivalent noise charge (ENC) as a function of the peaking time for the 15 read-out channels.

Figure 7.6 shows the energy resolution and the equivalent noise charge at 4.51 keV (Ti Kα) as a function of the peaking time for the 15 channels. All channels, except the slightly noisier CH10, show a FWHM energy resolution comprised between 120.1 eV and 128.0 eV at the optimal peaking time of 1.8 μs. The fitted energy spectra for all the channels are shown in Figure 7.7.

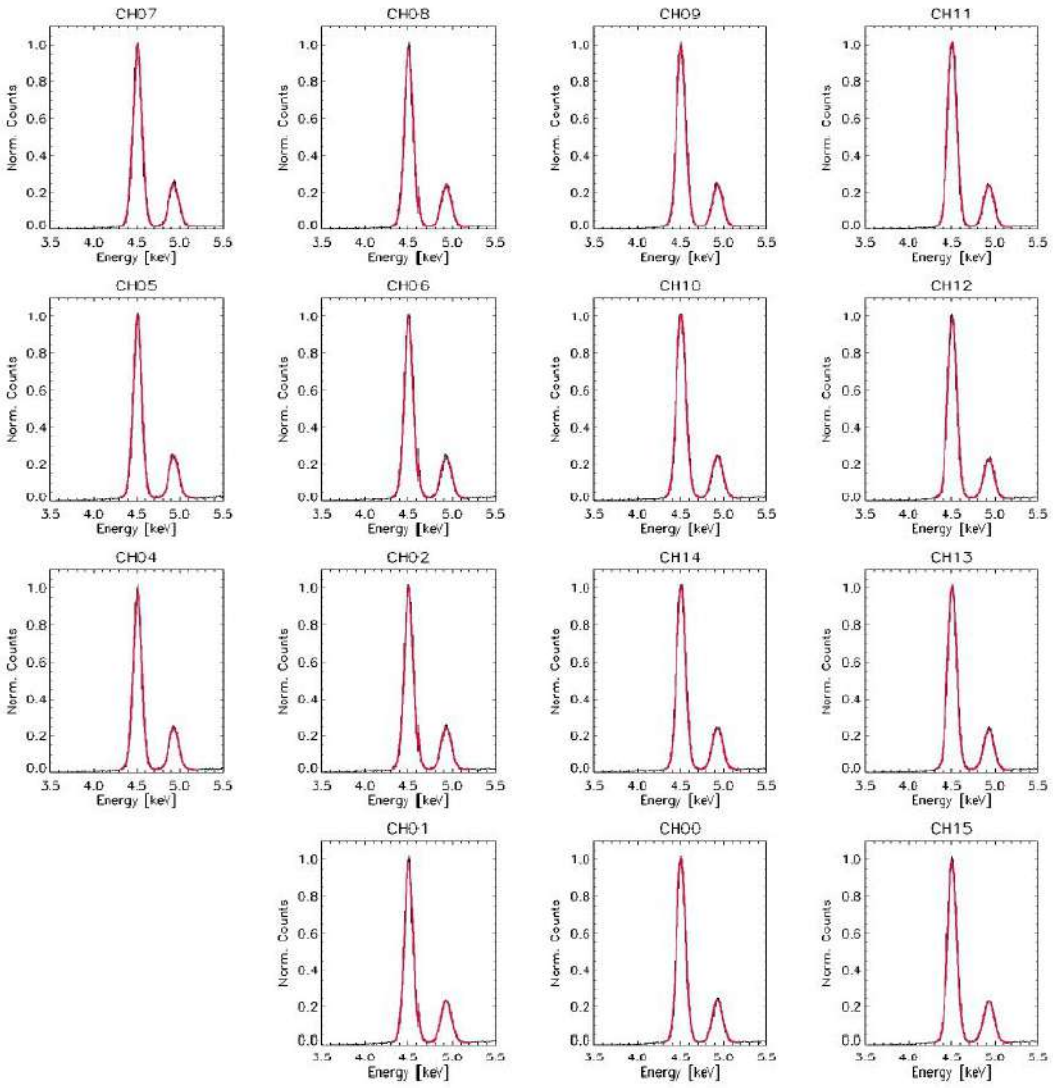

FIGURE 7.7: Fitted energy spectra of a Ti-anode X-ray tube. CH03 (on the bottom-left corner of the detector) has not been acquired due to problems during the CSA–anode interconnection.

A further analysis was performed to evaluate the presence of charge-shared events between neighbouring pixels. Although due to ionization the initial charge cloud lateral dimension is limited to a few microns, diffusion during charge drift in the silicon bulk is expected to lead to non-negligible cloud broadening. In these conditions, an appreciable fraction of charge-shared events can be observed, that can lead to a sensible worsening of the detector spectroscopic

performance. For this characterization campaign a non-collimated ^{55}Fe X-ray source was used to simultaneously illuminate the whole PixDD detector. In Figure 7.8 (top and bottom panels) two signals of 5.9 keV (Mn Kα) are shown. Top panels show the waveforms acquired by all the channels when a single event (multiplicity m = 1) is detected. For this event, the charge produced during the photon interaction was entirely collected by one channel (CH10). For comparison, bottom panels show a charge-shared event (m = 2), for which the charge cloud has been collected by two adjacent channel (CH10 and CH12). In order to quantitatively evaluate the amount of charge sharing between neighbouring channels, we analysed the dependence of the charge collected by the 4 central pixels with the signal of the 8 relative neighbouring pixels. In the following we present the analysis performed on CH10, but consistent results were obtained for the four central pixels. The acquired events were selected following the condition that more than 50% of the total charge was collected by CH10, this to ensure that the photon interaction took place in CH10 volume.

In Figure 7.9 each panel shows the distribution of the charge collected by CH10 (X-axis) versus the charge measured by the other pixels (Y-axis). Measurement points distributed parallel to the abscissa axis show single events (i.e. no charge sharing), while the points distributed following approximately the relation X + Y = K represent shared (double) events. From the plots is clear that a fraction of the events experienced charge sharing, and that sharing between more than two nearby pixels is less probable. Still a few triple-events are present, as it can been seen from the presence of measurement points not following the Y = K and the X + Y = K relations and from the signal distribution on CH08, CH11, CH02 and CH13.

By setting a threshold equal to 5 times the channel r.m.s noise for the event multiplicity determination, single events (m = 1) resulted to be 83.8% of the total, while double and triple (m = 2 and m = 3) events were quantified to be 15.8% and 0.4% respectively.

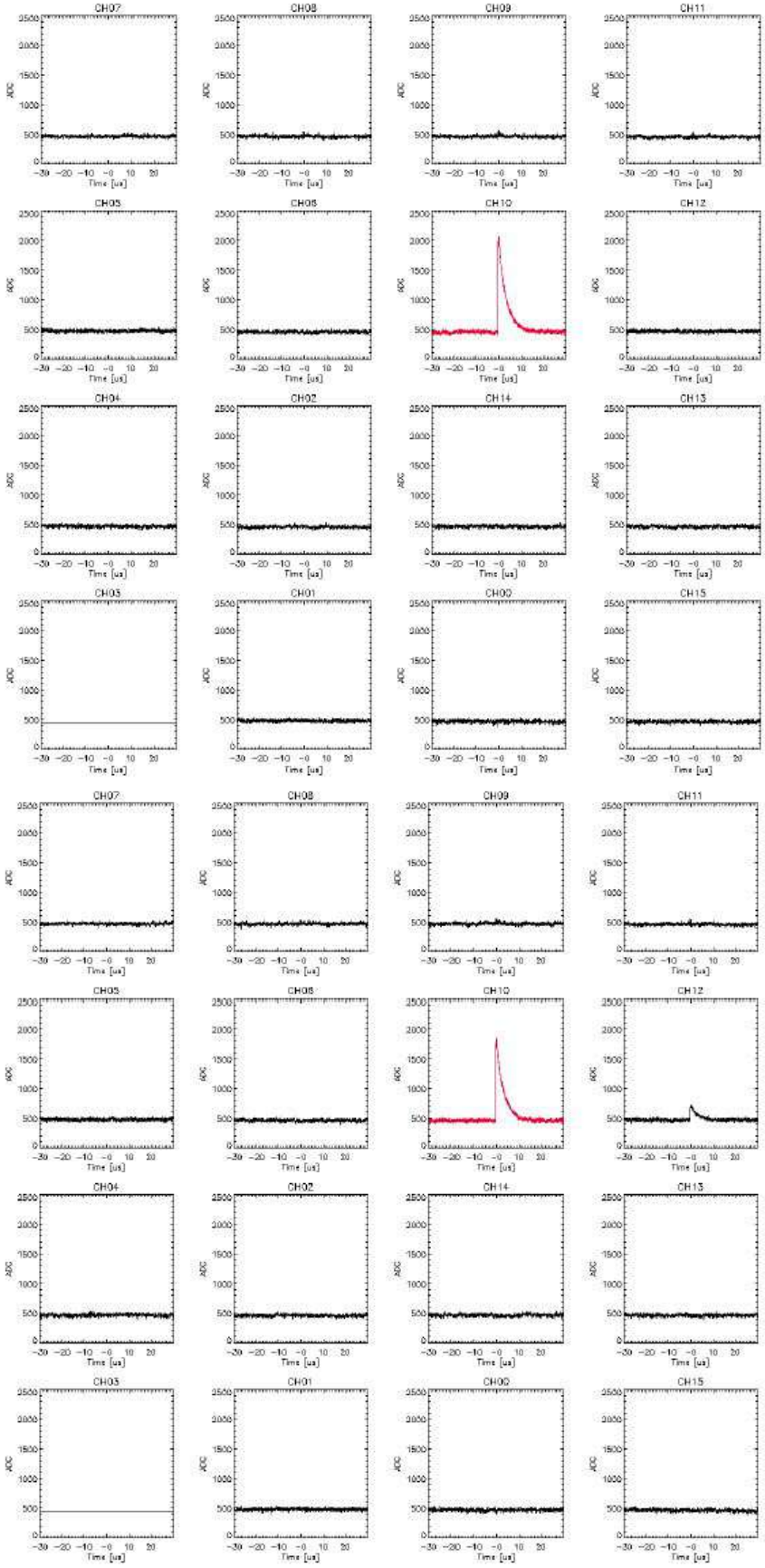

FIGURE 7.8: Two Mn Kα signals (5.9 keV) acquired with the multi-channel fast digitization system. Top panels show a single event (m = 1) waveform while bottom panels show a charge-shared event (m = 2) between CH10 and CH12.

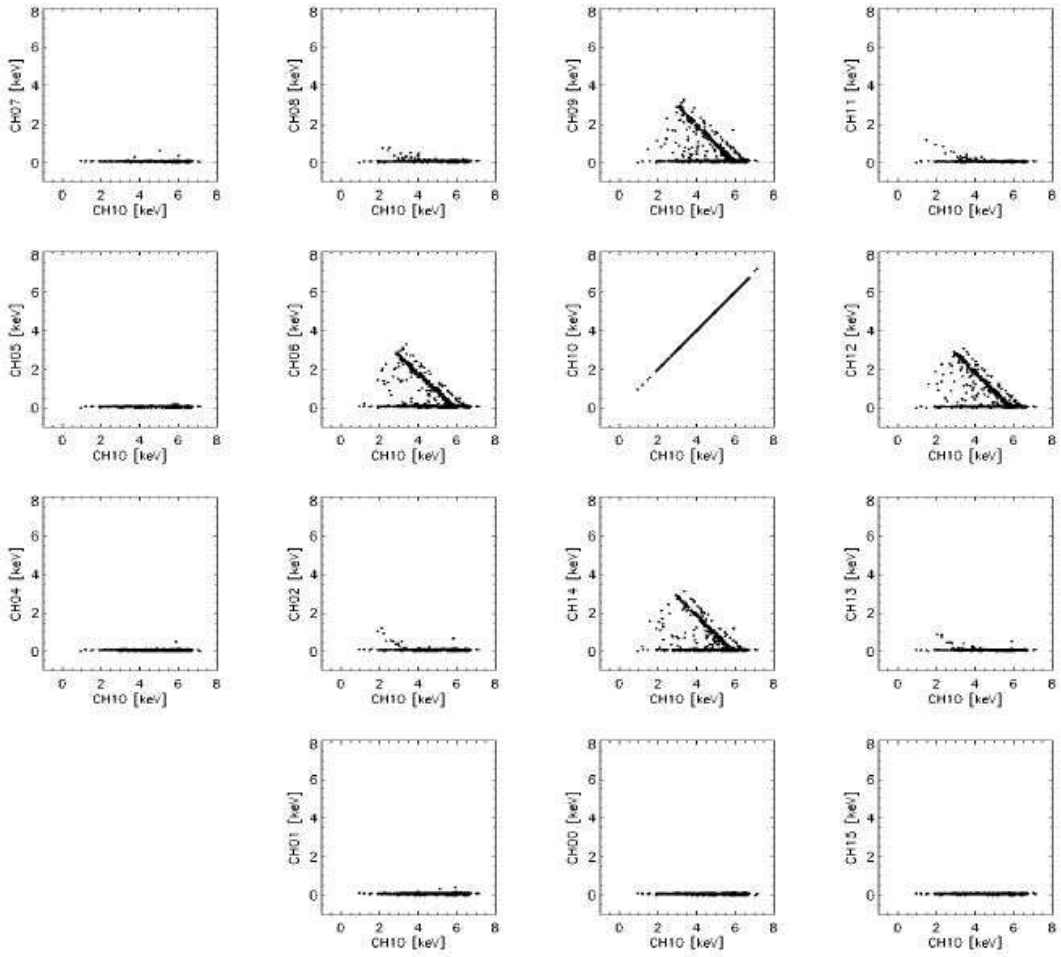

FIGURE 7.9: Distribution of the charge collected by CH10 (X-axis) versus the charge measured by the other pixels (Y-axis). Measurement points distributed parallel to the abscissa axis show single events (i.e. no charge sharing), while the points distributed following approximately the relation X + Y = K represent shared events.

7.3 Results and future perspectives

In the framework of the RedSoX Italian collaboration, a novel, pixelated, silicon drift detector (PixDD) has been designed and produced to fill the technological gap in the capability of realizing pixel silicon detectors with fast response, which are capable of asynchronously detect and trigger on the individual X-ray photons and can offer a nearly Fano-limited energy resolution and soft X-ray response at room temperature, as required by high throughput X-ray astronomy applications.

The whole system, composed of a 16 pixels 500 μm x 500 μm wide, has been integrated with ultra low-noise front-end electronics (SIRIO 3.4) and characterized at +27 °C at the INAF-IAPS laboratories, demonstrating outstanding noise figure (single channel ENC $\leq$ 10 e^- r.m.s.) and spectroscopic capabilities (ΔE $\leq$ 150 eV FWHM at 5.9 keV). The physical and electronic behaviour of the individual pixels have been studied to assess the charge sharing between neighbouring detector cells, resulting in a limited fraction of shared events ('16%) whose contribution to the energy resolution does not undermine the overall detector performance.

Further experimental activities have already taken place aimed at the design and production of a large PixDD detector, composed by 16 x 8 pixels with 300 x 300 μm^2 dimensions. The 16 x 8 PixDD will be read-out by a monolithic 16 x 8 channel ASIC (namely RIGEL) developed by Polytechnic of Milan and University of Pavia and currently in production. The PixDD–RIGEL hybrid will be flip-chip-bonded exploiting the bump bonding technique developed at the Karlsruhe Institute of Technology (KIT) [33].

Conclusion

The concrete effort to bring a detection system from the prototypal state through engineerization phase to the delivery of the completely characterized system has been my task. Future projects will profit of this demonstrative effort where monolithic multipixel SDD have been applied, some of them has been presented in this thesis.

In my work I had the opportunity to bring the detector systems of which I took care to a finalized stage following all single aspects.

For what matter the single element SDD optimization, I had the chance to increase my knowledge and to contribute in the field with the mapping of a detectors prototype in the intermediate stage of development and with the tests on the very promising prototype just designed and built.

The crowning of my effort took form when I could unpack and install the detector at the SESAME laboratory site in Amman. This has been the best demonstration of my two main targets:

- realization of a completely new dedicated state of the art detection system;
- construction and delivery of an integrated user ready system.

The availability of the new detector systems represent for the TwinMic and XAFS beamline a real quantum leap. This results has been made possible by a transversal collaboration between detector design, detector production, Front End Electronics development, complete engineering and of all other aspects. In each of this directions dedicated state of the art elements were developed on purpose. It is so that the 64-channel XAFS detector and the large solid angle TwinMic detector were able to reach unique results and will represent an important starting point for the next steps.

Having had the opportunity to follow the day by day work and taken part to the development and test of those detection systems, I have improved my knowledge and have given my contribution in this challenging research and development fields.

Appendix A

ReDSoX Collaboration

The ReDSoX, REsearch Drift for SOft X rays (https://web.infn.it/redsox2) Collaboration, Fig.A.1, was born buildings on a strong existing experience with the aim of connecting some universities and research institutes that had a common goal: the development of high energy resolution SDD for soft X-ray, with a dedicated very low noise front-end electronics, for applications in astrophysics and advanced light source [10].

FIGURE A.1: Logo of the ReDSoX Collaboration [10].

The collaboration of several institution has allowed us to develop state-of-the-art detectors that allow us to reach very ambitious scientific and technological objectives. It involves many institutions between universities and research institutes, some of these are INFN, TIFPA, INAF-IASF Bologna, INAF-IAPS Rome, FBK-Trento, POLIMI, Elettra Sincrotrone Trieste, ENEA, University of Pavia, University of Bologna, University of Udine, University of Trieste, ASI, ICTP, KTI.

The collaborative work within ReDSoX has allowed to reach otherwise impossible results.

Appendix B

XAFS-SESAME Detector System Timeline

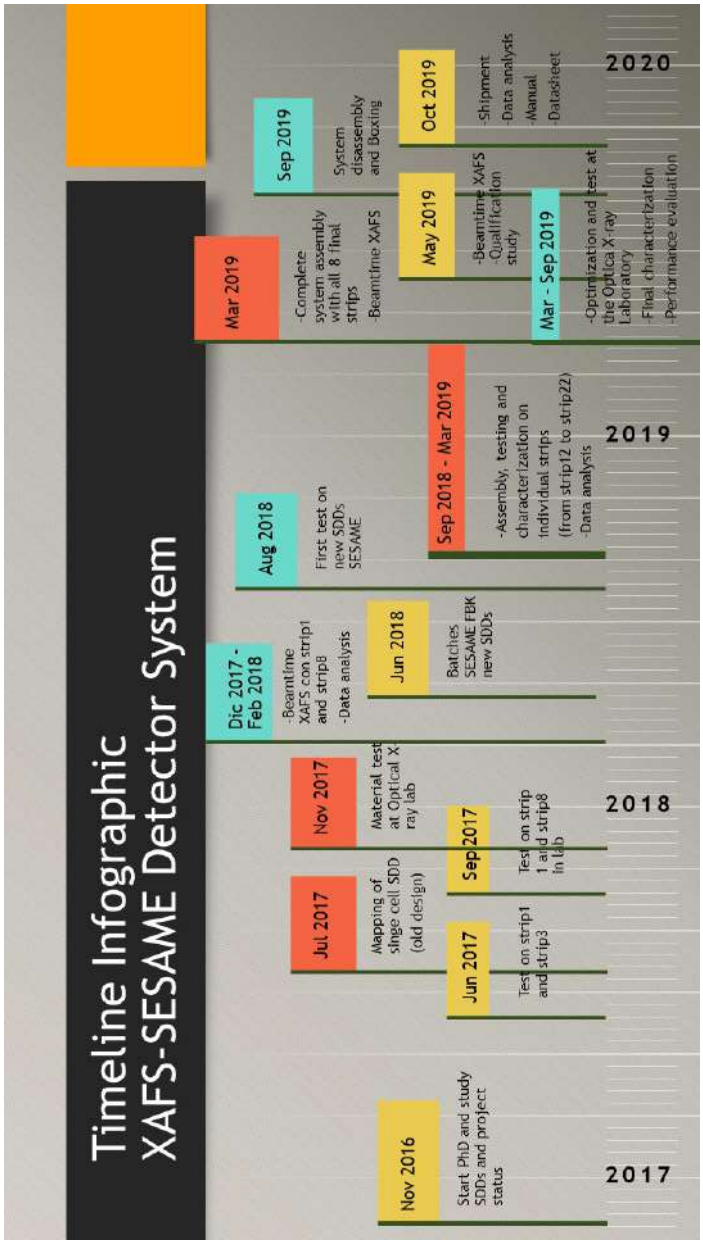

Appendix C

the XAFS-SESAME Detector System datasheet and FICUS software manual

The document **XAFS-SESAME Detector System Datasheet** and **XAFS-SESAME Detector System Datasheet** are attached below. They are the first version of the datasheet of the XAFS-SESAME Detector System and the FICUS (*Fluorescence Instrumentation Control Universal Sotfware*) software manual.

The XAFS-SESAME Detector System Datasheet the main descriptions of the detector system and the instrumentation supplied. It contains the list of objects accompanying the detector system, documentation regarding the size of the detector, the connections between the various parts of the instrument, the specifications and technical specifications of the power supplies.

The FICUS software is an integral part of the detector system: in fact, it has been designed to complete the instrument according to the requests and needs that have emerged from the continuous consultation with beamline scientists and users. The software has 3 different levels: each level corresponds to a different subject who uses it and, consequently, a different choice of options available. In particular, three levels are available:

- Detector Expert: dedicated to detector and software developers, allows the maximum degree of variation of the available parameters and the display of screens useful for development and debugging;
- Beamline Staff: dedicated to the staff of the beamline, allows an intermediate degree of variation of the parameters for the setting and the measurement;
- User: dedicated to all possible users of the beamline, allows a low degree of parameter variation but allows for data collection and pre-analysis.

FICUS has been tested and used in the field during all the acquisitions made and this has allowed to verify its performance and to further optimize it.

In particular, they include the Safety warnings for using the XAFS-SESAME Detector System.

These two documents are part of the documentation accompanying the instrument.

133

SESAME Detector System Datasheet

Contents

1 Overview

A Fluorescence Detector System for XAFS (X-ray Absorption Fine Structure) composed of 8 monolithic arrays of SDDs (Silicon Drift Detector), each having 8 cells of 9 mm^2 area, is being realized within the INFN ReDSoX Collaboration. It will be used for X-ray absorption spectroscopy at the Jordanian synchrotron light source SESAME that provides a photon beam with an energy range between 3 and 30 keV. Detailed characterization tests at ELETTRA Sincrotrone Trieste have demonstrated an energy resolution at the Mn 5.9 keV Ka line, for the monolithic array, below 170 eV FWHM at room temperature.

2 Description

The detector system was designed and implemented for X-Ray Fluorescence (XRF) and X-ray Absorption Fine Structure (XAFS) experiments. It is based on the state-of-the-art technology both for the sensor and for the readout electronics. It is composed of 8 rectangular monolithic arrays of SDDs, with a total sensitive area of 570 mm^2. It is specially designed from the XAFS beamline scientists' requests and optimized to work in an energy range of 3-30 keV.

The detection system, shown schematically in Figure 1, is a modular system consisting of eight planes arranged in an aluminum case

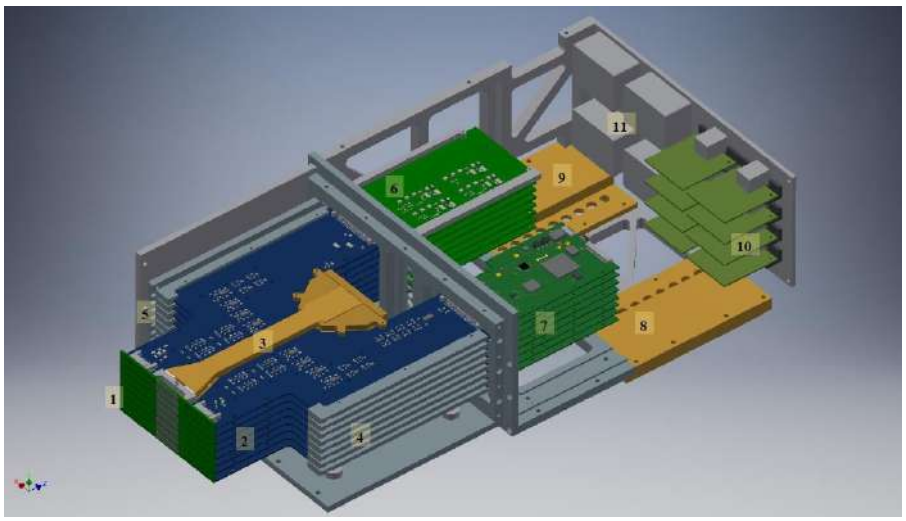

Figure 1: Detector system: (1) detectors and detector PCBs, (2) front-end PCBs, (3) brass profile with cooling liquid flowing inside, (4) insertion guides at flanks of detecting heads, (5) rails for eight detection heads, (6) power supply and filters PCBs, (7) back-end PCBs, (8) inlet cooling distribution, (9) outlet cooling distribution, (10) ethernet PCBs, (11) power supply connectors

Figure 2: Upper, front and right side of the detector system

135

Figure 3: Upper, back and left side of the detector system.

3 Applications

FICUS, after a preliminary selection of measurement parameters, performs the following tasks: data alignment of the cells, energy calibration, selection of the Region Of Interest (ROI). For example, during the measurement it is possible to obtain a spectrum in real time with some information such as FWMH and peak centroid (in ADC channels and in eV), count rate and dead time.

4 Cables and Connections

4.1 PC - Instrument

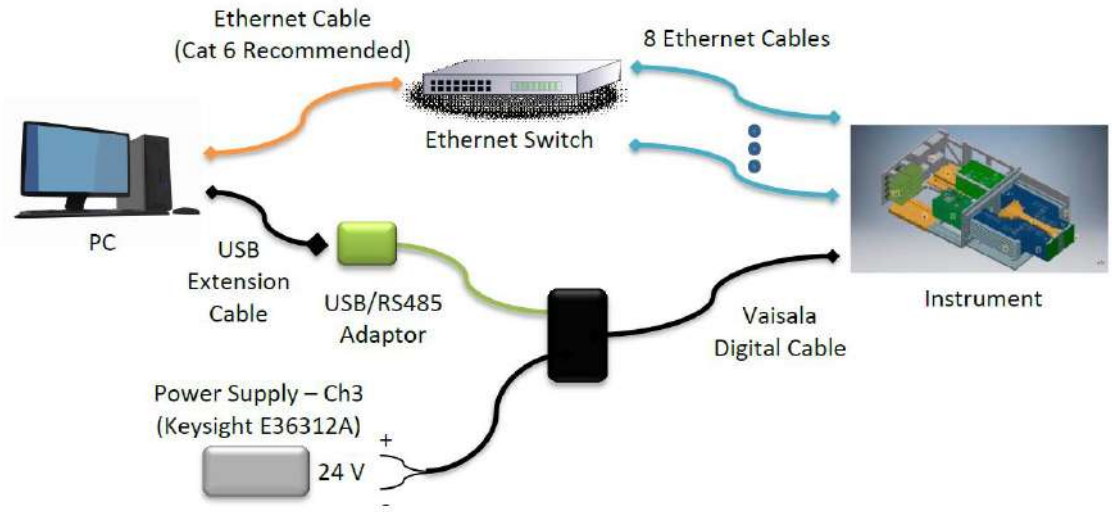

Figure 4: Diagram of the connections between the PC and the instrument

136

4.2 Power Supply - Instrument

4.2.1 HV Biasing

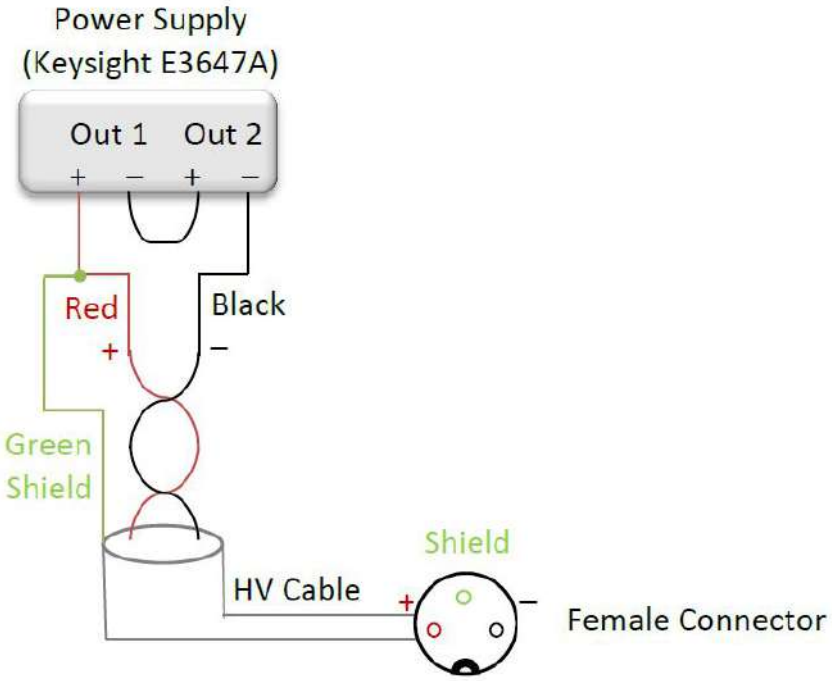

Figure 5: Diagram of the connections between the HV power supply and the instrument

4.2.2 Analogue PS Cable

Pin	Description
A	Unused*
B	−7.5 V Boards 1/2
C	+5 V Boards 1/2
D	Unused*
E	+5 V Boards 7/8
F	−7.5 V Boards 7/8
G	Shield
H	−7.5 V Boards 5/6
J	+5 V Boards 5/6
K	Unused*
L	+5 V Boards 3/4
M	−7.5 V Boards 3/4
N	Ground 3/4
P	Ground 1/2
R	Unused*
S	Ground 7/8
T	Ground 5/6
U	Unused*
V	Shield

ITT Cannon Trident
19-Pin Female Connector

Outside View

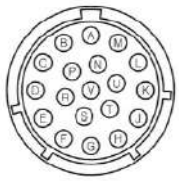

* Unused holes must be left empty (no pin inserted)

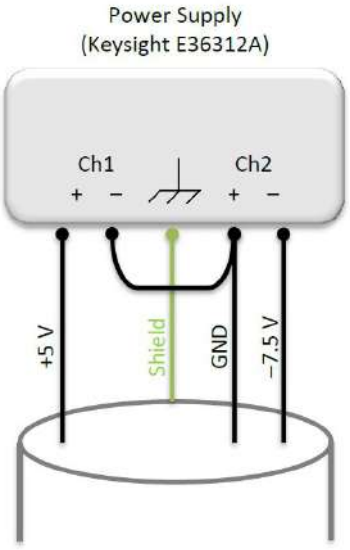

Figure 6: Diagram of the connections between the Analog power supply and the instrument

4.2.3 Back-End PS Cable

Pin	Description
A	+ Board 5
B	– Board 6
C	+ Board 7
D	– Board 7
E	+ Board 8
F	– Board 8
G	+ Board 1
H	– Board 2
J	+ Board 3
K	– Board 3
L	+ Board 4
M	– Board 4
N	– Board 5
P	+ Board 6
R	Unused*
S	– Board 1
T	+ Board 2
U	Unused*
V	Unused*

ITT Cannon Trident
19-Pin Female Connector

Outside View

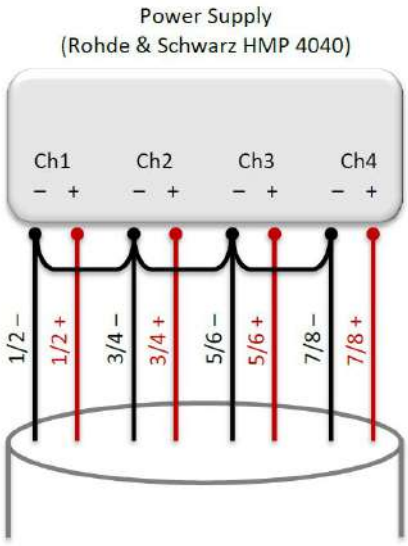

* Unused holes must be left empty (no pin inserted)

Figure 7: Diagram of the connections between the Digital power supply and the instrument

4.2.4 Peltier PS Cable

Pin	Description
A	+ Board 5
B	– Board 6
C	+ Board 7
D	– Board 7
E	+ Board 8
F	– Board 8
G	+ Board 1
H	– Board 2
J	+ Board 3
K	– Board 3
L	+ Board 4
M	– Board 4
N	– Board 5
P	+ Board 6
R	Unused*
S	– Board 1
T	+ Board 2
U	Unused*
V	Unused*

ITT Cannon Trident
19-Pin Female Connector

Outside View

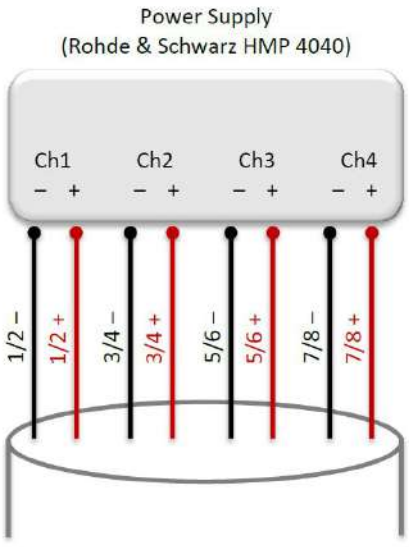

* Unused holes must be left empty (no pin inserted)

Figure 8: Diagram of the connections between the Peltier Cells power supply and the instrument

138
5 Specifications

E3647A HV power supply:
RS232 Interface (Ethernet, maybe, in the future)
There are two output channels: OUT1 and OUT2
It is possible Enable/disable output
For each of the two output channels, implement the following:
- Set maximum current on OUT1 and OUT2 to 1 mA
- Set voltage of OUT1 to 60 V (Ramp up and ramp down)
- Set voltage of OUT2 to 60 V (Ramp up and ramp down)
- Ramp up: gradually set voltages of OUT1 from 0 V to 60 V in steps of 5 V per second and after set voltages of OUT2 from 0 V to 60 V in steps of 5 V per second
- Ramp down: gradually set voltages of OUT2 from 60 V to 0 V in steps of 5 V per second and after set voltages of OUT1 from 60 V to 0 V in steps of 5 V per second
Lock/unlock instrument to protect system from accidental manual operation (if available)

E36312A Analog power supply:
Ethernet Interface
There are three output channels: OUT1 (yellow), OUT 2 (green) and OUT3 (blue)
For each of the three output channels, implement the following:
- enable/disable output OUT1, OUT2, OUT3
- Set maximum current on OUT1 to 1500 mA
- Set maximum current on OUT2 to 30 mA
- Set maximum current on OUT3 to 10 mA
- Set voltage of OUT1 to 5 V
- Set voltage of OUT2 to 7.5 V
- Set voltage of OUT3 to 24 V
- OVP (Over Voltage Protection) for each output channel: setted voltage +0.2 V
Lock/unlock instrument to protect system from accidental manual operation (if available)

HMP4040 Digital power supply:
Ethernet Interface
There are four output channels: CH1, CH2, CH3, and CH4
For each of the output output channels, implement the following:
- Enable/disable output (corresponds to OUTPUT button)
- Enable/disable output CH1, CH2, CH3, CH4
- Set maximum current on CH1 to 4.5 A
- Set maximum current on CH2 to 4.5 A
- Set maximum current on CH3 to 4.5 A
- Set maximum current on CH4 to 4.5 A
- Set voltage of CH1 to 4.5 V
- Set voltage of CH2 to 4.5 V
- Set voltage of CH3 to 4.5 V
- Set voltage of CH4 to 4.5 V
- OVP (Over Voltage Protection) for each output channel: setted voltage +0.2 V
Lock/unlock instrument to protect system from accidental manual operation

HMP4040 Peltier Cells power supply:
Ethernet Interface
There are four output channels: CH1, CH2, CH3, and CH4

139

For each of the output output channels, implement the following:
- Enable/disable output (corresponds to OUTPUT button)
- Enable/disable output CH1, CH2, CH3, CH4
- Set maximum current on CH1 to 3.0 A
- Set maximum current on CH2 to 3.0 A
- Set maximum current on CH3 to 3.0 A
- Set maximum current on CH4 to 3.0 A
- Set voltage of CH1 to 2.0 V (Ramp up and ramp down)
- Set voltage of CH2 to 2.0 V (Ramp up and ramp down)
- Set voltage of CH3 to 2.0 V (Ramp up and ramp down)
- Set voltage of CH4 to 2.0 V (Ramp up and ramp down)
- OVP (Over Voltage Protection) for each output channel: setted voltage +0.2 V
- Ramp up: gradually set voltages of each CH at the same time from 0 V to 2 V in steps of 0.1 V every 2 minutes
- Ramp down: gradually set voltages of each CH at the same time from 2 V to 0 V in steps of 0.1 V every 2 minutes
Lock/unlock instrument to protect system from accidental manual operation

6 Software

Following the beamline requirements, a custom software developed in LabVIEW for data acquisition and instrument management, FICUS (Fluorescence Instrumentation Control Universal Software), was specifically designed.

FICUS is a software designed to act on different levels: each level corresponds to a different subject who uses it and, consequently, a different choice of options available. In particular, three levels are available:

- **Detector Expert**: dedicated to detector and software developers, allows the maximum degree of variation of the available parameters and the display of screens useful for development and debugging;
- **Beamline Staff**: dedicated to the staff of the beamline, allows an intermediate degree of variation of the parameters for the setting and the measurement;
- **User**: dedicated to all possibile users of the beamline, allows a low degree of parameter variation but allows for data collection and pre-analysis.

For further details please see the *FICUS software manual for the SESAME-XAFS Detector System.*

7 Technical specification

7.1 Services instruments

The detector system also includes[1]:

1. Power supply Keysight E3647A [HV power supply]
   https://literature.cdn.keysight.com/litweb/pdf/5968-7355EN.pdf
2. Power supply Keysight E36312A [Analog power supply]
   https://literature.cdn.keysight.com/litweb/pdf/5992-2124EN.pdf
3. Power supply Rohde & Scwartz HMP4040 [Digital and Peltier Cells power supply]
   https://www.rohde-schwarz.com/it/prodotto/hmp4000-pagina-iniziale-del-prodotto_63493-47360.html?rusprivacypolicy=0
4. Cooling system chiller Lauda MC350 [Chiller]
   https://www.lauda.de/pimimport/assets/context/pdmarticle/85/8576/8576/attachments/Export.8576.2018-10-11-16-45-11.a8c336d7.pdf
5. Fluid cooling system Lauda Aqua 90 10 litre
   https://www.lauda.de/en/constant-temperature-equipment/heat-transfer-liquids/product/Aqua-90.html
6. PC Dell 3620 with lcd monitor
   https://www.dell.com/support/article/it/it/itdhs1/sln305332/guida-dell-system-precision-tower-3620?lang=eng
7. Aruba 2530-8G-PoE+Switch (j9774A) [Switch ethernet]
   https://www.arubanetworks.com/assets/ds/DS_2530SwitchSeries.pdf
8. Accessories: water tubes
   https://docs.rs-online.com/dd4f/0900766b8157a402.pdf
9. Accessories: ethernet cables

[1]The instrument name that is used within the instructions is indicated in square brackets.

141

8 Dimensions

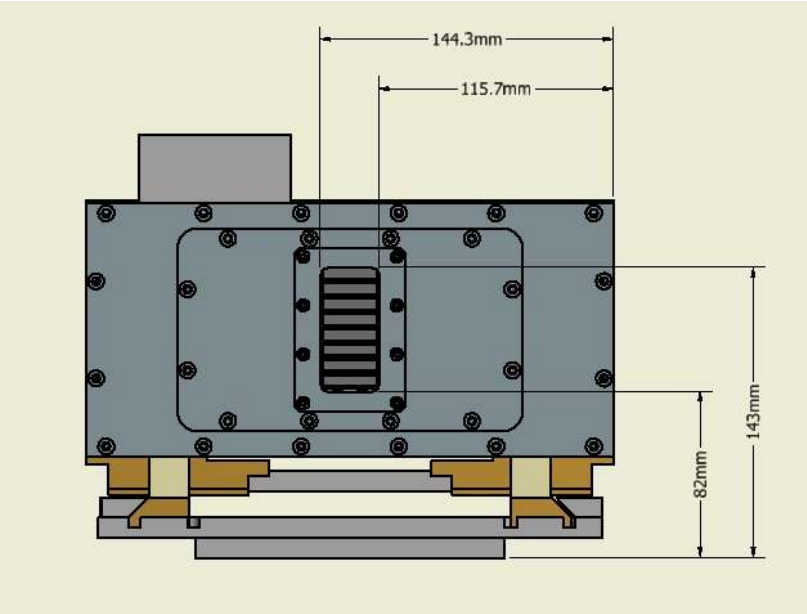

Figure 9: Front side of the detector system

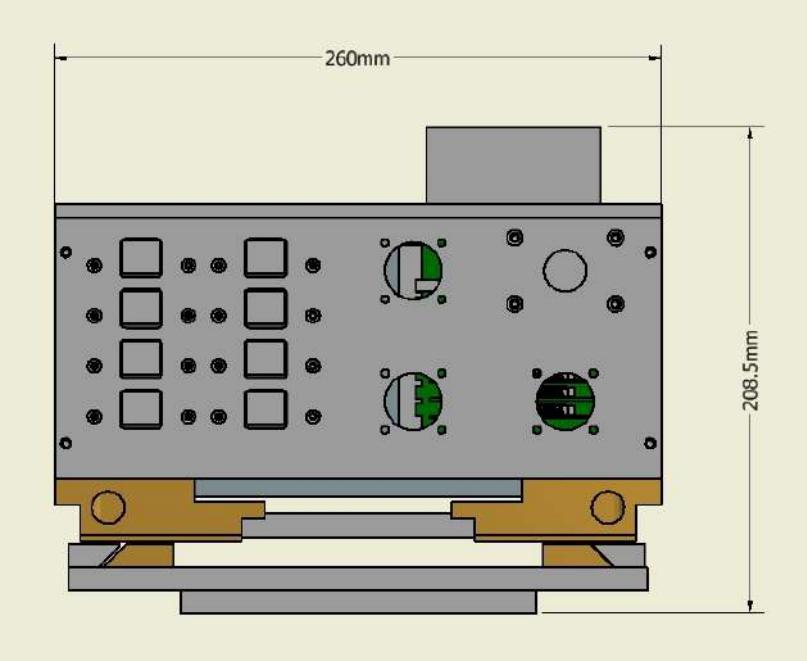

Figure 10: Back side of the detector system

142

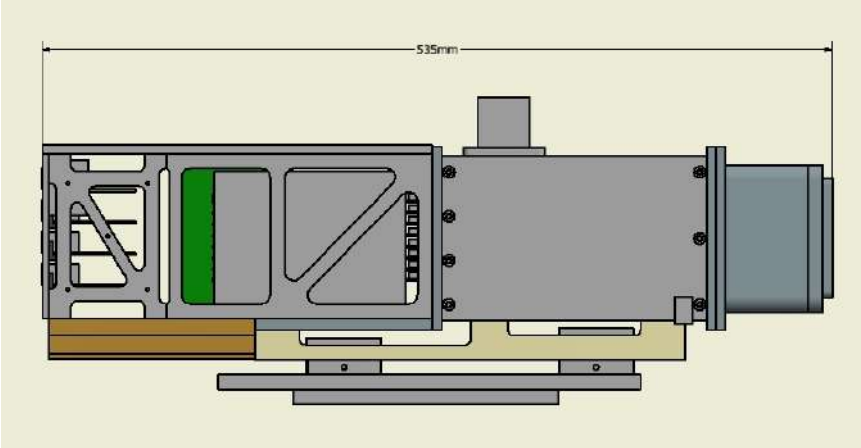

Figure 11: Right side of the detector system

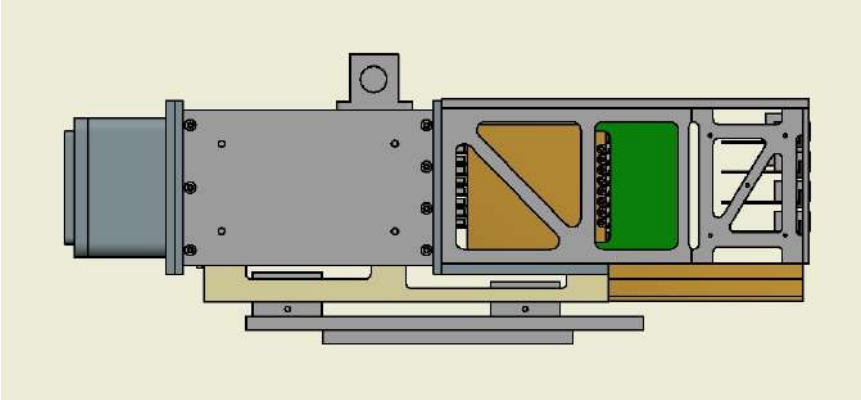

Figure 12: Left side of the detector system

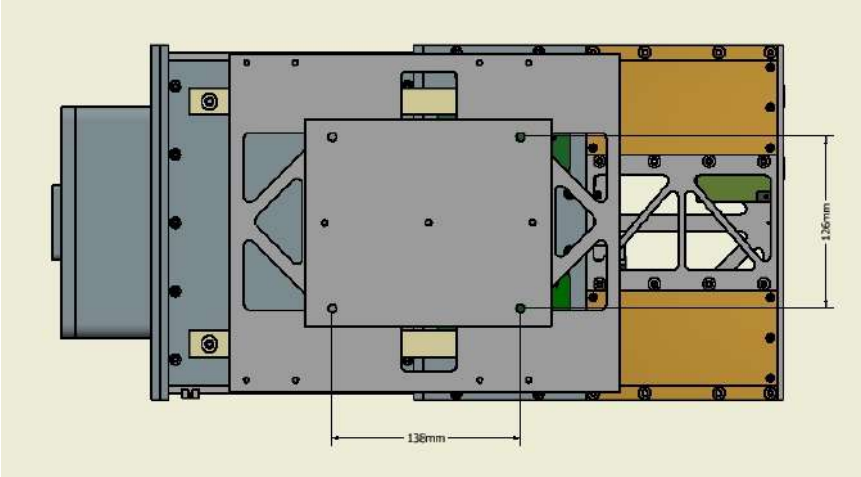

Figure 13: Down side of the detector system

143

9 Safety warnings for using the SESAME-XAFS Detector System

To use the SESAME-XAFS detector system correctly and avoid damaging the measuring system, you must carefully follow the on/off instructions and the software user's guide. It's very important:

- Never switch the HV power supply off and/or on suddenly: it is important gradually increase or decrease the voltage
- Never switch the Peltier cells power supply off and/or on suddenly: it is important gradually increase or decrease the voltage
- If the ambient and system temperatures change, it may be necessary to repeat the procedure for loading the appropriate settings, aligning the cells and calibrating the detector
- Make sure that the holes for the nitrogen/dry air vent are not obstructed
- Make sure that when the flushing is switched on (with appropriate flow rate) the window just swells up

9.1 Instructions for switching on

It is very important to follow the switch-on procedure following the steps in order and precisely.

- Turn on the PC
- Start flushing nitrogen / dry air [maximum flow rate of 2 liter/minute - **WARNING**: A higher flow rate would damage the inlet window and risk irreparably damaging the sensors]
- Turn on the power supply of the dew point temperature sensor [ch3 - analog power supply]
- Launch FICUS software
- Check that the dew point temperature is below 16 °C
  - Only if it is so, activate temperature stabilization and turn on the chiller set to 18 °C
  - If it is not so, wait for the dew point temperature to drop below this value thanks to the flushing
- Switch on the digital power supply [all ch1, ch2, ch3, ch4 together]
- Switch on the analog power supply [ch1 and ch2 of analog power supply]
- From FICUS software connect the detector system
- From FICUS software load the appropriate settings according to the condition and temperature of use (possible choice of 8 global setups)
- Switch on the HV power supply (setting recall mode1), gradually increase the voltage from 0 V to 60 V on ch1 and then from 0 V to 60 V on ch2
- Wait about 5 minutes for the temperature of the detector to stabilize
- Proceed with cell alignment (o load a previously saved alignment setting)
- Now it is possible activate measurement

144

- After stop the measurement, proceed with the calibration of the detector system (o load a previously saved calibration)
- If you want work in cooling mode (to lower cell temperature), start the instruction for cooling mode

9.2 Instructions for switching off

It is very important to follow the switch-off procedure following the steps in order and precisely.

- Gradually decrease the voltage from 60 V to 0 V on ch2 and then from 60 V to 0 V on ch1, and after switch off the HV power supply
- In FICUS close the acquisition window and disconnect the detector
- Switch off analog power [ch1 and ch2 analog power]
- Switch off the digital power supply [all ch1, ch2, ch3, ch4 together]
- Turn off FICUS software
- Turn off flushing nitrogen / dry air
- For long detector shutdown or if it is necessary, switch off the dew point temperature meter power supply [ch3 - analog power supply] and turn off the chiller
- Turn off the PC

9.3 Instructions for cooling mode

- Before starting the Peltier cell ignition procedure, check that the dew point temperature is below $-12\,^{\circ}\mathrm{C}$
- Never switch the Peltier cells power supply off and/or on suddenly: it is important gradually increase or decrease the voltage
- Switching on and off of the Peltier cells have to be gradual: power supply for 0.1 V steps every 2 min (maximum voltage 2 V)
- When the supply voltage of Peltier cells is 2 V, wait at least 5 minutes for the temperature of the detector to stabilize
- When the cooling mode is activated, remember to load the appropriate global settings [Tcool] in FICUS

10 Troubleshooting

In this section some possible errors or problems that may occur, along with how to fix them. **If the problem is not listed, please contact the ReDSoX Collaboration.**

- **TCP-IP or/and FPGA tests aren't successful for one or more strips** - There may be problems with FPGAs or communication boards. Try turning off the system (following the switch-off instructions) and, following the switch-on instructions, try switch it on again from the beginning.

145

- **One or more channels pass from active and functioning to non-active for no apparent reason** - There may be problems with FPGAs or communication boards. Try turning off the system (following the switch-off instructions) and, following the switch-on instructions, try switch it on again from the beginning. If the problem is not solved, try again the shutdown procedure by exiting the software and restarting the PC. And then reactivate everything by following the switch-on procedure. If the problem is not solved even in this way, contact the ReDSoX Collaboration.
- **One or more temperature values have abnormal and different values than normal, or are equal to zero** - Check that the chiller is on and set to the correct value. Try turning off the system (following the switch-off instructions) and, following the switch-on instructions, after a few minutes, try switch it on again from the beginning.
- **The value of the dew point temperature does not decrease with the nitrogen / dry air fluxing** - Check that the nitrogen/dry air flow is active and at the values recommended by the manual. Check that the window is intact and well stretched.
- **The sum signal of the channels appears deformed** - Try realigning the channels.
- **One or more power supplies do not turn on** - Check the correct connection of the power supply to the electric grid.

11 Information & Contact - ReDSoX Collaboration

The SESAME-XAFS detector system implementation is managed by the Istituto Nazionale di Fisica Nucleare (INFN) in collaboration with Elettra Sincrotrone Trieste, within the ReDSoX (Research Drift detectors for Soft X-ray) collaboration by INFN and Elettra (and other entities listed below in alphabetical order) thanks to ad hoc financing from the Ministry of Education, University and Research (MIUR).

In particular, this work has been made within the ReDSoX-2 INFN research project, supported with the contribution of the Italian Ministry of Education, University and Research within the EUROFEL Project and FBK-INFN agreement 2015-03-06.

146

FICUS software manual for the SESAME-XAFS Detector System

Contents

1 Overview

Following the beamline requirements, a custom software developed in LabVIEW for data acquisition and instrument management, FICUS (Fluorescence Instrumentation Control Universal Software), was specifically designed.

Figure 1: FICUS - Fluorescence Instrumentation Control Universal Software

147

2 Description

FICUS is a software designed to act on different levels: each level corresponds to a different subject who uses it and, consequently, a different choice of options available. In particular, three levels are available:

- **Detector Expert**: dedicated to detector and software developers, allows the maximum degree of variation of the available parameters and the display of screens useful for development and debugging;
- **Beamline Staff**: dedicated to the staff of the beamline, allows an intermediate degree of variation of the parameters for the setting and the measurement;
- **User**: dedicated to all possible users of the beamline, allows a low degree of parameter variation but allows for data collection and pre-analysis.

3 Applications

FICUS, after a preliminary selection of measurement parameters, performs the following tasks: data alignment of the cells, energy calibration, selection of the Region Of Interest (ROI). For example, during the measurement it is possible to obtain a spectrum in real time with some information such as FWMH and peak centroid (in ADC channels and in eV), count rate and dead time.

148

4 Guide for Detector Expert

Before starting any activity, please take a look at the **Safety warnings for using the SESAME-XAFS Detector System**, on page 52, and the **Instructions for switching on/off**, respectively on page 52 and 53.

This version of the software is recommended only for developers of the detector system in order to perform extensive testing and optimize performance.

After the launch of FICUS software, following the instructions recommended in this manual for switching on the detector system, the first window is the one shown in Fig. 2.

Figure 2: The first window of FICUS software

In the **System Monitor window** it is possible to see the dew point temperature of the system, the time, the status of the detectors and the status of the TCP Remote Server (red disconnected - green connected).

After connect of the detector, it is also possible to click on *System monitor* to know:

- the log of the dew point temperature [in Fig. 3 (a)]
- the log of the temperature of the strips [in Fig. 5 (a)]
- the log of the temperature of the LDOs [in Fig. 5 (b)]
- the log of the temperature of the FPGAs [in Fig. 5 (c)]
- the log of the temperature of the ADCs [in Fig. 5 (d)]
- the table with all the last measured temperatures [in Fig. 3 (b)]

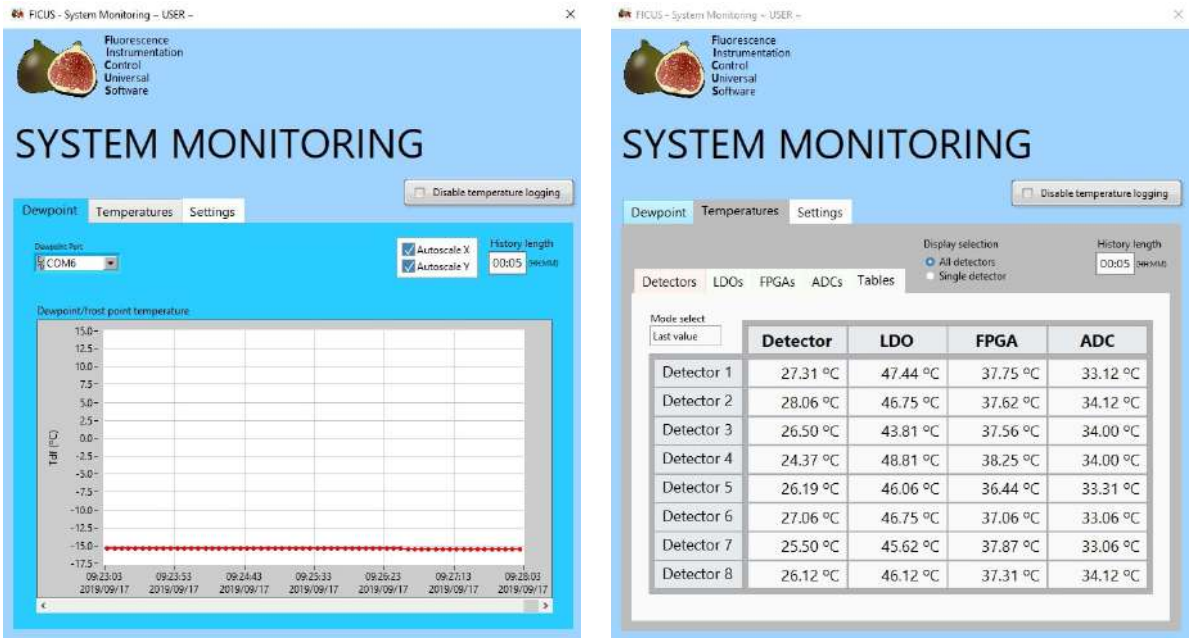

Figure 3: (**a**) The log of the dew point temperature. (**b**) the table with all the last measured temperatures (visible after connecting the detectors).

- the setting for measuring temperatures [in Fig. 4]

In the log it is possible to modify the time duration displayed and to set the extremes of the graph, or to set its auto setting.

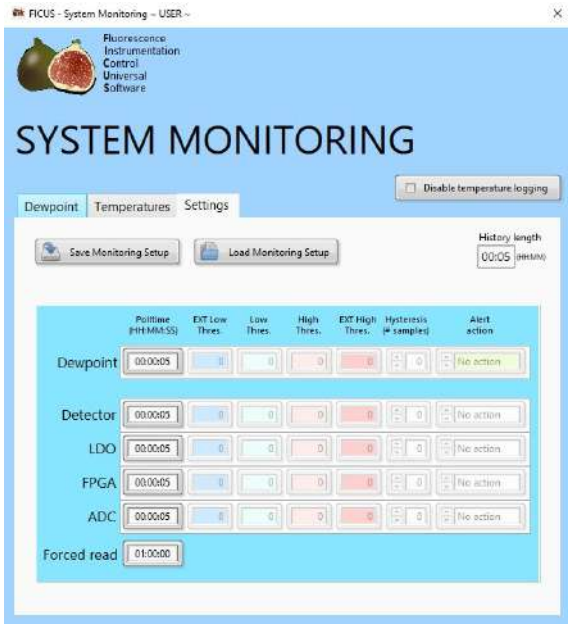

Figure 4: The setting for measuring temperatures.

150

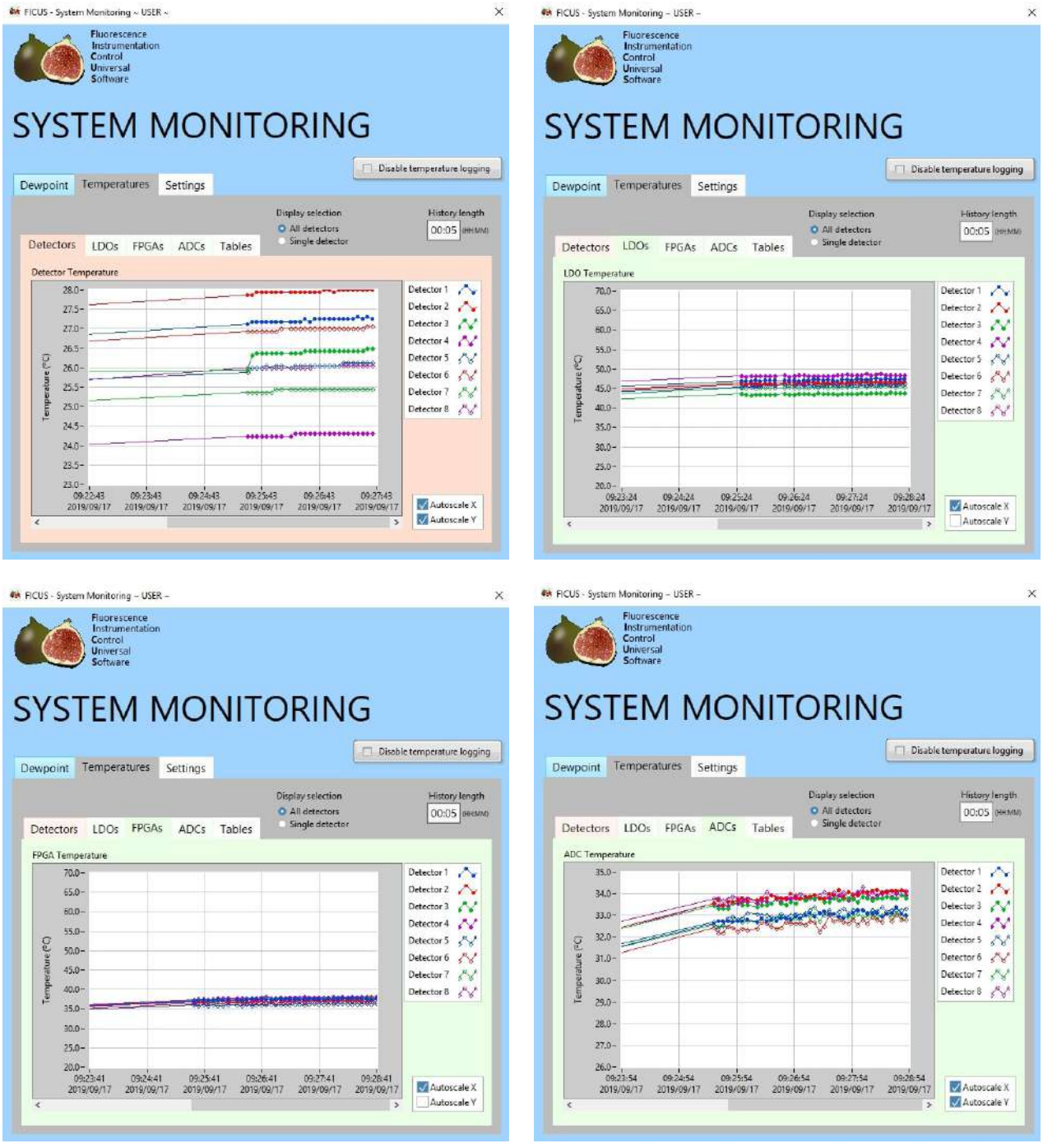

Figure 5: In clockwise direction starting from the top left (**a**) The log of the temperature of the strips (**b**) The log of the temperature of the LDOs (**c**) The log of the temperature of the FPGAs (**d**) the log of the temperature of the ASICs.

To connect the detector system click on *Connect* (in Fig. 2). The connection window in Fig. 6 (a) appears. Click on *Run TCP-IP and FPGA tests* and, if the test is successful, all the boxes will be colored green [Fig. 6 (b)] and you can proceed to the connection by clicking *OK*.

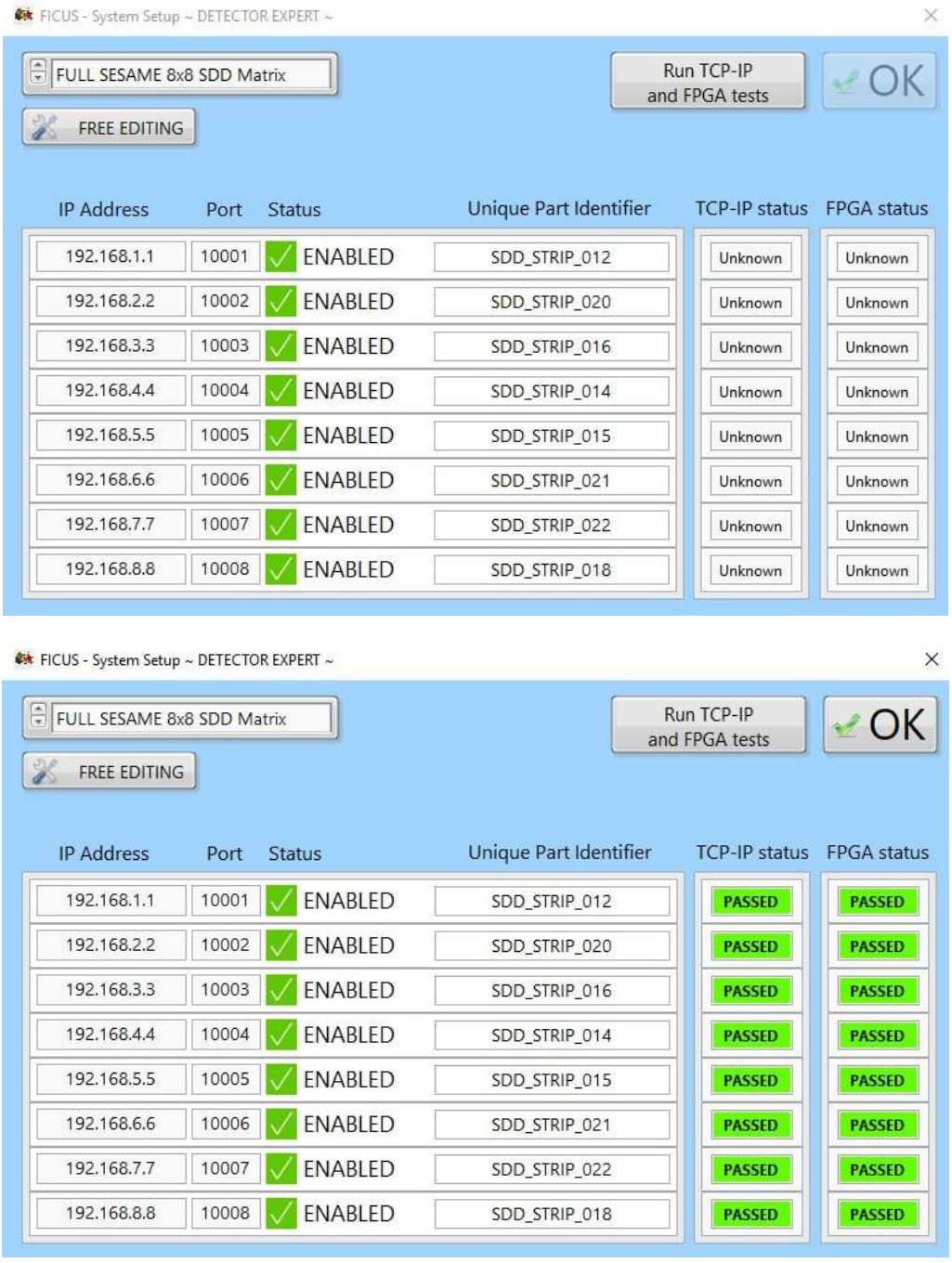

Figure 6: (**a**) The connection window - before connecting tests. (**b**) The connection window - after passing the connecting tests.

A message appears asking if you want to restore the previously used settings: press *OK* to proceed or *Cancel* to annul the setting restore [Fig. 7]. It is possible to see that the status of the detector has changed to CONNECTED.

The first window of the **FICUS settings** opens, in *Spectrum View* [Fig. 8]. Here, at the top from the left you can see the signals of the individual channels: 4 at a time (those highlighted in light green in the panel at the bottom left), and you can change which ones to select by clicking on the green arrows in the center on the right. In in the panel at the bottom left, in addition to the *Cell Status*, it is also possible to display the map of the *Enabled/Disabled* channels [Fig. 9 (a)], and

152

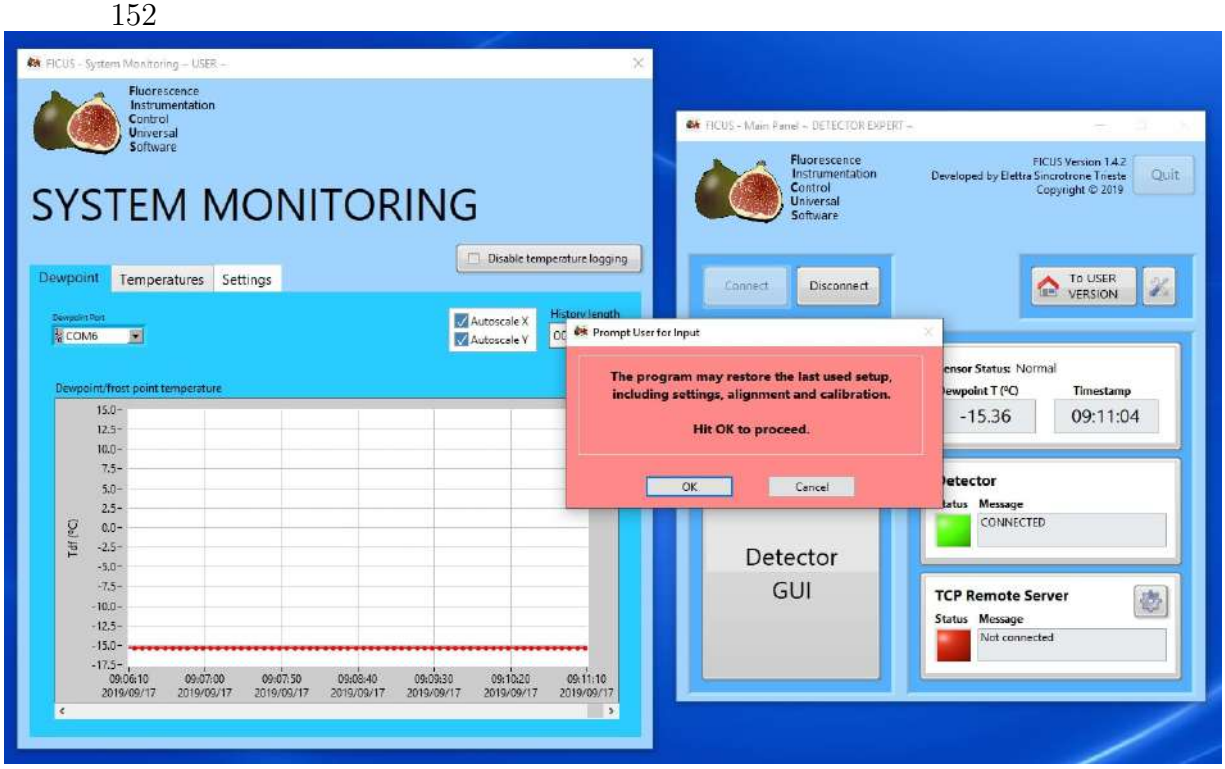

Figure 7: The final window for the connection.

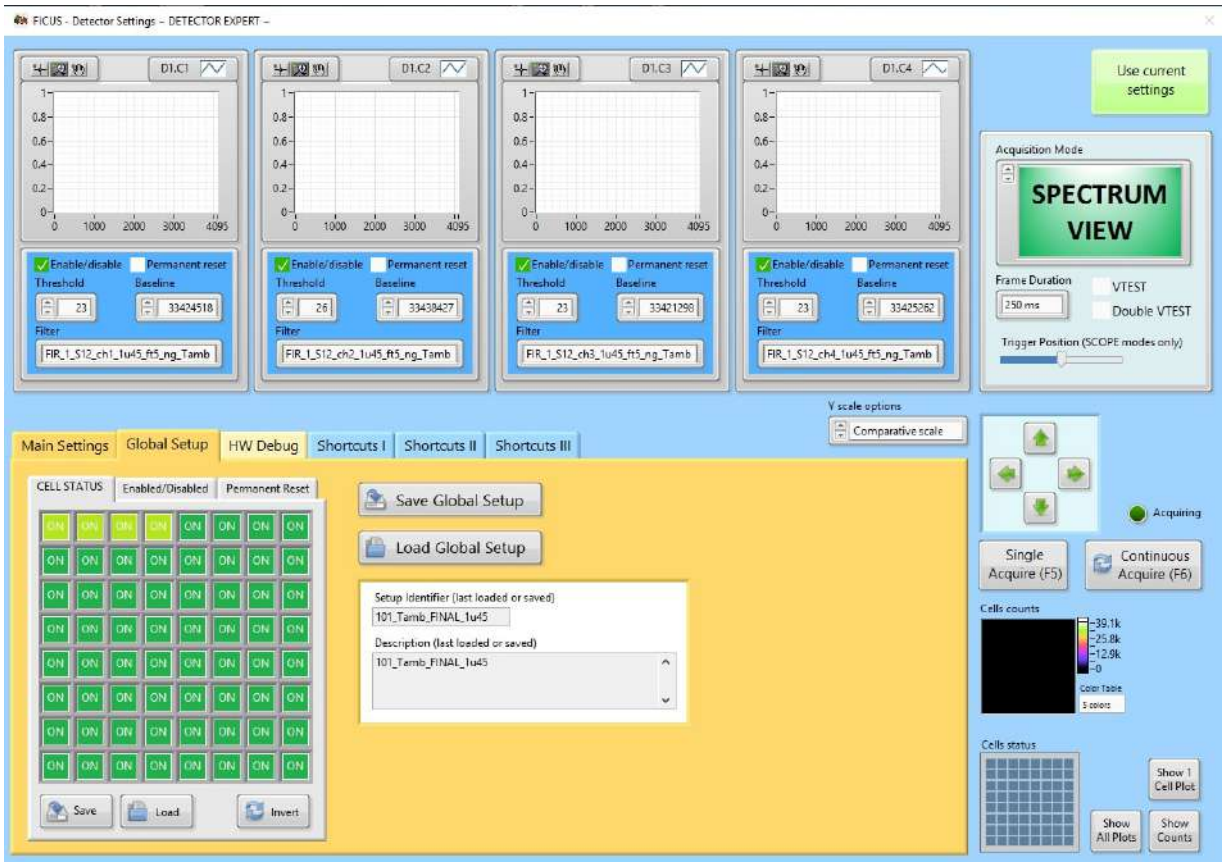

Figure 8: The first windows of the FICUS setting (with Global Setup).

the map of the channels in *Permanent Reset* [Fig. 9 (b)]. Within each box in the upper part, it is possible *Enable/disable* the channel, put the channel in *Permanent reset*, and manually set the *Threshold*, *Baseline* and *Filter*.

In the upper right corner, it is possible to enable and disable the test signals (*VTEST* and *Double VTEST*) and to select the *Frame Duration* (among the values: 5 ms, 7.5 ms, 10 ms, 25 ms, 50 ms, 75 ms, 100 ms, 250 ms, 500 ms, 750 ms, 1 s, 2.5 s, 5 s, 7.5 s, 10 s, and External Gate).
In the central part on the right there are buttons to activate the measurement: *Single Acquire (F5)* and *Continuous Acquire (F6)*, and a green dot indicating the acquisition in progress.
In the lower right part of the window there are: a graph with the Cells counts represented (with the graduated scale of colors next to it), one with the Cells status visible (where in grey it is an unavailable channel, in green an active and counting channel, in red an inactive and with error channel, in black a disabled channel, and in dark green an active and with no counts channel, placed in permanent reset). There are also three buttons (*Show 1 Cell Plot*, *Show All Plots*, *Show Counts*), which allow you to view respectively the detail of the signal of a channel [Fig. 11 (a)], the contemporary graph of all 64 channels [Fig. 10] and the counts of 64 channels [Fig. 11 (b)]. In this graphs it is possible to change X and Y scale of the histograms.

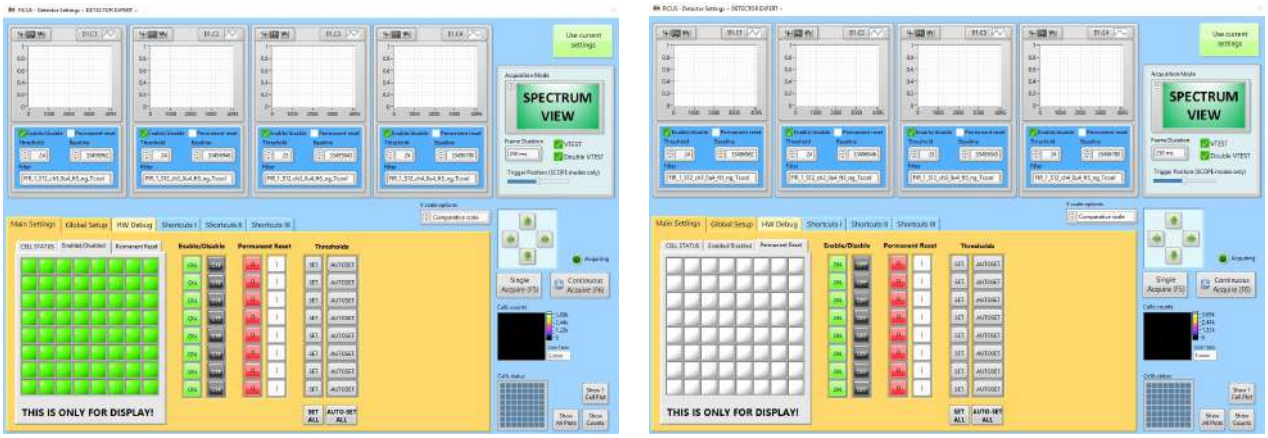

Figure 9: The windows of the FICUS setting, in Main Setting (**a**) Enabled/Disabled, and (**b**) Permanent Reset channels.

In the central part of the window, there is an additional menu that modifies the central part of the window by enabling further possible adjustments.
In *Global Setup* there is the possibility to save (assigning a name and notes) the current settings, with *Save Global Setup*, or to open settings already set and saved, with *Load Global Setup.* if you select the latter option in particular, a further window opens in which it is possible to choose from the 8 pre-set global setups: four different possible filter lengths (0.4, 0.7, 1, and 1.45 μs) at two possible cell temperatures (at room temperature, Tamb, and with cooled cells with voltage on the Peltier cells, Tcool) [Fig. 12 (a)]. After selecting the one you want, just click on *OK, load this setup*, and *Yes* at the next confirmation window that opens, as in Fig. 12 (b).

In *Main Setting* [Fig. 13] it is possible to *Enable/Disable* all the channels of one strip, put all the channels of one strip in *Permanent Reset*, and *Set* the *Threshold*, for each strip or for all strips at the same time, manually or in *Autoset*.

In *HW Debug* [Fig. 14] it is possible to see the *PART IDs* of every strips of the detector system and to *TEST* and *RESET*, if it necessary, for each strip or for all strips at the same time, the FPGAs.

In *Shortcuts I* [Fig. 15] it is visible the *MANAGE SETTING*. Here it is possible to *STORE*, *RECALL* and *APPLY* the current setting, for each strip or for all strips at the same time.

In *Shortcuts II* [Fig. 16] there are settings for the *Baselines* and for the *filters*; in particular, it is possible to *SET* the Baselines manually or in *Autoset* (based on the parameters provided in the I box), and upload the Filters, for each strip or for all strips at the same time.

In *Shortcuts I* [Fig. 17] it is possible to know the *ADC status* and the *RTD Table Filenames* for every strip. It is also possible to set the *Filter Binary Cut* and the *Reset Parameters*: *Trigger* (FIX/AUTO),

154

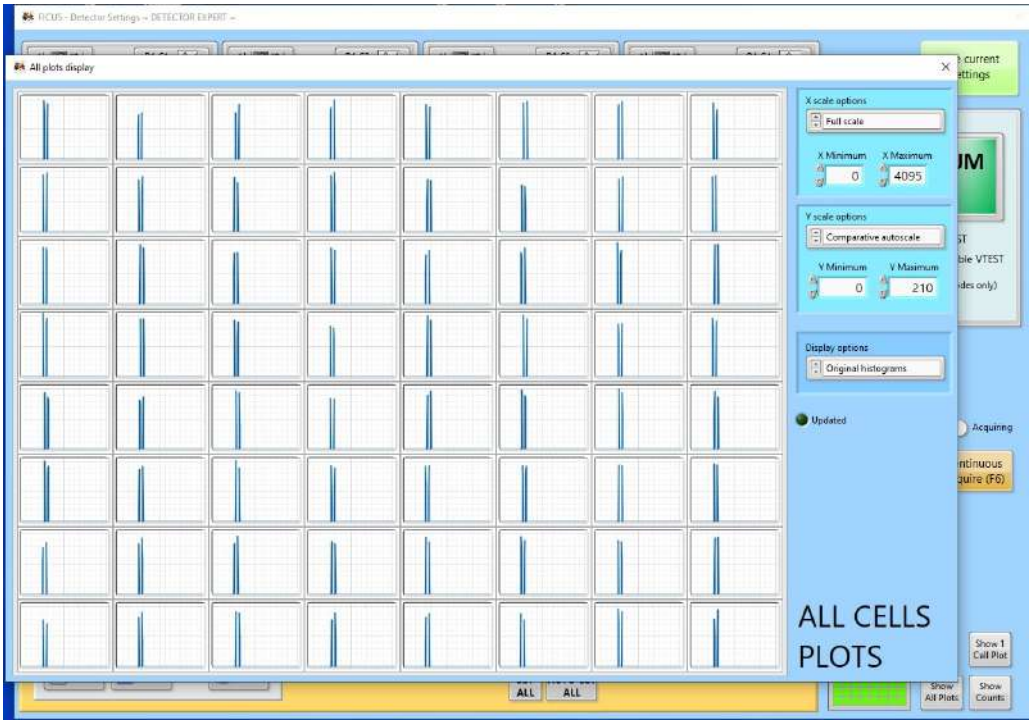

Figure 10: The windows of the FICUS with Show All Plots, with VTEST and Double VTEST enabled.

Frequency, *Width*, and *Delay*.

As it can be seen in Fig. 18, it is possible to change acquisition mode and switch from *Spectrum View* (used for normal acquisition) to *Scope View (RAW Data)* (used for RAW data acquisition), *Scope View (Filtered Data)* (used for acquisition of filtered RAW data), and *Scope View (Long Time)*.

When switching to *Scope View (RAW Data)* Acquisition Mode, the *Save rawdata* field appears in the middle of the page, through which you can set the duration of the raw acquisition, the file name and the save folder; during the acquisition, the Elapsed time after the end is indicated [Fig. 19].

When the settings are all set it is possible switch to acquisition window: to do so you have to return to the *Spectrum View Acquisition Mode* and click on the green button at the top right *Use current setting*. The FICUS acquisition window opens, which appears as in Fig. 20. To return to the settings just click on the *HW Setting* button.

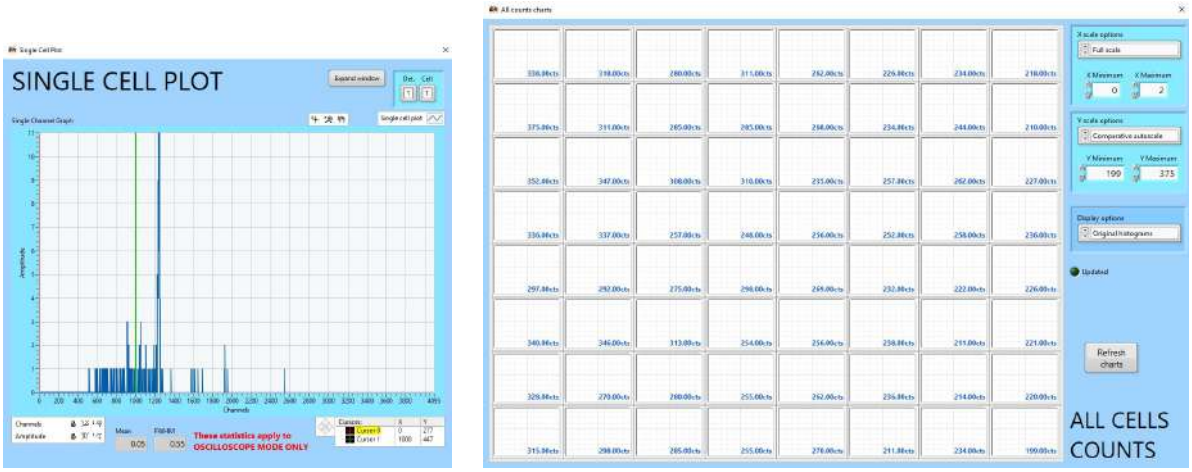

Figure 11: The windows of the FICUS with (**a**) Show 1 Cell Plot, and (**b**) Show Counts.

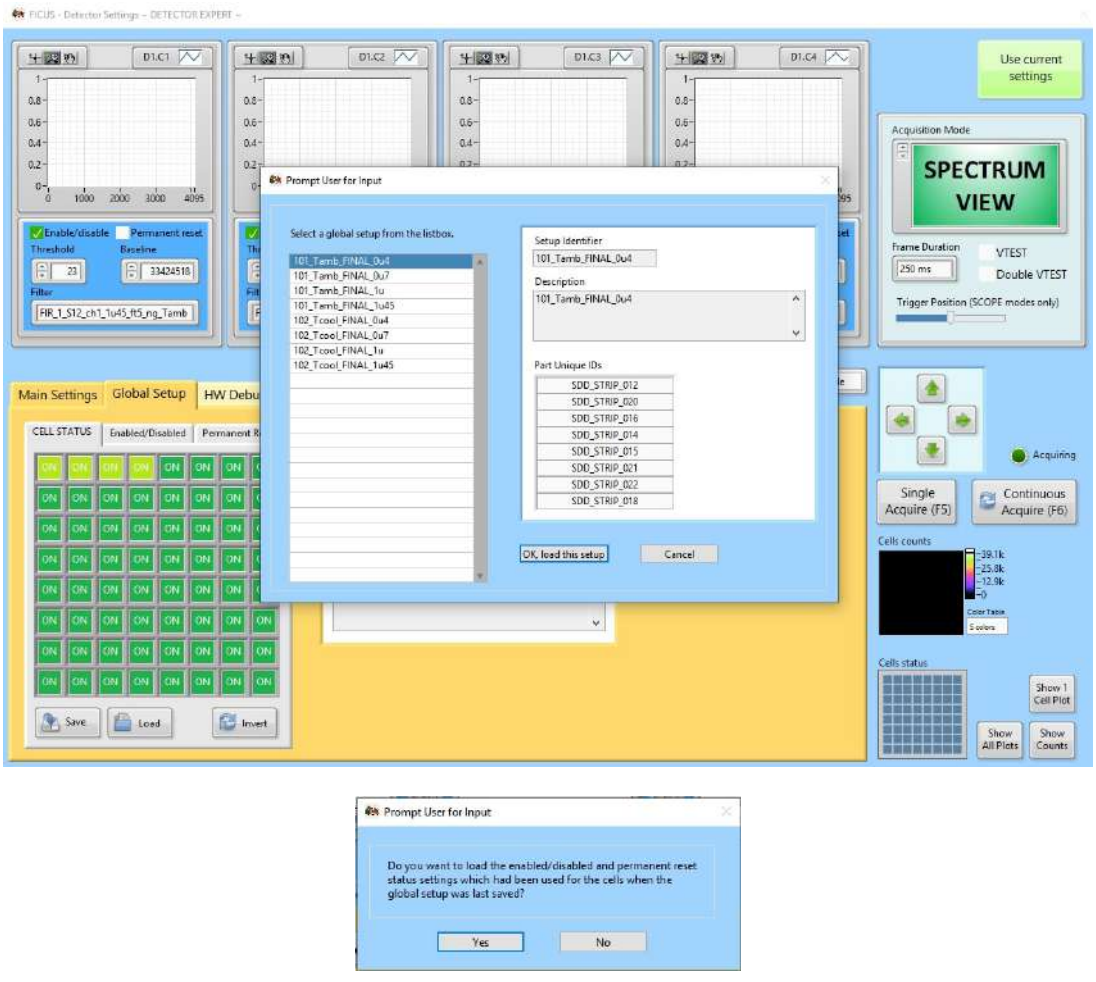

Figure 12: (**a**) The windows in which it is possible to choose from the 8 pre-set global setups, and (**b**) the confirmation window.

156

Figure 13: The windows of the FICUS setting (with Main Setting) in Spectrum View.

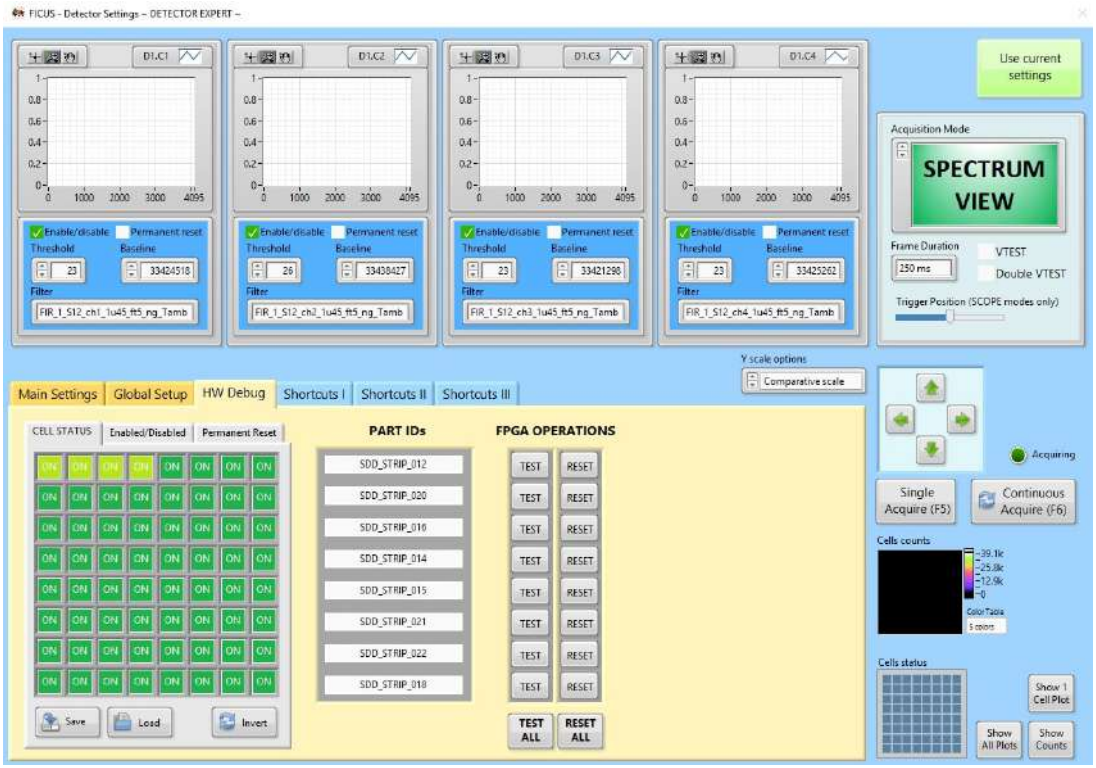

Figure 14: The windows of the FICUS setting (with HW Debug).

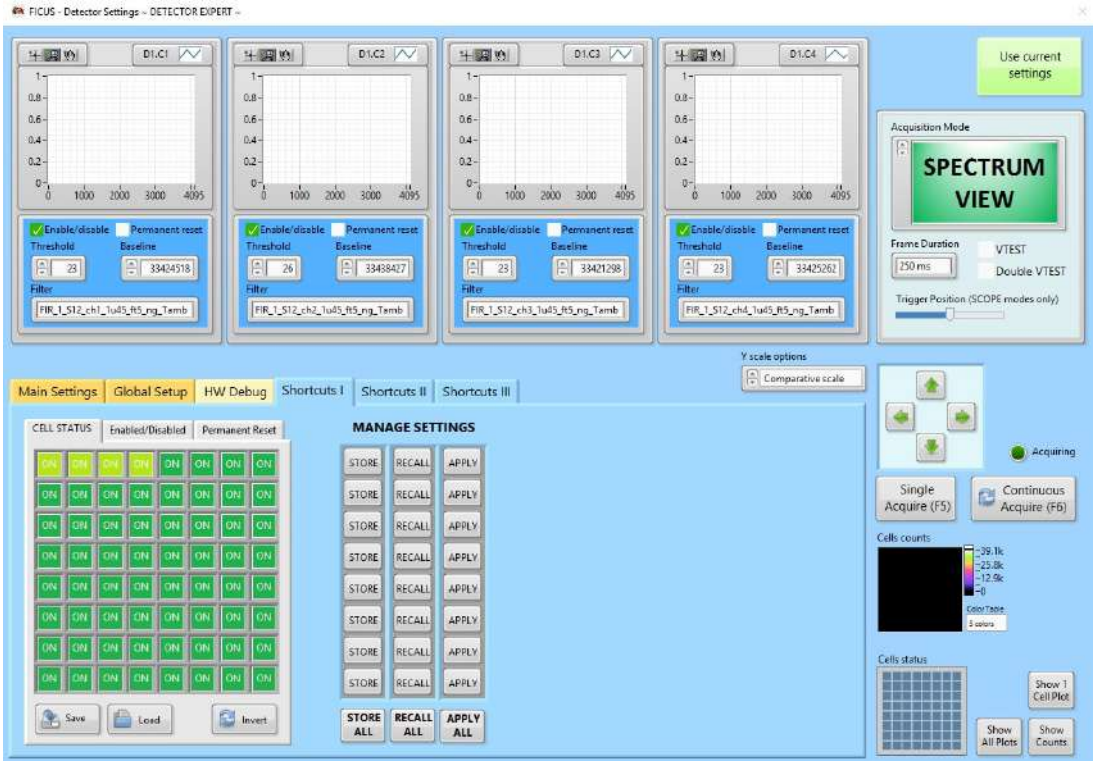

Figure 15: The windows of the FICUS setting (with Shortcuts I).

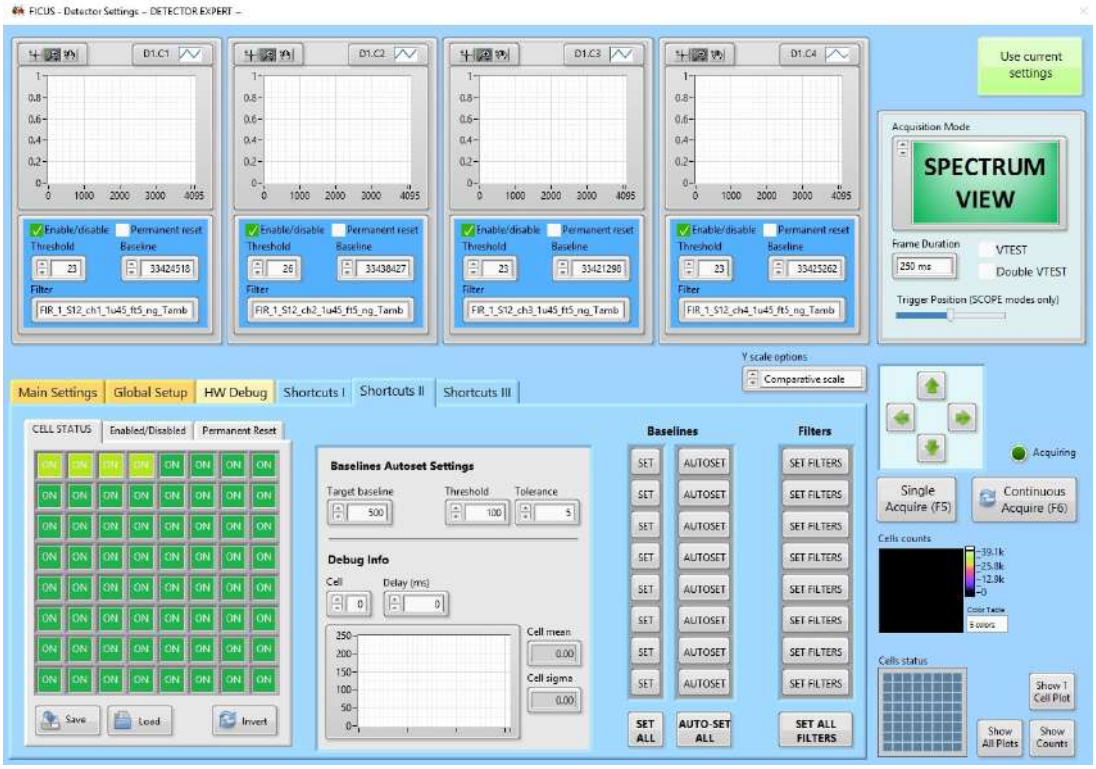

Figure 16: The windows of the FICUS setting (with Shortcuts II).

158

Figure 17: The windows of the FICUS setting (with Shortcuts III).

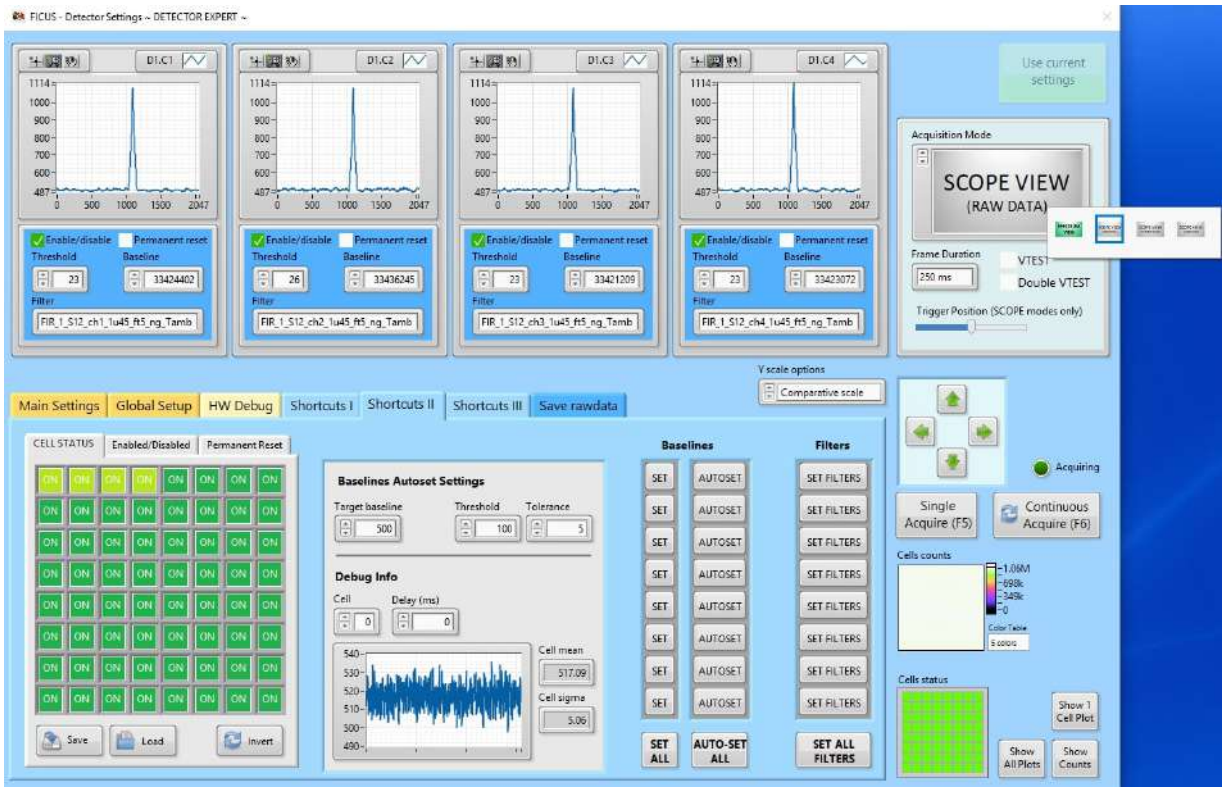

Figure 18: The windows of the FICUS setting (menu of Acquisition Mode).

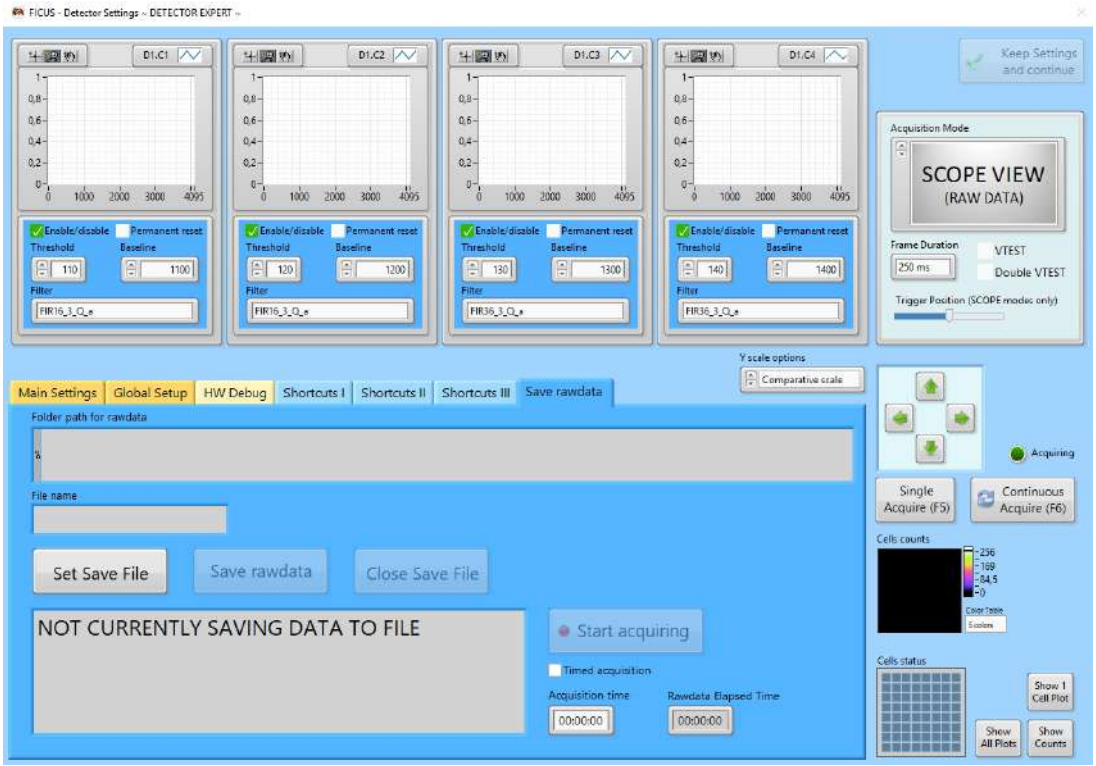

Figure 19: The windows of the FICUS setting (Scope View - rawdata).

160

Figure 20: The windows of the FICUS acquisition (Histogram), before alignment and starting the measurement.

The **FICUS acquisition window**, by clicking on the corresponding buttons in the upper right corner, it is possible to open the window of *System Monitor*, as shown in Figs. 3 - 4 - 5, and the *Diagnostic Info*, as shown in Figs. 21. The windows of Diagnostic Info are used to verify the correct functioning of the detector through detailed information regarding the status [Figs. 21 (a)], counts [Figs. 21 (b)], dead time [Figs. 21 (c)], and pile-up [Figs. 21 (d)] of all channels. From these windows (using the buttons in the upper part is *Show 1 Cell Plot* in Figs. 11 (a), *Show Counts* [Figs. 11 (b)], and *Show All Plots* [Figs. 22]) it is possible to have detailed information of the signal collected.

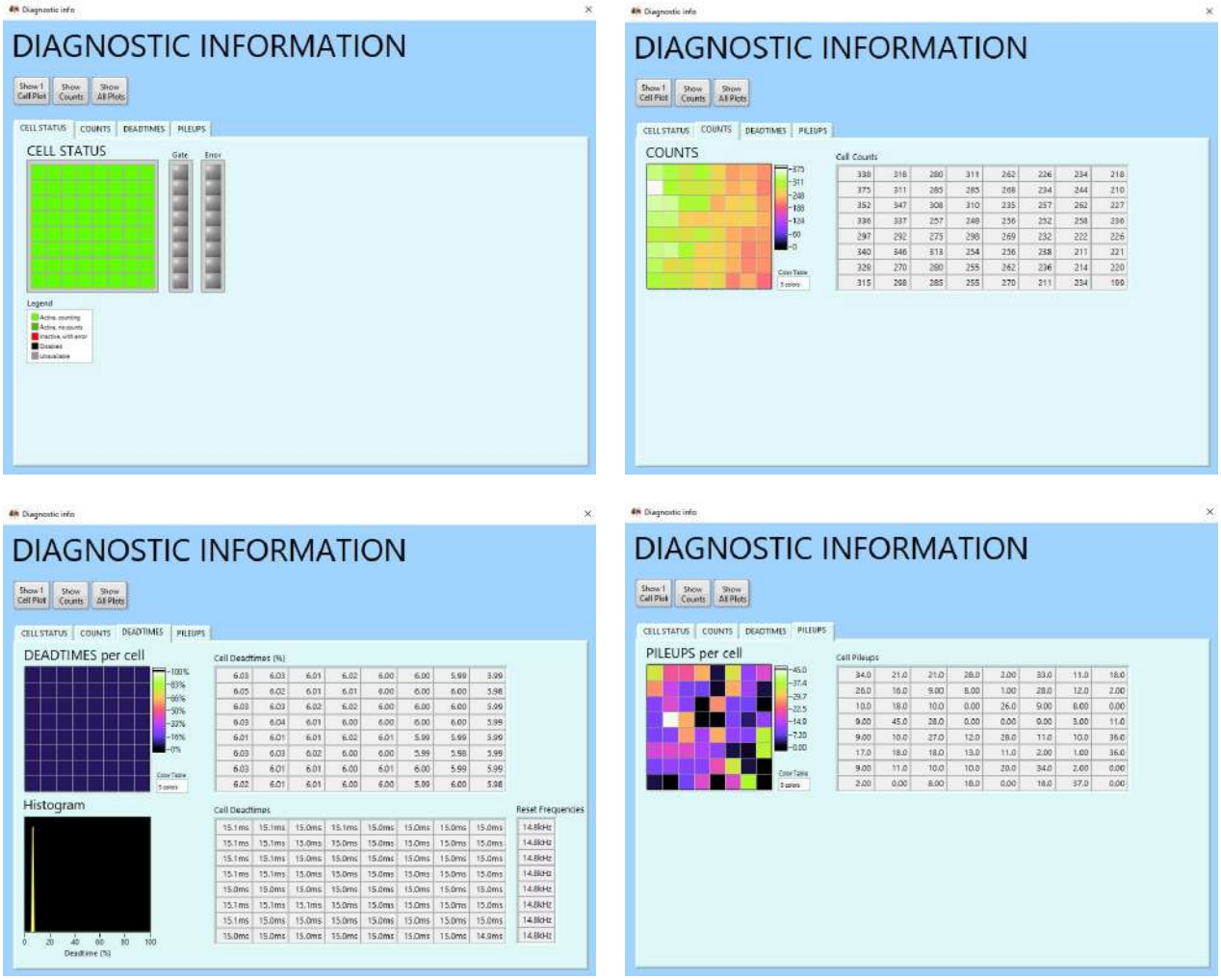

Figure 21: The windows of the FICUS Diagnostic Information (**a**) Cell Status, (**b**) Counts, (**c**) Deadtimes, (**d**) Pileups.

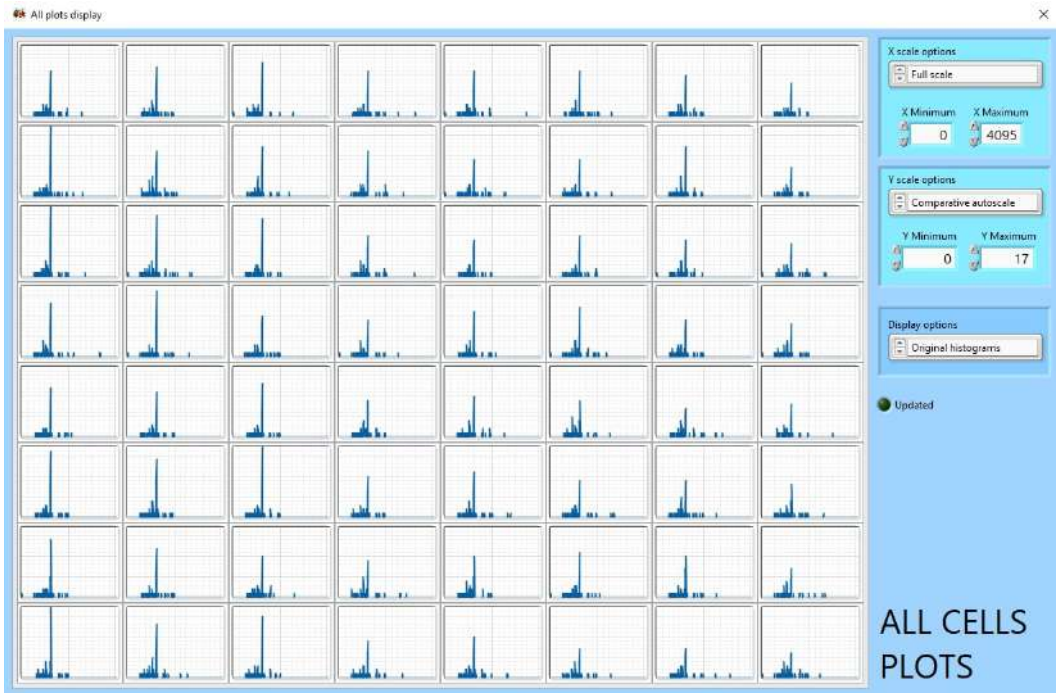

Figure 22: The windows of the FICUS with Show All Plot.

162

On the right of the FICUS acquisition window it is possible to know the count rate of the acquisition (in counts/s), an overview of information on the functioning of the cells and on the counts cell by cell. In addition, the TCP Remote Server connection information is also visible. Under this box, are visible the name and description of the Global Setup in use, and next to them there are buttons to open the *HW Setting*, *Alignment* and *Calibration* windows; next to each of them there is an indicator that has three possible aspects: *PASS* in green (which means that that setting was made), *WARNING* in yellow (which means that that setting has been done previously, but something has been changed since then and you may need to redo the setting), and *FAIL* in red (which means that that setting has never been done before and you need to do the setting).

Clicking on *Alignment* opens the window dedicated to it. The top and right parts of the **FICUS Alignment window** are always the same; through the mid-page menu it is possible to change the bottom-left part of the window. In the Alignment window, from the Figs. 23 to the Fig. 26, in the alignment window there is the possibility to load a pre-saved alignment (by clicking on *Load from file...*), to align the channels starting from a new acquisition (by starting the acquisition with the *Start/Stop acquiring* button) or to align the channels starting from saved data (by using the *Original data, load from file...* top left button).

On the right side, starting from the top, it is possible to select manually manually, indicating the detector (*Det.*) and cell (*Cell*), the channel with respect to which to align the others or select the box *Autoselect Cell* for automatic alignment (in which the software, using the chosen criterion, chooses the most appropriate box with respect to which to align the channels); in the graph, on which it is impossible to act, the channels with respect to which the system is aligning are displayed. To align is necessary to choose the *Alignment Parameters*: *Peak Reject* (selects only the peaks with the minimum required height compared to the highest), *Peak Width* (selects only the peaks with minimum required width), and the *number of Peak to Use*. Below it is possible, after starting the acquisition or loading the data and selecting the alignment parameters, to calculate the parameters (*Recalc parameters*, selecting *Live recalc*) and apply them, clicking on *Apply parameters*.

After starting the acquisition (click on *Flush* to restart from zero), at the top of the window it is possible to see the histogram (of all channels or only some channels) of the accumulated signal (it is possible change manually the ends of the axes or you can zoom by clicking on the magnifying glass symbol); two markers can be used to delimit the ends of the signal on which to make the alignment. An indicator is provided to indicate that the acquisition is in progress.

In the middle of the Alignment windows there is a menu that allows you to change the information displayed:

- *Alignment Results* - allows to display a preview of the aligned signal sum [in Fig. 25 (a)]
- *# Peaks* - allows to see how many peaks of the signal of each channel correspond to the set parameters, and therefore are useful for the alignment. When all channels have the same number of peaks (which is also the one chosen in *of Peak to Use*), the green light will light up. [in Fig. 24]
- *Centers* - allows you to see the position of the centroid, it is possible to select the peak [in Fig. 25 (b)]
- *Counts* - allows to see the counts of the cell [in Fig. 25 (c)]
- *Max Value* - allows to see the maximum counts of the cell [in Fig. 26 (a)]
- *Delta* - if there is an alignment with two peaks, it allows to know the distance between them: maximum [peak centers] - minimum [peak centers], the total of all channels and the total for each strip are also displayed [in Fig. 26 (b)]

- *FWHM* - allows to see the FWHM of the cell, it is possible to select the peak, and the total of all channels and the total for each strip are also displayed [in Fig. 23]

- *Norm. FWHM Quad (%)* - if there is a two peaks alignment, it allows to verify the best compromise between FWHM (which in the best of cases must be the smallest possible) and delta (which in the best of cases must be the largest possible), the total of all channels and the total for each strip are also displayed [in Fig. 26 (c)]

Figure 23: The windows of the FICUS Alignment (FWHM).

Figure 24: The windows of the FICUS Alignment (Peaks).

164

Figure 25: The windows of the FICUS Alignment: (**a**) Alignment Result, (**b**), Centers, (**c**) Counts.

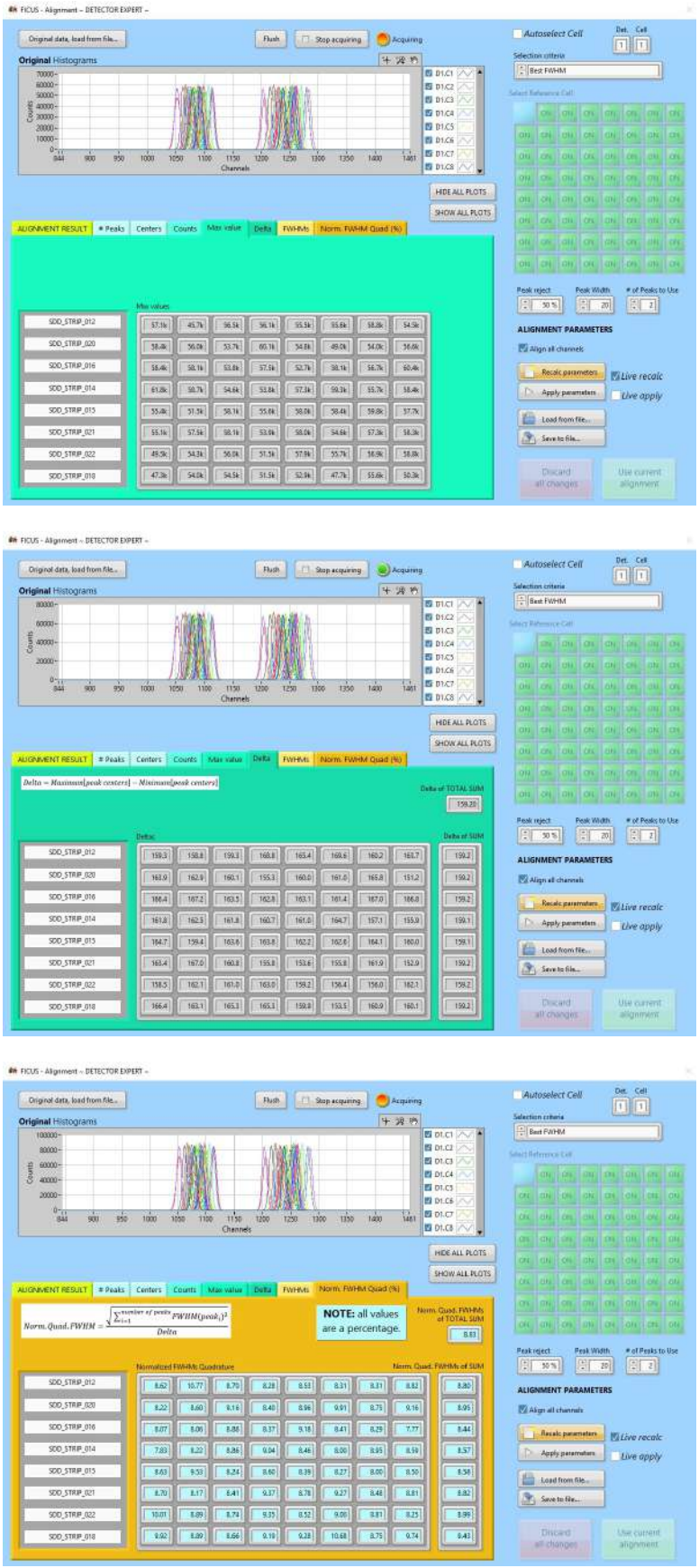

Figure 26: The windows of the FICUS Alignment: (**a**) Max Value, (**b**), Delta, (**c**) Norm. FWHM Quad (%).

166

To complete the alignment in a short time and effectively it is recommended:

- to cut through the cursors any signal baseline and escape peak, so as to leave highlighted the peaks on which to do alignment
- to use alignment parameters such as those in the figure
- to wait for the time necessary to have a good signal collection
- to have the same number of peaks on all channels (and then turn on the light in the *Peaks* box)

If it is necessary to leave the alignment procedure without completing it, click on *Discard all changes*. At the end of the procedure, when you have a good sum signal, (if you want you can save the alignment by clicking on the *Save to file...* button) and exit the alignment procedure by clicking on *Stop acquiring* and then on *Use current alignment*. This will re-open the acquisition window and the alignment indicator will be coloured green, as shown in Fig. 27.

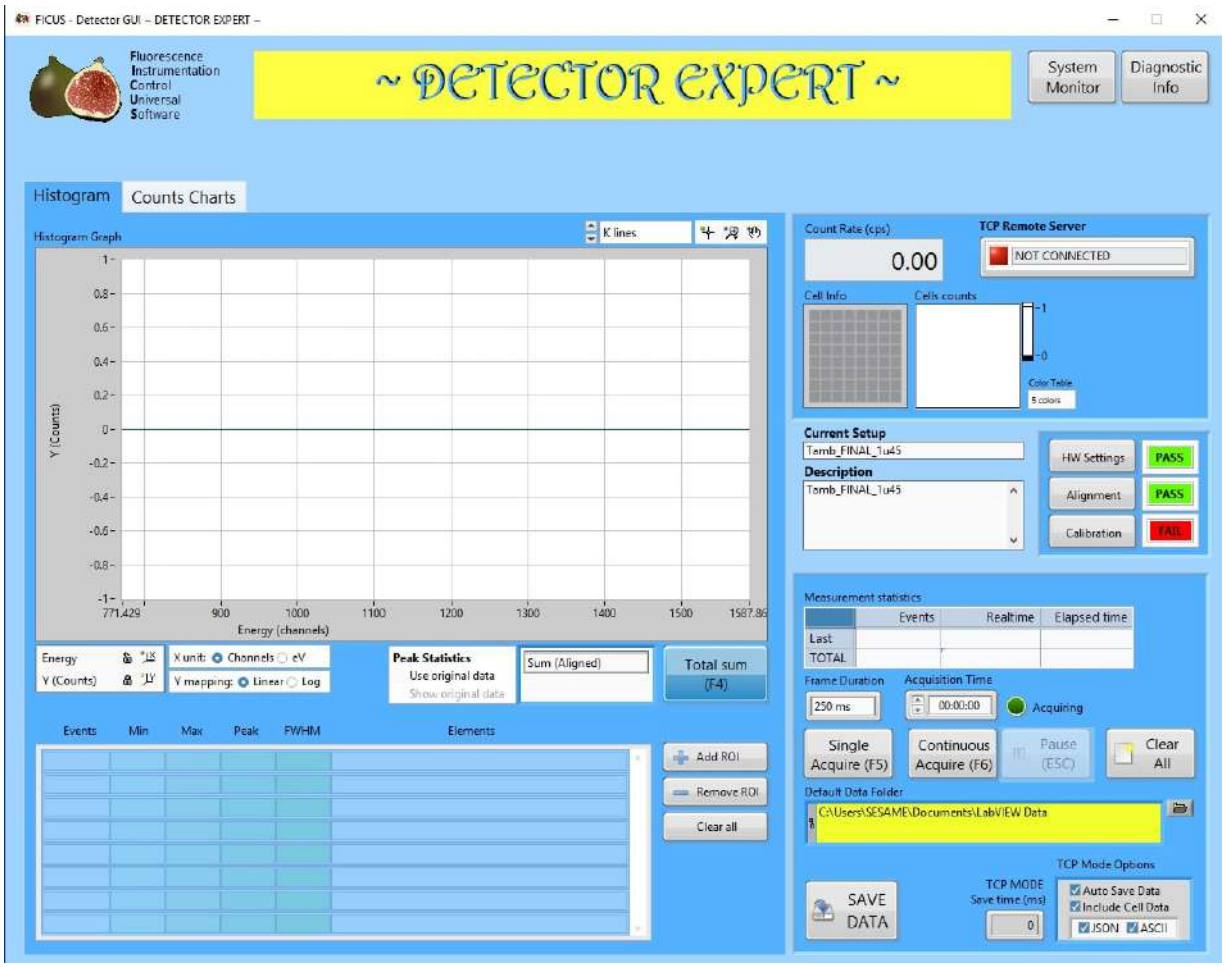

Figure 27: The windows of the FICUS acquisition (Histogram), after Alignment.

Back to the FICUS acquisition window, it is possible to start a measurement by setting the *Frame Duration* and the *Acquisition Time* (in format hh:mm:ss). For a single measurement equal to the duration of the frame click on *Single Acquire (F5)*, for a timed measurement just set the acquisition time and then click on *Continuous Acquire (F6)*. If instead it is wanted to start and stop the measurement manually, it is enough to leave the acquisition time field at zero.

The *Histogram Graph* box shows the accumulated graph of the sum signal [it is also possible to display the signal of the single channels by clicking on *Sum (Aligned)* an additional one will appear in which it is possible to choose which channel to display]. It is possible change manually the

ends of the axes or you can zoom by clicking on the magnifying glass symbol (to unlock the ladder just click on the bolt symbol). It is possible to choose whether to display the Y axis in linear or logarithmic scale, and the X axis in channels or in eV (this is possible only after having performed the calibration procedure).

Figure 28: The windows of the FICUS acquisition (Histogram), after the measurement by one minute with VTEST and Double VTEST.

During or after the acquisition it is possible to select Regions Of Interest (ROI) clicking on *Add ROI* and by positioning the sliders manually; up to 20 different ROIs can be selected (there are 4 colours and they repeat cyclically with no choice) [Fig. 28]. The table below shows the data of each ROI: *Events*, *Min* position, *Max* position, *Peak* position, and an estimate of the *FWHM* (is calculated as the width at half height considering the intersections of the sliders with the signal). If the calibration procedure has been performed, when eV is selected as the X unit, the ROI data also changes the unit of measurement and the table shows the list of the elements that may correspond to the selected peak in the ROI. The ROI can be removed individually by clicking on *Remove ROI* and selecting the one to be deleted, or all by clicking on *Clear all*.

After stopping or ending the acquisition, it is possible to perform the calibration: clicking on *Calibration* opens the window dedicated to it. **FICUS Calibration window** appears as in Fig. 29: the accumulated signal is visible and you can zoom in using the zoom button. A previously saved calibration file can be loaded (by clicking on *Load from file...*) or a new calibration can be performed. To do this it is necessary to click on *New point...* (to select a point on the x-axis) or on *New region...* (to select the region of the peak we are interested in using cursors, search for the maximum); in the window that appears, write the name of the element corresponding to the centre of the peak and then the corresponding energy. Repeat the procedure for all peaks you want to identify. If it

168

is necessary to delete one or all of the points inserted, it is possible to do so by clicking on *Delete Calibration Item...* or *Delete All Calibration Items*. To exit without saving or applying the calibration click on *Ignore Change*. When it is considered sufficient, (you can save the calibration by clicking on *Save to file...* and select the name of the file) it is possible to apply the calibration by clicking on *Use This Calibration*. This will re-open the acquisition window and the calibration indicator will be coloured green, as shown in Fig. 30.

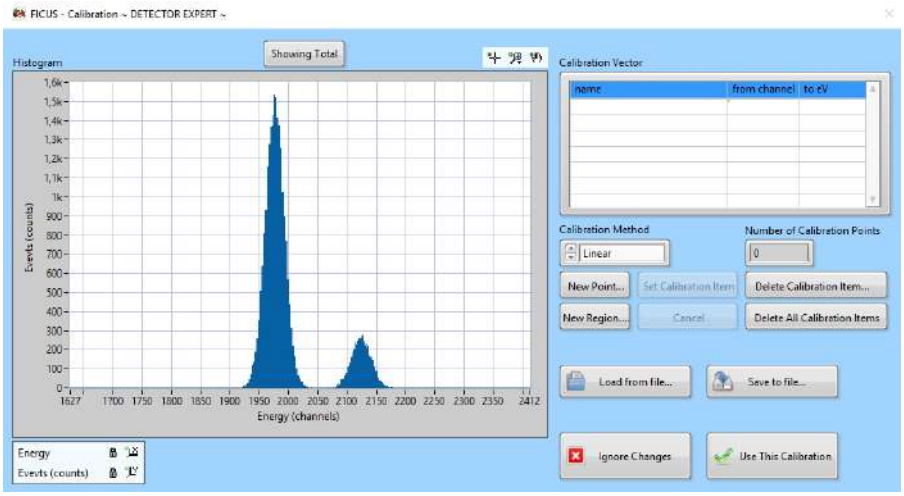

Figure 29: The windows of the FICUS Calibration.

Instead of the histogram, it is possible to display the *Counts Chart* to monitor the number of total counts and ROI counts [Fig. 30].

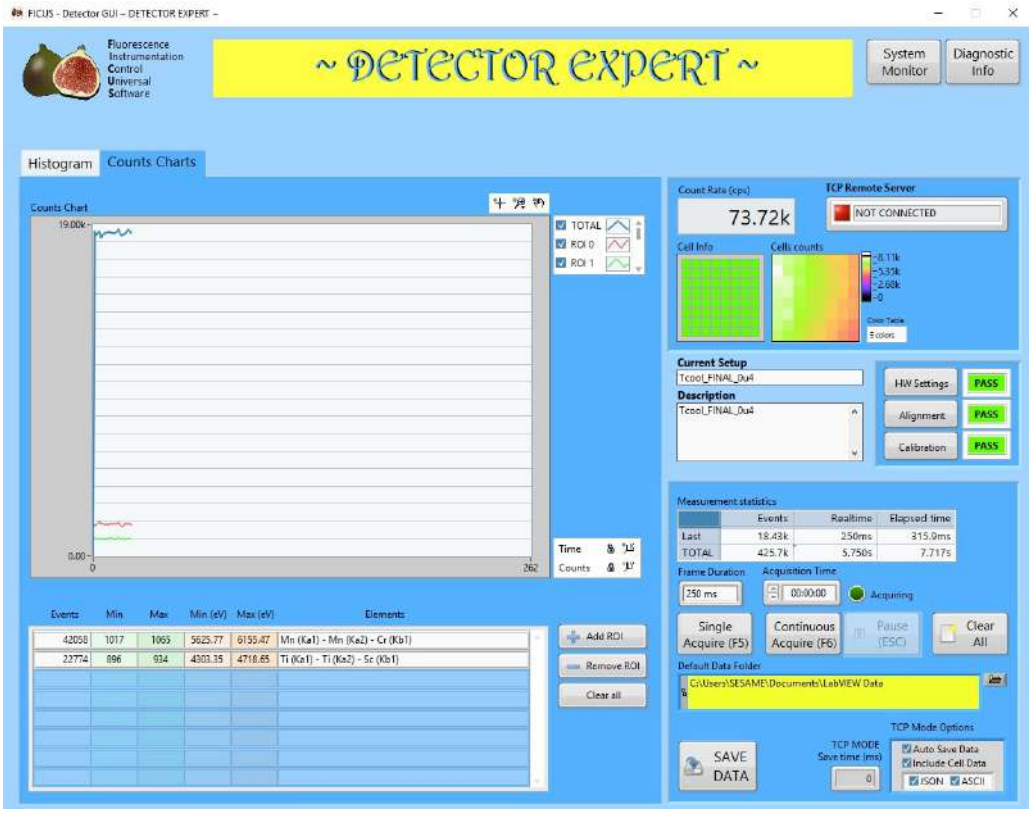

Figure 30: The windows of the FICUS acquisition (Counts Charts), after Alignment and Calibration.

To save the acquired data and the information related to them, just click on *SAVE DATA*, select the saving folder and indicate the name of the file.

To delete the acquisition data, and be ready to start with a new acquisition (continuing to work with the same alignment and calibration) just click on *Clear All*.

To switch off the system, carefully follow the switch-off procedure described in the section *Instructions for switching* on on page 53.

To close the FICUS software, from the acquisition window click on the *X*, the FICUS control window will appear [Fig. 31 (a)]. Click on *Disconnect*, a message will open to confirm disconnecting the detector, press *OK*, as shown in Fig. 31 (b). To close the software click on *Quit*, a confirmation message will open, press *OK*, as shown in Fig. 31 (c).

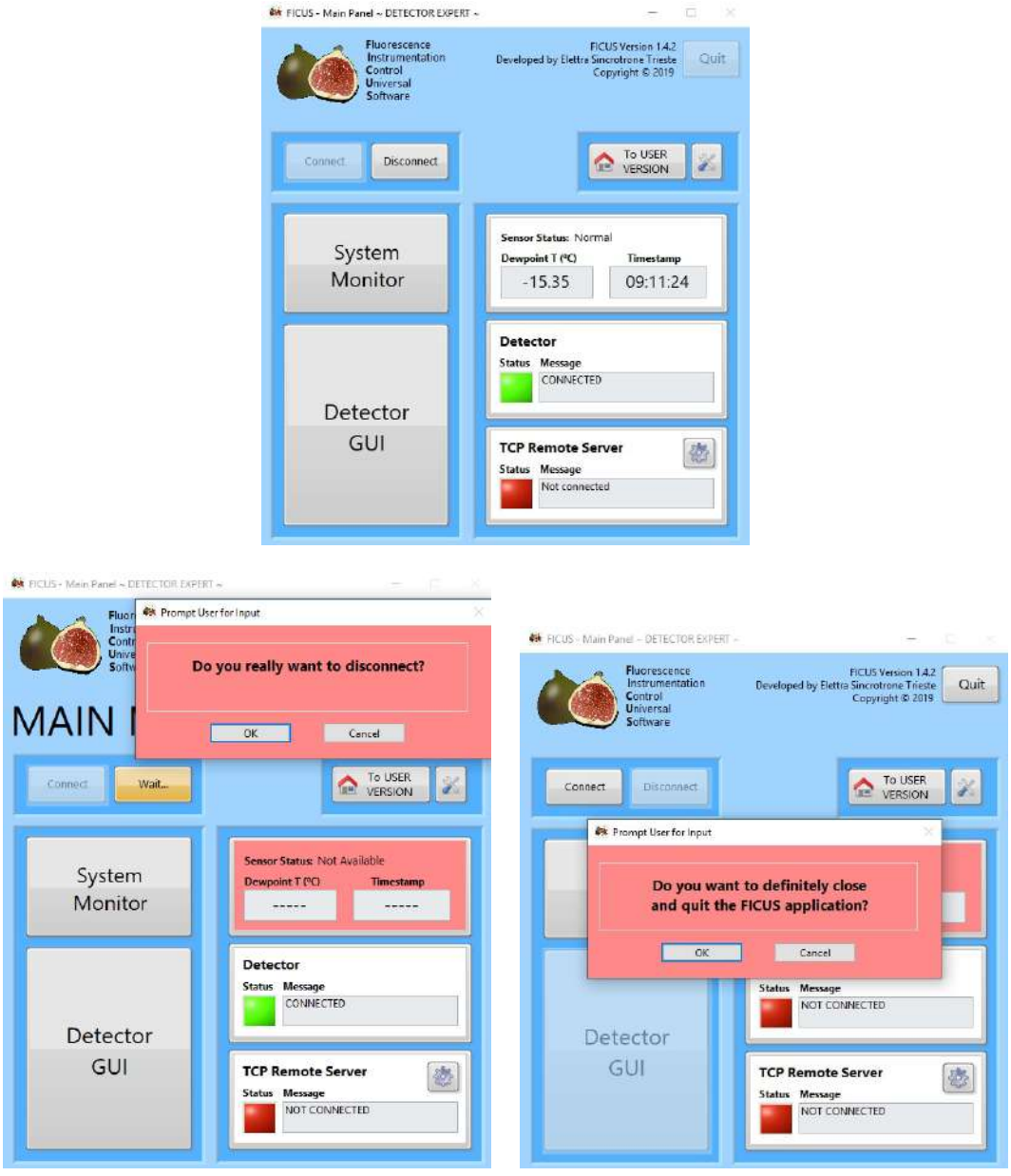

Figure 31: The FICUS control window (**a**) Connected, (**b**) With the message requesting confirmation to disconnect, (**c**) Disconnected and with the message requesting confirmation that the program has been closed.

5 Guide for Beamline Staff

Before starting any activity, please take a look at the **Safety warnings for using the SESAME-XAFS Detector System**, on page 52, and the **Instructions for switching on/off**, respectively on page 52 and 53.

This version of the software is recommended for the beamline staff in order to optimize the system settings for the planned measurements.

To pass from the FICUS software User version to the Beamline Staff version it is necessary to have the access codes.

Only the FICUS software Beamline Staff version can connect and disconnect the detectors.

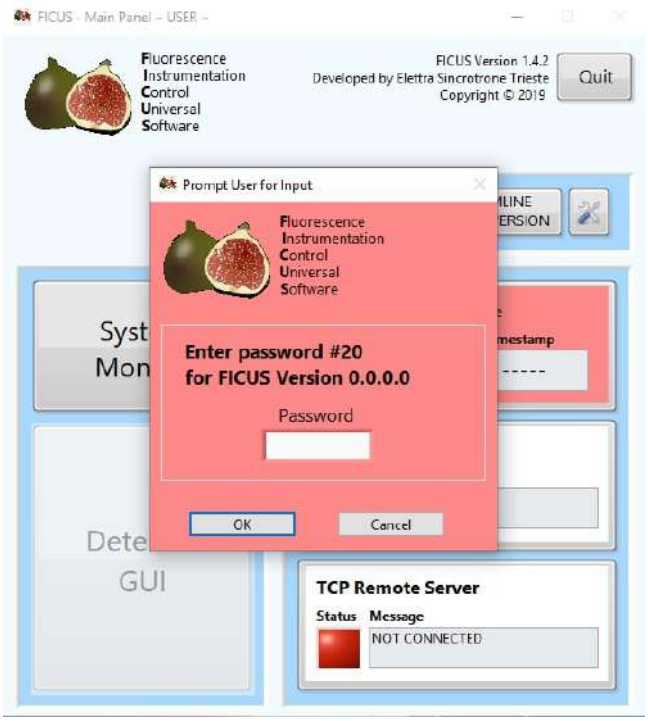

Figure 32: The FICUS control window: to pass from the FICUS software User version to the Beamline Staff version.

After the launch of FICUS software, following the instructions recommended in this manual for switching on the detector system, the first window is the one shown in Fig. 33.

In the **System Monitor window** it is possible to see the dew point temperature of the system, the time, the status of the detectors and the status of the TCP Remote Server (red disconnected - green connected).

After connect of the detector, it is also possible to click on *System monitor* to know:

- the log of the dew point temperature [in Fig. 34 (a)]
- the log of the temperature of the strips [in Fig. 35 (a)]
- the log of the temperature of the LDOs [in Fig. 35 (b)]
- the log of the temperature of the FPGAs [in Fig. 35 (c)]
- the log of the temperature of the ADCs [in Fig. 35 (d)]
- the table with all the last measured temperatures [in Fig. 34 (b)]

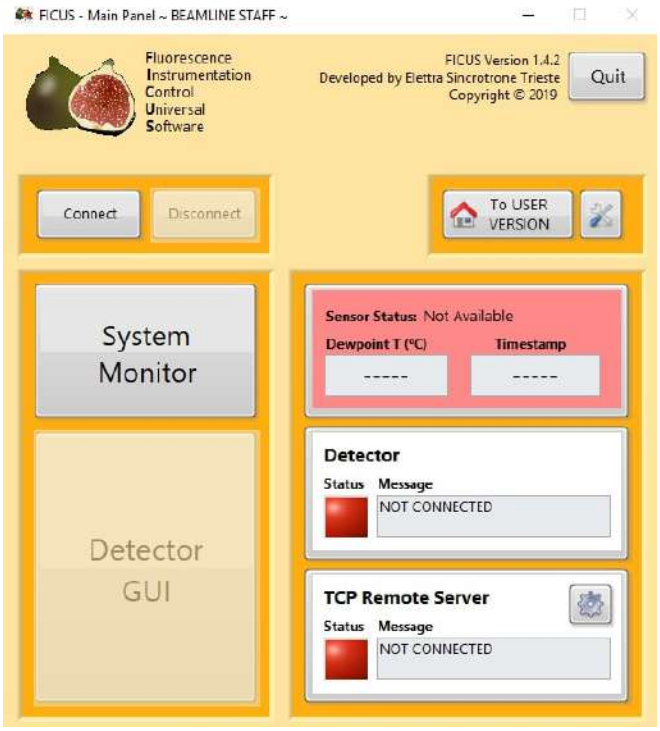

Figure 33: The first window of FICUS software

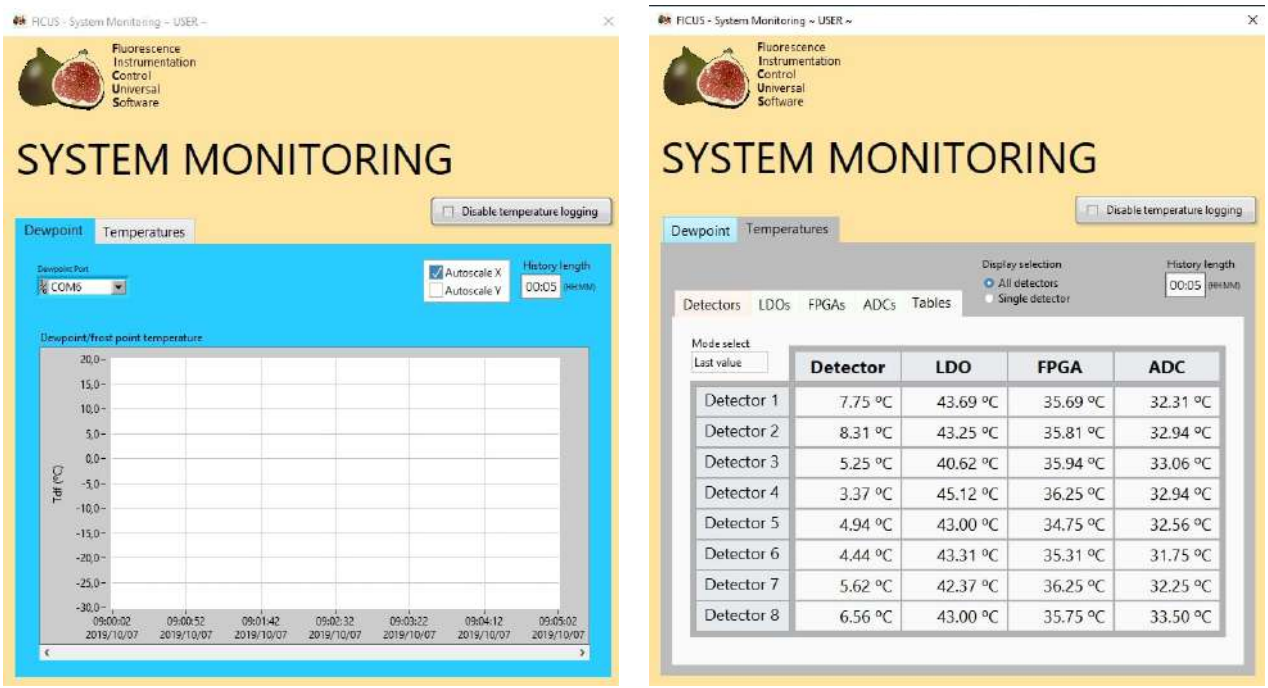

Figure 34: (**a**) The log of the dew point temperature. (**b**) the table with all the last measured temperatures (visible after connecting the detectors).

In the log it is possible to modify the time duration displayed and to set the extremes of the graph, or to set its auto setting.

172

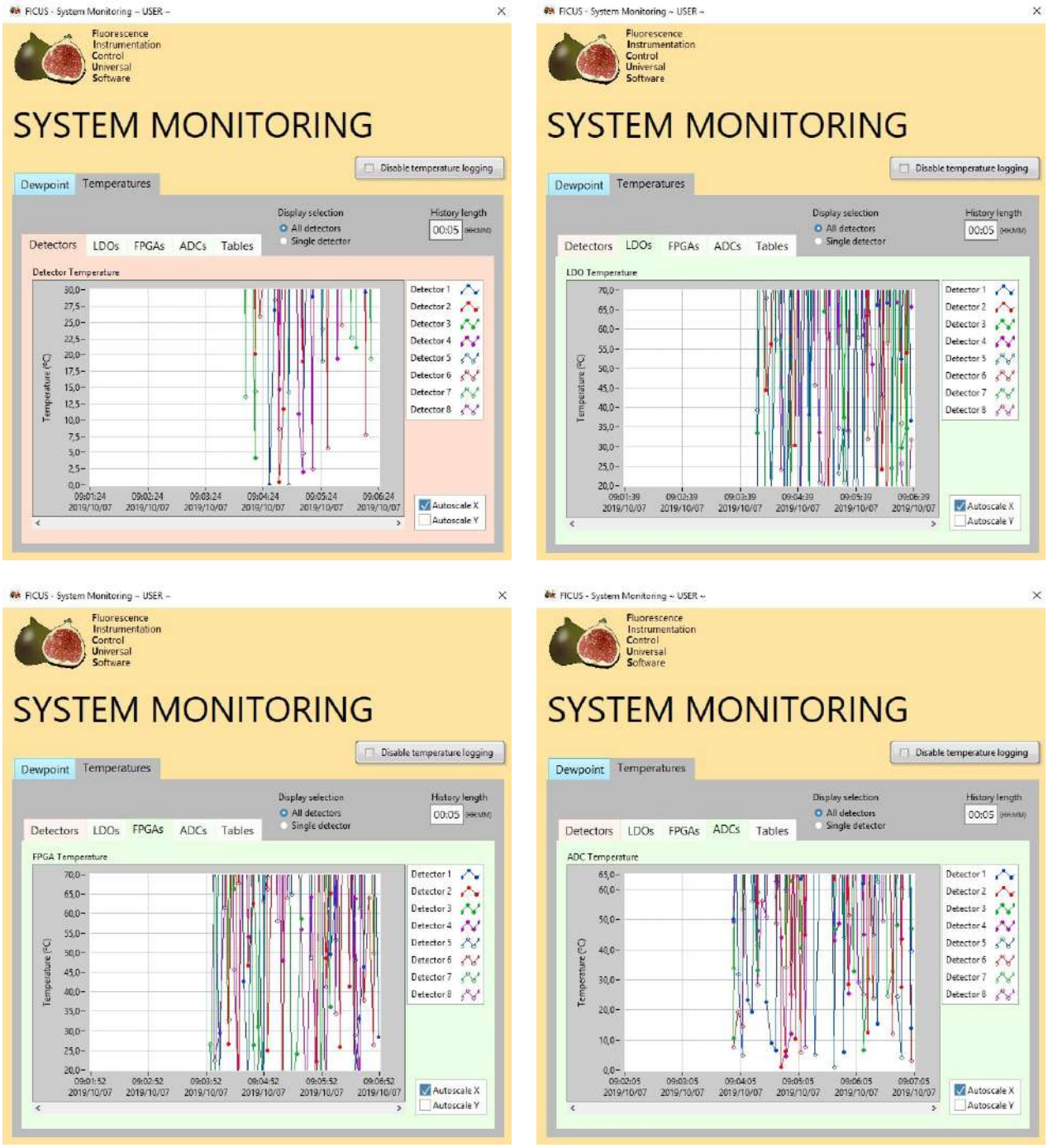

Figure 35: In clockwise direction starting from the top left (the values represented are derived from a simulation and purely figurative) (**a**) The log of the temperature of the strips (**b**) The log of the temperature of the LDOs (**c**) The log of the temperature of the FPGAs (**d**) the log of the temperature of the ASICs.

173

To connect the detector system click on *Connect* (in Fig. 33). The connection window in Fig. 36 (a) appears. Click on *Run TCP-IP and FPGA tests* and, if the test is successful, all the boxes will be colored green [Fig. 6 (b)] and you can proceed to the connection by clicking *OK*.

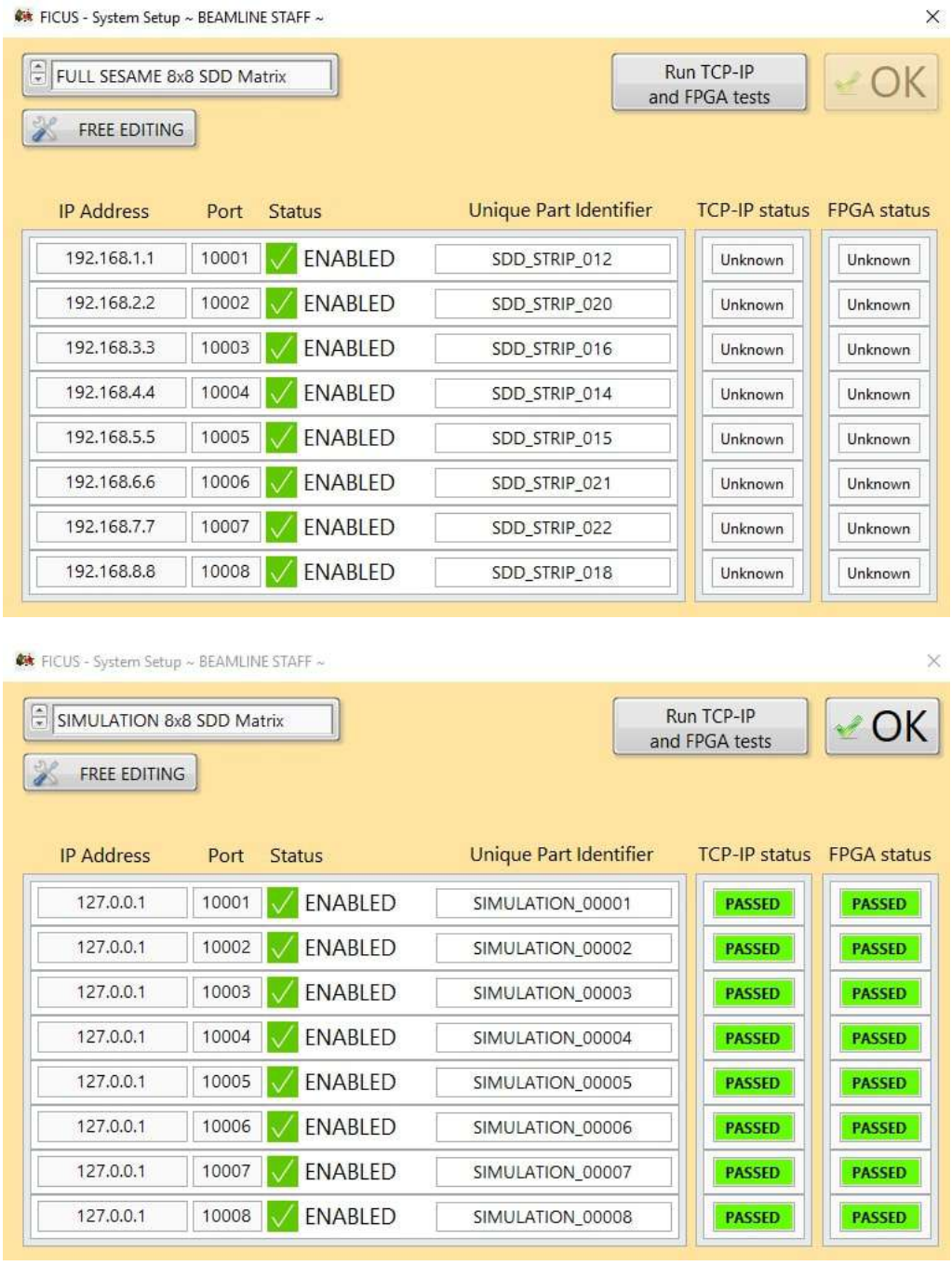

Figure 36: The connection window -(**a**) before connecting tests (**b**) The connection window - after passing the connecting tests (in simulation mode, for figurative use).

A message appears asking if you want to restore the previously used settings: press *OK* to proceed or *Cancel* to annul the setting restore [Fig. **??**]. It is possible to see that the status of the detector has changed to CONNECTED [Fig. **??**].

The first window of the **FICUS settings** opens, in *Spectrum View* [Fig. 38]. Here, at the top from the left you can see the signals of the individual channels: 4 at a time (those highlighted in light green in the panel at the bottom left), and you can change which ones to select by clicking on the green arrows in the center on the right. In in the panel at the bottom left, in addition to the *Cell Status*, it is also possible to display the map of the *Enabled/Disabled* channels [Fig. 39 (a)],

174

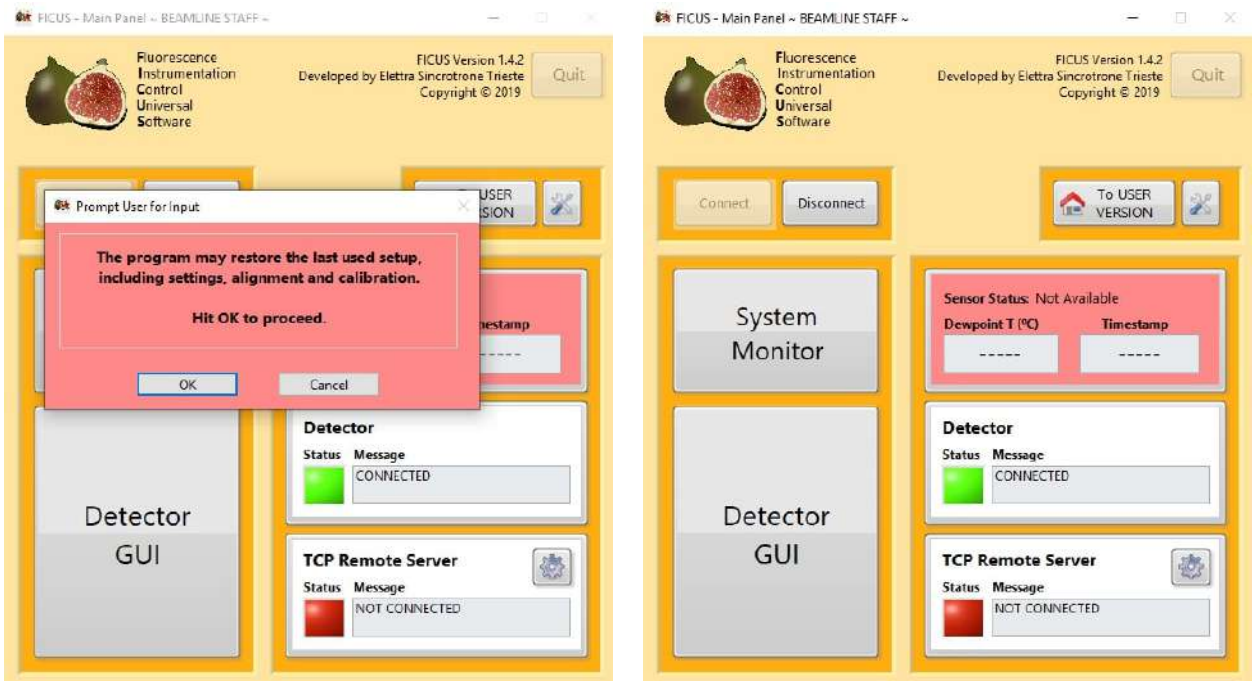

Figure 37: The FICUS control window: (**a**) during connection, with the message asking if you want to restore the previously used settings (**b**) After connection.

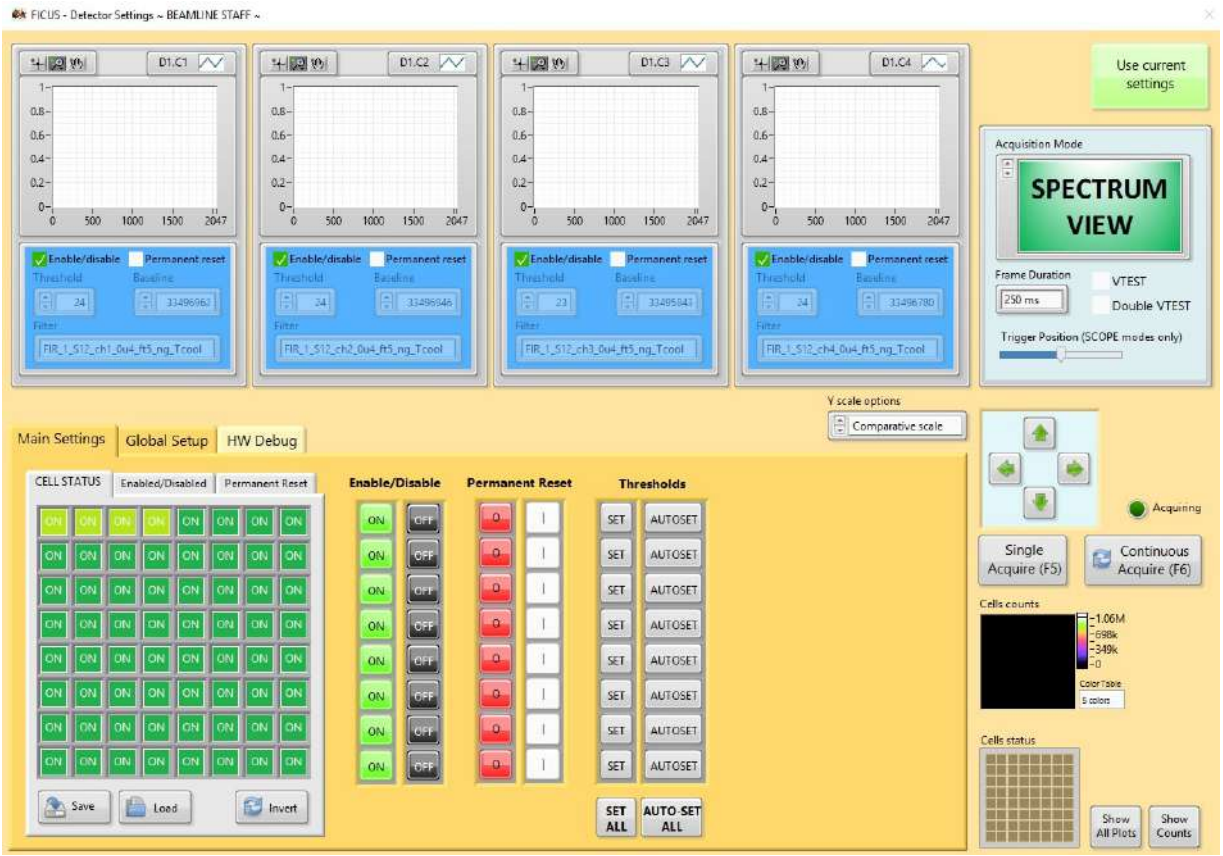

Figure 38: The first windows of the FICUS setting (with Global Setup).

and the map of the channels in *Permanent Reset* [Fig. 39 (b)]. Within each box in the upper part, it is possible *Enable/disable* the channel, put the channel in *Permanent reset*, and manually set the *Threshold*, *Baseline* and *Filter*.

175

In the upper right corner, it is possible to enable and disable the test signals (*VTEST* and *Double VTEST*) and to select the *Frame Duration* (among the values: 5 ms, 7.5 ms, 10 ms, 25 ms, 50 ms, 75 ms, 100 ms, 250 ms, 500 ms, 750 ms, 1 s, 2.5 s, 5 s, 7.5 s, 10 s, and External Gate).
In the central part on the right there are buttons to activate the measurement: *Single Acquire (F5)* and *Continuous Acquire (F6)*, and a green dot indicating the acquisition in progress.
In the lower right part of the window there are: a graph with the Cells counts represented (with the graduated scale of colors next to it), one with the Cells status visible (where in grey it is an unavailable channel, in green an active and counting channel, in red an inactive and with error channel, in black a disabled channel, and in dark green an active and with no counts channel, placed in permanent reset). There are also three buttons (*Show 1 Cell Plot*, *Show All Plots*, *Show Counts*), which allow you to view respectively the detail of the signal of a channel [Fig. 41 (a)], the contemporary graph of all 64 channels [Fig. 40] and the counts of 64 channels [Fig. 41 (b)]. In this graphs it is possible to change X and Y scale of the histograms.

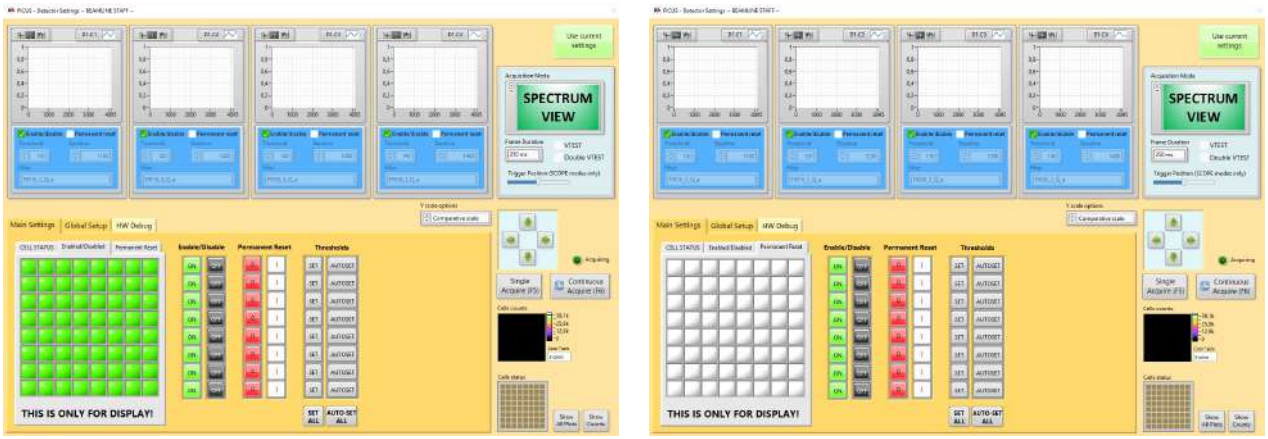

Figure 39: The windows of the FICUS setting, in Main Setting (**a**) Enabled/Disabled, and (**b**) Permanent Reset channels.

Figure 40: The windows of the FICUS with Show All Plots, with signal.

176

Figure 41: The windows of the FICUS with (**a**) Show 1 Cell Plot, and (**b**) Show Counts.

In the central part of the window, there is an additional menu that modifies the central part of the window by enabling further possible adjustments.
In *Global Setup* there is the possibility to save (assigning a name and notes) the current settings, with *Save Global Setup*, or to open settings already set and saved, with *Load Global Setup.* if you select the latter option in particular, a further window opens in which it is possible to choose from the 8 pre-set global setups: four different possible filter lengths (0.4, 0.7, 1, and 1.45 μs) at two possible cell temperatures (at room temperature, Tamb, and with cooled cells with voltage on the Peltier cells, Tcool) [Fig. 42 (a)]. After selecting the one you want, just click on *OK, load this setup*, and *Yes* at the next confirmation window that opens, as in Fig. 42 (b).

In *Main Setting* [Fig. 43] it is possible to *Enable/Disable* all the channels of one strip, put all the channels of one strip in *Permanent Reset*, and *Set* the *Threshold*, for each strip or for all strips at the same time, manually or in *Autoset*.

In *HW Debug* [Fig. 44] it is possible to see the *PART IDs* of every strips of the detector system and to *TEST* and *RESET*, if it necessary, for each strip or for all strips at the same time, the FPGAs.

As it can be seen in Fig. 45, it is possible to change acquisition mode and switch from *Spectrum View* (used for normal acquisition) to *Scope View (RAW Data)* (used for RAW data), *Scope View (Filtered Data)* (used for filtered RAW data), and *Scope View (Long Time)*.

When the settings are all set it is possible switch to acquisition window: to do so you have to return to the *Spectrum View Acquisition Mode* and click on the green button at the top right *Use current setting*. The FICUS acquisition window opens, which appears as in Fig. 46. To return to the settings just click on the *HW Setting* button.

The **FICUS acquisition window**, by clicking on the corresponding buttons in the upper right corner, it is possible to open the window of *System Monitor*, as shown in Figs. 34 - 35, and the *Diagnostic Info*, as shown in Figs. 47. The windows of Diagnostic Info are used to verify the correct functioning of the detector through detailed information regarding the status [Figs. 47 (a)], counts [Figs. 47 (b)], dead time [Figs. 47 (c)], and pile-up [Figs. 47 (d)] of all channels. From these windows (using the buttons in the upper part is *Show 1 Cell Plot* in Figs. 41 (a), *Show Counts* [Figs. 41 (b)], and *Show All Plots* [Figs. 40]) it is possible to have detailed information of the signal collected.

On the right of the FICUS acquisition window it is possible to know the count rate of the acquisition (in counts/s), an overview of information on the functioning of the cells and on the counts cell by cell. In addition, the TCP Remote Server connection information is also visible. Under this box, are visible the name and description of the Global Setup in use, and next to them there are buttons to open the *HW Setting*, *Alignment* and *Calibration* windows; next to each of them there is an indicator that has three possible aspects: *PASS* in green (which means that that setting was

177

made), *WARNING* in yellow (which means that that setting has been done previously, but something has been changed since then and you may need to redo the setting), and *FAIL* in red (which means that that setting has never been done before and you need to do the setting).

178

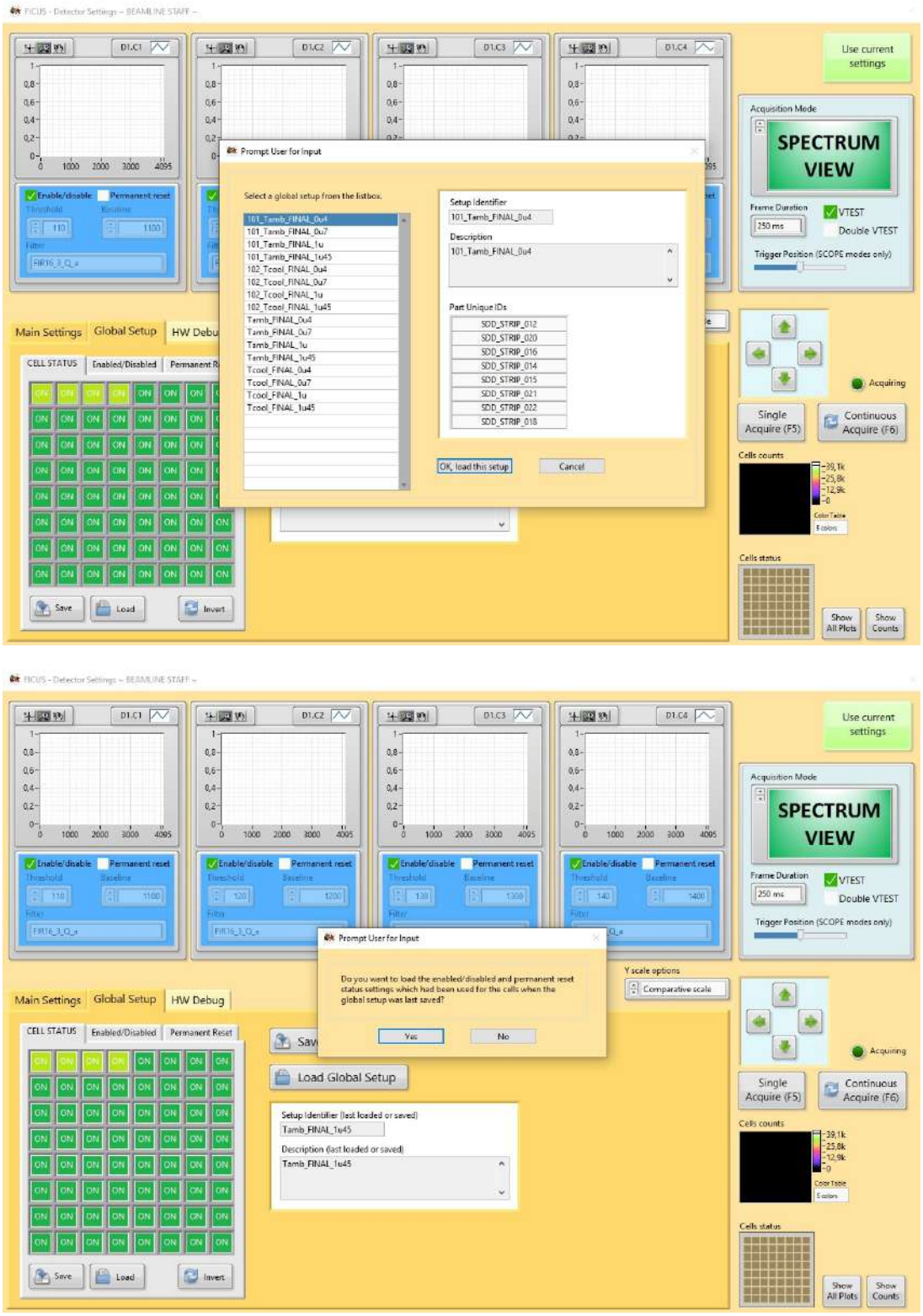

Figure 42: (**a**) The windows in which it is possible to choose from the pre-set global setups, and (**b**) the one with the confirmation window.

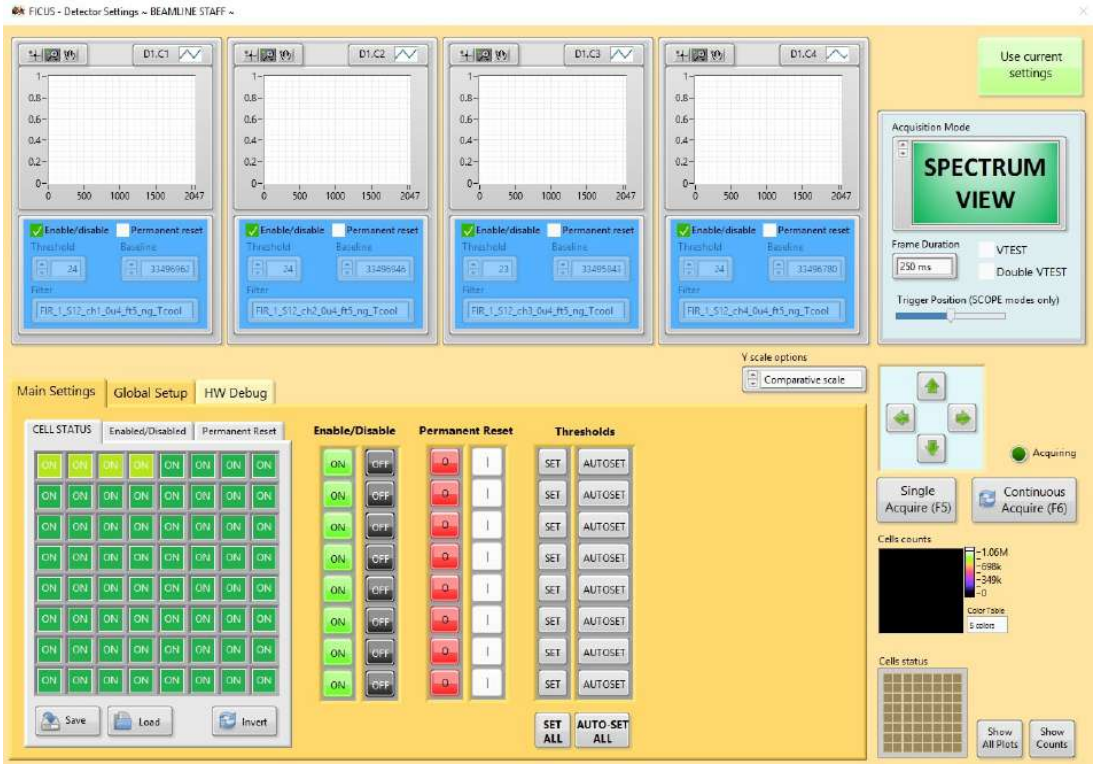

Figure 43: The windows of the FICUS setting (with Main Setting) in Spectrum View.

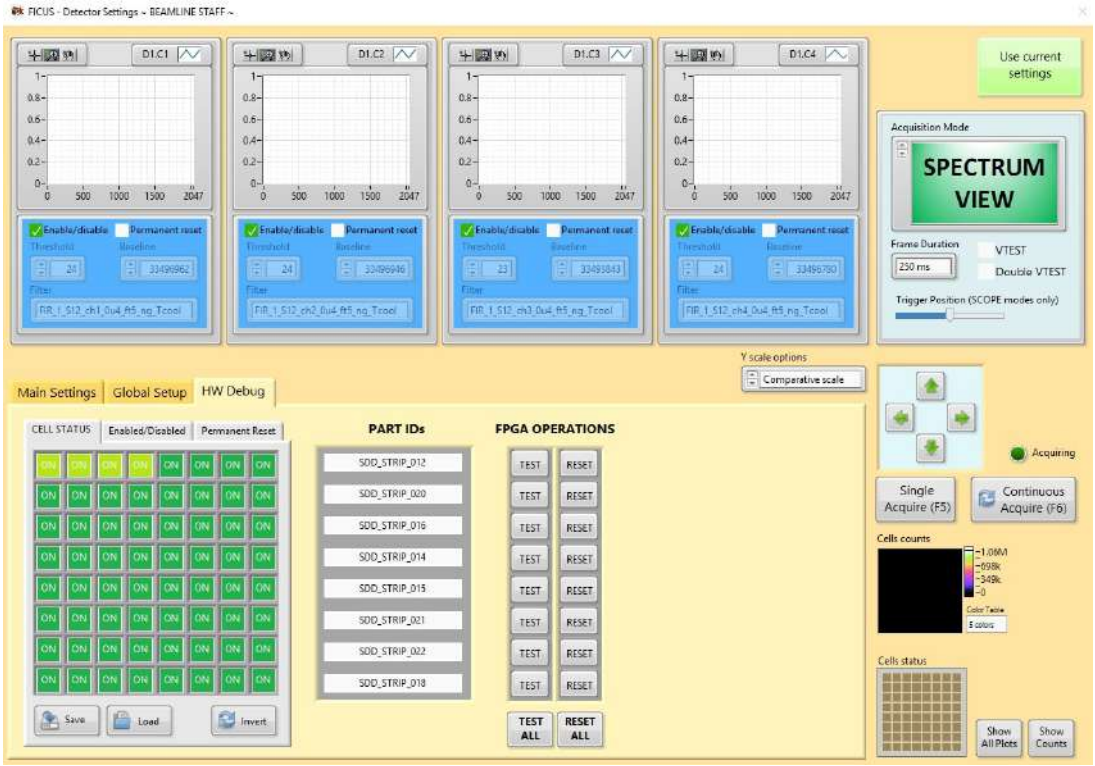

Figure 44: The windows of the FICUS setting (with HW Debug).

180

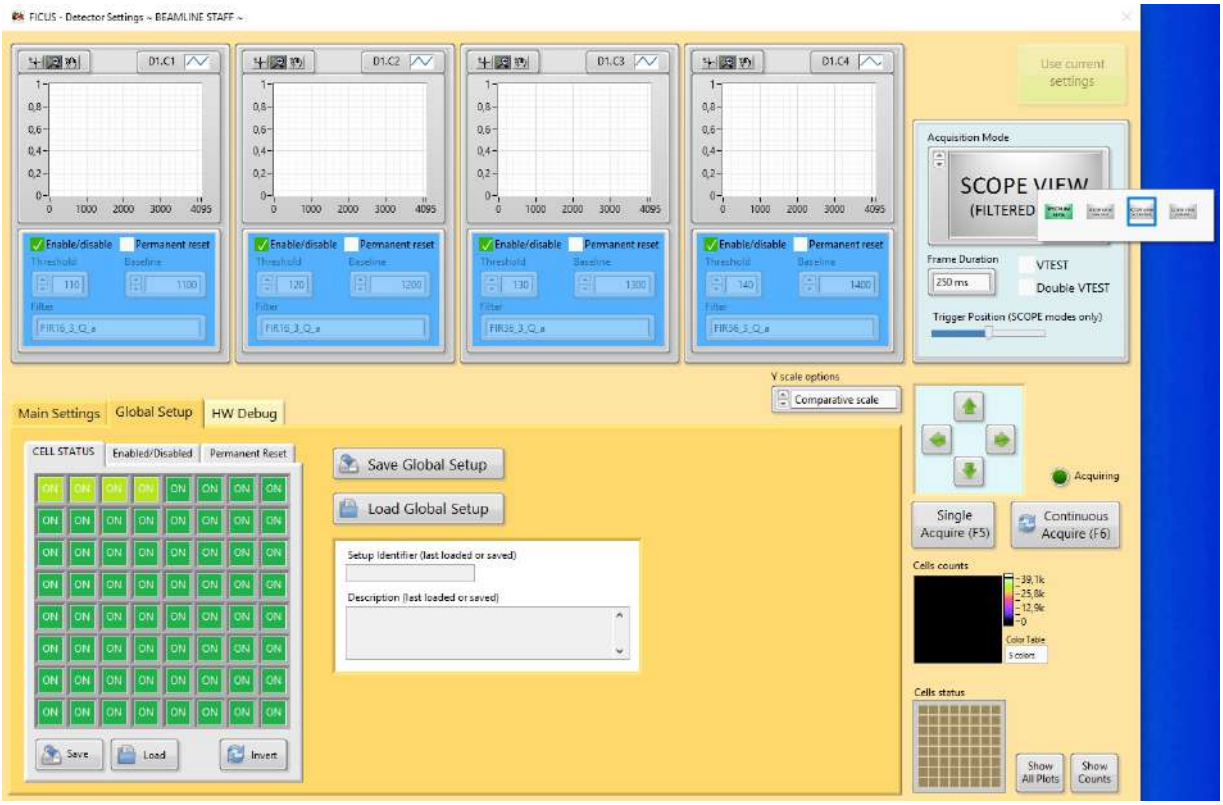

Figure 45: The windows of the FICUS setting (menu of Acquisition Mode).

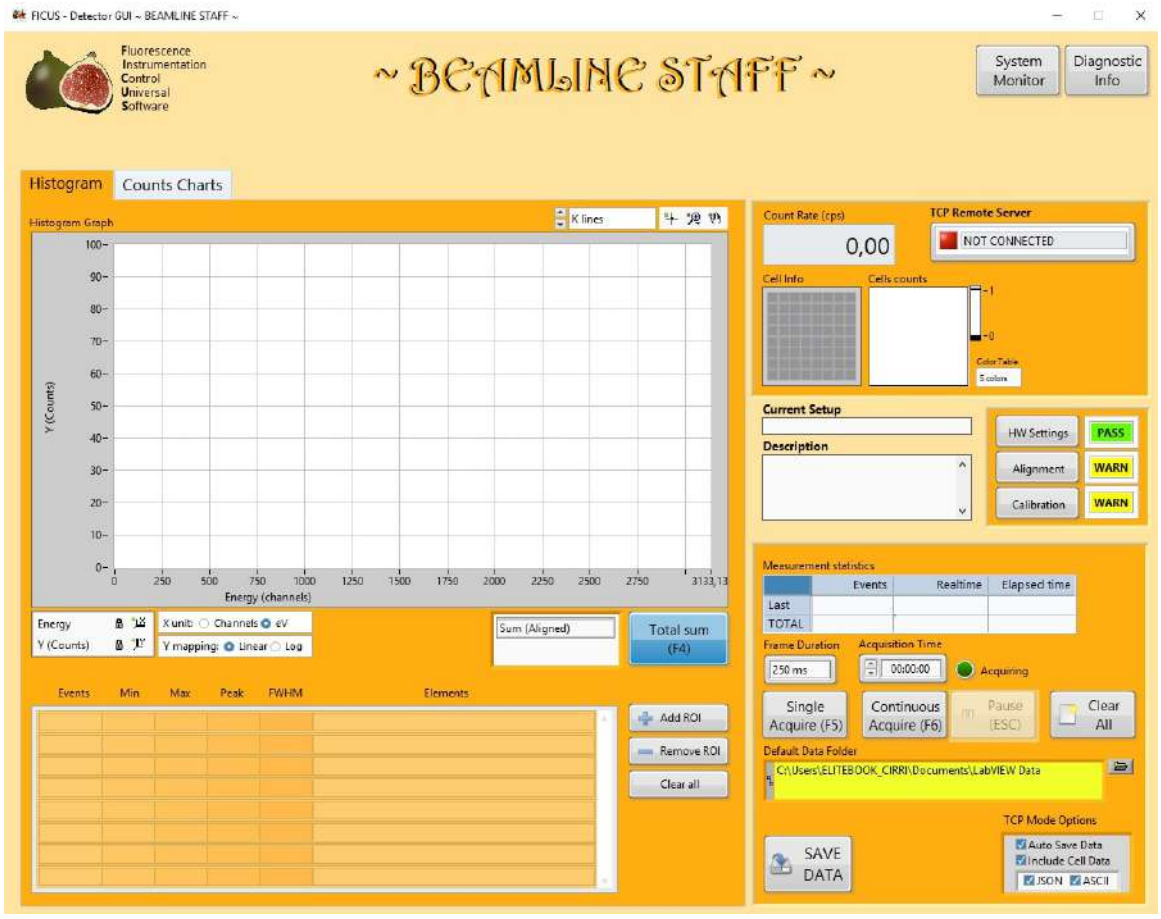

Figure 46: The windows of the FICUS acquisition (Histogram), before alignment and starting the measurement.

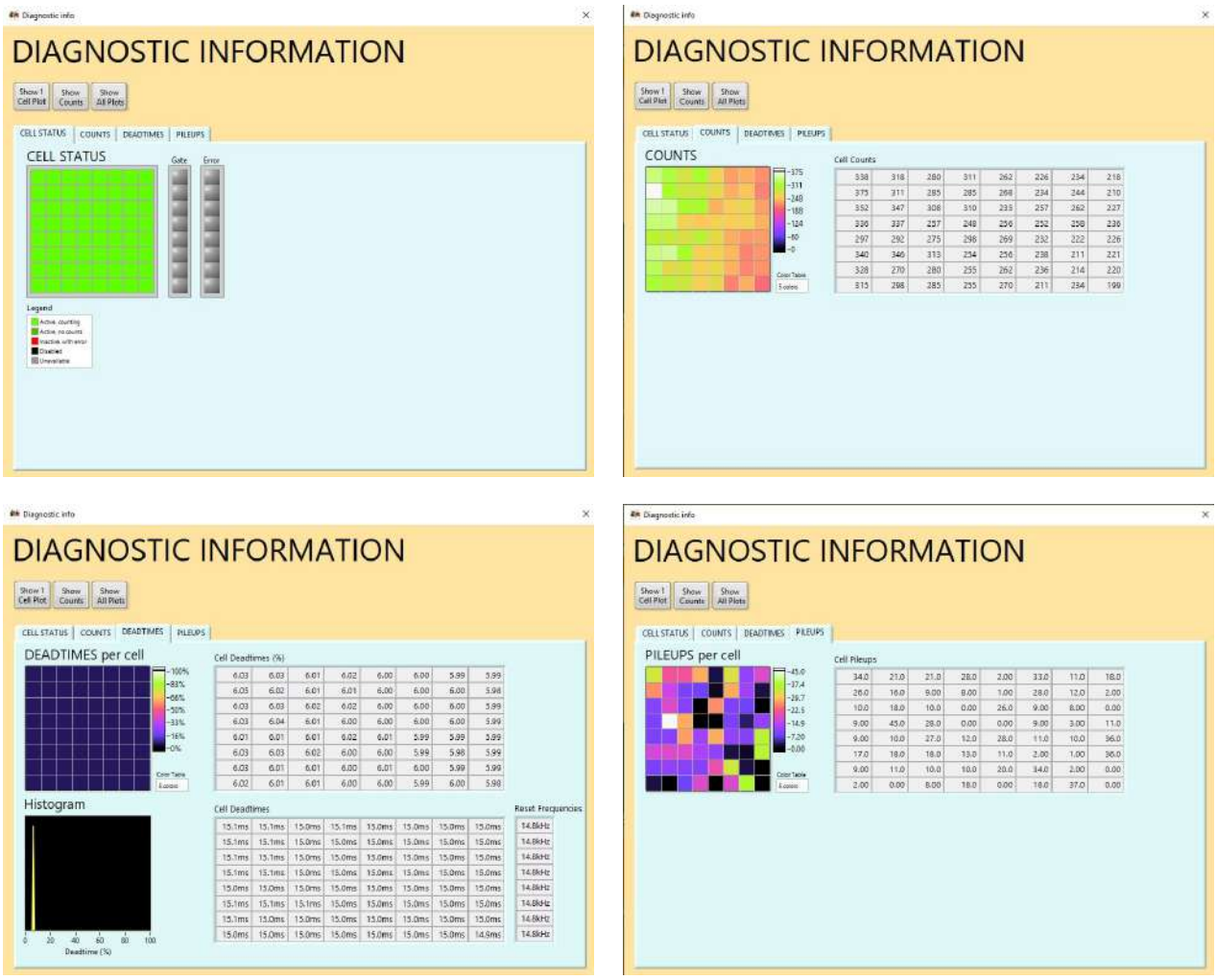

Figure 47: The windows of the FICUS Diagnostic Information (**a**) Cell Status, (**b**) Counts, (**c**) Deadtimes, (**d**) Pileups.

Clicking on *Alignment* opens the window dedicated to it. The top and right parts of the **FICUS Alignment window** are always the same; through the mid-page menu it is possible to change the bottom-left part of the window. In the Alignment window, from the Figs. 48 to the Fig. 26, in the alignment window there is the possibility to load a pre-saved alignment (by clicking on *Load from file...*), to align the channels starting from a new acquisition (by starting the acquisition with the *Start/Stop acquiring* button) or to align the channels starting from saved data (by using the *Original data, load from file...* top left button).

On the right side, starting from the top, it is possible to select manually manually, indicating the detector (*Det.*) and cell (*Cell*), the channel with respect to which to align the others or select the box *Autoselect Cell* for automatic alignment (in which the software, using the chosen criterion, chooses the most appropriate box with respect to which to align the channels); in the graph, on which it is impossible to act, the channels with respect to which the system is aligning are displayed. To align is necessary to choose the *Alignment Parameters*: *Peak Reject* (selects only the peaks with the minimum required height compared to the highest), *Peak Width* (selects only the peaks with minimum required width), and the *number of Peak to Use*. Below it is possible, after starting the acquisition or loading the data and selecting the alignment parameters, to calculate the parameters (*Recalc parameters*, selecting *Live recalc*) and apply them, clicking on *Apply parameters*.

After starting the acquisition (click on *Flush* to restart from zero), at the top of the window it is possible to see the histogram (of all channels or only some channels) of the accumulated signal (it is possible change manually the ends of the axes or you can zoom by clicking on the magnifying

182

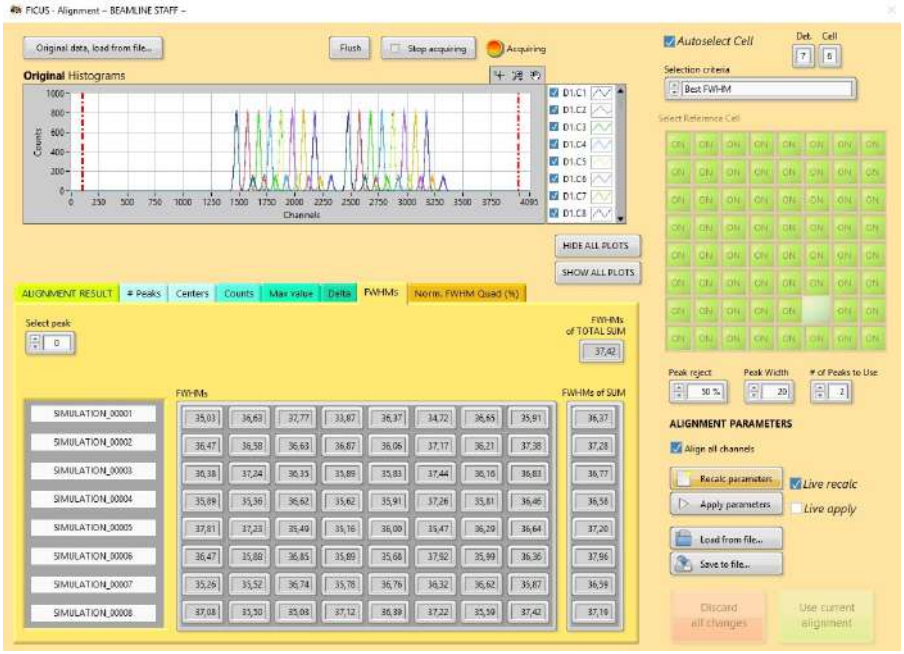

Figure 48: The windows of the FICUS Alignment (FWHM).

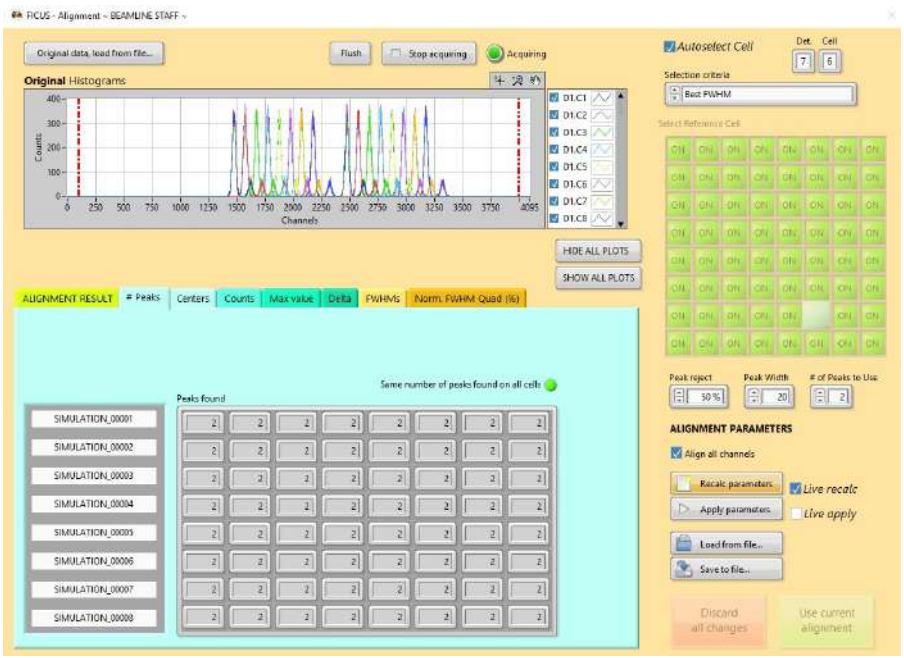

Figure 49: The windows of the FICUS Alignment (Peaks).

glass symbol); two markers can be used to delimit the ends of the signal on which to make the alignment. An indicator is provided to indicate that the acquisition is in progress.

In the middle of the Alignment windows there is a menu that allows you to change the information displayed:

- *Alignment Results* - allows to display a preview of the aligned signal sum [in Fig. 50 (a)]
- *# Peaks* - allows to see how many peaks of the signal of each channel correspond to the set parameters, and therefore are useful for the alignment. When all channels have the same number of peaks (which is also the one chosen in *of Peak to Use*), the green light will light up. [in Fig. 49]

183

- *Centers* - allows you to see the position of the centroid, it is possible to select the peak [in Fig. 50 (b)]
- *Counts* - allows to see the counts of the cell [in Fig. 50 (c)]
- *Max Value* - allows to see the maximum counts of the cell [in Fig. 51 (a)]
- *Delta* - if there is an alignment with two peaks, it allows to know the distance between them: maximum [peak centers] - minimum [peak centers], the total of all channels and the total for each strip are also displayed [in Fig. 51 (b)]
- *FWHM* - allows to see the FWHM of the cell, it is possible to select the peak, and the total of all channels and the total for each strip are also displayed [in Fig. 48]
- *Norm. FWHM Quad (%)* - if there is a two peaks alignment, it allows to verify the best compromise between FWHM (which in the best of cases must be the smallest possible) and delta (which in the best of cases must be the largest possible), the total of all channels and the total for each strip are also displayed [in Fig. 51 (c)]

To complete the alignment in a short time and effectively it is recommended:

- to cut through the cursors any signal baseline and escape peak, so as to leave highlighted the peaks on which to do alignment
- to use alignment parameters such as those in the figure
- to wait for the time necessary to have a good signal collection
- to have the same number of peaks on all channels (and then turn on the light in the *Peaks* box)

If it is necessary to leave the alignment procedure without completing it, click on *Discard all changes*. At the end of the procedure, when you have a good sum signal, (if you want you can save the alignment by clicking on the *Save to file...* button) and exit the alignment procedure by clicking on *Stop acquiring* and then on *Use current alignment*. This will re-open the acquisition window and the alignment indicator will be coloured green, as shown in Fig. 52.

Back to the FICUS acquisition window, it is possible to start a measurement by setting the *Frame Duration* and the *Acquisition Time* (in format hh:mm:ss). For a single measurement equal to the duration of the frame click on *Single Acquire (F5)*, for a timed measurement just set the acquisition time and then click on *Continuous Acquire (F6)*. If instead it is wanted to start and stop the measurement manually, it is enough to leave the acquisition time field at zero.

The *Histogram Graph* box [Fig. 53] shows the accumulated graph of the sum signal [it is also possible to display the signal of the single channels by clicking on *Sum (Aligned)* an additional one will appear in which it is possible to choose which channel to display]. It is possible change manually the ends of the axes or you can zoom by clicking on the magnifying glass symbol (to unlock the ladder just click on the bolt symbol). It is possible to choose whether to display the Y axis in linear or logarithmic scale, and the X axis in channels or in eV (this is possible only after having performed the calibration procedure).

184

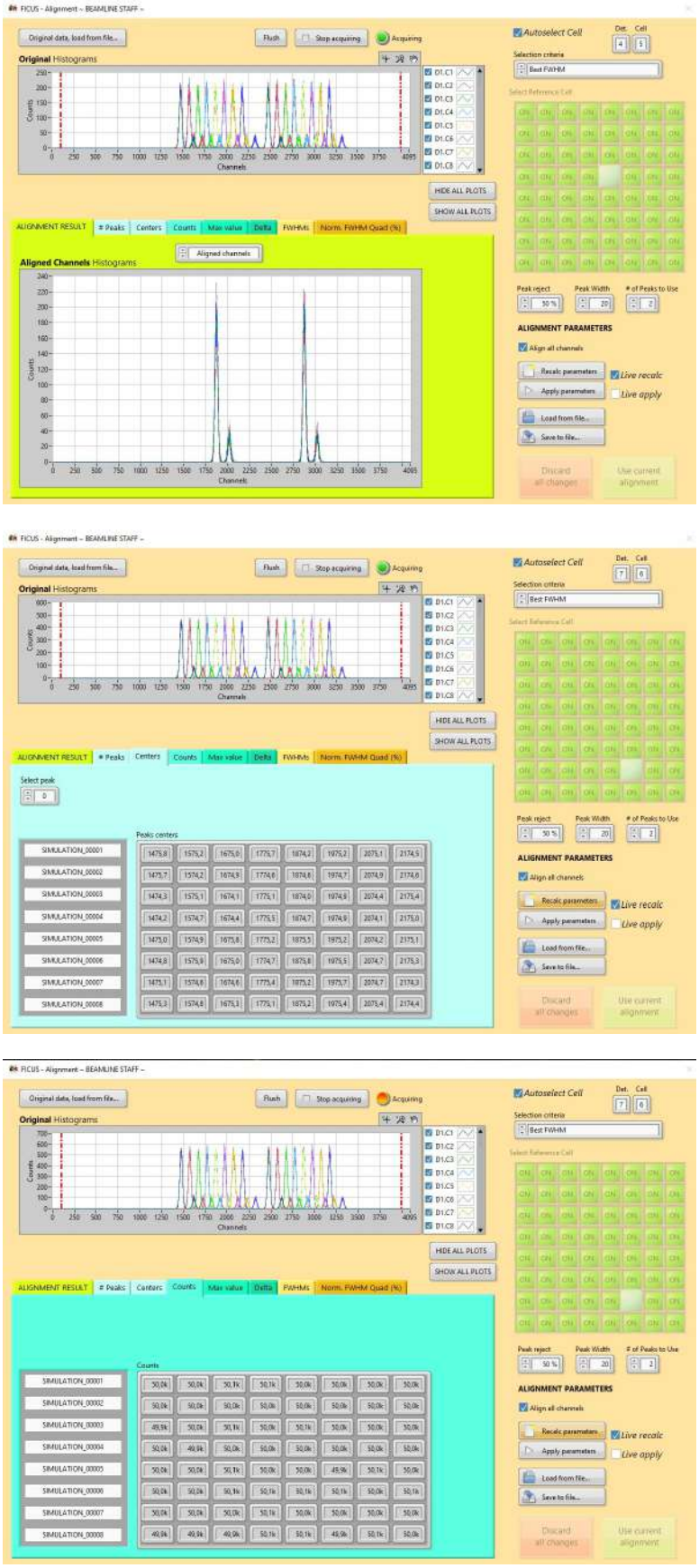

Figure 50: The windows of the FICUS Alignment: (**a**) Alignment Result, (**b**), Centers, (**c**) Counts.

Figure 51: The windows of the FICUS Alignment: (**a**) Max Value, (**b**), Delta, (**c**) Norm. FWHM Quad (%).

186

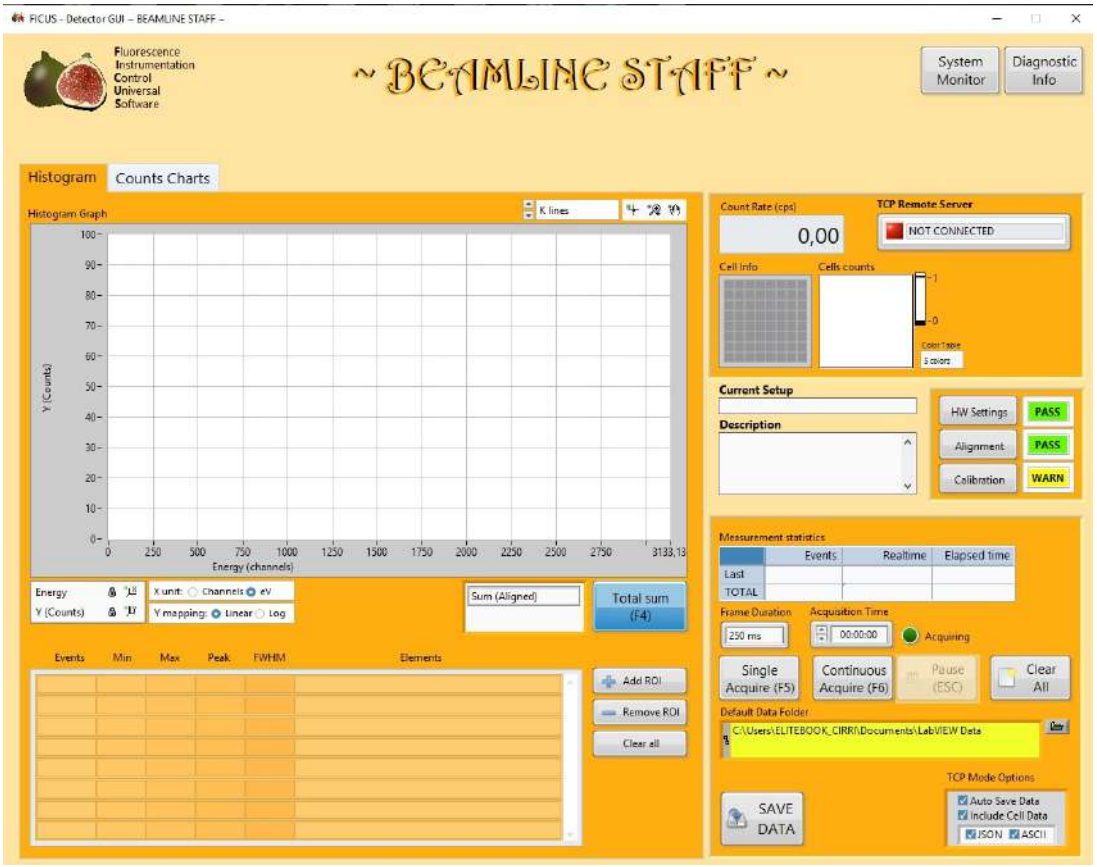

Figure 52: The windows of the FICUS acquisition (Histogram), after Alignment.

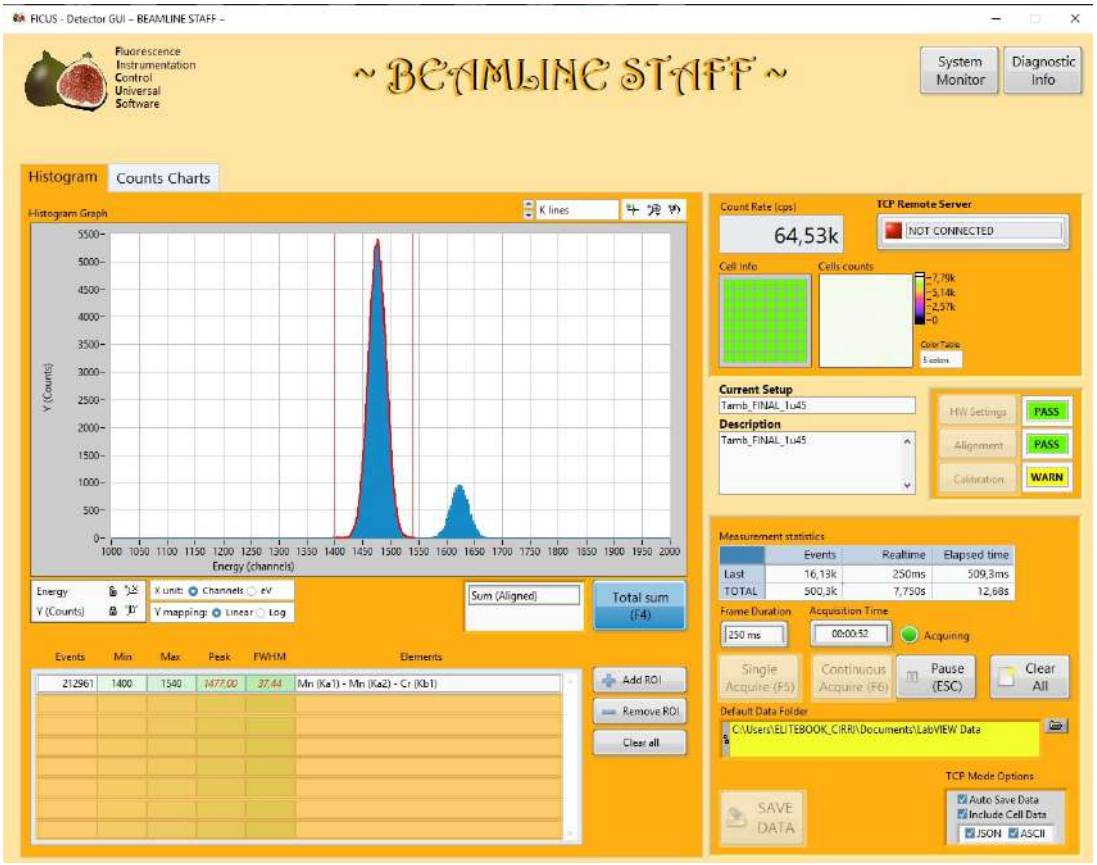

Figure 53: The windows of the FICUS acquisition (Histogram), after the measurement by one minute with a simulated signal.

During or after the acquisition it is possible to select Regions Of Interest (ROI) clicking on *Add ROI* and by positioning the sliders manually; up to 20 different ROIs can be selected (there are 4 colours and they repeat cyclically with no choice) [Fig. 54]. The table below shows the data of each ROI: *Events*, *Min* position, *Max* position, *Peak* position, and an estimate of the *FWHM* (is calculated as the width at half height considering the intersections of the sliders with the signal). If the calibration procedure has been performed, when eV is selected as the X unit, the ROI data also changes the unit of measurement and the table shows the list of the elements that may correspond to the selected peak in the ROI. The ROI can be removed individually by clicking on *Remove ROI* and selecting the one to be deleted, or all by clicking on *Clear all*.

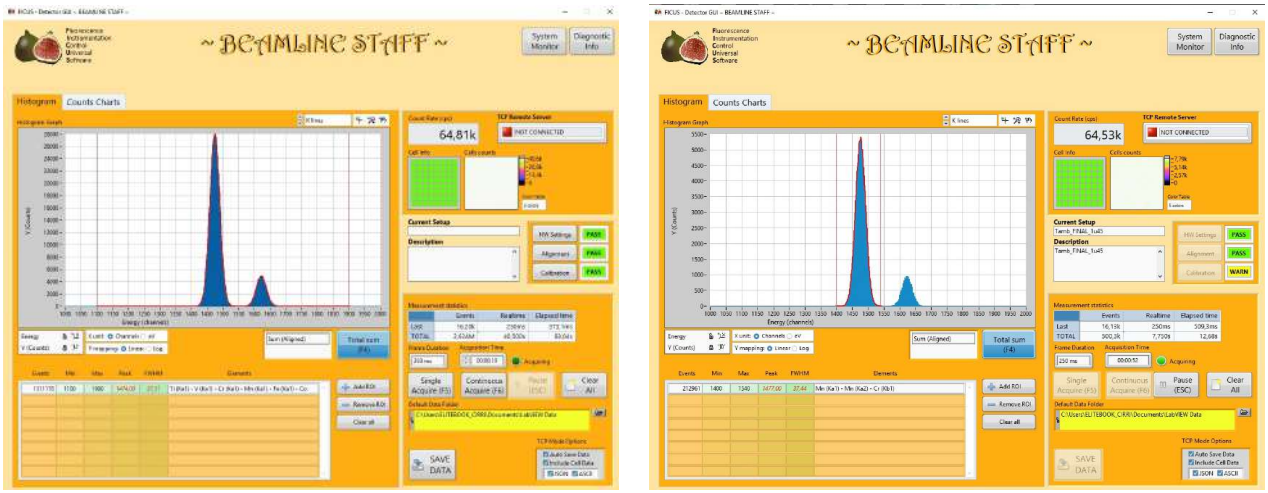

Figure 54: The windows of the FICUS acquisition: adding ROI.

After stopping or ending the acquisition, it is possible to perform the calibration: clicking on *Calibration* opens the window dedicated to it. **FICUS Calibration window** appears as in Fig. 55 (a): the accumulated signal is visible and you can zoom in using the zoom button. A previously saved calibration file can be loaded (by clicking on *Load from file...*) or a new calibration can be performed. To do this it is necessary to click on *New point...* (to select a point on the x-axis) or on *New region...* (to select the region of the peak we are interested in using cursors, search for the maximum); in the window that appears, write the name of the element corresponding to the centre of the peak and then the corresponding energy. Repeat the procedure for all peaks you want to identify. If it is necessary to delete one or all of the points inserted, it is possible to do so by clicking on *Delete Calibration Item...* or *Delete All Calibration Items*. To exit without saving or applying the calibration click on *Ignore Change*. When it is considered sufficient, (you can save the calibration by clicking on *Save to file...* and select the name of the file) it is possible to apply the calibration by clicking on *Use This Calibration* [Fig. 55]. This will re-open the acquisition window and the calibration indicator will be coloured green, as shown in Fig. 56.

Instead of the histogram, it is possible to display the *Counts Chart* to monitor the number of total counts and ROI counts [Fig. 56].

To save the acquired data and the information related to them, just click on *SAVE DATA*, select the saving folder and indicate the name of the file, as shown in Fig. 57.

To delete the acquisition data, and be ready to start with a new acquisition (continuing to work with the same alignment and calibration) just click on *Clear All*.

188

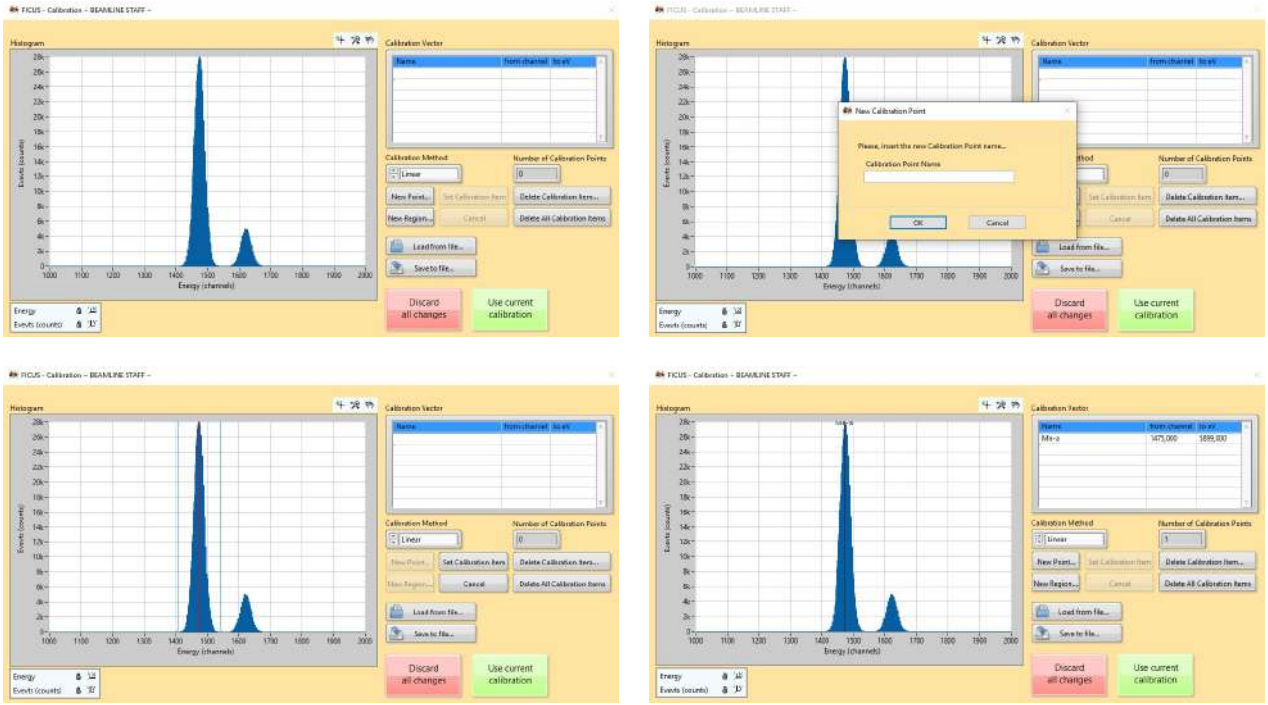

Figure 55: The windows of the FICUS Calibration.

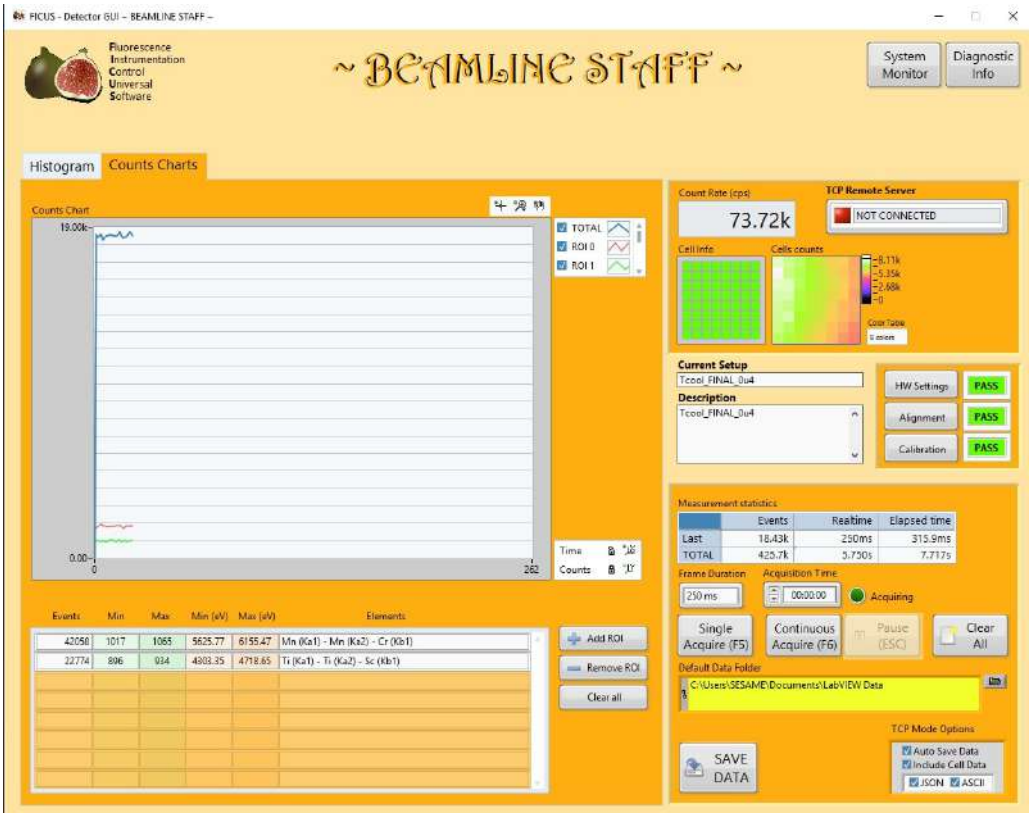

Figure 56: The windows of the FICUS acquisition (Counts Charts), after Alignment and Calibration.

189

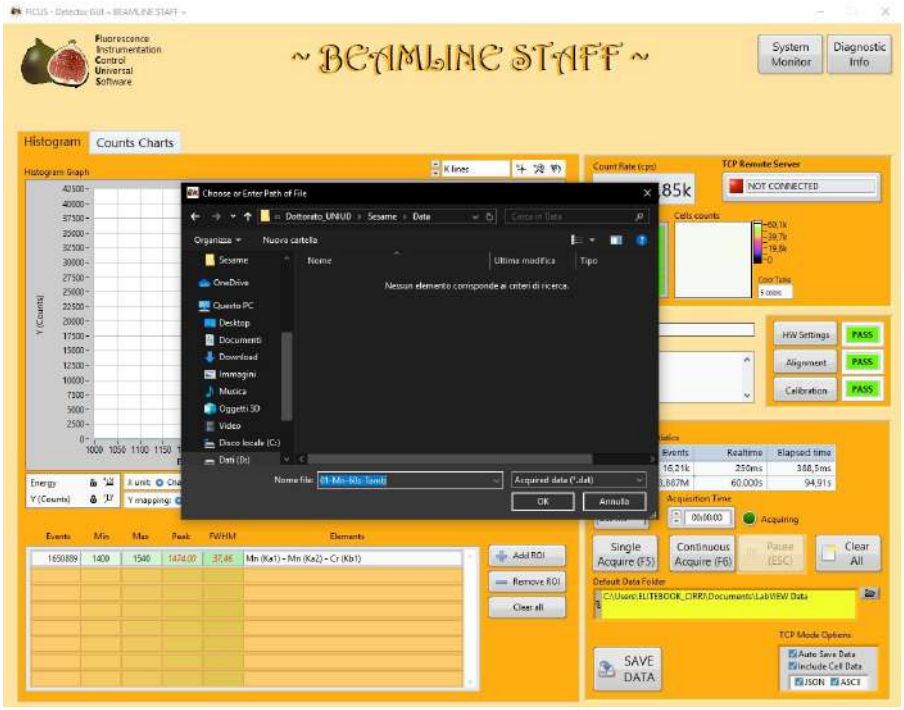

Figure 57: The windows of the FICUS acquisition: saving data.

To switch off the system, carefully follow the switch-off procedure described in the section *Instructions for switching* on on page 53.

To close the FICUS software, from the acquisition window click on the *X*, the FICUS control window will appear [Fig. 58 (a)]. Click on *Disconnect*, a message will open to confirm disconnecting the detector, press *OK*, as shown in Fig. 58 (b). To close the software [Fig. 58 (c)] click on *Quit*, a confirmation message will open, press *OK*, as shown in Fig. 58 (d).

190

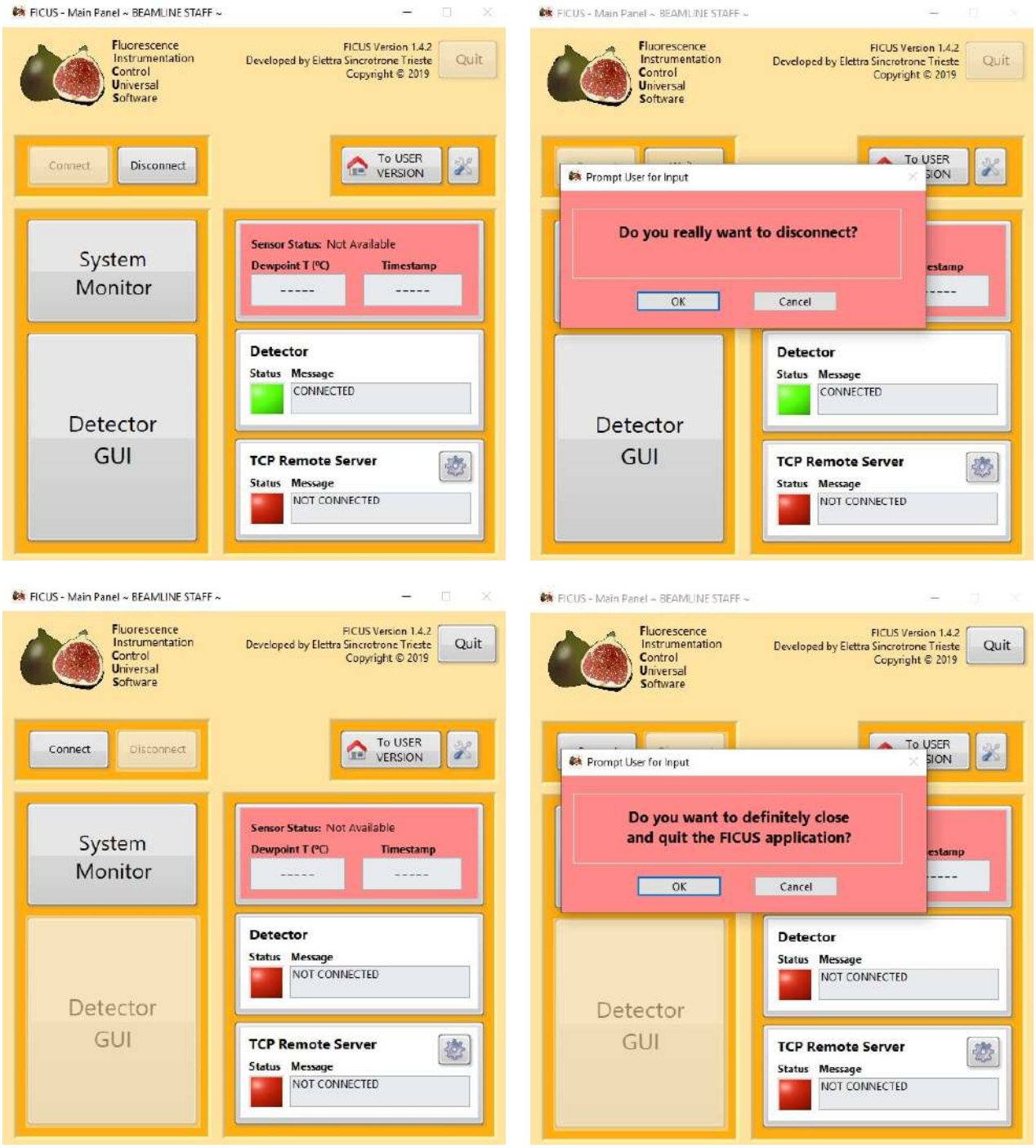

Figure 58: The FICUS control window (**a**) Connected, (**b**) With the message requesting confirmation to disconnect, (**c**) Disconnected, (**d**) Disconnected and with the message requesting confirmation that the program has been closed.

6 Guide for User

Before starting any activity, please take a look at the **Safety warnings for using the SESAME-XAFS Detector System**, on page 52, and the **Instructions for switching on/off**, respectively on page 52 and 53.

This version of the software is useful for the users in order to realize the planned measurements.

Only the FICUS software Beamline Staff version can connect and disconnect the detectors.

After the launch of FICUS software, please refer to the staff beamline for for switching on the detector system, the first window is the one shown in Fig. 59.

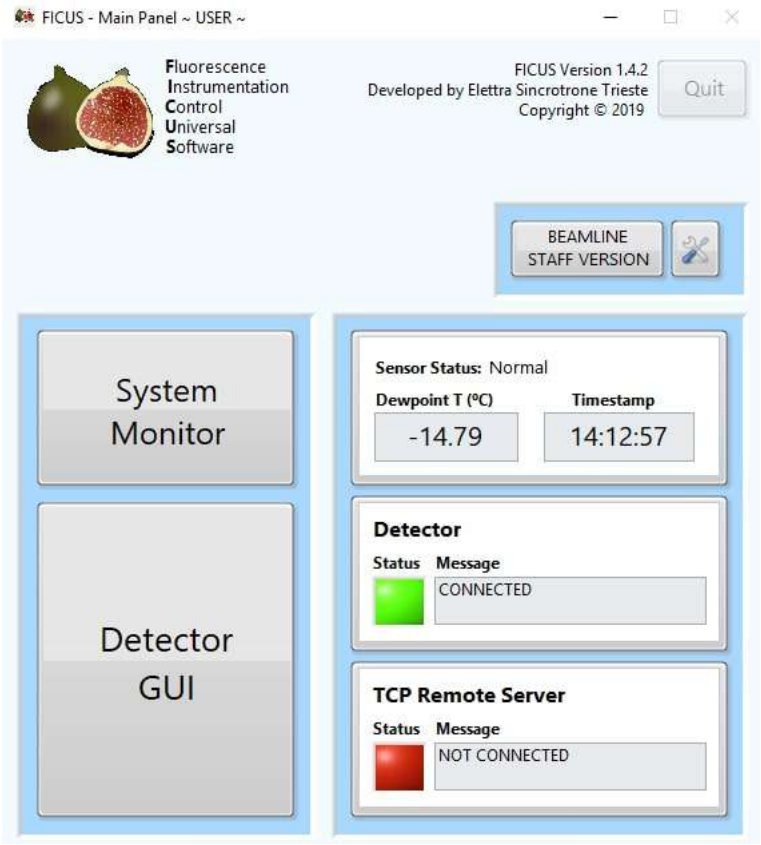

Figure 59: The first window of FICUS software

In the **System Monitor window** it is possible to see the dew point temperature of the system, the time, the status of the detectors and the status of the TCP Remote Server (red disconnected - green connected).

After connect of the detector, it is also possible to click on *System monitor* to know:

- the log of the dew point temperature [in Fig. 60 (a)]
- the log of the temperature of the strips [in Fig. 61 (a)]
- the log of the temperature of the LDOs [in Fig. 61 (b)]
- the log of the temperature of the FPGAs [in Fig. 61 (c)]
- the log of the temperature of the ADCs [in Fig. 61 (d)]
- the table with all the last measured temperatures [in Fig. 60 (b)]

192

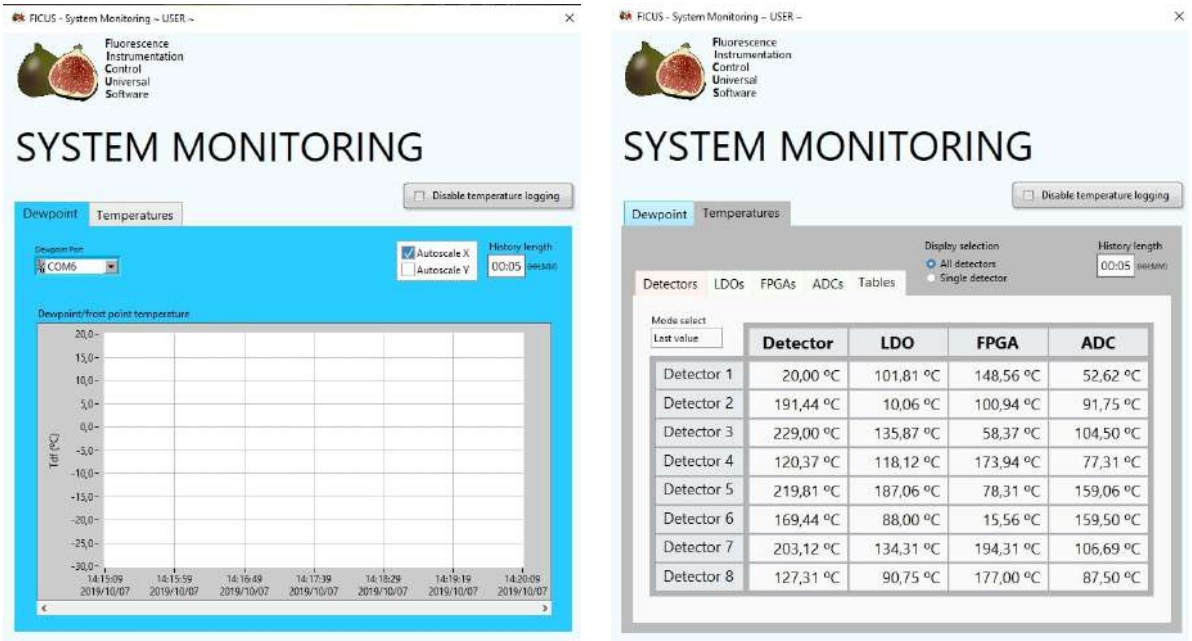

Figure 60: (**a**) The log of the dew point temperature. (**b**) the table with all the last measured temperatures (visible after connecting the detectors).

In the log it is possible to modify the time duration displayed and to set the extremes of the graph, or to set its auto setting.

All settings, channel alignment and calibration must be done, by those who have access, with FICUS Beamline Staff version.

The **FICUS acquisition window** opens, which appears as in Fig. 62. To return to the settings just click on the *HW Setting* button.

On the right of the FICUS acquisition window it is possible to know the count rate of the acquisition (in counts/s), an overview of information on the functioning of the cells and on the counts cell by cell. In addition, the TCP Remote Server connection information is also visible. Under this box, are visible the name and description of the Global Setup in use, and next to them there are buttons to open the *HW Setting*, *Alignment* and *Calibration* windows; next to each of them there is an indicator that has three possible aspects: *PASS* in green (which means that that setting was made), *WARNING* in yellow (which means that that setting has been done previously, but something has been changed since then and you may need to redo the setting), and *FAIL* in red (which means that that setting has never been done before and you need to do the setting).

It is possible to start a measurement by setting the *Frame Duration* and the *Acquisition Time* (in format hh:mm:ss). For a single measurement equal to the duration of the frame click on *Single Acquire (F5)*, for a timed measurement just set the acquisition time and then click on *Continuous Acquire (F6)*. If instead it is wanted to start and stop the measurement manually, it is enough to leave the acquisition time field at zero.

The *Histogram Graph* box [Fig. 63] shows the accumulated graph of the sum signal [it is also possible to display the signal of the single channels by clicking on *Sum (Aligned)* an additional one will appear in which it is possible to choose which channel to display]. It is possible change manually the ends of the axes or you can zoom by clicking on the magnifying glass symbol (to unlock the ladder just click on the bolt symbol). It is possible to choose whether to display the Y axis in linear or logarithmic scale, and the X axis in channels or in eV (this is possible only after having performed the calibration procedure).

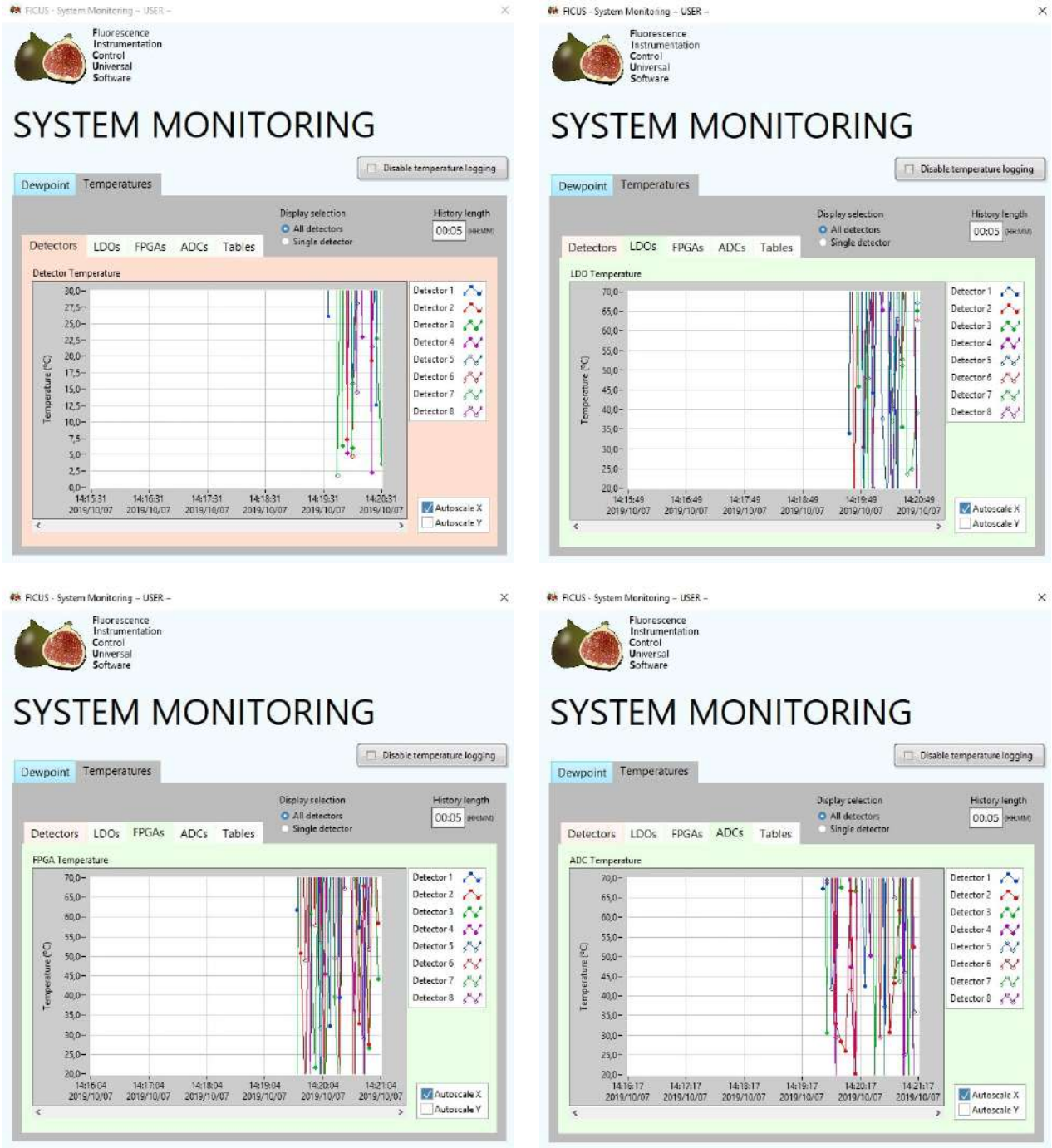

Figure 61: In clockwise direction starting from the top left (the values represented are derived from a simulation and purely figurative) (**a**) The log of the temperature of the strips (**b**) The log of the temperature of the LDOs (**c**) The log of the temperature of the FPGAs (**d**) the log of the temperature of the ASICs.

194

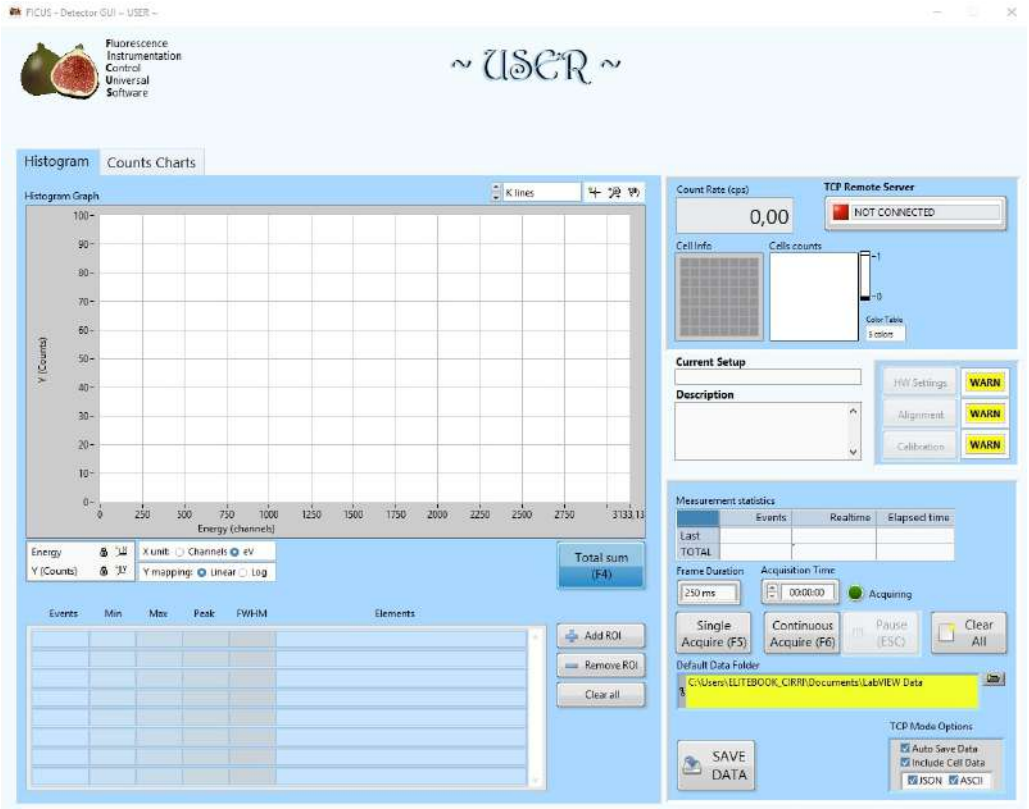

Figure 62: The windows of the FICUS acquisition (Histogram).

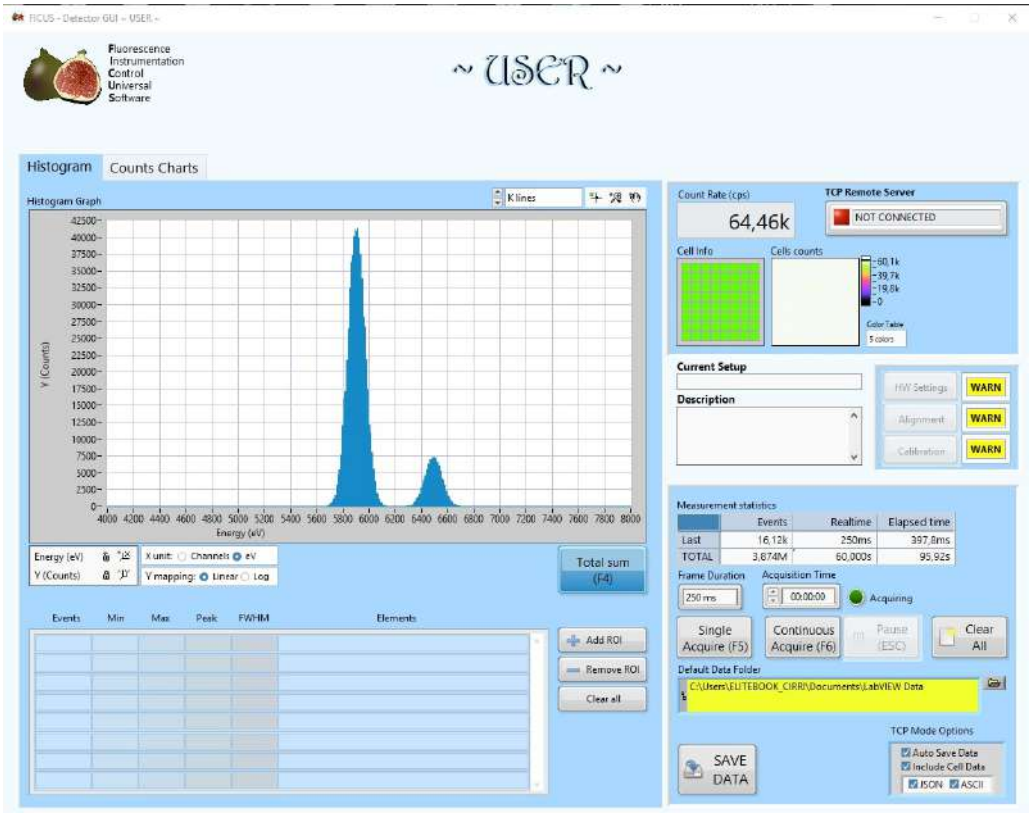

Figure 63: The windows of the FICUS acquisition (Histogram), after a measurement by one minute with a simulated signal.

During or after the acquisition it is possible to select Regions Of Interest (ROI) clicking on *Add ROI* and by positioning the sliders manually; up to 20 different ROIs can be selected (there are 4 colours and they repeat cyclically with no choice) [Fig. 65]. The table below shows the data of each ROI: *Events*, *Min* position, *Max* position, *Peak* position, and an estimate of the *FWHM* (is calculated as the width at half height considering the intersections of the sliders with the signal). If the calibration procedure has been performed, when eV is selected as the X unit, the ROI data also changes the unit of measurement and the table shows the list of the elements that may correspond to the selected peak in the ROI [Fig. 64]. The ROI can be removed individually by clicking on *Remove ROI* and selecting the one to be deleted, or all by clicking on *Clear all*.

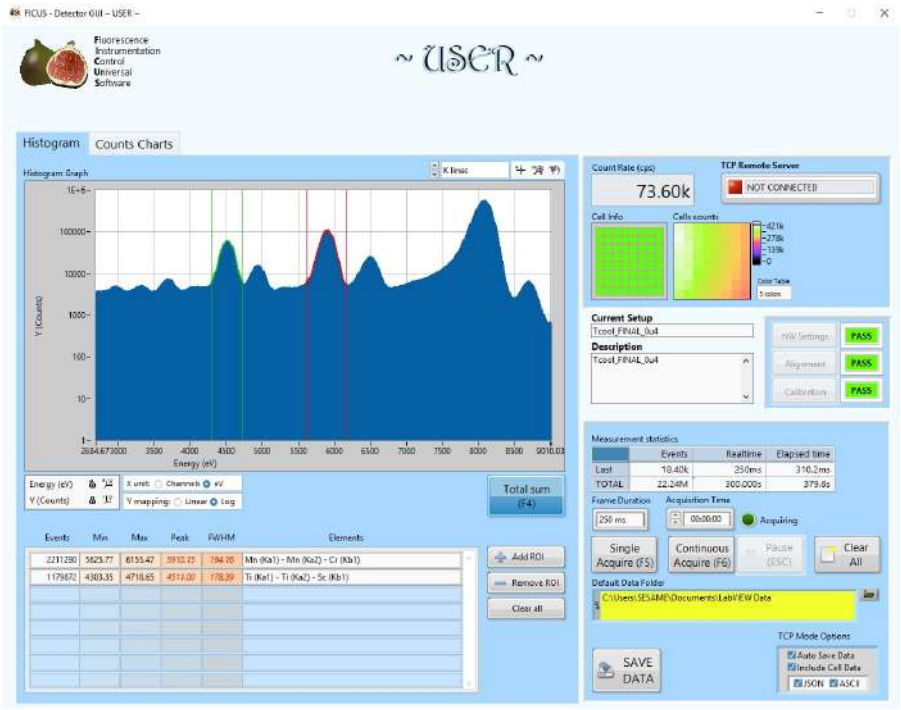

Figure 64: The windows of the FICUS acquisition (Histogram), after a real measurement by five minute.

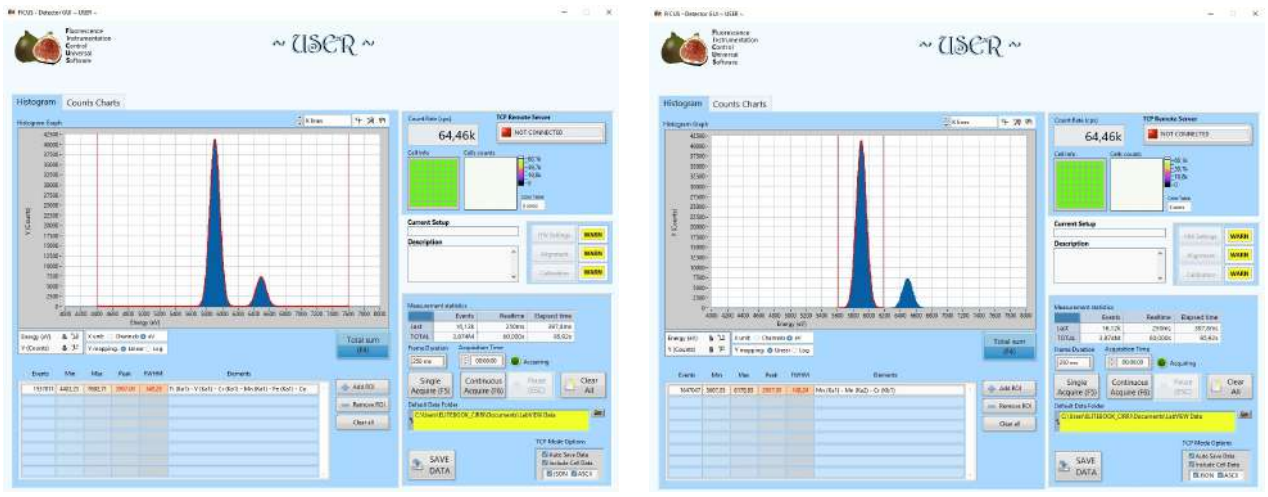

Figure 65: The windows of the FICUS acquisition: adding ROI.

Instead of the histogram, it is possible to display the *Counts Chart* to monitor the number of total counts and ROI counts [Fig. 66].

196

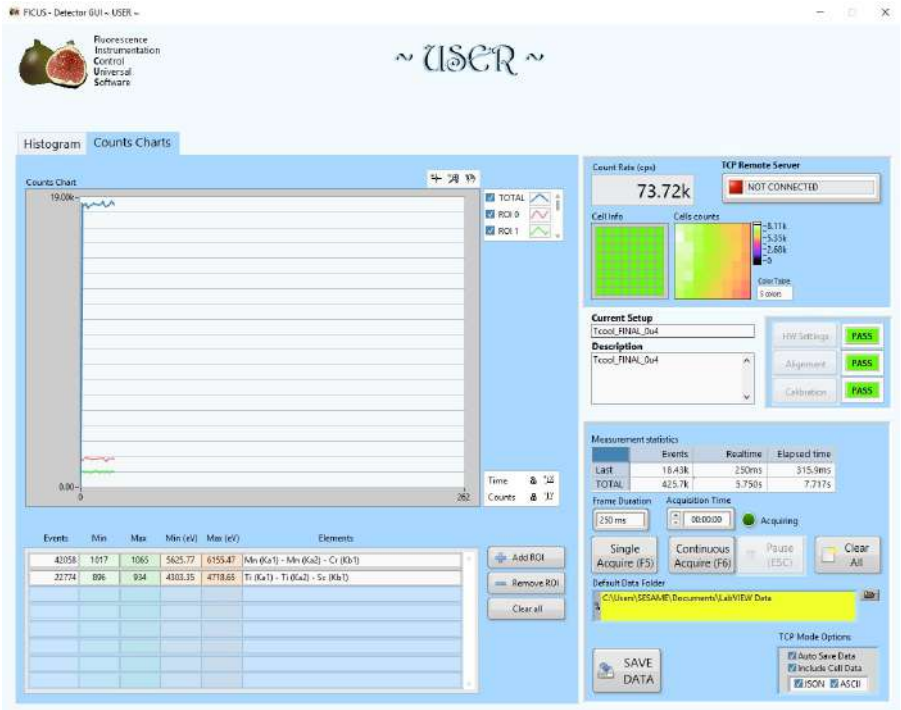

Figure 66: The windows of the FICUS acquisition (Counts Charts), after Alignment and Calibration.

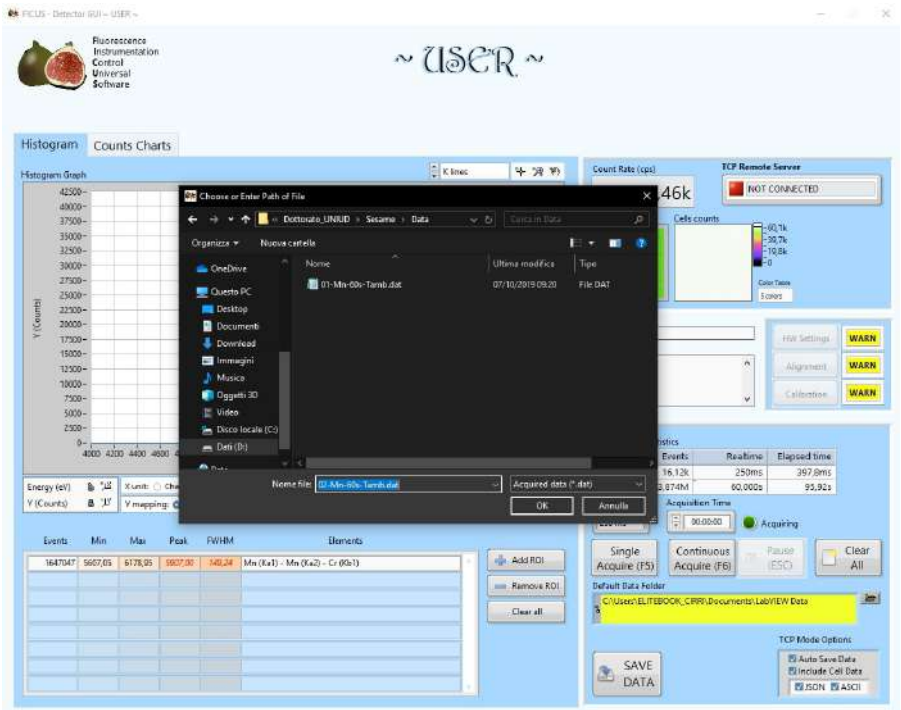

Figure 67: The windows of the FICUS acquisition: saving data.

To save the acquired data and the information related to them, just click on *SAVE DATA*, select the saving folder and indicate the name of the file, as shown in Fig. 67.

To delete the acquisition data, and be ready to start with a new acquisition (continuing to work with the same alignment and calibration) just click on *Clear All*.

Only the FICUS software Beamline Staff version can connect and disconnect the detectors.

197

7 Safety warnings for using the SESAME-XAFS Detector System

To use the SESAME-XAFS detector system correctly and avoid damaging the measuring system, you must carefully follow the on/off instructions and the software user's guide. It's very important:

- Never switch the HV power supply off and/or on suddenly: it is important gradually increase or decrease the voltage
- Never switch the Peltier cells power supply off and/or on suddenly: it is important gradually increase or decrease the voltage
- If the ambient and system temperatures change, it may be necessary to repeat the procedure for loading the appropriate settings, aligning the cells and calibrating the detector
- Make sure that the holes for the nitrogen/dry air vent are not obstructed
- Make sure that when the flushing is switched on (with appropriate flow rate) the window just swells up

7.1 Instructions for switching on

It is very important to follow the switch-on procedure following the steps in order and precisely.

- Turn on the PC
- Start flushing nitrogen / dry air [maximum flow rate of 2 liter/minute]
- Turn on the power supply of the dew point temperature sensor [ch3 - analog power supply]
- Launch FICUS software
- Check that the dew point temperature is below 16 °C
  - Only if it is so, activate temperature stabilization and turn on the chiller set to 18 °C
  - If it is not so, wait for the dew point temperature to drop below this value thanks to the flushing
- Switch on the digital power supply [all ch1, ch2, ch3, ch4 together]
- Switch on the analog power supply [ch1 and ch2 of analog power supply]
- From FICUS software connect the detector system
- From FICUS software load the appropriate settings according to the condition and temperature of use (possible choice of 8 global setups)
- Switch on the HV power supply (setting recall mode1), gradually increase the voltage from 0 V to 60 V on ch1 and then from 0 V to 60 V on ch2
- Wait about 5 minutes for the temperature of the detector to stabilize
- Proceed with cell alignment (o load a previously saved alignment setting)
- Now it is possible activate measurement

198

- After stop the measurement, proceed with the calibration of the detector system (o load a previously saved calibration)
- If you want work in cooling mode (to lower cell temperature), start the instruction for cooling mode

7.2 Instructions for switching off

It is very important to follow the switch-off procedure following the steps in order and precisely.

- Gradually decrease the voltage from 60 V to 0 V on ch2 and then from 60 V to 0 V on ch1, and after switch off the HV power supply
- In FICUS close the acquisition window and disconnect the detector
- Switch off analog power [ch1 and ch2 analog power]
- Switch off the digital power supply [all ch1, ch2, ch3, ch4 together]
- Turn off FICUS software
- Turn off flushing nitrogen / dry air
- For long detector shutdown or if it is necessary, switch off the dew point temperature meter power supply [ch3 - analog power supply] and turn off the chiller
- Turn off the PC

7.3 Instructions for cooling mode

- Before starting the Peltier cell ignition procedure, check that the dew point temperature is below $-12\,^{\circ}C$
- Never switch the Peltier cells power supply off and/or on suddenly: it is important gradually increase or decrease the voltage
- Switching on and off of the Peltier cells have to be gradual: power supply for 0.1 V steps every 2 min (maximum voltage 2 V)
- When the supply voltage of Peltier cells is 2 V, wait at least 5 minutes for the temperature of the detector to stabilize
- When the cooling mode is activated, remember to load the appropriate global settings [Tcool] in FICUS

8 Troubleshooting

In this section some possible errors or problems that may occur, along with how to fix them. **If the problem is not listed, please contact the ReDSoX Collaboration.**

- **TCP-IP or/and FPGA tests aren't successful for one or more strips** - There may be problems with FPGAs or communication boards. Try turning off the system (following the switch-off instructions) and, following the switch-on instructions, try switch it on again from the beginning.

199

- **One or more channels pass from active and functioning to non-active for no apparent reason** - There may be problems with FPGAs or communication boards. Try turning off the system (following the switch-off instructions) and, following the switch-on instructions, try switch it on again from the beginning. If the problem is not solved, try again the shutdown procedure by exiting the software and restarting the PC. And then reactivate everything by following the switch-on procedure. If the problem is not solved even in this way, contact the ReDSoX Collaboration.
- **One or more temperature values have abnormal and different values than normal, or are equal to zero** - Check that the chiller is on and set to the correct value. Try turning off the system (following the switch-off instructions) and, following the switch-on instructions, after a few minutes, try switch it on again from the beginning.
- **The value of the dew point temperature does not decrease with the nitrogen / dry air fluxing** - Check that the nitrogen/dry air flow is active and at the values recommended by the manual. Check that the window is intact and well stretched.
- **The sum signal of the channels appears deformed** - Try realigning the channels.
- **One or more power supplies do not turn on** - Check the correct connection of the power supply to the electric grid.

9 Information & Contact - ReDSoX Collaboration

The FICUS software was developed by Elettra Sincrotrone Trieste.

This software manual (about FICUS 1.4.2.0 and FICUS 1.4.2.1) has been prepared by the testers of the detector system (detector expert) of INFN-Ts.

The SESAME-XAFS detector system implementation is managed by the Istituto Nazionale di Fisica Nucleare (INFN) in collaboration with Elettra Sincrotrone Trieste, within the ReDSoX (Research Drift detectors for Soft X-ray) collaboration by INFN and Elettra (and other entities listed below in alphabetical order) thanks to ad hoc financing from the Ministry of Education, University and Research (MIUR).

In particular, this work has been made within the ReDSoX-2 INFN research project, supported with the contribution of the Italian Ministry of Education, University and Research within the EUROFEL Project and FBK-INFN agreement 2015-03-06.

Appendix D

Outreach

- 3 September 2019 - (talk) Studiare Fisica a Trieste 2019 - *The push towards the development of most advanced new microscopes and telescopes to gain a better comprehension of natural phenomena*, Trieste. Italy
- 21 June 2019 - (talk) Science Corner - *The push towards the development of most advanced new microscopes and telescopes to gain a better comprehension of natural phenomena*, Trieste. Italy
- 15 October 2018 - (talk) *Nuove frontiere dell'astrofisica X e gamma per H.E.R.M.E.S.*. University of Udine, Udine. Italy.

D.1 Talks/Posters

- 23 October 2019 - (talk) *New versatile monolithic multipixel detector systems based on Silicon Drift Detectors.* PhDay2019 - DMIF - UNIUD, Udine. Italy
- 27 September 2019 - (talk) *Novel monolithic array of Silicon Drift Detector systems designed for low-energy X-ray.* 105 Congresso Nazionale della Società Italiana di Fisica, L'Aquila. Italy
- 14 June 2019 - (talk) *The SDD system for TwinMic.* 5th ReDSoX Meeting, Rome. Italy
- 13 June 2019 - (talk) *The XAFS SDD system for SESAME.* 5th ReDSoX Meeting, Rome. Italy
- 3 April 2019 - (poster) *Novel Monolithic Array of Silicon Drift Detector Systems Designed for Low Energy X-ray.* VIII International Course Detectors and Electronics for High Energy Physics, Astrophysics, Space Applications and Medical Physics, INFN National Laboratories of Legnaro. Italy

- 18 October 2018 - (talk) *Characterization of the Detector System for the XAFS beam-line of the synchrotron light source SESAME.* High precision X-ray measurements, INFN-LNF Rome, Italy
- 25 September 2018 - (talk) *Work on GAGG crystals at Uniud.* Project Meeting HERMES, Rome. Italy
- 18 September 2018 - (talk) *Characterization of the Detector System for the XAFS beam-line of the synchrotron light source SESAME.* 104 Congresso Nazionale della Società Italiana di Fisica, Cosenza. Italy [awarded as the first best communication of section 6 - Applied physics, accelerators and cultural heritage]
- 28 May 2018 - (poster) *High precision mapping of single-pixel Silicon Drift Detector for application in astrophysics and advanced light source.* PM2018 - 14th Pisa Meeting on Advanced Detectors. La Biodola, Isola d'Elba. Italy
- 17 April 2018 - (talk) *Silicon Drift Detector: development of a monolithic array dedicated to advanced applications in the field of astrophysics and advanced light source beam lines detection system.* PhDay2018 - DMIF - UNIUD, Udine. Italy
- 3 October 2017 - (talk) *QuadSSD mapping.* Project Meeting, Rome. Italy
- 13 September 2017 - (talk) *Towards fast high energy resolution pixelated silicon drift detectors.* 103 Congresso Nazionale della Società Italiana di Fisica, Trento. Italy
- 6 March 2017 - (talk) *Sviluppo di sensori di silicio per spettroscopia X veloce di alta precisione.* PhDay2017 - DMIF - UNIUD, Udine. Italy
- 17 February 2017 - (talk) *Silicon Drift Detectors (SDD).* XXVII Giornate di Studio sui Rivelatori - Scuola F. Bonaudi, Cogne, Aosta. Italy.

Appendix E

List of Pubblications

- ALESINI, D., et al. *EuPRAXIA@ SPARC_LAB Conceptual Design Report.* 2018.
- BUFON, J., et al. A new large solid angle multi-element silicon drift detector system for low energy X-ray fluorescence spectroscopy. *Journal of Instrumentation,* 2018, 13.03: C03032.
- BUFON, J., et al. Large solid angle and high detection efficiency multi-element silicon drift detectors (SDD) for synchrotron based x-ray spectroscopy. In: *AIP Conference Proceedings.* AIP Publishing, 2019. p. 060061.
- CIRRINCIONE, D., on behalf of the ReDSoX Collaboration. First characterization of the detector system for the XAFS beam-line of the synchrotron light source SESAME. *Nuovo Cimento della Societa Italiana di Fisica C.* 2019, 42(5), 235.
- CIRRINCIONE, D., et al. High precision mapping of single-pixel Silicon Drift Detector for applications in astrophysics and advanced light source. *Nuclear Instruments and Methods in Physics Research Section A: Accelerators, Spectrometers, Detectors and Associated Equipment,* 2019, 936: 239—241.
- EVANGELISTA, Y., et al. Characterization of a novel pixelated Silicon Drift Detector (PixDD) for high-throughput X-ray astrophysics. *Journal of Instrumentation,* 2018, 13.09: P09011.
- FEROCI, M., et al. The large area detector onboard the eXTP mission. In: *Space Telescopes and Instrumentation 2018: Ultraviolet to Gamma Ray.* International Society for Optics and Photonics, 2018. p. 106991C.
- FERRARIO, M., et al. EuPRAXIA@ SPARC_LAB Design study towards a compact FEL facility at LNF. *Nuclear Instruments and Methods in*

Physics Research Section A: Accelerators, Spectrometers, Detectors and Associated Equipment, 2018, 909: 134–138.

- FUSCHINO, F., et al. HERMES: An ultra-wide band X and gamma-ray transient monitor on board a nano-satellite constellation. *Nuclear Instruments and Methods in Physics Research Section A: Accelerators, Spectrometers, Detectors and Associated Equipment,* 2019, 936: 199–203.

- KOUROUSIAS, G., et al. XRF topography information: Simulations and data from a novel silicon drift detector system. *Nuclear Instruments and Methods in Physics Research Section A: Accelerators, Spectrometers, Detectors and Associated Equipment,* 2019, 936: 80–81.

- RACHEVSKI, A., et al. The XAFS fluorescence detector system based on 64 silicon drift detectors for the SESAME synchrotron light source. *Nuclear Instruments and Methods in Physics Research Section A: Accelerators, Spectrometers, Detectors and Associated Equipment,* 2019, 936: 719–721.

- SAMMARTINI, M., et al. Pixel Drift Detector (PixDD) – SIRIO: an X-ray spectroscopic imaging system with high energy resolution at room temperature. *Nuclear Instruments and Methods in Physics Research Section A: Accelerators, Spectrometers, Detectors and Associated Equipment,* 2020, 953: 163114.

Bibliography

[1] *Brochure presenting the sesame project and its history, structure and scientific potential*. http://mag.digitalpc.co.uk/fvx/iop/esrf/sesamebrochure/. Accessed: 2019-08-11.

[2] *Bruce Ravel - Introduction to X-ray Absorption Spectroscopy*. https://www.bnl.gov/ps/userguide/lectures/Lecture-4-Ravel.pdf. Accessed: 2020-01-26.

[3] *Elettra Sincrotrone Trieste*. https://www.elettra.eu/index.html. Accessed: 2019-10-24.

[4] *General diagram of Synchrotron Soleil*. https://upload.wikimedia.org/wikipedia/commons/thumb/6/60/Sch%C3%A9ma_de_principe_du_synchrotron.jpg/1024px-Sch%C3%A9ma_de_principe_du_synchrotron.jpg. Accessed: 2020-01-26.

[5] *H.E.R.M.E.S. - High Energy Rapid Modular Ensemble of Satellites*. http://hermes.dsf.unica.it/. Accessed: 2019-10-17.

[6] *HERMES-SP (High Energy Rapid Modular Ensemble of Satellites - Scientific Pathfinder)*. http://www.hermes-sp.eu/. Accessed: 2019-10-17.

[7] *KETEK GmbH - AXAS-M - SDD Complete System*. https://www.ketek.net/sdd/complete-systems/axas-m/. Accessed: 2019-10-25.

[8] *KETEK GmbH - VITUS H80 - Silicon Drift Detector (SDD)*. www.ketek.net/sdd/vitus-sdd-modules/vitus-h80/. Accessed: 2019-10-25.

[9] *PyMca X-ray Fluorescence Toolkit, developed by the Software Group of the European Synchrotron Radiation Facility (ESRF)*. http://pymca.sourceforge.net/index.html. Accessed: 2019-10-27.

[10] *Redsox Collaboration*. https://web.infn.it/redsox2. Accessed: 2019-10-13.

[11] *Roberta Vecchi - La Fluorescenza X caratteristica*. https://www.ge.infn.it/~prati/Fisica%20Nucleare%20Applicata/articoli/Vecchi_XRF.pdf. Accessed: 2020-01-27.

[12] *Spettroscopia XAS*. https://it.wikipedia.org/wiki/Spettroscopia_XAS. Accessed: 2020-01-27.

[13] *Synchrotron-light for Experimental Science and Applications in the Middle East*. http://sesame.org.jo/sesame_2018/. Accessed: 2019-10-13.

[14] *Understanding energy resolution*. http://atomfizika.elte.hu/muszerek/Amptek/Documentation/Application%20Notes%20and%20FAQs/Understanding%20energy%20resolution.pdf. Accessed: 2020-01-28.

[15] *Xr-100CR Si-PIN X-Ray Detector*. https://www.amptek.com/products/si-pin-x-ray-detectors-for-xrf/xr-100cr-si-pin-x-ray-detector. Accessed: 2020-01-25.

[16] M. Ahangarianabhari, G. Bertuccio, D. Macera, P. Malcovati, M. Grassi, A. Rashevsky, I. Rashevskaya, A. Vacchi, G. Zampa, N. Zampa, et al., *A low-power CMOS ASIC for X-ray Silicon Drift Detectors low-noise pulse processing*, Journal of Instrumentation, 9 (2014), p. C03036.

[17] J. Allison, K. Amako, J. Apostolakis, P. Arce, M. Asai, T. Aso, E. Bagli, A. Bagulya, S. Banerjee, G. Barrand, et al., *Recent developments in geant4*, Nuclear Instruments and Methods in Physics Research Section A: Accelerators, Spectrometers, Detectors and Associated Equipment, 835 (2016), pp. 186–225.

[18] V. Baryshev, G. Kulipanov, and A. Skrinsky, *Review of x-ray fluorescent analysis using synchrotron radiation*, Nuclear Instruments and Methods in Physics Research Section A: Accelerators, Spectrometers, Detectors and Associated Equipment, 246 (1986), pp. 739–750.

[19] G. Bertuccio, M. Ahangarianabhari, C. Graziani, D. Macera, Y. Shi, M. Gandola, A. Rachevski, I. Rashevskaya, A. Vacchi, G. Zampa, et al., *X-Ray Silicon Drift Detector–CMOS front-End System with High Energy Resolution at Room Temperature*, IEEE Transactions on Nuclear Science, 63 (2016), pp. 400–406.

[20] G. Bertuccio, M. Ahangarianabhari, C. Graziani, D. Macera, Y. Shi, A. Rachevski, I. Rashevskaya, A. Vacchi, G. Zampa, N. Zampa, et al., *A Silicon Drift Detector-CMOS front-end system for high resolution X-ray spectroscopy up to room temperature*, Journal of Instrumentation, 10 (2015), p. P01002.

[21] G. Bertuccio and S. Caccia, *Progress in ultra-low-noise ASICs for radiation detectors*, Nuclear Instruments and Methods in Physics Research Section A: Accelerators, Spectrometers, Detectors and Associated Equipment, 579 (2007), pp. 243–246.

[22] G. Bertuccio and S. Caccia, *Noise Minimization of MOSFET Input Charge Amplifiers based on $\Delta\mu$ and ΔN $1/f$ models*, IEEE Transactions on Nuclear Science, 56 (2009), pp. 1511–1520.

[23] G. Bertuccio, D. Macera, C. Graziani, and M. Ahangarianabhari, *A CMOS charge sensitive amplifier with sub-electron equivalent noise charge*, in Nuclear Science Symposium and Medical Imaging Conference (NSS/MIC), 2014 IEEE, IEEE, 2014, pp. 1–3.

[24] D. H. Bilderback, P. Elleaume, and E. Weckert, *Review of third and next generation synchrotron light sources*, Journal of Physics B: Atomic, molecular and optical physics, 38 (2005), p. S773.

[25] F. Billè, G. Kourousias, E. Luchinat, M. Kiskinova, and A. Gianoncelli, *X-ray fluorescence microscopy artefacts in elemental maps of topologically complex samples: Analytical observations, simulation and a map correction method*, Spectrochimica Acta Part B: Atomic Spectroscopy, 122 (2016), pp. 23–30.

[26] J. Bufon, *Soluzioni innovative di rivelatori a deriva di silicio per sorgenti di luce di terza e quarta generazione*, PhD thesis, Università degli Studi di Trieste, 2016.

[27] J. Bufon, M. Ahangarianabhari, P. Bellutti, G. Bertuccio, S. Carrato, G. Cautero, S. Fabiani, G. Giacomini, A. Gianoncelli, D. Giuressi, et al., *A novel multi-cell silicon drift detector for Low Energy X-Ray Fluorescence (LEXRF) spectroscopy*, Journal of Instrumentation, 9 (2014), p. C12017.

[28] J. Bufon, M. Altissimo, G. Aquilanti, P. Bellutti, G. Bertuccio, F. Billè, R. Borghes, G. Borghi, G. Cautero, S. Ciano,

et al., *Large solid angle and high detection efficiency multi-element silicon drift detectors (SDD) for synchrotron based x-ray spectroscopy*, in AIP Conference Proceedings, vol. 2054, AIP Publishing, 2019, p. 060061.

[29] J. Bufon, A. Gianoncelli, M. Ahangarianabhari, M. Altissimo, P. Bellutti, G. Bertuccio, R. Borghes, S. Carrato, G. Cautero, A. Cicuttin, M. Crespo, S. Fabiani, M. Gandola, G. Giacomini, D. Giuressi, G. Kourousias, R. Menk, A. Picciotto, C. Piemonte, A. Rachevski, I. Rashevskaya, S. Schillani, A. Stolfa, A. Vacchi, G. Zampa, N. Zampa, and N. Zorzi, *Towards a multi-element silicon drift detector system for fluorescence spectroscopy in the soft X-ray regime*, X-Ray Spectrometry, 46 (2017), pp. 313–318. cited By 0.

[30] J. Bufon, S. Schillani, M. Altissimo, P. Bellutti, G. Bertuccio, F. Billè, R. Borghes, G. Borghi, G. Cautero, D. Cirrincione, et al., *A new large solid angle multi-element silicon drift detector system for low energy X-ray fluorescence spectroscopy*, Journal of Instrumentation, 13 (2018), p. C03032.

[31] R. Campana, Y. Evangelista, F. Fuschino, M. Ahangarianabhari, D. Macera, G. Bertuccio, M. Grassi, C. Labanti, M. Marisaldi, P. Malcovati, et al., *Characterization of the VEGA ASIC coupled to large area position-sensitive Silicon Drift Detectors*, Journal of Instrumentation, 9 (2014), p. P08008.

[32] R. Campana, F. Fuschino, C. Labanti, L. Amati, S. Mereghetti, M. Fiorini, F. Frontera, G. Baldazzi, P. Bellutti, G. Borghi, et al., *The X-Gamma Imaging Spectrometer (XGIS) onboard THESEUS*, arXiv preprint arXiv:1802.01674, (2018).

[33] M. Caselle, T. Blank, F. Colombo, A. Dierlamm, U. Husemann, S. Kudella, and M. Weber, *Low-cost bump-bonding processes for high energy physics pixel detectors*, Journal of Instrumentation, 11 (2016), p. C01050.

[34] A. Castoldi, C. Guazzoni, G. Montemurro, C. Liu, N. Zorzi, I. Rashevskaya, A. Rachevski, A. Vacchi, G. Zampa, and N. Zampa, *2-D mapping of the response of SDD cells of different shape in monolithic arrays for XRF spectroscopy*, in 2016 IEEE Nuclear Science

Symposium, Medical Imaging Conference and Room-Temperature Semiconductor Detector Workshop (NSS/MIC/RTSD), IEEE, 2016, pp. 1–3.

[35] F. Ceraudo, *Development of space instrumentation for high throughput x-ray astronomy*, Master's thesis, University of Roma Sapienza, 2016.

[36] W. Chen, G. Carini, J. Keister, Z. Li, and P. Rehak, *Development of thin-junction detector*, IEEE Transactions on Nuclear Science, 54 (2007), pp. 1842–1848.

[37] D. Cirrincione, M. Ahangarianabhari, F. Ambrosino, I. Bajnati, P. Bellutti, G. Bertuccio, G. Borghi, J. Bufon, G. Cautero, F. Ceraudo, et al., *High precision mapping of single-pixel Silicon Drift Detector for applications in astrophysics and advanced light source*, Nuclear Instruments and Methods in Physics Research Section A: Accelerators, Spectrometers, Detectors and Associated Equipment, (2018).

[38] A. Di Cicco, G. Aquilanti, M. Minicucci, E. Principi, N. Novello, A. Cognigni, and L. Olivi, *Novel XAFS capabilities at ELETTRA synchrotron light source*, in Journal of Physics: Conference Series, vol. 190, IOP Publishing, 2009, p. 012043.

[39] D. Einfeld, S. Hasnain, Z. Sayers, H. Schopper, and H. Winick, *SESAME, a third generation synchrotron light source for the Middle East region*, Radiation Physics and Chemistry, 71 (2004), pp. 693 – 700. 9th International Symposium on Radiation Physics (ISRP-9).

[40] Y. Evangelista, F. Ambrosino, M. Feroci, P. Bellutti, G. Bertuccio, G. Borghi, R. Campana, M. Caselle, D. Cirrincione, F. Ficorella, et al., *Characterization of a novel pixelated Silicon Drift Detector (PixDD) for high-throughput X-ray astrophysics*, Journal of Instrumentation, 13 (2018), p. P09011.

[41] S. Fabiani, *Development of the multicell SDD for Elettra and SESAME XAFS beamlines*, Nuovo Cimento della Societa Italiana di Fisica C, 40 (2017).

[42] S. Fabiani, M. Ahangarianabhari, G. Baldazzi, P. Bellutti, G. Bertuccio, M. Bruschi, J. Bufon, S. Carrato, A. Castoldi, G. Cautero, et al., *Development and tests of a new prototype detector for the XAFS beamline at Elettra Synchrotron in Trieste*, in Journal of Physics: Conference Series, vol. 689, IOP Publishing, 2016, p. 012017.

[43] M. Feroci, M. Ahangarianabhari, G. Ambrosi, F. Ambrosino, A. Argan, M. Barbera, J. Bayer, P. Bellutti, B. Bertucci, G. Bertuccio, et al., *The large area detector onboard the extp mission*, in Space Telescopes and Instrumentation 2018: Ultraviolet to Gamma Ray, vol. 10699, International Society for Optics and Photonics, 2018, p. 106991C.

[44] F. Fuschino, R. Campana, C. Labanti, Y. Evangelista, M. Feroci, L. Burderi, F. Fiore, F. Ambrosino, G. Baldazzi, P. Bellutti, et al., *HERMES: An ultra-wide band X and gamma-ray transient monitor on board a nano-satellite constellation*, Nuclear Instruments and Methods in Physics Research Section A: Accelerators, Spectrometers, Detectors and Associated Equipment, (2018).

[45] E. Gatti and P. F. Manfredi, *Processing the signals from solid-state detectors in elementary-particle physics*, La Rivista del Nuovo Cimento (1978-1999), 9 (1986), pp. 1–146.

[46] E. Gatti and P. Rehak, *Semiconductor drift chamber—An application of a novel charge transport scheme*, Nuclear Instruments and Methods in Physics Research, 225 (1984), pp. 608–614.

[47] E. Gatti and P. Rehak, *Review of semiconductor drift detectors*, Nuclear Instruments and Methods in Physics Research Section A: Accelerators, Spectrometers, Detectors and Associated Equipment, 541 (2005), pp. 47–60.

[48] A. Gianoncelli, J. Bufon, M. Ahangarianabhari, M. Altissimo, P. Bellutti, G. Bertuccio, R. Borghes, S. Carrato, G. Cautero, S. Fabiani, G. Giacomini, D. Giuressi, G. Kourousias, R. H. Menk, A. Picciotto, C. Piemonte, A. Rachevski, I. Rashevskaya, A. Stolfa, A. Vacchi, G. Zampa, N. Zampa, and N. Zorzi, *A new detector system for low energy X-ray fluorescence coupled with soft X-ray microscopy: First tests and characterization*, Nuclear Instruments and Methods in Physics Research Section A: Accelerators, Spectrometers, Detectors and Associated Equipment, 816 (2016), pp. 113 – 118.

[49] A. Gianoncelli, G. Kourousias, L. Merolle, M. Altissimo, and A. Bianco, *Current status of the TwinMic beamline at Elettra: a soft X-ray transmission and emission microscopy station*, Journal of Synchrotron radiation, 23 (2016), pp. 1526–1537.

[50] A. Gianoncelli, G. Kourousias, A. Stolfa, and B. Kaulich, *Recent developments at the TwinMic beamline at ELETTRA: an 8 sdd detector setup for low energy X-ray Fluorescence*, in Journal of Physics: Conference Series, vol. 425, IOP Publishing, 2013, p. 182001.

[51] C. Guazzoni, *The first 25 years of silicon drift detectors: A personal view*, Nuclear Instruments and Methods in Physics Research Section A: Accelerators, Spectrometers, Detectors and Associated Equipment, 624 (2010), pp. 247–254.

[52] E. J. Jaeschke, S. Khan, J. R. Schneider, and J. B. Hastings, *Synchrotron Light Sources and Free-Electron Lasers: Accelerator Physics, Instrumentation and Science Applications*, Springer, 2016.

[53] G. F. Knoll, *Radiation detection and measurement*, John Wiley & Sons, 2010.

[54] G. Kourousias, F. Billè, G. Cautero, J. Bufon, A. Rachevski, S. Schillani, D. Cirrincione, M. Altissimo, R. Menk, G. Zampa, et al., *XRF topography information: Simulations and data from a novel silicon drift detector system*, Nuclear Instruments and Methods in Physics Research Section A: Accelerators, Spectrometers, Detectors and Associated Equipment, (2018).

[55] A. Longoni, C. Fiorini, C. Guazzoni, S. Buzzetti, M. Bellini, L. Struder, P. Lechner, A. Bjeoumikhov, and J. Kemmer, *Xrf spectrometers based on monolithic arrays of silicon drift detectors: Elemental mapping analyses and advanced detector structures*, IEEE transactions on nuclear science, 53 (2006), pp. 641–647.

[56] B. G. Lowe and R. A. Sareen, *Semiconductor X-ray Detectors*, CRC Press, 2013.

[57] G. Lutz et al., *Semiconductor radiation detectors*, vol. 40, Springer, 1999.

[58] G. Margaritondo, *Synchrotron light: A success story over six decades*, Riv. Nuovo Cim., 40 (2017), p. 1.

[59] M. Marisaldi, C. Labanti, F. Fuschino, and L. Amati, *A broad energy range wide field monitor for next generation gamma-ray burst experiments*, Nuclear Instruments and Methods in Physics Research Section A: Accelerators, Spectrometers, Detectors and Associated Equipment, 588 (2008), pp. 37–40.

[60] M. Marisaldi, C. Labanti, and H. Soltau, *A pulse shape discrimination gamma-ray detector based on a silicon drift chamber coupled to a CsI (Tl) scintillator: prospects for a 1 keV-1 MeV monolithic detector*, IEEE Transactions on Nuclear Science, 51 (2004), pp. 1916–1922.

[61] S. Mobilio, F. Boscherini, and C. Meneghini, *Synchrotron Radiation*, Springer, 2016.

[62] F. Muleri, P. Soffitta, R. Bellazzini, A. Brez, E. Costa, M. Frutti, M. Mastropietro, E. Morelli, M. Pinchera, A. Rubini, et al., *A versatile facility for the calibration of x-ray polarimeters with polarized and unpolarized controlled beams*, in Space Telescopes and Instrumentation 2008: Ultraviolet to Gamma Ray, vol. 7011, International Society for Optics and Photonics, 2008, p. 701127.

[63] M. Newville, *Fundamentals of XAFS*, Reviews in Mineralogy and Geochemistry, 78 (2014), pp. 33–74.

[64] L. Pascolo, V. Borelli, V. Canzonieri, A. Gianoncelli, G. Birarda, D. E. Bedolla, M. Salomé, L. Vaccari, C. Calligaro, M. Cotte, et al., *Differential protein folding and chemical changes in lung tissues exposed to asbestos or particulates*, Scientific reports, 5 (2015), p. 12129.

[65] L. Pascolo, A. Gianoncelli, B. Kaulich, C. Rizzardi, M. Schneider, C. Bottin, M. Polentarutti, M. Kiskinova, A. Longoni, and M. Melato, *Synchrotron soft X-ray imaging and fluorescence microscopy reveal novel features of asbestos body morphology and composition in human lung tissues*, Particle and fibre toxicology, 8 (2011), p. 7.

[66] A. Rachevski, M. Ahangarianabhari, G. Aquilanti, P. Bellutti, G. Bertuccio, G. Borghi, J. Bufon, G. Cautero, S. Ciano, A. Cicuttin, et al., *The XAFS fluorescence detector system based on 64 silicon drift detectors for the SESAME synchrotron light source*,

Nuclear Instruments and Methods in Physics Research Section A: Accelerators, Spectrometers, Detectors and Associated Equipment, 936 (2019), pp. 719–721.

[67] A. Rachevski, M. Ahangarianabhari, P. Bellutti, G. Bertuccio, E. Brigo, J. Bufon, S. Carrato, A. Castoldi, G. Cautero, S. Fabiani, G. Giacomini, A. Gianoncelli, D. Giuressi, C. Guazzoni, G. Kourousias, C. Liu, R. H. Menk, G. V. Montemurro, A. Picciotto, C. Piemonte, I. Rashevskaya, Y. Shi, A. Stolfa, A. Vacchi, G. Zampa, N. Zampa, and N. Zorzi, *First results of a novel Silicon Drift Detector array designed for low energy x-ray fluorescence spectroscopy*, Nuclear Instruments and Methods in Physics Research Section A: Accelerators, Spectrometers, Detectors and Associated Equipment, 824 (2016), pp. 452 – 454. Frontier Detectors for Frontier Physics: Proceedings of the 13th Pisa Meeting on Advanced Detectors.

[68] A. Rachevski, G. Zampa, N. Zampa, I. Rashevskaya, A. Vacchi, G. Giacomini, A. Picciotto, A. Cicuttin, M. L. Crespo, and C. Tuniz, *X-ray spectroscopic performance of a matrix of silicon drift diodes*, Nuclear Instruments and Methods in Physics Research Section A: Accelerators, Spectrometers, Detectors and Associated Equipment, 718 (2013), pp. 353 – 355. Proceedings of the 12th Pisa Meeting on Advanced Detectors.

[69] A. Rashevsky, V. Bonvicini, P. Burger, P. Cerello, E. Crescio, P. Giubellino, R. Hernández-Montoya, A. Kolojvari, L. Montano, D. Nouais, et al., *Characteristics of the alice silicon drift detector*, Nuclear Instruments and Methods in Physics Research Section A: Accelerators, Spectrometers, Detectors and Associated Equipment, 461 (2001), pp. 133–138.

[70] A. Rashevsky, V. Bonvicini, P. Burger, S. Piano, C. Piemonte, and A. Vacchi, *Large area silicon drift detector for the alice experiment*, Nuclear Instruments and Methods in Physics Research Section A: Accelerators, Spectrometers, Detectors and Associated Equipment, 485 (2002), pp. 54–60.

[71] B. Ravel and M. Newville, *Athena, artemis, hephaestus: data analysis for x-ray absorption spectroscopy using ifeffit*, Journal of synchrotron radiation, 12 (2005), pp. 537–541.

[72] P. Rehak, E. Gatti, A. Longoni, J. Kemmer, P. Holl, R. Klanner, G. Lutz, and A. Wylie, *Semiconductor drift chambers for position and energy measurements*, Nuclear Instruments and Methods in Physics Research Section A: Accelerators, Spectrometers, Detectors and Associated Equipment, 235 (1985), pp. 224–234.

[73] L. Rossi, P. Fischer, T. Rohe, and N. Wermes, *Pixel detectors: From fundamentals to applications*, Springer Science & Business Media, 2006.

[74] M. Sakano, T. Nakamori, S. Gunji, J. Katagiri, S. Kimura, S. Otake, and H. Kitamura, *Estimating the radiative activation characteristics of a Gd3Al2Ga3o12: Ce scintillator in low earth orbit*, Journal of Instrumentation, 9 (2014), p. P10003.

[75] H. Schopper, *Italian Physical Society: The light of SESAME: A dream becomes reality*, Nuovo Cimento, Riv., 40 (2017), pp. 199–239.

[76] J. V. Smith, *Tutorial review. synchrotron x-ray sources: instrumental characteristics. new applications in microanalysis, tomography, absorption spectroscopy and diffraction*, Analyst, 120 (1995), pp. 1231–1245.

[77] V. Solé, E. Papillon, M. Cotte, P. Walter, and J. Susini, *A multiplatform code for the analysis of energy-dispersive x-ray fluorescence spectra*, Spectrochimica Acta Part B: Atomic Spectroscopy, 62 (2007), pp. 63–68.

[78] H. Spieler, *Semiconductor detector systems*, vol. 12, Oxford university press, 2005.

[79] L. Strüder, P. Lechner, and P. Leutenegger, *Silicon drift detector–the key to new experiments*, The Science of Nature, 85 (1998), pp. 539–543.

[80] S. M. Sze and K. K. Ng, *Physics of semiconductor devices*, John wiley & sons, 2006.

[81] A. Vacchi, A. Castoldi, S. Chinnici, E. Gatti, A. Longoni, F. Palma, M. Sampietro, P. Rehak, and J. Kemmer, *Performance of the ua6 large-area silicon drift chamber prototype*, Nuclear Instruments and Methods in Physics Research Section A: Accelerators, Spectrometers, Detectors and Associated Equipment, 306 (1991), pp. 187–193.

[82] A. Vacchi, P. Cox, P. Giacomelli, A. Castoldi, S. Chinnici, E. Gatti, A. Longoni, F. Palma, M. Sampietro, P. Rehak, et al., *Beam test of a large area silicon drift detector*, Nuclear Instruments and Methods in Physics Research Section A: Accelerators, Spectrometers, Detectors and Associated Equipment, 326 (1993), pp. 267–272.

[83] T. Yanagida, Y. Fujimoto, M. Koshimizu, K. Watanabe, H. Sato, H. Yagi, and T. Yanagitani, *Positive hysteresis of Ce-doped GAGG scintillator*, Optical Materials, 36 (2014), pp. 2016–2019.

[84] M. Yoneyama, J. Kataoka, M. Arimoto, T. Masuda, M. Yoshino, K. Kamada, A. Yoshikawa, H. Sato, and Y. Usuki, *Evaluation of GAGG: Ce scintillators for future space applications*, Journal of Instrumentation, 13 (2018), p. P02023.

Acknowledgements

I thank first of all the men and women who are part of the ReDSoX Collaboration from a human and professional point of view: it has been a pleasure to share with them these three years that have enriched and strengthened me, and it has been an honor to learn from them and work with them that have trained and guided me in scientific research and technological development. I also thank you because you are represented, and this was clear to me when for the first time I saw you all together at the first annual meeting of collaboration, all together: everyone who knows his field perfectly and does his job perfectly, but only the union of all can give a much greater value to what you do. The example that comes to mind is that of a house: every piece is important and every worker to build it does his best... but only by working together can they make the individual pieces together really become a house. A special thanks goes to those who in these years have allowed me to do all this, dedicating me patience and time, and passing on to me their knowledge and their way of working: Nicola, Gigi, Giulio, Sasha, Irina, Pino, Yuri, Marco, Fabio, Riccardo, Claudio, Stefano, Jernej, Bepo, Luigi, Matias, Nicola, Ralf, Alessandra, George, Giuliana and Luca.

I want to thank the professor Vacchi for being a mentor for me along the way, always acting as a guide but leaving me the opportunity to grow, and to discover and take the path most congenial to me.

A special thanks to my family that has always supported me and is always close even if far away, and to Marco his presence and his support.

A thought to those who shared with me joys and delusions, coffee (so many!), lunches or trips to Trieste: thanks Kevin, Marco & Debora (the last night of thesis was the sweetest thanks to you!), Emiliano, Marta, Nicolò, Andrea and Peppe! And thanks to Anna, who has been close to me in every circumstance, and who has attended to the growth of this thesis!

And thankful to me for having the courage to embark on this new adventure, it was tough, but I wouldn't change anything about what I did and what brought me here.